UNIVERSITÀ DI SIENA 1240

Dipartimento di Biotecnologie, Chimica e Farmacia

**Dottorato in Chemical and Pharmaceutical Science**

35° Ciclo

Coordinatore: Prof. Stefano Mangani

# Small organic molecules engineering for the optimization of components in new-generation photovoltaics

Settore scientifico disciplinare: CHIM-06

*Candidato/a*
Rossella Infantino
Consiglio Nazionale delle Ricerche (CNR)
Istituto di Chimica dei Composti
Organometallici (ICCOM)

*Firma digitale del/della candidato/a*
Rossella Infantino
29.05.2023
09:10:12
GMT+01:00

*Supervisore*
Maurizio Taddei
Università degli studi di Siena

*Co-supervisore/i*
Gianna Reginato
Consiglio Nazionale delle Ricerche (CNR)
Istituto di Chimica dei Composti
Organometallici (ICCOM)

Anno accademico di conseguimento del titolo di Dottore di ricerca

2022/23

Università degli Studi di Siena
Dottorato in Chemical and Pharmaceutical Sciences
35° Ciclo

*Data dell'esame finale*
07/06/2023
*Commissione giudicatrice*
*Matteo Bonomo*
*Luca de Vico*
*Robert Langer*
*Barbara Richichi*

# Table of Contents

## Chapter 1: Introduction 1

## Chapter 2: Enhanced light harvesting efficiency by Foster Resonance Energy Transfer in Dye-Sensitized Solar Cells (DSSCs) 40

## Chapter 3: Testing novel combinations of organic dyes with copper-based electrolytes in dye-sensitized solar cells 94

## Chapter 4: Hole Transporting Materials (HTM) for Perovskite Solar Cells 125

# Abstract

This Ph.D. work involves the design, synthesis, and characterization of some new organic materials as components for new generation photovoltaics. Among new generation photovoltaics, dye-sensitized solar cells (DSSC) stand out for their simple manufacturing and peculiar working mechanism while and perovskite solar cells (PSCs) display remarkable high efficiencies. For these reasons these kind of devices have been the matter of great attention in recent years, aiming to optimize their components in order to improve efficiencies.

The first part of this work is related on the synthesis and characterization of a new organic photosensitizer designed for improving Light Harvesting Efficiency (LHE) in DSSC. In particular we focused on a metal-free antenna (donor) - sensitizer (acceptor) covalent adduct (dyad), aiming to obtain a molecular system characterized by high molar attenuation coefficient and broad absorption spectrum in the visible region. Our target was that of exploiting Förster Resonance Energy Transfer (FRET) as a mean to transfer energy within the new antenna-acceptor system. To do that two molecular fragments with complementary light absorption properties were designed and prepared to be joined together using a "click" reaction as late-stage connection. The molecular fragments and the final dyad were spectroscopically characterized using absorption and emission spectroscopy techniques, and it was possible to prove that energy transfer occurred between the two units.

In the second part of the work the fabrication and testing of DSSC devices during a period of visiting of Prof. Marina Freitag's laboratory at Newcastle University is discussed. Three different sensitizers, developed by our research group, were employed together with three copper-based redox mediators, which are particularly suitable for indoor applications. Co-sensitization with commercially available organic sensitizers was also tested as a complementary method to expand absorption. Such experiments showed how the dyes were suitable for application in DSSCs in combination with Cu complex-based liquid electrolytes, one of them reaching a remarkable efficiency.

In the third part of this Ph.D. project two new Hole Transporting Materials (HTM) for PSC were prepared.  The project was carried out in collaboration with the group of Prof. Aldo Di Carlo at C.H.O.S.E., University of Rome Tor Vergata, were the work of fabrication and characterization of the devices was carried out. The HTMs were characterized by a dimeric structure featuring two different phenothiazine (PTZ) cores, in order to induce a different geometric orientation of the donor units, in turn influencing the compounds packing in the solid phase and possibly affecting the performances of the devices. Before carrying out the synthesis, detailed computational study were performed in collaboration with Prof. Adalgisa Sinicropi, University of Siena. The two compounds were prepared efficiently using Pd-catalyzed couplings, a family of catalytic reactions which represent one of the most straightforward and general methods for the preparation of photovoltaic materials and provided very good efficiencies when used to prepare PSC with "inverted" dopant-free *p-i-n* structure, a cell architecture which has been identified as a promising strategy to yield devices with a high intrinsic stability.

# Chapter 1

# Introduction

## 1.1. Climate change: Global overview

According to a recently-published document by NASA "Global warming is the long-term heating of Earth 's surface observed since the pre-industrial period (between 1850 and 1900) due to human activities, primarily fossil fuel burning, which increases heat-trapping greenhouse gas levels in Earth's atmosphere. Since the pre-industrial period, human activities are estimated to have increased Earth's global average temperature by about 1 degree Celsius (1.8 degrees Fahrenheit), a number that is currently increasing by more than 0.2 degrees Celsius (0.36 degrees Fahrenheit) per decade. The current warming trend is unequivocally the result of human activity since the 1950s and is proceeding at an unprecedented rate over millennia" (Figure 1.1).[1]

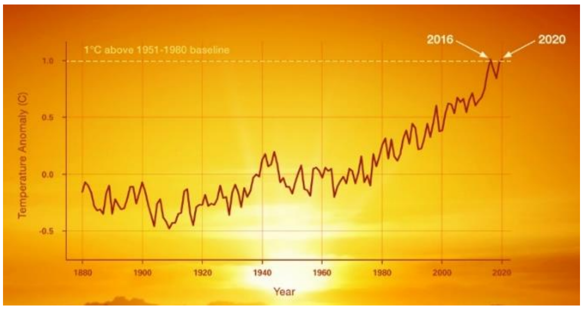

Figure 1.1: *change in global surface temperature relative to 1951-1980 average temperatures, with the year 2020 tying with 2016 for the hottest on record.*[1]

In the past decade, the need for a global transition of the energy system has increased, in response to wide-ranging goals related to climate change and decarbonisation, energy security, job creation, equity and energy access.[2] To achieve these goals, decision makers have enacted new renewable energy policies. In May 2021, the International Energy Agency (IEA) published its "Net Zero by 2050" scenario, which underscores the urgency of ending fossil fuel use.[3] In the lead-up to the United Nations (UN) Climate Conference (COP26) in November 2021, 151 countries submitted new and updated Nationally Determined Contributions towards reducing greenhouse gas emissions under the Paris Agreement.[4]

Furthermore, the year 2021 showed the end of cheap fossil fuels. Starting in September, price of coal, oil and natural gas has reached the highest recorded levels, surpassing the 1973 oil crisis. This was caused by resurgence of energy demand after COVID-19 lockdowns and was exacerbated by the Russian Federation invasion of Ukraine, contributing to an unprecedented worldwide commodity shock. In response to high energy prices, many countries responded with short-term strategies to diversify fossil fuel imports, ramp up production and subsidise energy use to shield consumers. Most of these have benefited the fossil fuel industry, leading to rapidly rising profits and dangerously locking the world into a path of even faster global warming. Given that "we are facing the biggest global energy crisis in history",[5] the exploitation of renewable sources such as solar energy, wind energy, etc. has become unavoidable.

Indeed, the interest in this field is currently increasing even though with significant differences depending to the type of source and sector of use.

## 1.2. Renewable energy trends: Power

Considering trends in the final energy use, it has been observed that the renewable share of the “worst-performing” sectors has grown the slowest. Between 2015 and 2019, the renewable share in transport increased only 0.5 percentage points, while in heating and cooling it grew only one percentage point. The share of renewables in the power sector, meanwhile, increased more than three percentage points. At the same time, these percentage point increases corresponded to larger growth of the share in each sector – 13.5% in power, 9.7% in heating and cooling, 15.1% in transport (Figure 1.2).[5]

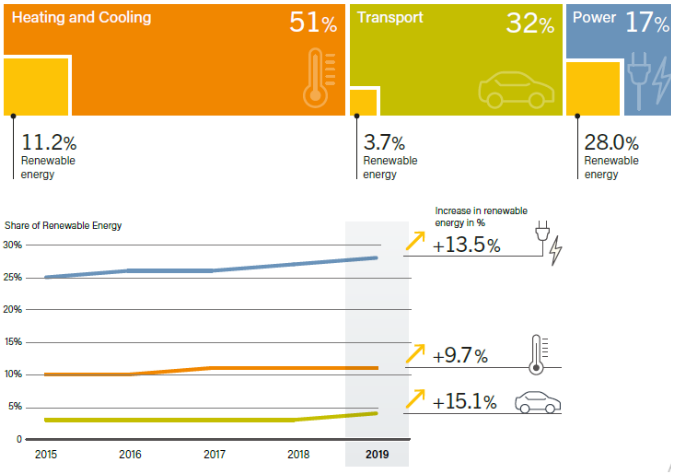

Figure 1.2: *renewable energy in total final energy consumption, by final energy use, 2019.*[5]

During a year of tentative economic recovery, the renewable power sector took a large step forward, deploying a record amount of new capacity and extending to new geographic areas. Renewable power capacity additions grew 17% in 2021 to reach a new high of more than 314 GW of added capacity, driven by the record expansion in solar PV and wind power[5,6] (Figure 1.3). Worldwide, the total installed renewable power capacity grew 11% to reach around 3146 GW. However, these trends remain far from the deployment needed to keep the world on track to reach net zero emissions by 2050. To reach the average milestones set by the IEA’s “Net Zero” scenario by 2050, and by the World Energy Transitions Outlook scenarios from the International Renewable Energy Agency (IRENA), the world would need to add 825 GW of renewables each year until 2050[7] (Figure 1.3, bottom). Among renewables, solar PV and wind power comprised the bulk of new power additions, driven by supportive government policies and low costs. After staying resilient in 2020, these markets saw significant growth in 2021, with solar PV up 26% and wind power up 7%.

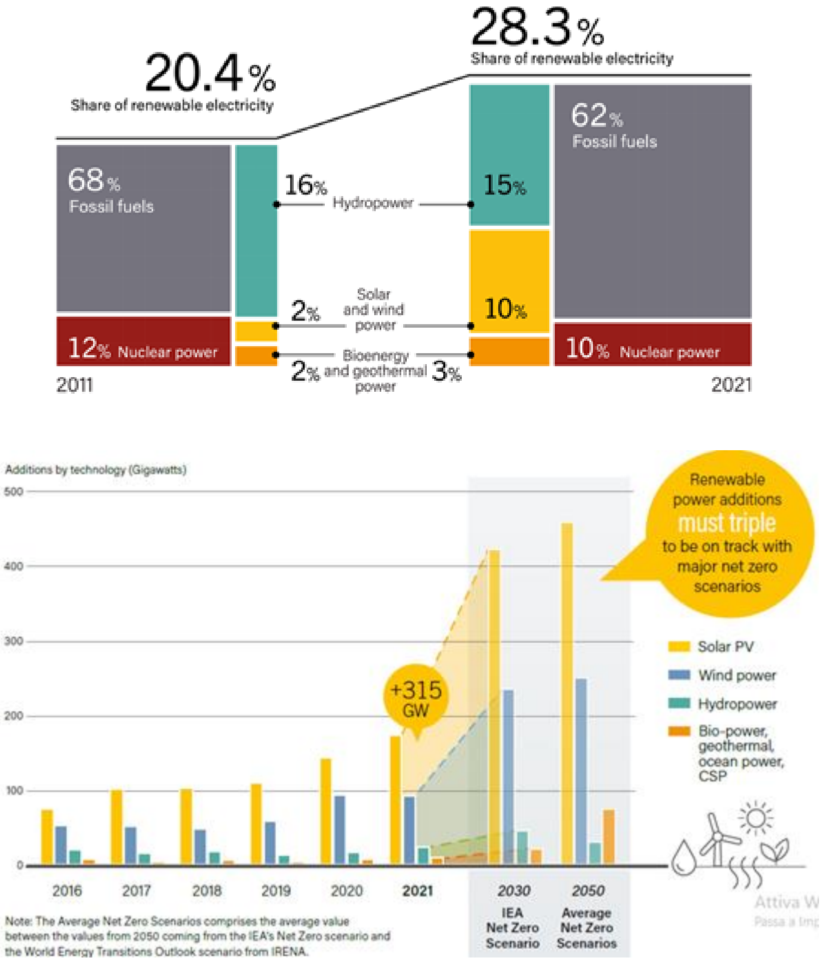

Figure 1.3*: (top) share of renewable energy in electricity generation* 2011 and 2021; (bottom) *annual additions of renewable power capacity, by technology and total, 2016-2021, and additions required to achieve net zero scenarios for 2030 and 2050.*[5]

Although capacity additions for onshore wind power decreased in 2021 compared to 2020, 16 GW of offshore wind additions propelled the market to record-setting overall additions of 102 GW, representing 32% of the renewable energy total. Hydropower capacity additions reached 27 GW, due to the commissioning of several large projects in China. The remaining renewable energy additions were from bio-power and, to a lesser extent, geothermal and ocean power. The solar photovoltaics (PV) market maintained its record-breaking streak with new capacity installations totalling an estimated 175 gigawatts (GW) in 2021, increasing 36 GW compared to 2020.[5,8] This was the largest annual capacity increase ever recorded and brought the cumulative global solar PV capacity to 942 GW (Figure 1.4). The market continued its steady growth despite disruptions across the solar value chain, due mainly to sharp increases in the costs of raw materials and shipping. Solar PV generation continued to play a substantial role in numerous countries. By the end of 2021, at least seven countries had enough capacity installed to meet at least 10% of their electricity demand from solar PV, up from only two countries in 2020.

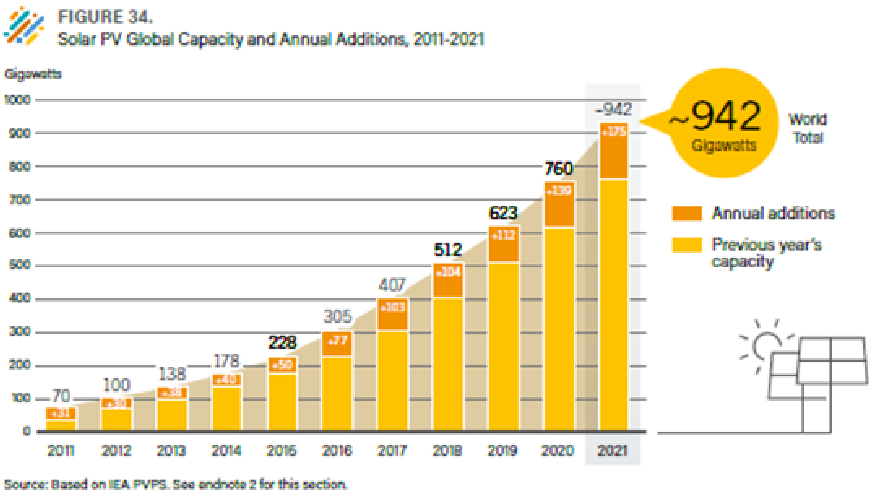

Figure 1.4: *solar PV global capacity and annual additions, 2011-2021.*[5]

## 1.3. Progress in photovoltaics

As can be inferred by the previous discussion, solar energy has a tremendous potential as a clean, abundant, widely distributed and economical energy source, but, despite the increasing commercial success of PV systems, it still has some drawbacks that limit its further exploitation: it is diffuse (ca. 170 W $m^{-2}$) and intermittent, so it must be converted into useful forms of energy (electricity or fuel) that can be stored and distributed.

Photovoltaic devices, *i. e.* devices able to directly convert light into electricity, are the most widely used solar energy technology not only because they are relatively cheap, but also due to their simplicity of installation and use. The first device was developed in the 1950’s at Bell Laboratories, using a silicon-based semiconductor.[9] Since then, PV technology has seen many developments, especially over the last 30 years, in terms of device characteristics as well as applications:[10] for instance, Si-based panels have been used for decades in space applications, supplying power to satellites. Moreover, PV technologies are well suited for application in remote regions, such as desert areas, where other sources such as wind energy and wave energy cannot be used due to the geographical constraints.[11]

The working principle of a photovoltaic cell requires a material, or a combination of materials, able to harvest visible light and use the absorbed energy to generate separated electrons and holes, which can then be used to produce an electric current (*see below*). Based on the nature and physical properties of the materials employed, three main classes of solar cells can be identified:

- Silicon-based solar technology (*First generation*)
- Thin-film PV cells (*Second generation*)
- Emerging (organic and hybrid) photovoltaics (*Third generation*)

### 1.3.1. First generation: Silicon-Based Solar Cells

More than 90% of today's commercial PV systems use crystalline silicon cells.[12] The success of these devices is based not only on their long lifetime, good efficiency and low installation costs, but also on the fact that the key materials used are abundant, nontoxic and easy to recycle at end-of-life of the cell. The semiconductor used can be mono- or polycrystalline silicon. Monocrystalline solar cell are made using a single crystal of silicon (Si), produced with high accuracy by the Czochralski process.[13] Although monocrystalline solar modules are more efficient, reaching a record solar-to-power efficiency of 24.4%[14] (for a definition *see below*, paragraph 1.6.) they are also more expensive because of the higher production costs of the semiconducting material and the complicated production procedures; for this reason, modules based on polycrystalline silicon are those most commonly applied in practice (record efficiency: 20.4%).[14] This technology is based on the concept of the *p-n* junction, consisting of two consecutive silicon semiconductor slices with opposite doping. This *wafer* of approximate 200-300 µm thickness, is created by doping the growing crystals of silicon with 0.1% of atoms of Group III (B or Al for *p*-type silicon) and Group V (P o As for *n*-type silicon). At the interface, the electrons flow from the negative region to the positive one, generating an in-built electric field and creating the so-called *space-charge region*. When light hits the device at a proper angle of impact, electrons in the p-type region are promoted to the conduction band, leaving holes in the valence band. The electron-hole pairs diffuse toward the space-charge region; once there, electrons are taken across the junction by action of the in-built potential ($V_{bi}$), leaving holes behind (charge separation). Once in the n-region, the electrons then diffuse towards the contact and enter the external circuit. The cycle is over when such electrons re-enter the device and fill the holes at the p-side.[15] The same, but opposite, process happens for holes generated on the n-side (Figure 1.5).

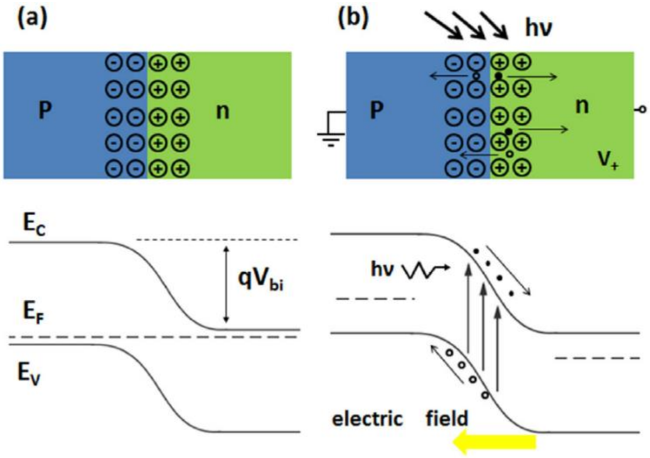

Figure 1.5*: diagram of a p-n junction (a) at the equilibrium and (b) under illumination (Reproduced from ref.* [16]*).*

## 1.3.2. Second generation: Thin Film Technology

Thin- films solar cells are made by deposing several thin layers of photovoltaic and semiconducting materials on a substrate such as glass, plastic or metal. They are very much thinner than first- generation crystalline silicon solar cells, since their thickness can vary from few hundred nanometers to tens of micrometers. Their flexibility, lightness and attractive look make them the perfect candidates for buildings integration.[17] The working principle of these devices is once again based on a p-n junction, in which cadmium sulfide (CdS) generally represents the n-side and several different materials are used as light-harvesting p-side. Depending on the semiconductors used in combination with CdS, thin films solar panels can be divided into five categories:

*1. Amorphous Silicon (a-Si)*[18]*:* the most widely used thin-film technology and the most similar to the standard silicon wafer panel. Amorphous silicon is a much better option than its counterparts (CdTe, CIGS) in terms of toxicity and durability. In addition to that, the amount of silicon used is lower than in traditional Si–based cells and manufacturing is more economic. On the other hand, such kind of cells are less efficient (highest efficiency, 14.0% [19]) and thus are typically used for small load requirements like consumer electronics.

*2. Cadmium Telluride (CdTe)*[20]*:* the second most popular thin film option after a-Si. Despite being potentially competitive with silicon in terms of high efficiencies (22.1 %),[19] CdTe unfortunately presents other significant drawbacks: cadmium is a relatively toxic element, and tellurium supplies are limited.

*3. Copper Indium Gallium Selenide (CIGS)*[21]*:* this class of cells reached efficiencies as high as 23.3%.[19] Unfortunately, also in this case, the use of rare and toxic elements such as indium and gallium would produce not negligible environmental problems.

*4. Copper zinc tin sulfide (CZTSSe)*[22]*:* this material, also known as kesterite, is an attractive alternative to CIGS since it is composed by non-toxic, earth-abundant and low-cost elements. Despite that, the current relatively low efficiencies (13.3%)[19] still prevent a commercial application of this technology.

5. *Gallium Arsenide (GaAs)*[23]: the most expensive among thin-film technologies, GaAs holds a world record 28.8% efficiency for all single-junction solar cells. Due to their cost and the scarcity of gallium reserves, these devices are primarily used for technologically advanced applications (*e. g.* on spacecrafts) or for versatile, mass-scale installments of PV energy in unusual environments.

Despite their very good qualities, the market diffusion of thin-film cells never reached more than 20% in the last 30 years and has recently declined to less than 10%.[12]

## 1.3.3. Third generation: emerging PV technologies

Devices based on single p-n junction are bound by the Shockley-Queisser limit, a thermodynamic theory which sets a maximum efficiency that cannot be overcome. Semiconductors can absorb only photons with energy equal or higher respect to their own band gap, so electrons excited by photons with higher energy relax to the band edges, releasing surplus energy as heat (thermalization loss). For this reason, this maximum conversion efficiency depends on the proper band gap energy of each photovoltaic material inside the cell and can vary from 31% to 41%.[24] Emerging photovoltaics are new generation solar cells which are potentially able to overcome the Shockley-Queisser limit to achieve higher efficiencies. The main possibility to achieve this goal is to build multi-junction cells containing layers of various different photoactive materials. The sum of their different band gaps leads to an expansion of the solar spectrum range of absorption.[25] In this regard, impressive results have been obtained with a four-junction cell made of Ga-As-In-based semiconductors, under a concentrator photovoltaic system. This has set the world record to an impressive 47% of solar-to-power efficiency,[19] but the high costs of production limit any practical application.

During the past two decades, alternative designs of PV cells based on molecular organic systems and hybrid organic/inorganic materials have been developed. This category includes: dye-sensitized solar cells (DSSC),[26] organic photovoltaics (OPV)[27] and perovskite solar cells (PSCs).[28] DSSC and OPV are based on the use of organic or metal-organic light-harvesting materials, and can in principle offer many advantages compared to first and second generation technologies, such as easier building integration (windows, façades), cheap manufacturing, good performances (also in non-standard illumination and temperature conditions) and lower requirements in terms of quantity and quality of raw materials.[29] Nevertheless, their inferior efficiencies compared to silicon-based devices are still preventing their commercial application. Perovskite solar cells (PSCs), on the other hand, have recently undergone an exceptionally quick development and are therefore currently considered the most promising alternative to traditional Si-based PV modules. Originally introduced in 2009 as a variation of the typical DSSC structure,[30] they make use of mixed organic-inorganic metal halide perovskites (MHPs), *e.g.* methylammonium lead iodide or formamidinium lead iodide ($MAPbI_3$ or $FAPbI_3$, respectively),[31] as light-harvesting materials, sandwiched between hole- and electron-conducting layers. In about a decade of research, the efficiency of single junction PSCs increased to a certified level of 25.2%.[32]

Although PSCs have recently shown impressive efficiencies if compared with DSSC and OPV, and thus currently appear as the best performing third-generation photovoltaics technology, it must be pointed out that doubts on the possibility of their actual future large scale deployment have not yet been eliminated, mostly due to issues of limited stability and processability, as well as the use of toxic components such as lead. On the other hand, it is important to note that DSSC and OPV still hold significant promising applications, especially in the growing field of indoor photovoltaics to power small electronic appliances for internet of things (IoTs) applications.[33]

In paragraphs 1.4. and 1.5., respectively, DSSCs and PSCs, two of the main subjects of this Ph.D. thesis, will be described in more detail. A description of the most important parameters used for cell characterization is reported in paragraph 1.6.

## 1.4. Dye-sensitized Solar cells (DSSC)

In 1991, Grätzel and O'Reagan reported the fabrication of a new kind of solar cell: the dye-sensitized solar cell, in short DSSC, or Grätzel cell.[34] DSSCs constitute an alternative to classical inorganic p–n junction solar cells as they rely on a different working mechanism, combining molecular systems and nanoparticles to create a device that mimics photosynthesis. Although DSSC devices exhibit good power conversion efficiencies of over 13% under full sun illumination (standard AM1.5G),[35] larger scale modules still present much lower values,[36] hindering their wide outdoor deployment. Nevertheless, the research progress during the past ten years in the field of DSSCs is marked by important breakthroughs towards their use for a sustainable future. These considerable advances were made by developing new dye systems, new redox shuttles and hole transport materials. DSSCs remain a competitive third generation alternative photovoltaic technology for their simple preparation methods and the fabrication without the use of toxic materials, which will help to convert solar energy in a sustainable way, and finally for design flexibility, which allows DSSCs to be implemented in many different environments, from transparent smart windows to consumer electronics and indoor applications, which enables the powering of the next digital revolution of widely distributed sensors forming the Internet of Things (IoT).[37]

### 1.4.1. Structure of the cell and operating principles

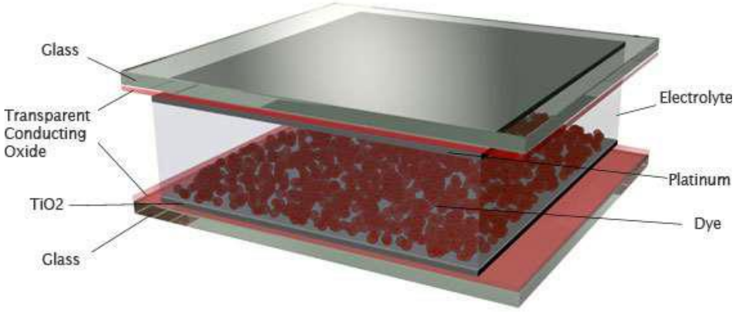

Figure 1.6*: structure and main components of a DSSC.*

The basic components of a dye-sensitized solar cell (DSSC) are the dye-sensitized semiconductor electrode (or photoanode), the redox electrolyte and the counter electrode (cathode). The photoanode is composed by a conducting glass sheet, upon which a few µm-thick layer of a nanocrystalline, wide band gap semiconductor (typically $TiO_2$) is deposed. The electrode is sensitized towards the harvesting of visible light by adsorption of a monolayer of dye molecules on its surface. Thanks to its nanocrystalline and mesoporous structure, the semiconductor layer has a very high surface area, allowing adsorption of a large amount of dye molecules, thus ensuring a very efficient light absorption process (*see below*). The redox mediator (electrolyte) is responsible of transporting positive charges to the counter electrode, which is typically located in parallel close to the working electrode (Figure 1.6). The detailed working principle is depicted in Figure 1.7. When light is absorbed by the dye (D), an electron is excited to a higher energy level as a result of a transition between an occupied and an unoccupied frontier molecular orbital (FMO). The excited dye (D*) "injects" an electron into the conduction band of $TiO_2$ (Figure 1.7, reaction n. 1). This electron transfer process occurs on the femto- to picosecond time scale. Electrons in the semiconductor are charge compensated by ions in the surrounding electrolyte, and their transport through the semiconductor layer is driven by electronic drift-diffusion. As a result, they tend to migrate towards the back electrode contact where their density is smaller.

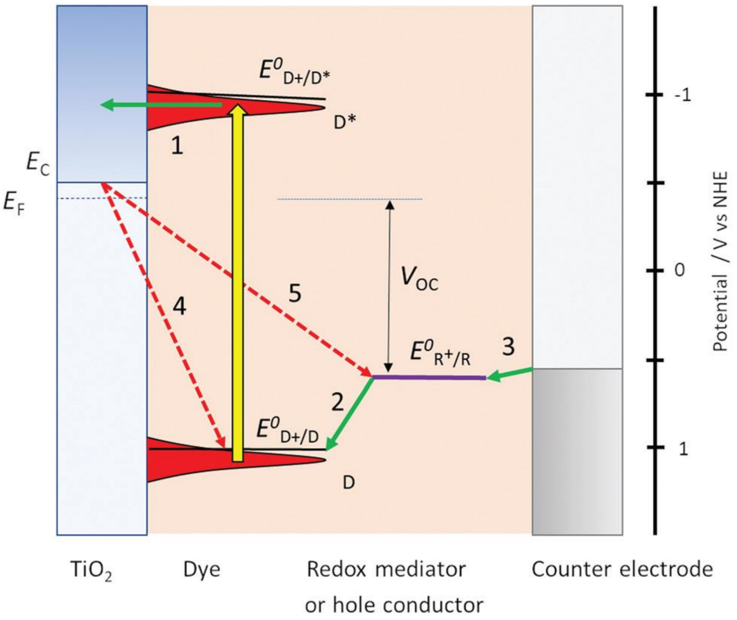

Figure 1.7: *basic diagram of the dye-sensitized solar cell, displaying the working mechanism and the energy levels of the different components.*[37]

Electrons are collected to the electrode contact on a millisecond time scale under full sunlight illumination. The photoanode is in contact with an electrolyte containing a redox mediator ($R^+/R$, that is a redox couple composed by the same compound in two different oxidation states) that regenerates the dye (*i.e.* reduction of the oxidized dye $D^+$, Figure 1.7, reaction n. 2), and also transfers positive charges from the working to the counter electrode, by means of diffusion of $R^+$. At the counter electrode $R^+$ is reduced to R (Figure 1.7, reaction n. 3). The dye regeneration process is typically on the microsecond time scale and must be fast enough to prevent recombination of electrons from the semiconductor to the oxidized dye (Figure 1.7, reaction n. 4). Electrons can also recombine with the oxidized form of the redox mediator (Figure 1.7, reaction n. 5, often referred to as "dark current"). The ground-state energy level of the dye is located just below $E^0(D^+/D)$, the standard reduction potential of the dye, and is often referred to as the HOMO (highest occupied molecular orbital) level. The energy level of the excited dye D* is obtained by adding the absorbed photon energy. The lowest excited state level is obtained by adding $E_{0-0}$ (the zero–zero transition energy), and is referred to as the LUMO (lowest unoccupied molecular orbital) level. D* levels should be higher than the conduction band of the semiconductor to ensure sufficient driving force for efficient electron injection. Fluorescence of the dye and non-radiative decay processes are competing with the injection reaction. For optimum DSSC performance, D* should possess sufficient electronic overlap, while at the same time the conduction band energy of the semiconductor should be as high as possible to obtain a good output voltage in the DSSC. There should also be a good matching between the energy levels of dye and redox mediator: sufficient driving force for reduction of the oxidized dye is needed to drive this reaction fast enough to prevent losses through electron/dye recombination. The voltage output of the DSSC is the potential difference between the working electrode and counter electrode. The potential of the counter electrode is close to that of the redox potential of the electrolyte, and equal to it when no current is flowing, under open-circuit conditions.

In the following paragraphs, the relevant properties of the various cell components will be discussed in more detail.

## 1.4.2. Photoelectrode

The standard device structure of a DSSC is the sandwich cell, in which both working and counter electrodes are based on conducting glass substrates that are placed face-to-face, with a thin layer of the redox electrolyte in between. The distance between the electrodes is usually determined by a thermoplastic frame that also acts as the sealing, and is typically about 25 µm. An even narrower spacing is favourable, as this decreases the resistance due to redox mediator diffusion in the electrolyte.[38] The photo electrode consists of fluorine-doped tin oxide (FTO) glass with the mesoporous $TiO_2$ film sintered on top, whose thickness usually ranges from few to 12-15 µm, depending on the other materials characteristics and the desired cell appearance. An optional thin and dense $TiO_2$ layer (the so-called blocking layer), whose function is to decrease electron recombination from the FTO to the redox electrolyte, can be located between the FTO and the mesoporous $TiO_2$. A light-scattering $TiO_2$ layer can be added on top of the mesoporous layer to improve light capture in the device. The counter electrode comprises FTO glass with a catalyst, such as Pt nanoparticles, carbon, or a conducting polymer deposited onto of it. The sandwich structure allows for (semi)-transparent solar cell devices and the possibility for illumination from either side, provided that the counter electrode is transparent. The most applied semiconductor in DSSCs is $TiO_2$ with the anatase crystal structure, which has a bandgap of ~3.2 eV, thus absorbing only UV light. A flat and dense $TiO_2$ electrode with an adsorbed dye monolayer would not absorb enough light to give practically relevant solar-to-electric conversion efficiencies. Therefore, to harvest a large part of the solar spectrum, $TiO_2$ electrodes possessing high-surface areas are used, such as the mesoporous $TiO_2$ electrode.

## 1.4.3. Photosensitizers

The dye (photosensitizer) is the beating heart of a DSSC. Its plays a crucial role, not only for its effect on the device efficiency, but also to determine its stability and overall appearance. An ideal DSSC sensitizer should possess several specific properties:[39]

1. absorption spectrum centred in the visible and near-infrared regions (where solar emission is maximized, see Figure 1.23, paragraph 1.6) and high molar attenuation coefficients, necessary for a high light-harvesting efficiency;
2. strong and permanent linkage to the semiconductor, obtained thanks to one, or more, anchoring groups, which should also be able to promote electron injection, minimizing interfacial charge-transfer resistance;
3. matching of its frontier orbitals energy levels with those of the electrolyte and semiconductor: the energy level of the lowest unoccupied molecular orbital (LUMO) must be higher than the conduction band edge of the $TiO_2$ to have a good electron injection from the excited dye. On the other hand, the energy level of the highest occupied molecular orbital (HOMO) must be lower than the standard oxidation potential of the redox couple to permit an efficient regeneration of the oxidized dye;
4. low tendency to aggregate on $TiO_2$ surface, since aggregation negatively affects electron injection by promoting intermolecular energy transfer processes. This problem can be avoided by a precise optimization of the dye structure or by the use of additives (co-adsorbents).
5. high thermal, photo and electrochemical stability.

DSSC sensitizers can be classified into several categories, based on their structure or their relevant photo- and electrochemical properties. In terms of structure, the two most common categories are metal coordination complexes and fully organic dyes, whose main features are described below.

*Metal coordination complexes*

Transition metal-based complexes have been critical to the early development of DSSCs, being also the best performing sensitizers for more than a decade after the adoption of the modern mesoporous metal oxide-based architecture described above.

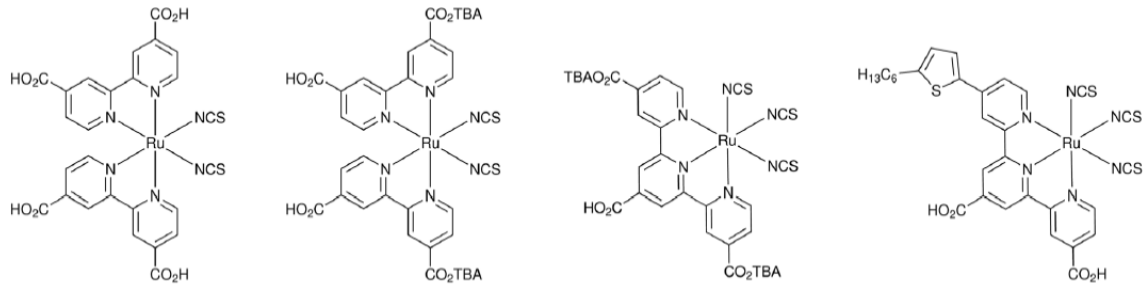

N3 N719 Black Dye TUS-38

Figure 1.8*: structures of the first Ru-based sensitizers.*

Ru-containing dyes such as **N3**[40], **N719**[41] and Black Dye[42] are commercially available and remain common benchmarking materials in the DSSC literature (Figure 1.8). These dyes are used in a variety of DSSC-based applications with PCEs (power conversion efficiency, see paragraph 1.6) reported at >11% in many cases. Derivatives of these dyes such as **TUS-38**, in which a hexylthiophene group replaces one of the three anchors of Black Dye, have shown further improved efficiencies (11.9% PCE).[43] These dyes give excellent PCEs with the commonly used $I^-/I_3^-$ redox shuttle (*see below*); however, performances are generally diminished when the 1-electron metal-based redox shuttles (such as cobalt and copper complexes) are used, which, conversely, have fuelled the more recent increases in PCE to beyond 14%[44] when paired with metal-free dyes. $TiO_2$ surface protection is generally considered to be lower with metal-based dyes, which often incorporate relatively few alkyl chains. These insulating alkyl groups have proven critical to sensitizer design with respect to organic dyes as they provide an umbrella type effect that slows electron transfers from the $TiO_2$ surface to the electrolyte (reaction n.**5** in Figure 1.7). Indeed, in recent years the interest in ruthenium-containing sensitizers has clearly decreased, while the focus of the research community progressively shifted towards the employment of metal-free organic dyes.

*Organic sensitizers*

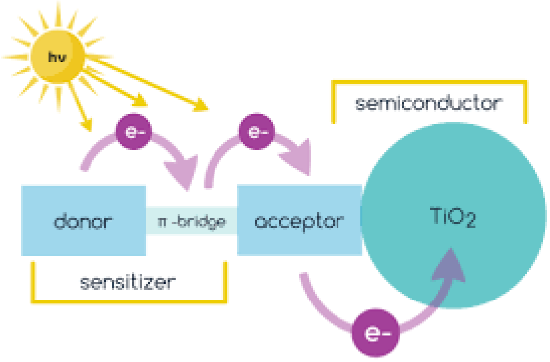

Figure 1.9*: cartoon showing a dye with D-π-A structure anchored onto $TiO_2$, and the relevant electron transfer processes (reproduced from ref.*[45]).

The category of metal-free dyes constitutes a potential alternative to ruthenium complexes because of their low cost (considerably lower than that of noble metal complexes) and, secondly, for avoiding the risk of dispersing heavy metals into the environment. In addition to that, they usually have higher molar extinction coefficients compared to those of ruthenium-based dyes and, most importantly, their photophysical and electrochemical properties can be easily tuned by fine optimization of their structure. Accordingly, organic dyes have been intensely explored within DSSC devices over the last decade, with progressively more sophisticated designs tailored to attain specific properties. Currently, most of the organic dyes reported in the literature are based on an alternating donor–acceptor (D-A) architecture. Such approach relies on the use of building blocks that have little or no visible light absorption themselves, but when combined can generate broadly absorbing dyes due to intramolecular charge transfer (ICT) events,[37] in which a significant transfer of electron density is observed upon the transition between ground- and excited state.

Usually, a conjugated π-bridge is inserted between donor and acceptor fragments to generate D-π-A systems (Figure 1.9), allowing to increase or decrease the conjugation lengths and thus to adjust the optical energy gaps.[46] As mentioned above, in a D-π-A dye, light absorption is usually due to an intramolecular charge transfer process (ICT) from the donor unit, where the HOMO is mostly localized, to the acceptor group, where the LUMO is usually located. Subsequently, electrons are injected from the dye LUMO to the conduction band of $TiO_2$, where the acceptor, which has also the role of anchoring group, is directly bound. The conjugated spacer (π) ensures the electron flow and, at the same time, separates the donor part from the acceptor one and, consequently, from the $TiO_2$ surface, reducing losses due to charge recombination. On the other hand, this kind of structures have two main drawbacks that need to be tackled in order to obtain efficient sensitizers:

1. they can present serious aggregation on the semiconductor surface;
2. they often have relatively narrow light-harvesting spectra, which should be extended to the near-infrared region to maximize LHE.

In the design of an efficient dye each of these building blocks can be modified trying to overcome such drawbacks, thus reducing as much as possible the aggregation on the semiconductor surface and broadening the light-harvesting spectra, which should be extended to the near-infrared region to maximize LHE.

### *D-π-A dyes: donor group*

The donor group is characterized by electron donating ability and should lie as far as possible from the $TiO_2$ surface, while being as close as possible to the redox electrolyte. The choice of a donor group is crucial because it affects the HOMO energy level of the dye, its absorption properties and aggregation, as well as the charge recombination rate. Some of the donor group variations explored to date are reported in Figure 1.10 and include coumarins[47] (**e**), indoline[48] (**b**), tetrahydroquinoline[49] (**d**), anthracene[50] (**g**), carbazole[51] (**c**), *N,N*-dialkylaniline[52] (**h**), and phenothiazine[53] (**f**), however triarylamine[54] (**a**), with various different substituents in the terminal 4 and 4' positions, has been the most widely used unit because of its strong electron-donating ability coupled with good hole transport properties. The first application of a triarylamine as donor group in DSSC dates back to 2004.[50]

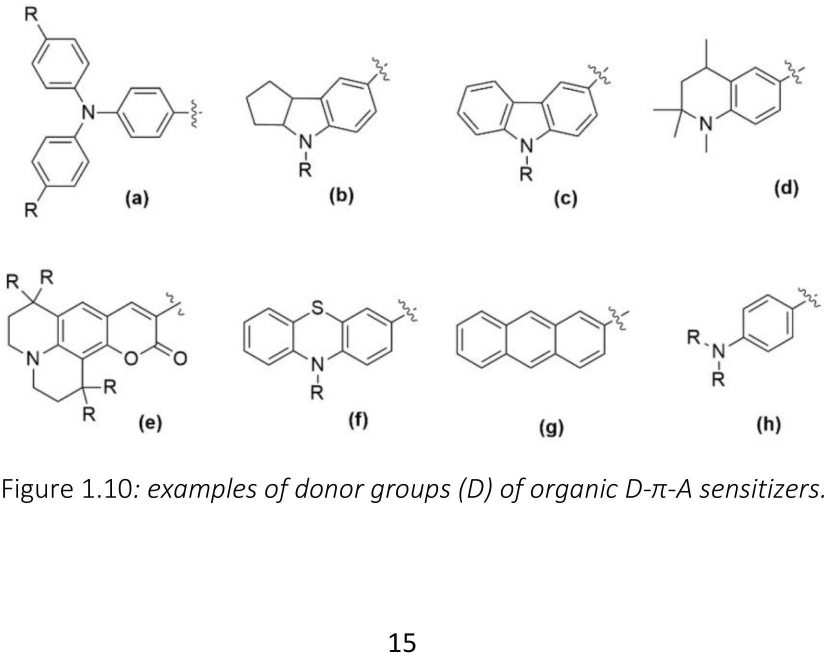

Figure 1.10*: examples of donor groups (D) of organic D-π-A sensitizers.*

*D-π-A* dyes: *π-spacer*

Donating and acceptor moieties are connected by a conjugated bridge that ensures the transfer of electron density between them, promoting the intramolecular charge separation following photoexcitation. In particular, increasing the conjugation length will usually cause a reduction of the difference in energy between HOMO and LUMO levels, leading to a red shift (*i.e.* shift to longer wavelengths) of the absorption spectrum of the dye. Historically, the first sensitizers studied were spacer-free, while introduction of polyvinyl groups (**i**, Figure 1.11) revealed the fundamental role of extended conjugation.[50] The real breakthrough was the introduction of heteroaromatic cores towards light harvesting optimization. The first heteroaromatic core, thiophene (**l**), was introduced by Hagfeldt *et al.* to obtain the famous dye **D5**[55] (Figure 1.11) and after that, a large number of more complex and highly extended π-spacers have been designed, ultimately leading to the D-A-π-A framework.[56] In such structure, the additional acceptor unit acts as an electron trap to separate charges and facilitate migration to the final acceptor; moreover, it enhances long term stability thanks to a general lowering of molecular energy levels, while the downshift of the LUMO energy level also means a more intense light absorption in the near-IR region of the spectrum. Various groups have been presented as additional acceptors, such as benzothiadiazole[57] (**m**), benzotriazole[58] (**n**), dithenosilole[59] (**q**), diketopirrolopirrole[60] (**o**) (Figure 1.11).

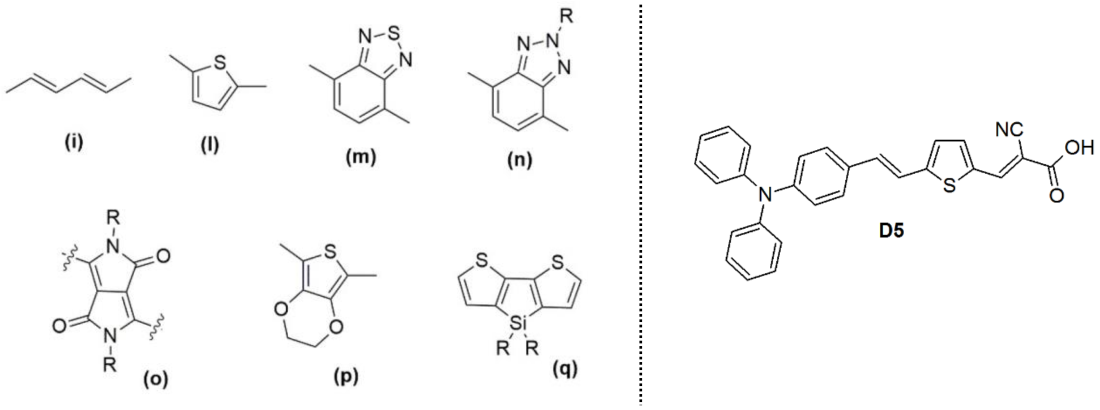

Figure 1.11*: examples of π-spacers of organic D-π-A sensitizers (left) and structure of dye* **D5** *(right)*.

Besides the nature of the π-spacer, introduction of alkyl- or alkoxyl- chains on the molecular backbone has been proven useful not only to disaggregate dye molecules, reducing intramolecular energy transfer, but also in shielding the semiconductor surface.[61] Several studies, in fact, established that electrolyte ions could penetrate through the sensitizer layer to the semiconductor surface, lowering the open-circuit voltage $V_{oc}$ (see paragraph 1.6) and reducing the stability of the device. Such effect can be limited by the presence of alkyl substituents. However, this cannot be considered a general rule to design a good sensitizer, in fact the introduction of very long chains could also be detrimental, resulting in a worse dye loading on $TiO_2$, due to steric effects (thus lowering the photocurrent). In addition, the presence of many bulky chains could distort the planar structure of the dye, limiting the conjugation of the system and thus affecting its light harvesting properties.[62]

*D-π-A* dyes*: anchoring group*

Due to its position in contact with the semiconductor surface, this moiety has to couple a significant electron-withdrawing capability, needed to assure a good injection rate, with a strong anchoring to the $TiO_2$, which could positively affect the lifetime of a DSSC device.

One of the most used anchoring groups for DSSC is the cyanoacrylic acid moiety:[63] the carbonitrile and carboxylic functions confer the electron withdrawing capacity, while the carboxylic acid is also responsible for anchoring the dye to $TiO_2$ thanks to formation of a titanate ester linkage, which is accompanied by the capacity to induce fast and efficient electron injection into the semiconductor. However, this anchoring moiety does not own an optimal stability, due to the possible cleavage from $TiO_2$. In this regard, Sun *et al.* reported a plausible degradation mechanism involving reaction with adventitious water present in the electrolyte (Figure 1.12).[64]

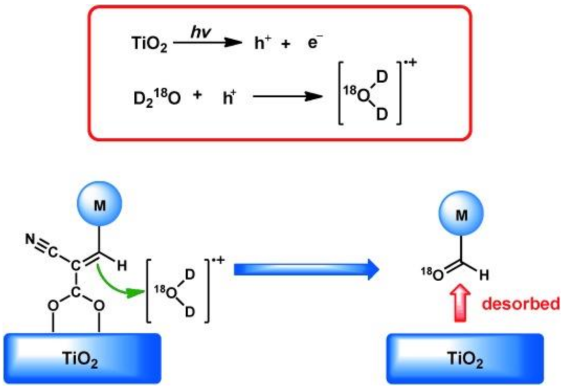

Figure 1.12*: proposed degradation mechanism of cyanoacrylic acid-based dyes (from ref.* [64]*)*

For this reason, many potential alternative anchoring groups have been investigated in the last years to ensure better long-term stability as well as efficient electron injection (Figure 1.13). Cathecols[65] (**w**), pyridines[66] (**v**), alkoxysilyl-groups [44,67](**t**), phosphonic acids[68] (**u**), sulfonic acids[69] (**y**) and hydroxamic acids [70] (**x**) have been considered as alternative anchoring groups, due to their structural similarity to carboxylic acid. However, sensitizers bearing such groups have usually displayed lower power conversion efficiencies than those obtained with their carboxylic acid-containing analogues.

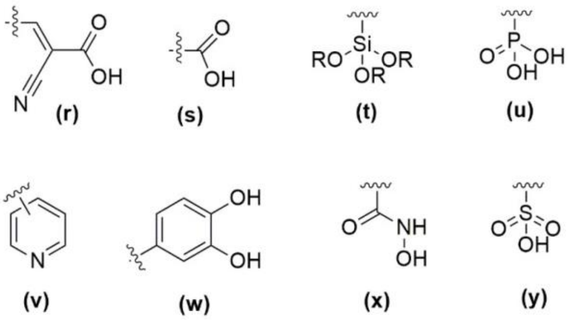

Figure 1.13*: examples of acceptor/anchoring groups (A) of organic D-π-A sensitizers*

## 1.4.4. Charge transporting materials

Charge transporting materials (CTMs) are responsible for electron transfer between the electrodes; therefore, they must be able to both regenerate the oxidized dye following light absorption and be reduced at the counter electrode. All parameters defining the efficiency of solar cells including the short-circuit photocurrent density ($J_{SC}$), open-circuit photovoltage ($V_{OC}$) and the fill factor (*ff*) (see paragraph 1.6. for a definition) are influenced by the properties of the charge transporting materials and their interface interaction with the electrodes. CTMs can be integrated in DSSCs in the liquid, quasi-solid and solid state.[71,72] Liquid CTMs (also named electrolytes) in solar cells comprise an organic, aqueous or ionic solution of a redox couple, such as $I^-/I_3^-$[73], copper[74] or cobalt[75] coordination complexes, or organic molecules.[76] The fundamental differences between the various charge transport materials are the charge mobility and charge-transfer mechanism.[71] While in liquid electrolytes there is a prevalence of ionic conductivity, in polymeric and solid-state CTMs the mechanism can be a combination of ionic and electronic transport, or a predominantly electronic process.

In order to transport charges between the electrodes efficiently, charge transport materials in DSSCs must fulfil several requirements:

(i) minimal overpotential, but with a driving force large enough to efficiently regenerate the sensitizer;

(ii) low recombination rates with the metal oxide semiconductor and the conductive substrate;

(iii) minimal mass transport limitations for fast diffusion through the mesoporous semiconductor towards the counter electrode;

(iv) absence of unwanted chemical and physical interactions with other components of the solar cell to improve overall stability;

(v) no competitive light absorption with respect to the dye.

Currently, there is no ideal electrolyte system capable of fulfilling all requirements, but several successful systems have been discovered nonetheless. Their advantages and drawbacks will be discussed in more detail in Chapter 3, paragraph 3.3

### 1.4.5. Counter-electrode

The DSSC device is completed by a cathode usually made by depositing on the glass substrate of a thin layer of Pt, which is able to catalyse the reduction of the electrolytic couple. Due to the limited availability of platinum, intense efforts have been dedicated to the research of more readily available materials.[77] For instance, carbon-based materials are attractive candidate to replace platinum as the counter electrode in DSSCs, as they are less expensive, more abundant, can present a high surface area, good catalytic activity, electrical conductivity and thermal stability, are resistant to corrosion, and have a high reactivity for redox mediator reduction.[37] Mixtures of graphite and carbon black,[78] carbon nanotubes,[79] conducting polymers,[80] and cobalt or nickel sulfide,[81] have all been tested. Finally, PEDOT (poly(3,4-ethyleneedioxythiophene)), first discovered at the Bayer AG research laboratories in the 1980s[82] and widely applied as substrate for antistatic and opto-electronic applications, is also a very promising cathodic material due to its high conductivity, outstanding visible light transmittance and extraordinary stability. Although PEDOT is an insoluble polymer, it can be easily electrodeposited from its monomer in solution, resulting in excellent conductivity.

## 1.5. Perovskite Solar Cells

Perovskites are extraordinary materials that have revolutionized the field of photovoltaics. They, however, are not novel compounds: natural perovskite is a mineral species composed primarily of calcium titanate ($CaTiO_3$), and was discovered already in 1839 in the Ural Mountains of Russia by Gustav Rose, who named it after the Russian mineralogist Lev Perovski.[83] By extension, a large class of compounds that have the same crystalline structure as $CaTiO_3$ and possess the general formula $ABX_3$ are referred to as perovskites. While there are several types of perovskites, those employed in solar cells, as well as other fields of optoelectronics, are semiconducting hybrid organic-inorganic materials (*see below*) exhibiting some highly valuable properties such as direct bandgap, high optical absorption coefficient over the visible and near-infrared range, increased mobility of charge carriers, low exciton binding energy,[83] sharp optical band edge and tunable band gap by substitution of the cations and/or anions in the crystal structure.[84] The most commonly used perovskite is methylammonium lead Iodide ($CH_3NH_3PbI_3$), having very good optical and electronic properties thanks to its absorption onset at about 800 nm, corresponding to a band gap of approx. 1.55 eV, and its decent absorption over the whole visible spectrum.[85]

In 2009, Kojima *et al.* evaluated for the first time $CH_3NH_3PbI_3$ (methylammonium lead iodide, or $MAPbI_3$) and $CH_3NH_3PbBr_3$ (methylammonium lead bromide, or $MAPbBr_3$) as sensitizers for dye-sensitized solar cells in the presence of a liquid electrolyte, obtaining PCEs of 3.81 and 3.13%,[30] respectively. However, because of stability issues and the instant dissolution of perovskite in the liquid electrolyte, this innovation received little attention from photovoltaic researchers. To address those shortcomings, Kim *et al.* developed a solid-state, highly efficient (PCE 9.7%), and stable PSC in 2012 by replacing the liquid electrolyte with a solid hole conductor.[86] After this discovery, PSCs have been intensely studied because of the unique properties of these light-harvesting materials, resulting in record photovoltaic efficiencies well above 20%. These advances have contributed to further research interests in perovskite research community, resulting in a tremendous rise in the number of publications in the last few years.[87] In the following paragraphs, the main properties of the perovskite absorbers, as well as the most common solar cell structures and the characteristics of the other cell components will be briefly discussed.

### 1.5.1. Hybrid Organic-Inorganic Perovskites

As mentioned above, all compounds that have a structure analogous to naturally occurring perovskite mineral ($CaTiO_3$) are called perovskites, and usually share the $ABX_3$ general formula. In such compounds (Figure 1.14) “A” is a large monovalent cation which occupies the cubo-octahedral sites in a cubic space, “B” is a small divalent metal cation occupying the octahedral sites, and “X” is an anion (typically a halogen; however, it can also be oxygen, carbon, or nitrogen).

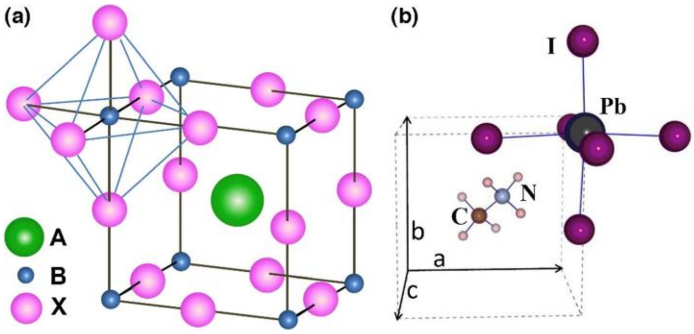

Figure 1.14*: $ABX_3$ perovskite structure showing the $BX_6$ octahedron and the larger A cation in a cubo-octahedral site; (b) the unit cell of cubic $MAPbI_3$ perovskite (Reproduced from ref.* [85]).

The most important component of perovskite composition is cation “A”, because it determines its structure and crystal size, both features which influence directly the stability and the optoelectronic properties of the material. In typical hybrid organic/inorganic perovskites “A” has charge +1 and is usually an organic cation like $CH_3NH_3^+$ (methylammonium), $C_2H_5NH_3^+$ (ethylammonium) or $HC(NH_2)_2^+$ (formamidinium). “B”, on the other hand, has charge +2 and is a metal ion such as $Pb^{2+}$ or, less commonly, $Sn^{2+}$ or $Cu^{2+}$. Finally, “X” is a halide ion, usually $Cl^-$ $Br^-$ or $I^-$.

### 1.5.2. Device architecture and working mechanism

Common perovskite solar cells are composed of five layers, allowing for different combinations of the materials used: a transparent electrode, an n-type electron-transporting semiconductor (ETM), the photoactive perovskite, a hole-transporting material, *i.e.* a p-type semiconductor (HTM), and finally a metal electrode.

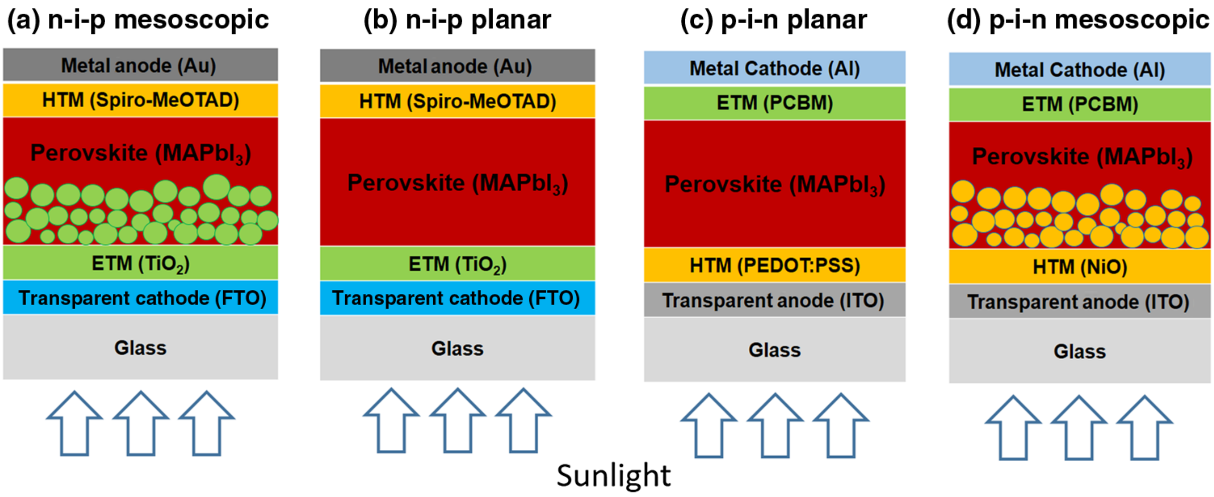

Figure 1.15*: schematic showing the layered structures of four typical perovskite solar cell architectures: (a) n-i-p mesoscopic, (b) n-i-p planar, (c) p-i-n planar, and (d) p-i-n mesoscopic (from ref.* [88]*).*

Depending on the order of deposition of the materials constituting the cell, two main architectures can be recognized, the direct or normal architecture (Figure 1.15 a,b) and the inverted architecture (Figure 1.15 c,d). The normal structure is also known as *n-i-p* configuration, while the inverted structure as *p-i-n* configuration, where *n* refers to the electron transport material, *i* to the perovskite and *p* to the hole transport material. In both configurations, the perovskite layer can be deposited onto a semiconducting layer with a mesoscopic nanostructure or a planar structure. Therefore, a total of four possible configurations is possible.

Regular *n-i-p* structure

The conventional *n-i-p* mesoscopic structure was the first arrangement of perovskite photovoltaics to be tested. The interest in PSCs increased after the so-called mesoscopic device structures were formed by substituting the liquid electrolyte with a solid-state hole conducting material.[86] The assembly begins with a transparent glass cathode followed by the electron transporting material (ETM). The structure is then layered with a mesoporous metal oxide containing the perovskite, followed by the hole transport material (HTM), and capped with a metallic anode. This initial advancement in PSCs created an important field of interest for photovoltaic researchers and consequently led to the development of other PSC device configurations. The planar architecture is an evolution of the mesoscopic structure, where the perovskite light harvesting layer is sandwiched between the ETM and HTM. The absence of a mesoporous metal oxide layer leads to an overall simpler structure without the need for high temperature processing.

Inverted *p-i-n* structure

In the case of the *p-i-n* planar perovskite architecture, the HTM layer is deposited first, followed by the ETM layer. It was discovered that perovskites are capable of transporting the holes themselves, which led Jeng *et al.* to develop the first planar hetero-junction PSC with an inverted structural design.[89] With this advancement, the inverted *p-i-n* configuration has led to the exploration of several organic and inorganic materials to be used as HTM.[90] Inverted PSCs allow low-temperature processing and reached high efficiencies exceeding 20%.[91,92]

The main charge transfer processes taking place inside the cells are illustrated in Figure 1.16. Photoexcitation (**1**, yellow arrow) generates electrons and holes in the perovskite layer (in the CB and VB, respectively). The electrons are injected into the ETM (**2**, cyan arrow) and the holes are instead transferred to the HTM (**3**, purple arrow). Finally, the charges are collected at the respective electrodes and from there they enter the external circuit (**4**), where they can recombine to generate an electric current. However, various unwanted processes can also take place in the cell (dotted arrows), leading to a decrease in performance, such as: radiative or non-radiative excited state decay as a consequence of exciton annihilation, transfer of electrons backwards from the conduction band of the ETM to the perovskite, backward hole transfer at the HTM/perovskite interface, charge recombination at the ETM/HTM interface (occurring only in case of incomplete coverage of the perovskite).[93]

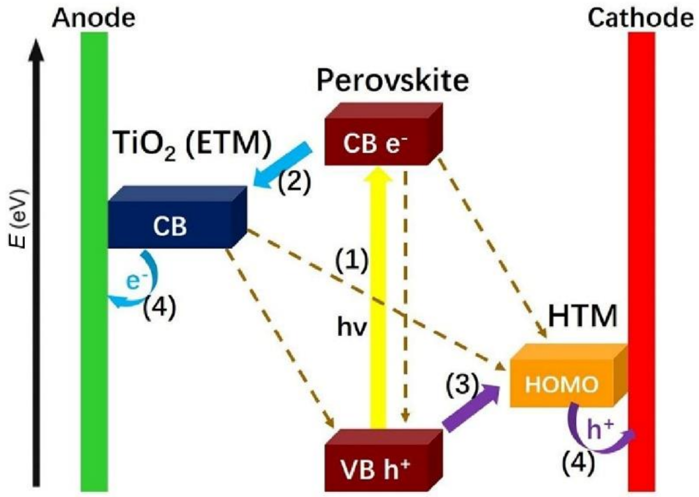

Figure 1.16*: schematic representation of the working mechanism of a perovskite solar cell, and of the unwanted charge recombination events (reproduced from ref.* [94]*).*

Obviously, to have an efficient device, the rates of the charge recombination processes should be lower than those of the charge generation, separation and extraction processes (1) - (4). Therefore, it is very important to determine the time scale and dynamics of the various charge transfer processes taking place at the different interfaces, to enable further optimizations and performance improvements. Furthermore, the values of the energy levels of each component are crucial for the performance of the cell.

The valence band (VB) and conduction band (CB) energies of the most common hybrid perovskite ($MAPbI_3$) are at −5.43 eV and −3.9 eV with respect to vacuum, respectively, and the CB of $TiO_2$ (as a typical ETM) is at −4.0 eV; therefore, the electron-transfer between excited $MAPbI_3$ and $TiO_2$ is thermodynamically favored. Similarly, to allow regeneration of the perovskite, the HOMO energy level of the HTM must be above the energy of the valence band of the latter. It is therefore necessary to carefully select compounds capable of carrying out the electron transfer quickly and effectively, making the HTM one of the crucial elements for the optimal functioning of the cell. In the next paragraph the characteristics of this component will be examined in detail.

### 1.5.3. Hole-Transporting Materials (HTM)

The hole-transporting material plays a significant role in determining the performances of PSCs. It usually performs a double function:

1) to extract positive charges (holes) from the perovskite layer and transport them to the anode;

2) to minimize the charge recombination and reduce the degradation at the metal-perovskite interface (preventing the direct contact between the perovskite and the metal contact).

An ideal HTM should exhibit the following properties:

- a highest occupied molecular orbital (HOMO) energy level well-aligned to the valence band energy (VB) of the perovskite;
- minimal absorption in the visible and near-IR regions of the solar spectrum;
- good hole mobility;
- excellent thermal and photo-chemical stability;
- low cost;

The scientific community has shown enormous interest in studying HTMs to understand and improve their performance. A very large number of different types of hole transporters have been reported, both organic and inorganic in nature (organics can then be further subdivided into small molecules and polymers). To date, Spiro-OMeTAD (2,2',7,7'-*tetrakis*-(*N,N'*-di-*p*-methoxyphenylamine)-9,9'-spirobifuorene, Figure 1.17, left) has been selected as a benchmark in PSCs, having achieved the highest PCE values.[95] Spiro-OMeTAD has a HOMO level at approximately −5.13 eV *vs.* vacuum, exhibits a moderate hole mobility in the range of $10^{-5}$ to $10^{-4}$ $cm^2$ $V^{-1}$ $s^{-1}$, and presents high solubility in organic solvents such as toluene or chlorobenzene, giving a thin, nearly colourless film. However, its price is prohibitive and therefore its use hampers progresses towards the development of low-cost perovskite solar cells.[96] The reason for its high cost lies in the complicated multi-step synthetic procedure, which makes scaling-up difficult. Furthermore, in view of its moderate hole mobility, Spiro-OMeTAD also requires the use of chemical doping to increase the film conductivity values (*see below*); however, the use of additives is problematic, since the hygroscopic nature of the dopants makes the HTM highly hydrophilic, leading to chemical degradation and thus negatively affecting the stability of the whole device.[97] Similar to Spiro-OMeTAD, poly[*bis*(4-phenyl)(2,4,6-trimethylphenyl) amine] (PTAA) (Figure 1.17, right) is the most commonly used HTM for *p-i-n* type PSCs. Typically, a thin layer of undoped PTAA is used. Very recently, Bakr and co-workers reported a certified PCE of 22.3% with PTAA in *p-i-n* perovskite solar cells.[92]

However, the even higher cost of PTAA compared to Sprio-OMeTAD (1980 $ per g) makes it unviable toward the mass production of PSC.[98]

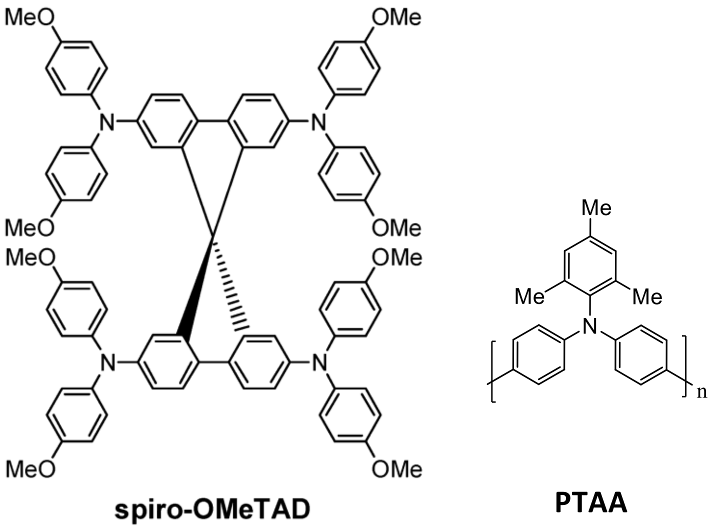

Figure 1.17*: structures of Spiro-OMeTAD (left) and PTAA (right) hole-transporting materials.*

*Chemical doping*

Chemical doping is an important method in organic electronics to improve the efficiency of devices; in fact it allows to increase the conductivity and reduce the ohmic losses at the interface with the electrodes. The basic principle of doping for HTMs is to use a chemical agent to remove electrons from their HOMO, to generate intrinsic holes (Figure1.18).

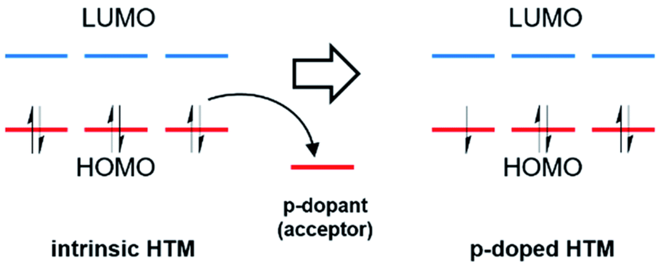

Figure 1.18*: schematic illustration of the p-type molecular doping mechanism, where the dopant is an acceptor (reproduced from ref.* [99]).

The introduction of additional carriers leads to an increase in the charge carrier-density of the organic semiconductor, with a consequent enhancement of conductivity. The key requirement for an efficient doping process is the electron affinity of the dopant with respect to the energy levels of an organic semiconductor.[99] A number of p-type dopants have been developed and manufactured, including 2,3,5,6-tetrafluoro-7,7,8,8-tetracyanoquinodimethane (F4TCNQ), benzoyl peroxide, as well as copper(II) and cobalt(III) complexes (Figure 1.19).[100]

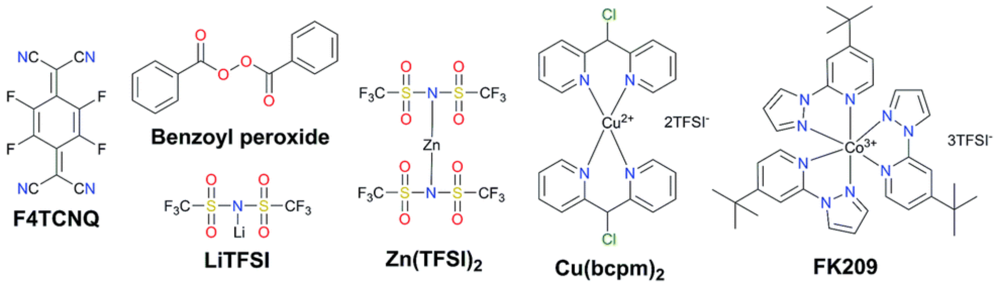

Figure 1.19*: chemical structures of different p-type dopants for HTM employed in PSCs (reproduced from ref.* [99]).

To date, the most used doping formulation for Spiro-OMeTAD consists in a combination of *tris*(2-(1H-pyrazol-1-yl)-4-tert-butylpyridine)cobalt(III) tri[*bis*(trifluoromethane)sulfonimide] (**FK209**) and lithium *bis*(tri-fluoromethanesulfonyl)imide (**LiTFSI**) together with 4-*tert*-butylpyridine (TBP), which is mostly used to improve interfacial morphology.[101]

For the above reasons, research is still active to find better alternatives to Spiro-OMeTAD as HTM for PSCs. The compounds under study can be broadly classified in three different categories:

- Organic HTMs
- Organometallic HTMs
- Inorganic HTMs

### 1.5.3.1. Organic HTMs

*Small molecule HTMs*

Flexible molecular structure and efficient photo-electrical properties make the organic small molecular HTMs ideal candidates to fabricate PSCs with high performances, possibly capable to overcome potential disadvantages such as high costs, complicated multistep synthesis, expensive precursors, tedious purification process and poor hole mobility.[96] Furthermore, it must be pointed out that the HOMO energy level of Spiro-OMeTAD (−5.13 eV) presents a very large energy offset relative to the valence band (VB) of perovskite (−5.43 eV) causing a sizeable reduction in the cell potential.[102] Therefore, alternative conjugated skeletons promoting strong intermolecular interactions *via* π–π stacking and possessing a simplified structure can be of great interest. In particular, D-A-D structures are very promising, as variations in the electron-withdrawing cores can tune their optical and electronic properties. Indeed, an electron-withdrawing group might tend to minimize HOMO energy level, bringing it closer to the perovskite VB and thus achieving a higher $V_{oc}$ in a PSC. Moreover, in solid thin films, intermolecular interactions via π-π stacking can induce a high crystallinity of the materials, resulting in high charge carrier mobilities. Accordingly, D–A-D conjugated small molecules are very well-suited for the formation of efficient HTLs (Figure 1.20)[103] and, indeed, several alternative structure have been proposed: they include thiophene derivatives, 3,4-ethylenedioxythiophene, pyrene, acene,[104,105] benzodithiophene,[106] carbazole,[107] fluoranthene,[108] indacenodithiophene,[109] phenoxazine,[110] spirofluorene[111] and triazatruxene [112] derivatives.

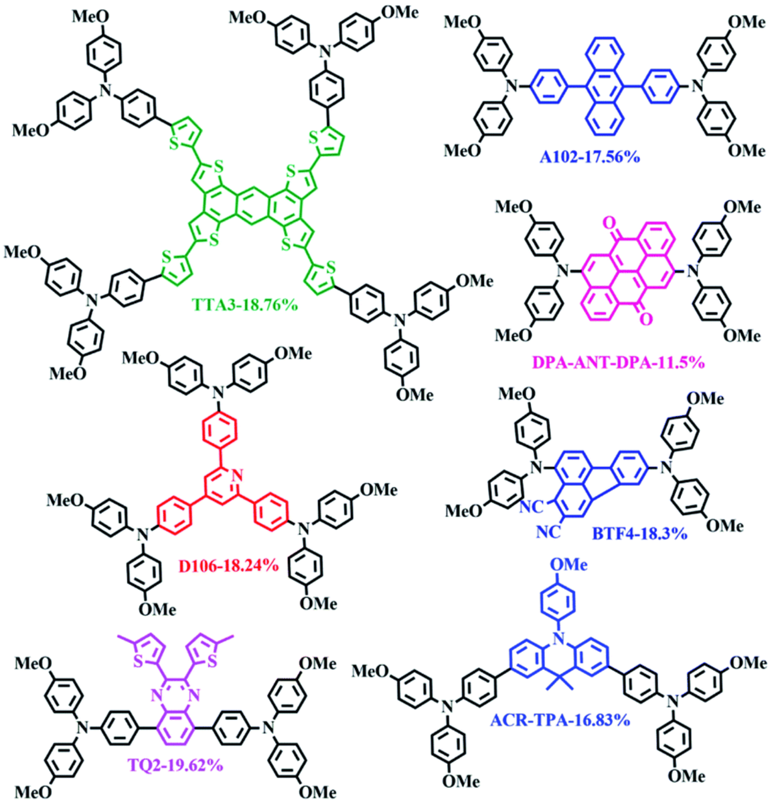

Figure 1.20: *chemical structures of organic small molecules HTM for PSCs, with the corresponding device efficiencies (reproduced from ref.* [103]).

## *Polymeric HTMs*

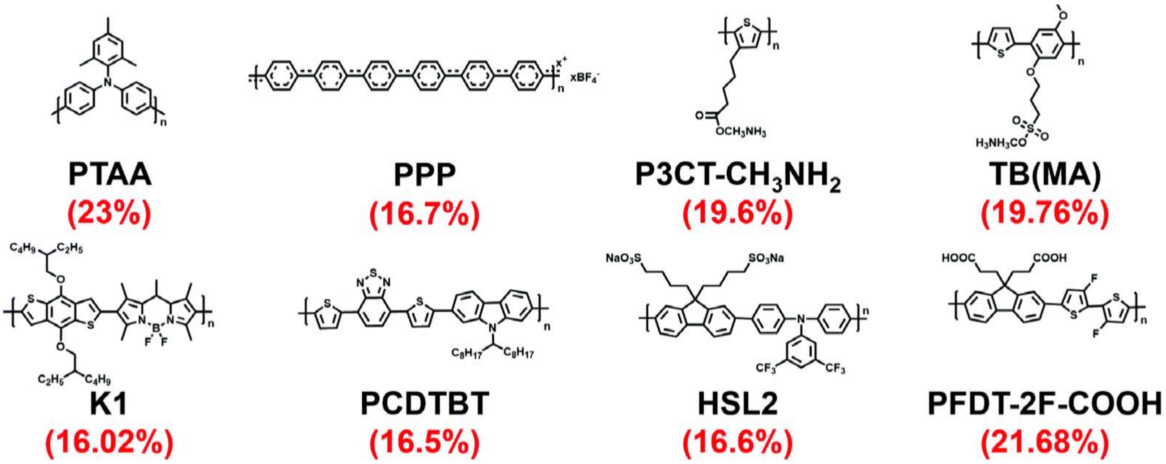

Figure 1.21*: chemical structures of the representative dopant-free polymeric HTMs for n–i–p and p–i–n PSCs. Device efficiencies are given in the parentheses (reproduced from ref.* [96]).

Apart from small molecules, polymers are also promising candidates for dopant-free HTMs (Figure 1.21). Benefiting from a long conjugated chain, charges can be transported through both intermolecular hopping and intramolecular transfer mechanisms. Therefore, polymeric HTMs usually have high hole mobility without the need for dopants, despite some inevitable problems in the preparation, especially due to batch-to- batch variation in molecular weights and to the necessity of tedious purification.[96]

### 1.5.3.2. Organometallic HTMs

In addition to organic small molecules and polymers, organometallic compounds can also be employed as dopant-free HTMs.[113] Organometallic HTMs generally present phthalocyanine or porphyrin cores, which form complexes with divalent metal cations like $Cu^{2+}$, $Ni^{2+}$, $Co^{2+}$, and $Zn^{2+}$.[114] Such compounds show good stability under thermal and photochemical stress, furthermore, by modifying the substituents on the peripheral, non-peripheral and metal central positions, it is possible to easily tune their optoelectronic properties. Benefiting from a high intrinsic hole mobility, these metal–organic complexes can effectively transport holes without any dopant. It is worth noting that phthalocyanine and porphyrin generally have strong light absorption, making them not ideally suited to work as HTMs for inverted PSCs.[115]. In 2015, Ke *et al.* demonstrated a room-temperature, fully vacuum-processed planar PSCs with copper phthalocyanine (CuPc) as the HTM[116] (Figure 1.22). The best-performing device achieved an efficiency of 15.42% (with $V_{OC}$ of 1.04 V and *ff* of 77.47%). To investigate the stability, the authors stored encapsulated cells in air with humidity of 20% at room temperature in the dark. After 1000 h, the PCE of the CuPc-based device only decreased from 14.21% to 13.83%, while spiro-OMeTAD devices showed a sharp decrease in the PCE from 13.66% to 8.38%. Jiang *et al.* synthesized a solution-processable CuPC derivative termed as CuPc-TIPS[117]. The PSCs that adopted CuPc-TIPS as the HTM combined with a low-cost carbon cathode afforded a decent PCE of 14.0% under 100 mW $cm^{-2}$.

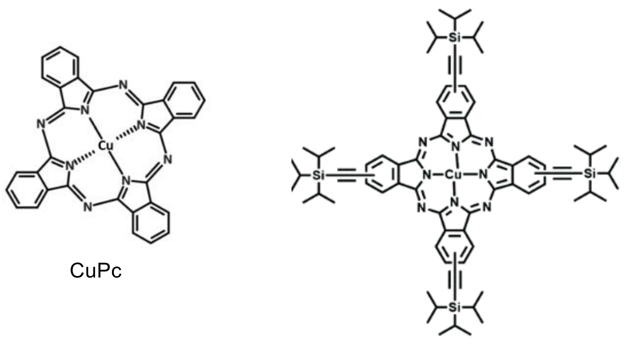

CuPc

CuPc-Tips

Figure 1.22*: chemical structures of representative Cu-phthalocyanines-based HTMs.*

### 1.5.3.3. Inorganic materials

Although in the field of HTMs organic compounds seem currently to attract the most attention, inorganic HTMs appear also promising in the perspective of large-scale application, due to their high charge carrier mobility, low manufacturing costs and very good stability. However, their use in PSCs is still relatively unexplored. Nickel oxide (NiO) is certainly the most studied inorganic HTM as it is a robust, abundant and low cost material. The best performing cells incorporating NiO showed a PCE of 17.3%.[118] Copper (Cu) has also been successfully employed to produce Cu-based inorganic HTMs at low cost. The first was explored by Kamat, who used copper iodide (CuI) obtaining cells with an overall efficiency of over 6%.[119] A remarkable result was obtained with copper thiocyanate (CuSCN) which in 2014 showed 12.4% efficiency[120] and two years later 16% in a work by Nazeeruddin *et al.*.[121] Other non-toxic and air-stable inorganic HTMs for PSCs incorporating transition metals, such as $MoO_3$ and $VO_x$, have been tested, but the results have not been impressive in terms of efficiency.[122]

## 1.6. Photovoltaic parameters

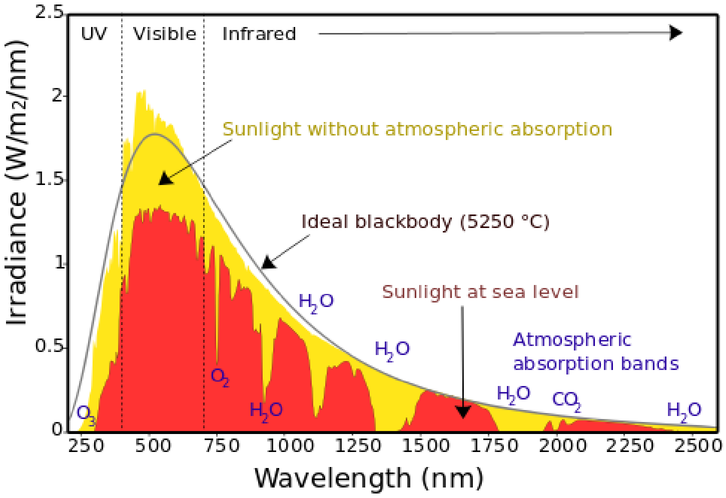

Figure 1.23*: solar spectrum and atmospheric absorbing gases from 240 nm to 2.5 µm wavelengths.*

The radiative energy coming from the Sun and reaching our planet is unevenly distributed in the ultraviolet (UV, ~ 8%), visible (Vis, ~ 40%) and infrared (IR, ~ 52%) regions. The spectrum of light reaching the sea level of our planet (red area in Figure 1.23) is slightly modified in intensity and shape compared to that outside the atmosphere (yellow area) because of reflection, diffraction, and adsorption by atmospheric molecules. For this reason, a parameter has been introduced to quantify the actual value of solar radiation incident on photovoltaic modules: air mass (AM), defined as the optical path length of extra-terrestrial light through the Earth's atmosphere (*e.g.* AM1 is the radiation that reaches sea level when the Sun is at the zenith). Generally, for solar cell characterization, a standardized spectrum called AM1.5 (which corresponds to a solar zenith angle of 48.2°, representative of mid-latitudes) is used. The AM1.5 solar spectrum entails a power flux of about 970 W $m^{-2}$, which is usually normalized to give

1000 W $m^{-2}$ (*i.e.* 100 mW $cm^{-2}$), a quantity often termed “one Sun”.[123,124] In all cases, solar cell performances are defined by the following six parameters:[125]

*Incident photon-to-electron conversion efficiency (IPCE)*

The IPCE parameter is defined as the ratio between the number of electrons flowing through the external circuit due to electric current generation by the cell and the number of incident photons at each wavelength, and is represented by equation (1.1).

$$IPCE\ (\%) = 1240(\ eV\ nm)\frac{J_{ph}(mA\ cm^{-2})}{\lambda(nm)I(mW\ cm^{-2})} \tag{1.1}$$

$\lambda$ and $I$ are the wavelength and the intensity of the monochromatic light at which the short-circuit photocurrent density, $J_{ph}$, is generated by the cell (corresponding to a situation in which the two electrodes are directly connected in the external circuit, *see below*). 1240, on the other hand, is a numerical factor, which takes into account the conversion from current density to number of electrons and from light intensity to number of photons. When referred to a DSSC (see paragraph 1.4. for a description of the working mechanism) the IPCE can also be expressed as the product of four different factors, as represented in equation (1.2):

$$IPCE\ (\%) = LHE(\lambda) \times \Phi_{inj} \times \Phi_{reg}\ \times \eta_{cc}\ (\lambda) \tag{1.2}$$

Where *LHE (λ)* is the light-harvesting efficiency for photons of wavelength $\lambda$, $\Phi_{inj}$ and $\Phi_{reg}$ are the quantum yields for electron injection and dye regeneration, respectively, and $\eta_{CC}$ is the charge collection efficiency. Therefore, plotting the IPCE values *vs.* excitation wavelength (IPCE spectrum, Figure 1.24) can be a useful tool to evaluate the ability of a new DSSC sensitizer to convert photons of different wavelengths into electrons. Indeed, the IPCE is strictly related to some intrinsic characteristic of the dye, the light-harvesting properties and the injection quantum yield, as well as to external factors, such as the amount of dye adsorbed on the semiconductor and the electron transfer process through the external circuit.

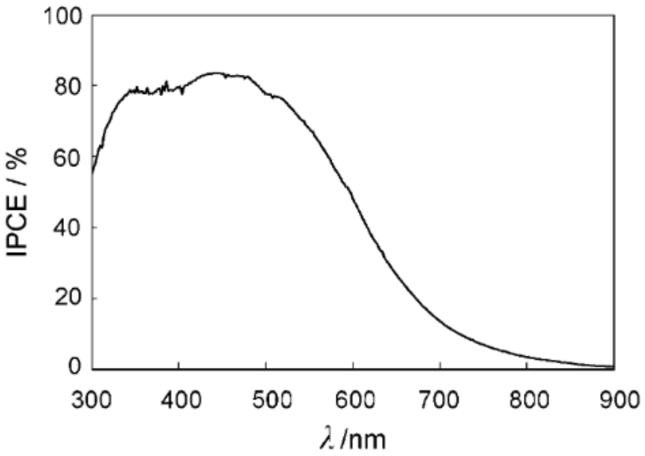

Figure 1.24*: typical IPCE spectrum of a DSSC.*

*Photocurrent/voltage curve (J/V curve)*

The photovoltaic performance of solar cells, including DSSCs and PSCs, can be easily evaluated by measuring the corresponding *J/V* curves (Figure 1.25) under standard AM 1.5 simulated sunlight (100 mW cm$^{-2}$). In such an experiment, the cell is placed under tension and the potential is linearly swept from the open-circuit voltage $V_{oc}$ (for a definition, *see below*) to 0; the current generated by the device is measured and plotted against *V*. The key-parameters typically extracted from *J/V* curves are the open-circuit voltage ($V_{oc}$), short-circuit photocurrent density ($J_{sc}$), fill factor (*ff*) and solar energy-to-electricity conversion efficiency ($\eta$) also commonly referred to as power conversion efficiency (PCE).

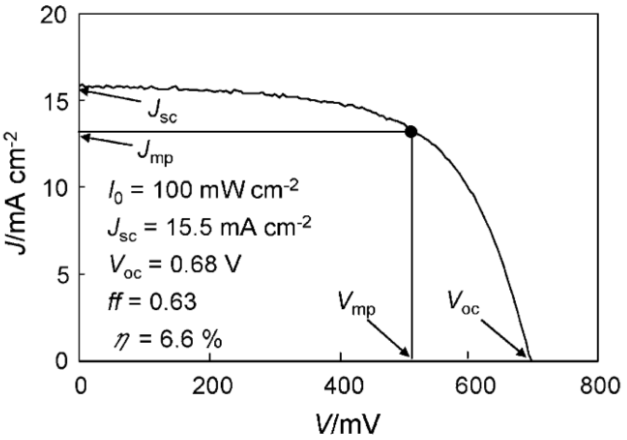

Figure 1.25*: typical J/V curve of a solar cell.*

*Open-circuit voltage ($V_{oc}$)*

The $V_{oc}$ parameter is the difference in electric potential between the two electrodes of a solar cell under illumination when the circuit is open. Once again, when referring to DSSCs (*see above*), the $V_{oc}$ parameter can be mathematically expressed in relation to several properties of the cell materials, according to equation (1.3):

$$V_{OC} = E_F - E_{RED} \qquad \text{where} \qquad E_F = \frac{E_{cb}}{e} + \frac{k_B T}{e}\ln\left(\frac{n}{N_{cb}}\right) \tag{1.3}$$

Where *e* is the elementary charge, $k_B$ is the Boltzmann constant, *T* is the absolute temperature, $E_{cb}$ is the energy level of the conduction band of TiO$_2$, *n* is the density of conduction band electrons in TiO$_2$, $N_{cb}$ is the effective density of conduction band states and $E_{redox}$ is the redox potential of the redox couple. $E_F$ is the Fermi level at the equilibrium and its value is set by the conduction band energy ($E_{cb}$) of the TiO$_2$, but from the expression on the right it can be easily seen that it depends also on the electron density (*n*) in the conduction band of the semiconductor; *n* is intimately connected with the electron injection and recombination kinetics and, accordingly, with the photoactivated material properties.

*Short-circuit photocurrent density (Jsc):*

The $J_{sc}$ value expresses the photocurrent per unit area (mA cm$^{-2}$) when a solar cell under irradiation is short-circuited, that is when electrical impedance and difference in electric potential are next to zero. $J_{sc}$ is the maximum value of photocurrent density produced by an ideal cell under irradiation. In a DSSC, this value is intimately connected with the interaction between the light-harvesting material and $TiO_2$, and depends on light-absorption capability, electron-injection efficiency and dye-regeneration efficiency, while in the case of PSCs is crucially related to the efficiency of charge transfer from the perovskite to the hole transporting material (HTM). Therefore, in a DSSC an increase in $J_{sc}$ can be achieved through fine design of the structure of the dyes and consequent proper modification of their photoelectrochemical properties.

*Fill factor (ff)*

The fill factor is defined as the ratio between the maximum power output (product of current density and voltage at the maximum power point, $J_{mp} \cdot V_{mp}$) and the product of $J_{sc}$ and $V_{oc}$ (equation 1.4).

$$ff = \frac{J_{mp} \cdot V_{mp}}{J_{sc} \cdot V_{oc}} \tag{1.4}$$

*ff* is determined from the *J/V* curve and is an indication of how ideal is the behaviour of the cell. Graphically, it can be seen as how much of the area of the rectangle for $J_{sc} \cdot V_{oc}$ is filled by that described by $J_{mp} \cdot V_{mp}$ (Figure 1.25). In a real cell, power is dissipated through the resistance of the contacts, during charge transport and through leakage currents (such as recombination and dark current, *see above*, paragraph 1.4.1.), which means that the fill factor will always be smaller than 1, affecting the photovoltaic performances. Careful fabrication of the device is mandatory to maximize this parameter.

*Solar energy-to-electricity conversion efficiency (η)*

The $\eta$ value is defined as the ratio between the maximum output electrical power of a solar cell and the energy of incident sunlight ($I_0$, generally 100 mW cm$^{-2}$, as mentioned above).

$$\eta = \frac{J_{sc}(mA\ cm^{-2}) \cdot V_{oc}\,(V) \cdot ff}{I_0(mV\ cm^{-2})} \tag{1.5}$$

As can be seen, equation (1.5) contains many of the photovoltaic parameters ($V_{oc}$, $J_{sc}$, *ff*) described above, highlighting how the optimization of each one of them is crucial to maximize the electrical yield of the device.

## 1.7. Outline of the work

This Ph.D. research work concerned the design, synthesis and characterization of organic molecules able to fulfil different roles in photovoltaic devices, with a particular focus on the preparation of new photoactive and conductive organic materials aimed at enhancing Dye-sensitized Solar Cells (DSSC) and Perovskites Solar Cells (PSC) performances.

Concerning DSSCs, the main section of the work focused on the design, synthesis and characterization of new organic photosensitizers, which, as previously shown (see paragraph 1.4.3.), can be considered the heart of the device, being directly responsible for the conversion of solar energy into electric current. A part of the work was carried out in the course of a four-month internship in the group of Prof. Marina Freitag, Newcastle University (UK), during which the assembly and testing of DSSCs built with organic dyes in combination with copper-based electrolytes were investigated (*see below*). On the other hand, the activity on PSCs consisted in the design and synthesis of new small organic hole transporting materials (HTMs) for *p-i-n* devices, since they have the important task of charge extraction from perovskite layer and transfer at the interface.

In accordance with the different subjects considered during the research activity, this thesis will be divided into three chapters, whose contents are briefly outlined below.

- In chapter 2, the work carried out for improving DSSC performances by increasing their Light Harvesting Efficiency (LHE) is described. This parameter strongly depends on the light-gathering capacity of the photosensitizer. For increasing light harvesting efficiency, our approach was that of synthetizing a new metal-free antenna (donor) – sensitizer (acceptor) covalent adduct (dyad), aiming to obtain a molecular system with a high molar attenuation coefficient and a broad absorption spectrum in the visible region. The desired result was expected to be achieved by exploiting Förster Resonance Energy Transfer (FRET) as a mean to transfer energy within the new antenna-acceptor system. The basic principle of this mechanism will be described. The design of the dyad took into account the need to assemble two molecular fragments having complementary light absorption properties to capture different wavelength portions, while at the same time displaying a good overlap between the donor emission band and the acceptor absorption band. To ensure the fulfilment of such important requisite, a reference sensitizer was first synthesized and fully characterized from a spectroscopic and electrochemical point of view. This allowed to select a suitable donor molecule (antenna) with the proper spectroscopic properties to obtain an enhanced FRET transfer to the sensitizer. A suitable synthetic strategy was then developed to assemble the dyad. To join the two fragments, a simple and robust methodology, allowing a late-stage connection to enhance the flexibility of the overall synthetic route, was required. A copper-catalyzed azide/alkyne cycloaddition (CuAAC)[126,127] was thus employed, in order to efficiently generate a triazole bridge between the two scaffolds functional units. The molecular dyad was finally characterized by means of different absorption and emission spectroscopy techniques, to demonstrate that an actual energy transfer occurred between the two units.

- In the following chapter, the preparation and evaluation of the performances of the DSSC devices carried out during the internship at Newcastle University will be discussed. The cells incorporated three copper-based redox mediators previously introduced by the host group for the fabrication of DSSCs with improved efficiencies under indoor and ambient lighting.

Indeed, the goal of the activity was exactly that of evaluating if such copper-based redox shuttles could work efficiently also in combination with sensitizers developed by our research group. To this end, three dyes were considered, the first of which, called **RI114**, was synthetized in the first part of this Ph.D. project, and had never been tested in DSSC until now. The second dye selected was **BTD-DTP2**,[128] an organic photosensitizer previously prepared by our research group, featuring a very similar structure to **RI114**, but a different donor unit, which allowed to differentiate its electrochemical properties. The third dye, **TTZ5** (also synthetized by our laboratory),[129] was instead based on a totally different scaffold. The latter two molecules had been previously used in photovoltaic cells in combination with a $I^-/I_3^-$ electrolyte, leading to good-to-excellent efficiencies, and it was therefore very interesting to study their photovoltaic performances in combination with electrolytes based on a different redox couple. In addition, the effect of co-sensitization with other organic sensitizers was also assessed. A series of preliminary studies were carried out making use of different characterization techniques, whose results will be discussed in detail.

- The third goal of this Ph.D. project was to synthetize new organic molecules containing phenothiazine (PTZ) units as Hole Transporting Materials for Perovskite Solar Cells (PSC). The lack of long-term stability is actually the main issue that is hampering large-scale PSC production. As a potential solution, the development of cells with “inverted” dopant-free *p-i-n* structure has been identified as a promising strategy to yield devices with a higher intrinsic stability, provided that the right materials are used. Donor-acceptor compounds containing PTZ rings decorated with triphenylamine (TPA) groups have already been employed as HTMs in perovskite solar cells leading to interesting results. Our aim in this work was that to prepare new small molecules, characterized by a dimeric structure, which had not been investigated before and might be suitable to build PSCs with inverted *p-i-n* architecture. Two molecules were designed featuring two different central cores, in order to induce a different geometric orientation of the donor units, in turn influencing the compounds packing in the solid phase and possibly affecting the performances of the devices. A detailed computational study, in collaboration with the group of prof. Adalgisa Sinicropi, University of Siena, has been performed before carrying out the synthesis and electrochemical characterization of such compounds, which will be reported in Chapter 4. The results of the PSC fabrication and characterization work, carried out by the group of Prof. Aldo Di Carlo at C.H.O.S.E., University of Rome Tor Vergata, will also be discussed.

# References

[1] NASA, “Global warming vs. climate change,” can be found under https://climate.nasa.gov/global-warming-vs-climate-change/, **2022**.

[2] International Renewable Energy Agency, *IRENA’s Energy Transition Support to Strengthen Climate Action: Insight to Impact 2022*, **2022**.

[3] International Energy Agency, “Net Zero by 2050 Scenario,” can be found under https://www.iea.org/data-and-statistics/data-product/net-zero-by-2050-scenario, **2021**.

[4] Zero Net Tracker, “Post-COP26 Snapshot,” can be found under https://zerotracker.net/analysis/post-cop26-snapshot, **2021**.

[5] REN21, *Renewables 2022 Global Status Report*, **2022**.

[6] Global Wind Energy Council, *Global Wind Report 2022*, **2022**.

[7] International Renewable Energy Agency, *World Energy Transitions Outlook: 1.5°C Pathway*, **2021**.

[8] M. Hutchins, “A year in PV: Technology trends in 2021,” can be found under https://www.pv-magazine.com/2021/12/27/a-year-in-pv-technology-trends-in-2021/, **2021**.

[9] *Bell Laboratories Record* **1954**, *32*, 232.

[10] R. A. Marques Lameirinhas, J. P. N. Torres, J. P. de Melo Cunha, *Energies (Basel)* **2022**, *15*, 1823.

[11] A. H. Alami, M. Ramadan, M. A. Abdelkareem, J. J. Alghawi, N. T. Alhattawi, H. A. Mohamad, A.-G. Olabi, *Thermal Science and Engineering Progress* **2022**, *29*, 101208.

[12] Fraunhofer Institute for Solar Energy Systems, “Photovoltaics Report 2022,” can be found under https://www.ise.fraunhofer.de/content/dam/ise/de/documents/publications/studies/Photovoltaics-Report.pdf, **2022**.

[13] N. Rathore, N. L. Panwar, F. Yettou, A. Gama, *International Journal of Ambient Energy* **2021**, *42*, 1200–1217.

[14] M. A. Green, E. D. Dunlop, G. Siefer, M. Yoshita, N. Kopidakis, K. Bothe, X. Hao, *Progress in Photovoltaics: Research and Applications* **2023**, *31*, 3–16.

[15] S. R. Wenham, M. A. Green, *Progress in Photovoltaics: Research and Applications* **1996**, *4*, 3–33.

[16] Y. Hou, Z. Mei, X. Du, *J Phys D Appl Phys* **2014**, *47*, 283001.

[17] S. Strong, *Building Integrated Photovoltaics*, **2005**.

[18] J. Jean, P. R. Brown, R. L. Jaffe, T. Buonassisi, V. Bulović, *Energy Environ Sci* **2015**, *8*, 1200–1219.

[19] NREL, “Best research-cell efficiency chart,” can be found under https://www.nrel.gov/pv/cell-efficiency.htm, **2023**.

[20] L. Kranz, S. Buecheler, A. N. Tiwari, *Solar Energy Materials and Solar Cells* **2013**, *119*, 278–280.

[21] M. Nakamura, K. Yamaguchi, Y. Kimoto, Y. Yasaki, T. Kato, H. Sugimoto, *IEEE J Photovolt* **2019**, *9*, 1863–1867.

[22] W. Wang, M. T. Winkler, O. Gunawan, T. Gokmen, T. K. Todorov, Y. Zhu, D. B. Mitzi, *Adv Energy Mater* **2014**, *4*, 1301465.

[23] N. Papež, R. Dallaev, Ş. Ţălu, J. Kaštyl, *Materials* **2021**, *14*, 3075.

[24] W. Shockley, H. J. Queisser, *J Appl Phys* **1961**, *32*, 510–519.

[25] M. Yamaguchi, T. Takamoto, K. Araki, N. Ekins-Daukes, *Solar Energy* **2005**, *79*, 78–85.

[26] A. Hagfeldt, G. Boschloo, L. Sun, L. Kloo, H. Pettersson, *Chem Rev* **2010**, *110*, 6595–6663.

[27] O. Inganäs, *Advanced Materials* **2018**, *30*, 1800388.

[28] J.-P. Correa-Baena, A. Abate, M. Saliba, W. Tress, T. Jesper Jacobsson, M. Grätzel, A. Hagfeldt, *Energy Environ Sci* **2017**, *10*, 710–727.

[29] P. Peumans, A. Yakimov, S. R. Forrest, *J Appl Phys* **2003**, *93*, 3693–3723.

[30] A. Kojima, K. Teshima, Y. Shirai, T. Miyasaka, *J Am Chem Soc* **2009**, *131*, 6050–6051.

[31] J. Pastuszak, P. Węgierek, *Materials* **2022**, *15*, 5542.

[32] H. Min, D. Y. Lee, J. Kim, G. Kim, K. S. Lee, J. Kim, M. J. Paik, Y. K. Kim, K. S. Kim, M. G. Kim, T. J. Shin, S. il Seok, *Nature* **2021**, *598*, 444–450.

[33] H. Zheng, D. Li, C. Ran, Q. Zhong, L. Song, Y. Chen, P. Müller-Buschbaum, W. Huang, *Solar RRL* **2021**, *5*, 2100042.

[34] B. O'Regan, M. Grätzel, *Nature* **1991**, *353*, 737–740.

[35] D. Zhang, M. Stojanovic, Y. Ren, Y. Cao, F. T. Eickemeyer, E. Socie, N. Vlachopoulos, J. E. Moser, S. M. Zakeeruddin, A. Hagfeldt, M. Grätzel, *Nat Commun* **2021**, *12*, 1777.

[36] L. Vesce, P. Mariani, M. Calamante, A. Dessì, A. Mordini, L. Zani, A. di Carlo, *Solar RRL* **2022**, *6*, 2200403.

[37] A. B. Muñoz-García, I. Benesperi, G. Boschloo, J. J. Concepcion, J. H. Delcamp, E. A. Gibson, G. J. Meyer, M. Pavone, H. Pettersson, A. Hagfeldt, M. Freitag, *Chem Soc Rev* **2021**, *50*, 12450–12550.

[38] L. Han, N. Koide, Y. Chiba, A. Islam, R. Komiya, N. Fuke, A. Fukui, R. Yamanaka, *Appl Phys Lett* **2005**, *86*, 213501.

[39] Y. Ooyama, Y. Harima, *European J Org Chem* **2009**, 2903–2934.

[40] M. K. Nazeeruddin, F. de Angelis, S. Fantacci, A. Selloni, G. Viscardi, P. Liska, S. Ito, B. Takeru, M. Grätzel, *J Am Chem Soc* **2005**, *127*, 16835–16847.

[41] S. Ito, T. N. Murakami, P. Comte, P. Liska, C. Grätzel, M. K. Nazeeruddin, M. Grätzel, *Thin Solid Films* **2008**, *516*, 4613–4619.

[42] H. Ozawa, Y. Okuyama, H. Arakawa, *Dalton Transactions* **2012**, *41*, 5137–5139.

[43] H. Ozawa, T. Sugiura, T. Kuroda, K. Nozawa, H. Arakawa, *J Mater Chem A Mater* **2016**, *4*, 1762–1770.

[44] K. Kakiage, Y. Aoyama, T. Yano, K. Oya, J. I. Fujisawa, M. Hanaya, *Chemical Communications* **2015**, *51*, 15894–15897.

[45] E. Krawczak, *Informatyka, Automatyka, Pomiary w Gospodarce i Ochronie Środowiska* **2019**, *9*, 86–90.

[46] Z. D. Sun, J. S. Zhao, K. Ayyanar, X. H. Ju, Q. Y. Xia, *RSC Adv* **2020**, *10*, 10569–10576.

[47] K. Hara, K. Sayama, Y. Ohga, A. Shinpo, S. Suga, H. Arakawa, *Chemical Communications* **2001**, 569–570.

[48] T. Horiuchi, H. Miura, S. Uchida, *Chemical Communications* **2003**, 3036–3037.

[49] R. Chen, X. Yang, H. Tian, L. Sun, *J Photochem Photobiol A Chem* **2007**, *189*, 295–300.

[50] T. Kitamura, M. Ikeda, K. Shigaki, T. Inoue, N. A. Anderson, X. Ai, T. Lian, S. Yanagida, *Chemistry of Materials* **2004**, *16*, 1806–1812.

[51] N. Koumura, Z. S. Wang, S. Mori, M. Miyashita, E. Suzuki, K. Hara, *J Am Chem Soc* **2006**, *128*, 14256–14257.

[52] K. Hara, M. Kurashige, S. Ito, A. Shinpo, S. Suga, K. Sayama, H. Arakawa, *Chemical Communications* **2003**, *2*, 252–253.

[53] H. Tian, X. Yang, R. Chen, Y. Pan, L. Li, A. Hagfeldt, L. Sun, *Chemical Communications* **2007**, 3741–3743.

[54] S. Hattori, T. Hasobe, K. Ohkubo, Y. Urano, N. Umezawa, T. Nagano, Y. Wada, S. Yanagida, S. Fukuzumi, *Journal of Physical Chemistry B* **2004**, *108*, 15200–15205.

[55] D. P. Hagberg, T. Edvinsson, T. Marinado, G. Boschloo, A. Hagfeldt, L. Sun, *Chemical Communications* **2006**, 2245–2247.

[56] Y. Wu, W. Zhu, *Chem Soc Rev* **2013**, *42*, 2039–2058.

[57] S. Qu, C. Qin, A. Islam, Y. Wu, W. Zhu, J. Hua, H. Tian, L. Han, *Chemical Communications* **2012**, *48*, 6972–6974.

[58] Z. S. Huang, C. Cai, X. F. Zang, Z. Iqbal, H. Zeng, D. bin Kuang, L. Wang, H. Meier, D. Cao, *J Mater Chem A Mater* **2015**, *3*, 1333–1344.

[59] S. Ko, H. Choi, M. S. Kang, H. Hwang, H. Ji, J. Kim, J. Ko, Y. Kang, *J Mater Chem* **2010**, *20*, 2391–2399.

[60] M. J. Yun, S. I. Cha, S. H. Seo, D. Y. Lee, *Sci Rep* **2014**, *4*, 5322.

[61] Z. Wang, M. Liang, Y. Hao, Y. Zhang, L. Wang, Z. Sun, S. Xue, *J Mater Chem A Mater* **2013**, *1*, 11809–11819.

[62] J. I. Nishida, T. Masuko, Y. Cui, K. Hara, H. Shibuya, M. Ihara, T. Hosoyama, R. Goto, S. Mori, Y. Yamashita, *Journal of Physical Chemistry C* **2010**, *114*, 17920–17925.

[63] J. H. Delcamp, A. Yella, M. K. Nazeeruddin, M. Grätzel, *Chemical Communications* **2012**, *48*, 2295–2297.

[64] C. Chen, X. Yang, M. Cheng, F. Zhang, L. Sun, *ChemSusChem* **2013**, *6*, 1270–1275.

[65] Y. Ooyama, T. Yamada, T. Fujita, Y. Harima, J. Ohshita, *J Mater Chem A Mater* **2014**, *2*, 8500.

[66] S. Ahmad, E. Guillén, L. Kavan, M. Grätzel, M. K. Nazeeruddin, *Energy Environ Sci* **2013**, *6*, 3439–3466.

[67] K. Kakiage, Y. Aoyama, T. Yano, T. Otsuka, T. Kyomen, M. Unno, M. Hanaya, *Chemical Communications* **2014**, *50*, 6379–6381.

[68] A. Abate, R. Pérez-Tejada, K. Wojciechowski, J. M. Foster, A. Sadhanala, U. Steiner, H. J. Snaith, S. Franco, J. Orduna, *Physical Chemistry Chemical Physics* **2015**, *17*, 18780–18789.

[69] L. Zhang, J. M. Cole, *ACS Appl Mater Interfaces* **2015**, *7*, 3427–3455.

[70] W. R. McNamara, R. C. Snoeberger, G. Li, C. Richter, L. J. Allen, R. L. Milot, C. A. Schmuttenmaer, R. H. Crabtree, G. W. Brudvig, V. S. Batista, *Energy Environ Sci* **2009**, *2*, 1173–1175.

[71] R. Harikisun, H. Desilvestro, *Solar Energy* **2011**, *85*, 1179–1188.

[72] I. Benesperi, H. Michaels, M. Freitag, *J Mater Chem C Mater* **2018**, *6*, 11903–11942.

[73] G. Boschloo, A. Hagfeldt, *Acc Chem Res* **2009**, *42*, 1819–1826.

[74] Y. Saygili, M. Söderberg, N. Pellet, F. Giordano, Y. Cao, A. B. Munoz-García, S. M. Zakeeruddin, N. Vlachopoulos, M. Pavone, G. Boschloo, L. Kavan, J. E. Moser, M. Grätzel, A. Hagfeldt, M. Freitag, *J Am Chem Soc* **2016**, *138*, 15087–15096.

[75] S. M. Feldt, E. A. Gibson, E. Gabrielsson, L. Sun, G. Boschloo, A. Hagfeldt, *J Am Chem Soc* **2010**, *132*, 16714–16724.

[76] J. Burschka, V. Brault, S. Ahmad, L. Breau, M. K. Nazeeruddin, B. Marsan, S. M. Zakeeruddin, M. Grätzel, *Energy Environ Sci* **2012**, *5*, 6089–6097.

[77] J. Wu, Z. Lan, J. Lin, M. Huang, Y. Huang, L. Fan, G. Luo, Y. Lin, Y. Xie, Y. Wei, *Chem Soc Rev* **2017**, *46*, 5975–6023.

[78] A. Kay, M. Grätzel, *Solar Energy Materials and Solar Cells* **1996**, *44*, 99–117.

[79] K. Suzuki, M. Yamaguchi, M. Kumagai, S. Yanagida, *Chem Lett* **2003**, *32*, 28–29.

[80] K. Saranya, Md. Rameez, A. Subramania, *Eur Polym J* **2015**, *66*, 207–227.

[81] J. Yang, C. Bao, K. Zhu, T. Yu, F. Li, J. Liu, Z. Li, Z. Zou, *Chemical Communications* **2014**, *50*, 4824–4826.

[82] W. Wei, H. Wang, Y. H. Hu, *Int J Energy Res* **2014**, *38*, 1099–1111.

[83] S. Kazim, M. K. Nazeeruddin, M. Grätzel, S. Ahmad, *Angewandte Chemie - International Edition* **2014**, *53*, 2812–2824.

[84] X. Wang, L. L. Deng, L. Y. Wang, S. M. Dai, Z. Xing, X. X. Zhan, X. Z. Lu, S. Y. Xie, R. bin Huang, L. S. Zheng, *J Mater Chem A Mater* **2017**, *5*, 1706–1712.

[85] I. Hussain, H. P. Tran, J. Jaksik, J. Moore, N. Islam, M. J. Uddin, *Emergent Mater* **2018**, *1*, 133–154.

[86] H. S. Kim, C. R. Lee, J. H. Im, K. B. Lee, T. Moehl, A. Marchioro, S. J. Moon, R. Humphry-Baker, J. H. Yum, J. E. Moser, M. Grätzel, N. G. Park, *Sci Rep* **2012**, *2*, 591.

[87] S. Pitchaiya, M. Natarajan, A. Santhanam, V. Asokan, A. Yuvapragasam, V. Madurai Ramakrishnan, S. E. Palanisamy, S. Sundaram, D. Velauthapillai, *Arabian Journal of Chemistry* **2020**, *13*, 2526–2557.

[88] Z. Song, S. C. Watthage, A. B. Phillips, M. J. Heben, *J Photonics Energy* **2016**, *6*, 022001.

[89] J. Y. Jeng, Y. F. Chiang, M. H. Lee, S. R. Peng, T. F. Guo, P. Chen, T. C. Wen, *Advanced Materials* **2013**, *25*, 3727–3732.

[90] J. Chen, N. G. Park, *Journal of Physical Chemistry C* **2018**, *122*, 14039–14063.

[91] Y. Wang, W. Chen, L. Wang, B. Tu, T. Chen, B. Liu, K. Yang, C. W. Koh, X. Zhang, H. Sun, G. Chen, X. Feng, H. Y. Woo, A. B. Djurišić, Z. He, X. Guo, *Advanced Materials* **2019**, *31*, 1902781.

[92] X. Zheng, Y. Hou, C. Bao, J. Yin, F. Yuan, Z. Huang, K. Song, J. Liu, J. Troughton, N. Gasparini, C. Zhou, Y. Lin, D. J. Xue, B. Chen, A. K. Johnston, N. Wei, M. N. Hedhili, M. Wei, A. Y. Alsalloum, P. Maity, B. Turedi, C. Yang, D. Baran, T. D. Anthopoulos, Y. Han, Z. H. Lu, O. F. Mohammed, F. Gao, E. H. Sargent, O. M. Bakr, *Nat Energy* **2020**, *5*, 131–140.

[93] Z. Yu, L. Sun, *Adv Energy Mater* **2015**, *5*, 1500213.

[94] X. Yang, H. Wang, B. Cai, Z. Yu, L. Sun, *Journal of Energy Chemistry* **2018**, *27*, 650–672.

[95] N. J. Jeon, H. G. Lee, Y. C. Kim, J. Seo, J. H. Noh, J. Lee, S. il Seok, *J Am Chem Soc* **2014**, *136*, 7837–7840.

[96] X. Yin, Z. Song, Z. Li, W. Tang, *Energy Environ Sci* **2020**, *13*, 4057–4086.

[97] Y. Sun, C. Wang, D. Zhao, J. Yu, X. Yin, C. R. Grice, R. A. Awni, N. Shrestha, Y. Yu, L. Guan, R. J. Ellingson, W. Tang, Y. Yan, *Solar RRL* **2018**, *2*, 1700175.

[98] E. H. Jung, N. J. Jeon, E. Y. Park, C. S. Moon, T. J. Shin, T.-Y. Yang, J. H. Noh, J. Seo, *Nature* **2019**, *567*, 511–515.

[99] K. Rakstys, C. Igci, M. K. Nazeeruddin, *Chem Sci* **2019**, *10*, 6748–6769.

[100] J. Burschka, A. Dualeh, F. Kessler, E. Baranoff, N. L. Cevey-Ha, C. Yi, M. K. Nazeeruddin, M. Grätzel, *J Am Chem Soc* **2011**, *133*, 18042–18045.

[101] A. Abate, T. Leijtens, S. Pathak, J. Teuscher, R. Avolio, M. E. Errico, J. Kirkpatrik, J. M. Ball, P. Docampo, I. McPherson, H. J. Snaith, *Physical Chemistry Chemical Physics* **2013**, *15*, 2572–2579.

[102] Z. Hawash, L. K. Ono, Y. Qi, *Adv Mater Interfaces* **2018**, *5*, 1700623.

[103] P. Murugan, T. Hu, X. Hu, Y. Chen, *J Mater Chem A Mater* **2022**, *10*, 5044–5081.

[104] S. Kazim, F. J. Ramos, P. Gao, M. K. Nazeeruddin, M. Grätzel, S. Ahmad, *Energy Environ Sci* **2015**, *8*, 1816–1823.

[105] P. Qin, H. Kast, M. K. Nazeeruddin, S. M. Zakeeruddin, A. Mishra, P. Bäuerle, M. Grätzel, *Energy Environ Sci* **2014**, *7*, 2981.

[106] Y. Liu, Z. Hong, Q. Chen, H. Chen, W. H. Chang, Y. (Michael) Yang, T. bin Song, Y. Yang, *Advanced Materials* **2016**, *28*, 440–446.

[107] F. Al-Zohbi, Y. Jouane, S. Benhattab, J. Faure-Vincent, F. Tran-Van, S. Vedraine, J. Bouclé, N. Berton, B. Schmaltz, *New Journal of Chemistry* **2019**, *43*, 12211–12214.

[108] X. Sun, F. Wu, C. Zhong, L. Zhu, Z. Li, *Chem Sci* **2019**, *10*, 6899–6907.

[109] X. Liu, E. Rezaee, H. Shan, J. Xu, Y. Zhang, Y. Feng, J. Dai, Z. K. Chen, W. Huang, Z. X. Xu, *J Mater Chem C Mater* **2018**, *6*, 4706–4713.

[110] M. Cheng, B. Xu, C. Chen, X. Yang, F. Zhang, Q. Tan, Y. Hua, L. Kloo, L. Sun, *Adv Energy Mater* **2015**, *5*, 1401720.

[111] J. Zhang, B. Xu, L. Yang, C. Ruan, L. Wang, P. Liu, W. Zhang, N. Vlachopoulos, L. Kloo, G. Boschloo, L. Sun, A. Hagfeldt, E. M. J. Johansson, *Adv Energy Mater* **2018**, *8*, 1701209.

[112] K. Rakstys, S. Paek, P. Gao, P. Gratia, T. Marszalek, G. Grancini, K. T. Cho, K. Genevicius, V. Jankauskas, W. Pisula, M. K. Nazeeruddin, *J Mater Chem A Mater* **2017**, *5*, 7811–7815.

[113] T. Duong, J. Peng, D. Walter, J. Xiang, H. Shen, D. Chugh, M. Lockrey, D. Zhong, J. Li, K. Weber, T. P. White, K. R. Catchpole, *ACS Energy Lett* **2018**, *3*, 2441–2448.

[114] Y. Matsuo, K. Ogumi, I. Jeon, H. Wang, T. Nakagawa, *RSC Adv* **2020**, *10*, 32678–32689.

[115] M. Urbani, G. de La Torre, M. K. Nazeeruddin, T. Torres, *Chem Soc Rev* **2019**, *48*, 2738–2766.

[116] W. Ke, D. Zhao, C. R. Grice, A. J. Cimaroli, G. Fang, Y. Yan, *J Mater Chem A Mater* **2015**, *3*, 23888–23894.

[117] X. Jiang, Z. Yu, H. B. Li, Y. Zhao, J. Qu, J. Lai, W. Ma, D. Wang, X. Yang, L. Sun, *J Mater Chem A Mater* **2017**, *5*, 17862–17866.

[118] J. H. Park, J. Seo, S. Park, S. S. Shin, Y. C. Kim, N. J. Jeon, H.-W. Shin, T. K. Ahn, J. H. Noh, S. C. Yoon, C. S. Hwang, S. il Seok, *Advanced Materials* **2015**, *27*, 4013–4019.

[119] J. A. Christians, R. C. M. Fung, P. v Kamat, *J Am Chem Soc* **2014**, *136*, 758–764.

[120] P. Qin, S. Tanaka, S. Ito, N. Tetreault, K. Manabe, H. Nishino, M. K. Nazeeruddin, M. Grätzel, *Nat Commun* **2014**, *5*, 3834.

[121] V. E. Madhavan, I. Zimmermann, C. Roldán-Carmona, G. Grancini, M. Buffiere, A. Belaidi, M. K. Nazeeruddin, *ACS Energy Lett* **2016**, *1*, 1112–1117.

[122] P.-P. Zhang, Z.-J. Zhou, D.-X. Kou, S.-X. Wu, *International Journal of Photoenergy* **2017**, *2017*, 6109092.

[123] C. Honsberg, S. Bowden, “Standard Solar Spectra,” can be found under https://www.pveducation.org/pvcdrom/appendices/standard-solar-spectra, **2019**.

[124] National Renewable Energy Laboratory, “Reference Air Mass 1.5 Spectra,” can be found under https://www.nrel.gov/grid/solar-resource/spectra-am1.5.html, **2004**.

[125] Y. Ooyama, Y. Harima, *ChemPhysChem* **2012**, *13*, 4032–4080.

[126] M. Meldal, C. W. Tornøe, *Chem Rev* **2008**, *108*, 2952–3015.

[127] E. Haldón, M. C. Nicasio, P. J. Pérez, *Org Biomol Chem* **2015**, *13*, 9528–9550.

[128] A. Dessì, D. A. Chalkias, S. Bilancia, A. Sinicropi, M. Calamante, A. Mordini, A. Karavioti, E. Stathatos, L. Zani, G. Reginato, *Sustain Energy Fuels* **2021**, *5*, 1171–1183.

[129] A. Dessì, M. Calamante, A. Mordini, M. Peruzzini, A. Sinicropi, R. Basosi, F. Fabrizi de Biani, M. Taddei, D. Colonna, A. di Carlo, G. Reginato, L. Zani, *Chem. Commun.* **2014**, *50*, 13952–13955.

# Chapter 2

# Enhanced light harvesting efficiency by Foster Resonance Energy Transfer in Dye-Sensitized Solar Cells (DSSCs)

## 2.1. Introduction

As depicted in Chapter 1, Dye-Sensitized Solar Cells (DSSCs) demonstrated to be a promising and less expensive alternative to silicon-based solar cells for specific applications (e.g. BIPV).[1] DSSCs efficiency depends on the optimization and compatibility of each of their components, which are studied to improve specific photovoltaic parameters like photovoltage ($V_{oc}$), for example by changing the support oxide, photocurrent ($J_{sc}$), using different dyes, or stability, by changing the electrolyte or the sealant.[2] Therefore, different strategies can be explored to improve the efficiency of such devices. As described in Chapter 1, the dye is the core of the device having the important task to absorb sunlight and transfer the electron generated by photoexcitation into the conduction band (CB) of the titanium dioxide, therefore $J_{sc}$ values can be increased by improving the light harvesting efficiency (LHE) of the dye.[3]

### 2.1.1. Increasing Light Harvesting Efficiency (LHE)

In a DSSC, LHE is defined as the fraction of light intensity absorbed by the dye at a certain wavelength, according to equation (2.1):[4]

$$LHE = A = {}^{I_A}/_{I_0} \tag{2.1}$$

where A is absorptance, $I_A$ is the absorbed light intensity and $I_0$ is the incident one. Also, IPCE is defined as the number of electrons generated by the solar cell divided by the number of incident photons, which is proportional to LHE or absorptance. The generated $J_{sc}$ can thus be calculated by expression (2.2):

$$J_{sc} = \int qIPCE(\lambda)F(\lambda)d\lambda = \int qLHE\,(\lambda)\varphi(\lambda)\eta(\lambda)\,F(\lambda)d\lambda \tag{2.2}$$

where $q$ is the electron charge, $\varphi(\lambda)$ is the electron injection quantum yield, $\eta(\lambda)$ is the charge collection efficiency and $F(\lambda)$ is the incident photon flux. Since $\varphi(\lambda)$ and $\eta(\lambda)$ are only weakly dependent on the wavelength λ, equation (2.2) can be simplified to the following form:

$$J_{sc} \propto \int qLHE(\lambda)F(\lambda)d\lambda = \int qA(\lambda)F(\lambda)d\lambda \tag{2.3}$$

Equation (2.3) clearly shows the direct proportionality between the photocurrent density and the light harvesting efficiency. Ideally, all photons below a threshold wavelength of about 920 nm should be harvested and converted into electric current.[5] Moreover, there is also another important property required for the light collection, the directionality that the sensitizer must possess in its excited state. This directionality should be engineered to provide an efficient electron transfer via good electronic coupling between the lowest unoccupied molecular orbital (LUMO) of the sensitizer and the conduction band of $TiO_2$.[6] In summary, in order to improve the light harvesting efficiency (LHE) of the device, the dye should have three fundamental properties:

1. high light absorption capacity;
2. optimal ability to transfer the electron into the conduction band of the $TiO_2$;

3. a wide absorption spectrum.

To satisfy the first and the second requirement, the employment of a metal-free organic dye is considered advantageous (see paragraph 1.4.3), as the organic dyes strongly absorb light, which results in high molar attenuation coefficients (ε). Unfortunately, they usually do it only in a narrow spectral window thus it might be a very difficult task to design a single sensitizer able to absorb light efficiently over the entire visible and near-IR spectrum, that is from 400 to 920 nm, and fulfills all the requirements necessary to obtain high device performances. A valid approach is to use the *co-sensitization* concept.[7] Mixtures of two or more sensitizers as ‘‘dyes cocktails’’ with complementary absorption spectra are attached to the $TiO_2$ surface to achieve panchromatic sensitization. Nonetheless, co-sensitization requires a tedious optimization process to find suitable chemisorption conditions.[7,8] The performances greatly depend on the concentration ratio of the dyes in the dyeing bath and the adsorption time. Indeed, the limited number of sites available on the $TiO_2$ surface reduces the amount of dyes which can be loaded on the electrodes. Recently another concept has been proposed to broaden the spectral absorption window by the sensitising dye, taking inspiration from biological photosynthetic organisms.[9] To capture light energy efficiently, during evolution Nature has developed a very efficient molecular system: the light-harvesting antenna.[10] Photons of different colours are absorbed by the different pigments of a specific chromophore (the antenna or donor – the colored triangles in Figure 2.1), then the excitation energy is funnelled to a different molecular unit (the acceptor – D-P-A assembly in Figure 2.1) through very rapid and efficient energy transfers.[9]

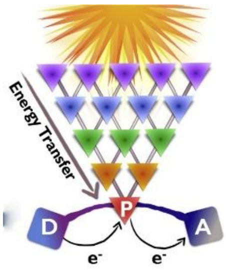

*Figure 2.1. Schematization of a possible artificial photosynthetic system.*[11] *The colored triangles indicate the chromophores constituting the antenna systems; the D–P–A assembly corresponds to the reaction center*

Following this approach, we decided to synthesise a new metal-free antenna-acceptor adduct, aiming to obtain a molecular system with a high molar attenuation coefficient and expanded absorption spectrum width. Our intention was that of verify that such molecular design would really improve the light harvesting and consequently the DSSC efficiency. To this end, we imagined to use two different molecular fragments with complementary absorption bands. The desired result was expected to be achieved by exploiting Förster Resonance Energy Transfer (FRET) as a mean to transfer energy within the new antenna-acceptor system. Indeed, a variety of elegant structures have been prepared in previous years and significant light-harvesting efficiencies have been achieved with artificial antenna-acceptor systems.[12]

## 2.1.2. Forster Resonance Energy transfer

Forster Resonance Energy transfer (FRET) is a mechanism by which one molecule may transfer its excitation energy non radiatively to another molecule separated by a short distance.[13] The theoretical analysis was well developed by Theodor Förster. This non-radiative transfer mechanism is schematically illustrated in Figure 2.2. An electron from a donor molecule (D) is excited (1) by a photon and then relaxes to its lowest excited singlet state (2). If the acceptor molecule is not too far, the energy released when the electron returns to the ground state (S) may simultaneously excite the acceptor group (3). This non-radiative process is referred to as "resonance". After excitation, the acceptor relaxes to its lowest excited state and from there emits a photon, returning to the ground state (4-5).

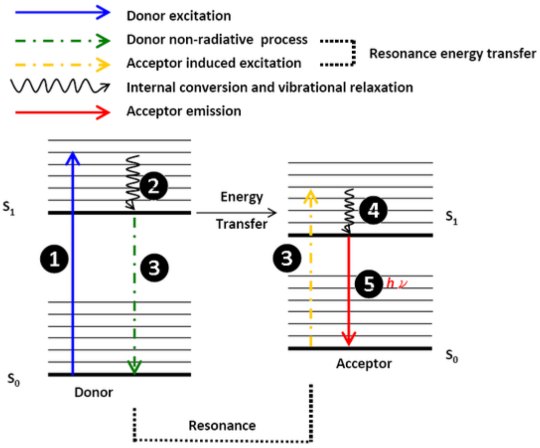

*Figure 2.2: Schematic diagram of Förster Resonance Energy Transfer (FRET).*[14]

The final result is that the acceptor has become excited due to the indirect absorption of a photon to which it would otherwise be insensitive.[15] The FRET efficiency (E) is the quantum yield of the energy transfer transition, *i.e.,* the fraction of energy transfer event occurring per donor excitation event. The FRET efficiency is given by:

$$E = \frac{K_{ET}}{K_F + K_{ET} + \Sigma k_i} \qquad (2.4)$$

Where $K_{ET}$ is the rate of FRET, $K_F$ is the rate of radiative relaxation (i.e., fluorescence), and $k_i$ are the non-radiative relaxation rates (e.g., internal conversion, intersystem crossing, external conversion etc.). Within a point dipole-dipole approximation, the FRET efficiency can be related to the donor-acceptor distance via:

$$E = \frac{1}{1+(\frac{r}{R_0})^6} \qquad (2.5)$$

Where $r$ is the distance between donor and acceptor chromophores and $R_0$ is the characteristic distance (the Förster distance or Förster radius) with a 50% transfer efficiency. From equation (2.5) it clearly emerges that the efficiency of FRET critically depends on the distance between the two chromophores, quickly declining with the sixth power of r. Therefore, to have an efficient FRET it is mandatory to find ways to control the distance between donor and acceptor, possibly always keeping it within the limits of $R_0$. The Förster radius is expressed as:

$$(R_0)^6 = 8.8 \times 10^{23}\, k^2 n^{-4} Q_0\, J \tag{2.6}$$

Where $k$ indicates the orientation factor of the dipole (depending on the freedom of rotation of the molecules), $n$ is the refractive index of the solution, $Q_0$ is the donor fluorescence quantum yield and $J$ represents the overlap integral, depending on both the emission spectrum of the donor and the molar attenuation coefficient of the acceptor. The overlap is given by:

$$J = \int_0^\infty F_D(\lambda)\epsilon_A(\lambda)\lambda^4 d\lambda \tag{2.7}$$

Where $F_D(\lambda)$ is the normalized emission spectrum of the donor, $\varepsilon_A(\lambda)$ the molar attenuation coefficient of the acceptor, and $\lambda$ is the wavelength. Indeed, to enhance the FRET efficiency, an extended overlap between the emission spectrum of the donor and the absorption spectrum of the acceptor is necessary. The overlap integral between the donor and the acceptor stands for the overlap of spectra, as shown in Figure 2.3.

In conclusion, for an efficient FRET effect it is therefore essential to employ a pair of fluorescent dyes with these properties:

1. large separation of the absorption spectra between donor and acceptor;
2. good overlap (>30%) between the fluorescence spectrum of the donor and the absorption spectrum of the acceptor;
3. large separation between the fluorescence spectrum of the donor and that of the acceptor.

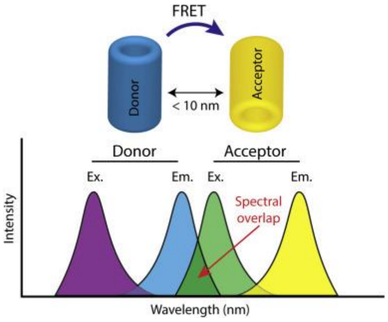

*Figure 2.3: Scheme of spectral overlap between donor and acceptor molecules.*[16]

Currently, the FRET effect is exploited in many sectors. For example, it is widely used in biology where it is applied to the study of protein-protein interactions, to determine the stoichiometry of protein complexes, for the analysis of protein conformational changes, for DNA sequencing, etc.[17] It is also used in sunlight conversion systems based on luminescent solar concentrators, to expand the light-harvesting capability of the devices.[18] Analogously, as far as DSSC are concerned, [19] it appears clear that, in principle, the FRET effect can be used to broaden the absorption range of a normal chromophore, using the emission of a second chromophore that behaves as donor. In this case, the widening of the light absorption range can result in an increase in LHE.[20] A large number of works report the use of antenna-donor couples to achieve such result, but usually in those studies no bond between the two chromophores is established.[13] For example, Hardin *et al.*[21] demonstrated that the chromophore **PTCD1**, having a high luminescence, once dissolved in the liquid electrolyte of a DSSC can absorb highly energetic photons and effectively transfer them to the dye zinc-phthalocyanin **TT1** (Figure 2.4). This leads to an increase in bandwidth of absorption of the phthalocyanine dye, with a consequent increase of the efficiency of the DSSC.

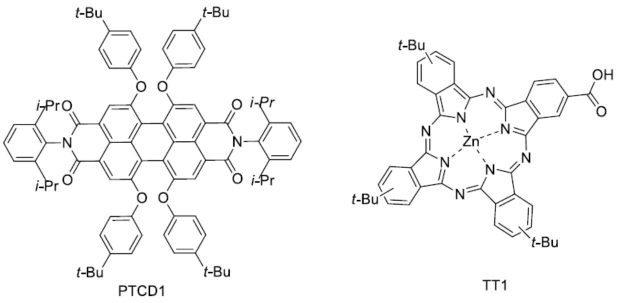

*Figure 2.4: structure of **PTCD1** and **TT1***

Mor *et al.*[22] observed a significant increase of the generated photocurrent (up to 25%) in solid-state DSSCs prepared using $TiO_2$ nanotubes sensitized with the **SQ1** molecule, a dye with absorption maximum in the near infrared, as the acceptor (Figure 2.5). The effect was observed when the donor **DCM-pyran**, whose absorption maximum is in the visible range, was dispersed in the solid hole-conductor **Spiro-OMeTAD**, which was interleaved with the **SQ-1**-sensitized $TiO_2$ nanotubes.

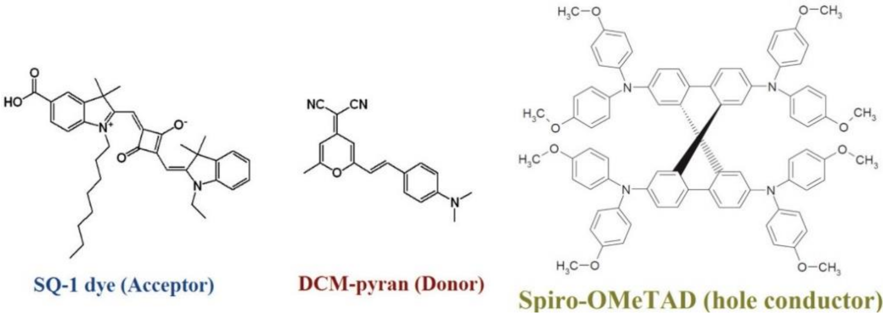

*Figure 2.5: structures of the acceptor **SQ-1** dye, donor **DCM-pyran**, and the hole conductor **Spiro-OMeTAD***

FRET-effect was demonstrated also in other papers reporting another squaraine[23] or a zinc phthalocyanine[24] as dye/acceptor molecule in combination with a small donor[23] or a polymer[24] as antennas, respectively.

As a strategy to better control the distance between the donor and the acceptor units, Odobel *et al.*[25] developed a supramolecular approach, which exploited FRET to increase the efficiency of DSSC. In this work a zinc porphyrin dye was modified by covalently binding an acceptor to the structure. Subsequently, exploiting the preference for the penta-coordination of the Zn porphyrins, a molecular interaction between the donor and the antenna (DPP) was established

(Figure 2.6). It has thus been observed that this type of interaction was able to broaden the light absorption band and demonstrated an indisputable superiority compared to the systems seen so far. Furthermore, this type of association was quite stable.

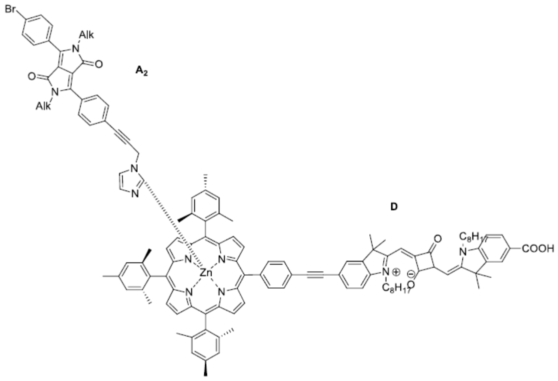

*Figure 2.6: Supramolecular approach between dye D and antenna system A2.*

Other applications of this supramolecular approach have been reported by the same authors using the same porphyrin dye and a BODIPY[26] as antenna, and by Ko *et al.* employing a ruthenium phthalocyanine[27] complexed by an organic antenna.

A similar approach was reported again by Odobel *et al.*, who, in another work, demonstrated how the FRET is also operational in a new type of dye-antenna system connected by covalent bonds (Figure 2.7) [8] In particular, they synthesized a panchromatic dye (simply denoted as **T**) in which three chromophore units, a BODIPY, a porphyrin (ZnP), and a squaraine (SQ) were linked together through covalent bonds. Again, an efficient intramolecular energy transfer was observed among the three chromophores as well as a 30% increase of the light-to-current conversion efficiency in the corresponding DSSCs compared to the cells built with the squaraine dye alone.

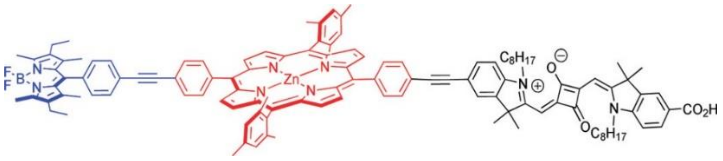

*Figure 2.7: structure of **T**-dye.*

Despite the impressive result presented in this work, there were still some drawbacks that limited the efficiency of this approach. First, the synthesis of the triadic system **T** was very challenging and was based on a final statistical Heck alkynylation to join the three fragments, which limited the final yield of **T** and forced the authors to conduct a tedious chromatographic purification. Furthermore, although the different units presented a good spectral overlap, they were relatively “standard” components deriving from commercially available compounds, which were not optimized towards ideal functioning in DSSC: as a result, the overall cell efficiency was still relatively low, not surpassing 4.0%.

Taking inspiration from the above studies, it was thus reasoned that a more refined approach could be that of choosing a metal-free organic dye capable of giving highly efficient DSSCs *per se* and find a way to modify its structure to connect it with a tailor-made antenna, displaying an emission spectrum perfectly overlapped with the dye absorption. If the connection could be made at the end of the synthesis (ideally by joining the two complete units), exploiting an easy and reproducible synthetic method, this would also provide an opportunity to screen different antennas with the same dye, or even to prepare combinatorial antenna-dye libraries, allowing to compare the relative spectroscopic properties and the performances of the corresponding solar cells.

## 2.2. Design of a new antenna-dye molecular system

According to the concept presented in the previous paragraph, the goal of this project was to provide a proof-of-principle of such approach by synthesizing an organic photosensitizer for $TiO_2$ composed by two covalently attached portions: an acceptor dye and a donor (or antenna) moiety. The two fragments should have complementary light absorption properties to capture different light portions, while at the same time displaying a good overlap between the donor emission band and the acceptor absorption band. Furthermore, it should be possible to join them by means of a simple and robust methodology, allowing a late-stage connection that would improve the flexibility of the overall synthetic route.

A classic approach applied in organic synthesis to achieve this kind of goal has long been the use of so-called “click” reactions, whose concept was defined in 2001 by Kolb, Finn and Sharpless as a mean to bind two molecular building blocks together in a facile, selective, and high-yielding reaction under mild, water-tolerant conditions with little or no by-products.[28] The most used “click” reaction that can fulfill these conditions is the CuI-catalyzed azide/alkyne cycloaddition (CuAAC).[29] In 2002, the research groups of Fokin and Sharpless [28] and of Meldal *et al.*[30] independently reported the efficient CuI catalysis of the azide/alkyne cycloaddition. Indeeed, the non-catalyzed azide/alkyne reaction has been known since 1893 as Huisgen reaction, and produces a mixture of 1,4 and 1,5-disubstitution products[31] whereas, the CuAAC reaction of terminal alkynes is completely selective in the formation of the 1,4-disubstituted triazoles. The reasons for its success are that this “click” reaction is very easy to carry out,widely applicable and high yielding without producing by-products. Indeed, it is unaffected by a variety of functional groups and can be achieved with many sources of catalysts and solvents, including aqueous systems.[29] For all these reasons in our design, it was decided to use a triazole bridge between the two functional units comprising the molecular dyad (Figure 2.8), as it could possibly be easily generated using CuAAC reaction.

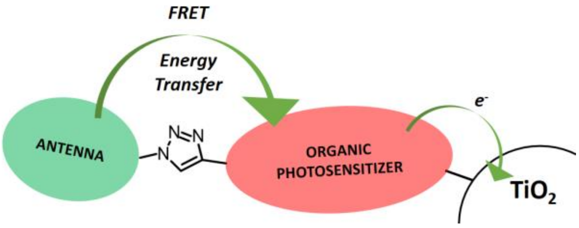

*Figure 2.8: schematic representation of FRET between couple antenna-acceptor dye bonded by triazole bridge.*

Following this idea, we decided to design and synthesize an acceptor organic sensitizer (dye), to study its optical and electrochemical properties, and after that prepare a suitable donor molecule (antenna), with the proper spectroscopic properties to obtain an enhanced FRET transfer.

### 2.2.1. Design of the model acceptor molecule (dye)

As described in Chapter 1.4.3, most of metal-free organic sensitizers have been assembled with a typical electron donor–π–acceptor (D–π–A) configuration. Recently, a novel ‘‘D–A–π–A’’ concept for designing organic sensitizers has been introduced (Figure 2.9a), in which several kinds of electron-withdrawing units (such as benzothiadiazole,[32] benzotriazole,[33] quinoxaline,[34] phthalimide,[35] *etc.*) are incorporated into the π-bridge to tailor molecular structures, optimize energy levels[36] and widen the relatively narrow low-energy absorption bands to take advantage of a larger portion of the visible spectrum. Indeed, it has been shown that the incorporated electron-withdrawing additional acceptor can (i) facilitate the electron transfer from the donor to the acceptor/anchor; (ii) tailor the solar cell performance through facile additional structural modifications; (iii) conveniently tune the molecular energy gap and, most importantly, (iv) improve the sensitizer photo-stability.[37]

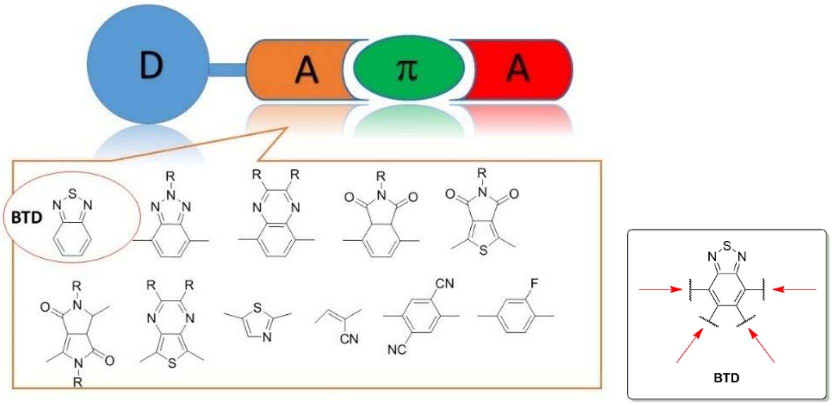

*Figure 2.9: a) Structures of organic D–A–π–A sensitizers as well as building blocks for additional electron-withdrawing acceptors;[37] b) BTD-free positions for structure modifications.*

As an important building block, benzo-2,1,3-thiadiazole (BTD, Figure 2.9b) is a strong electron withdrawing unit with a five-membered heterocyclic ring, exhibiting an enhanced electron-deficient character. The four substitution positions on the phenyl ring of BTD provide ample opportunity for convenient structure modification. The highest occupied molecular orbital (HOMO) and the lowest unoccupied molecular orbital (LUMO) of organic compounds can be readily tailored with incorporation of BTD in their structures, inspiring researchers to develop BTD-based organic sensitizers for DSSCs [36]. In particular, previous work reported by the group where this thesis work was carried out [38] showed the synthesis and application of a class of BTD-based *D-A-π-A* sensitizers.. In such study, the conjugated scaffold of the molecules was completed by connecting BTD with a dithieno[3,2-*b*:2',3'-*d*]pyrrole (DTP)[39]moiety (Figure 2.10). Indeed, the DTP unit had already been successfully inserted in DSSC sensitizers, exhibiting two main favourable features: (a) it can be easily modified by introducing different substituents on the bridging nitrogen, allowing the tuning of important properties such as the solubility in organic solvents;[19] (b) it possesses a wide π-conjugation due to the co-planarity of its bridged tricyclic system. Among the reported compounds, **BTD-DTP1** was characterized by the simplest structure, presenting only a small *n*-hexyl substituent on the dithienopyrrole nitrogen and a bare triphenylamine donor. Compound **BTD-DTP2**, on the other hand, was decorated with a bulky biphenyl group flanked by *n*-octyloxy chains, which was expected to improve the compound solubility, as well as limit charge recombination phenomena in the cells after adsorption on $TiO_2$. Indeed, in **BTD-DTP2** the long alkoxy chains present on the biphenyl side group assumed an almost perpendicular orientation relative to the dye backbone, supporting the possibility of forming an efficient insulating layer on the semiconductor surface and suppress dye aggregation. Spectroscopic characterization of the molecules in solution revealed for **BTD-DTP2** an absorption band well-centred in the visible region, with maxima located in the 525-536 nm range depending on the solvent.

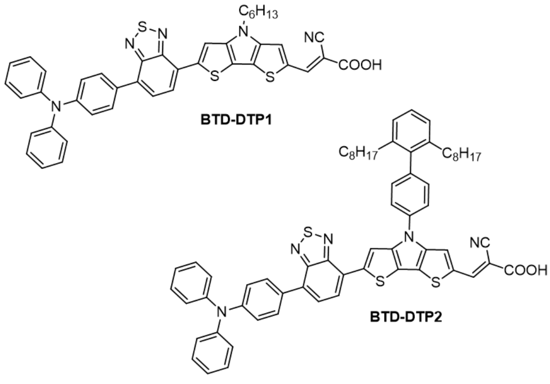

**BTD-DTP1** $\lambda_{abs}$ = 544 nm ($CHCl_3$), 532 nm(THF)
**BTD-DTP2** $\lambda_{abs}$ = 536 nm ($CHCl_3$), 525 nm(THF)

*Figure 2.10: Structure of the benzothiadiazole (BTD)-dithienopyrrole (DTP) dyes previously reported by the research group where this thesis was carried out.*

Moreover, electrochemical impedance spectroscopy (EIS) studies demonstrated that the bulky biphenyl substituent present in dye **BTD-DTP2** could screen efficiently the semiconductor surface in full working cells and thus reduce charge recombination rates at the $TiO_2$/dye/electrolyte interface.

On the other hand, Xie et al.[40] synthetized a series of indoline-based sensitizers, aiming to compare the effect of inserting different auxiliary groups (electron-rich or deficient) into the π-spacer (Figure 2.11). Upon the incorporation of strong electron withdrawing groups like BTD or benzoxadiazole (BOD), the D–A–π–A dyes denoted as **WS-54** and **WS-55** manifested a broader light response compared to the other structures, which resulted in a smaller hypsochromic shift after adsorption onto $TiO_2$ and induced the appearance of an additional sub-absorption band in the 400–450 nm region. Accordingly, the photovoltaic efficiency of the corresponding DSSCs was greatly improved when changing the auxiliary group from EDOT (dye **WS-53**, PCE = 0.24%) to BDT (dye **WS-54**, PCE = 7.14%).

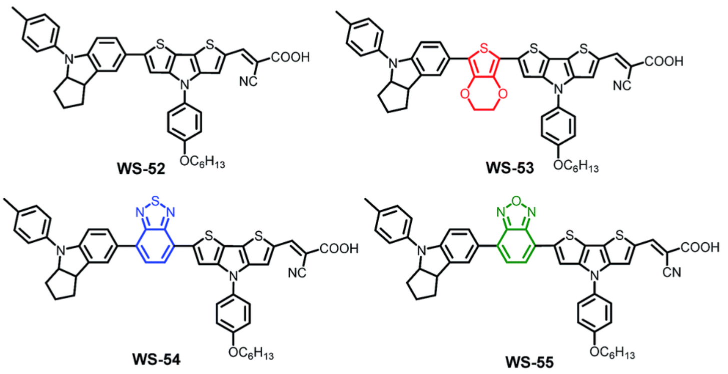

*Figure 2.11: molecular structures of dyes* ***WS-52, WS-53, WS-54*** *and* ***WS-55*** *containing different auxiliary groups* [40].

Based on the above considerations, with the aim to induce a bathochromic shift and widen light absorption compared to that of compound **BTD-DTP2**, we decided to design and synthetize a new molecule (denoted as **RI114**) simply by replacing the triphenylamine donor with a more strongly donating indoline group (Figure 2.12).

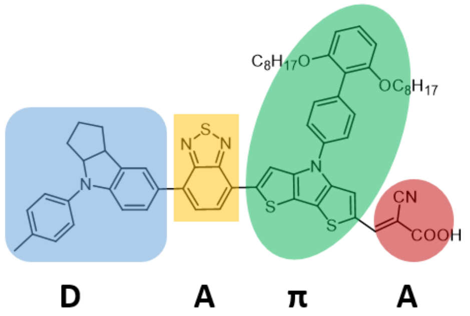

*Figure 2.12: Structure of the standard D-A-π-A dye* ***RI114*** *designed in this work.*

### 2.2.2. Synthesis of the model acceptor sensitizer **RI114**

The synthetic strategy employed to prepare the model acceptor **RI114** sensitizer is presented in the following paragraphs. The retrosynthetic approach to prepare the molecule is presented in Scheme 2.1. The strategy we used was based on Pd-catalyzed cross-couplings, a family of closely related catalytic reactions which represent one of the most straightforward and general methods for the formation of carbon-carbon bonds and for the introduction of new functional groups, both carbon- and heteroatom based.[41] This class of reactions is widely used in the field of dye synthesis, since it makes possible to individually synthetize each section of the molecule and then assemble the complete sensitizer in few step.[42]

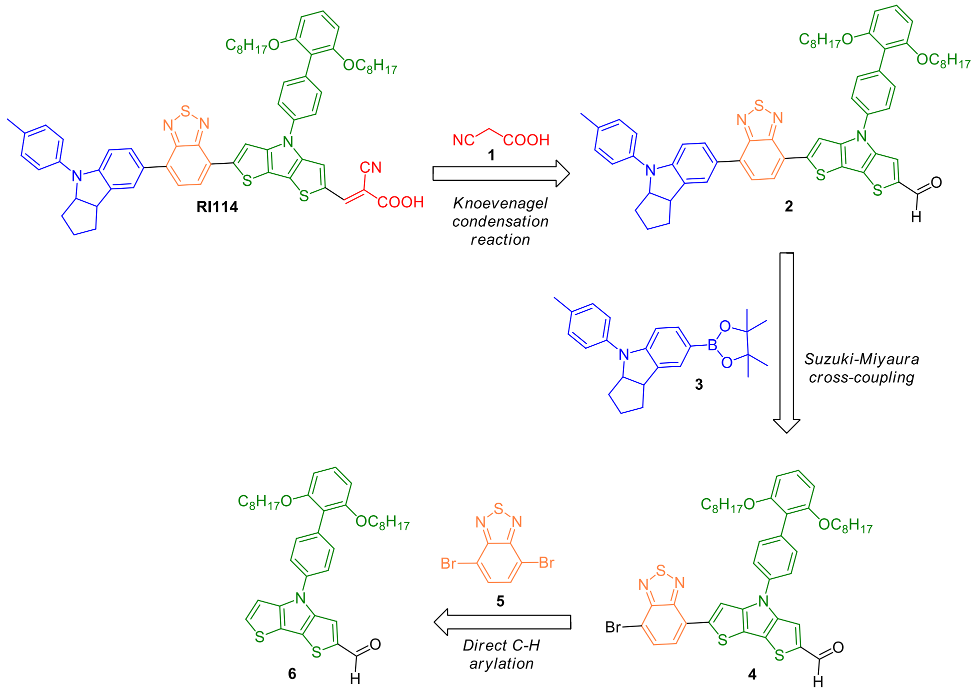

*Scheme 2.1: retrosynthetic approach for dye* ***RI114****; colours represent the building blocks: blue (donor), orange (intermediate acceptor), green (π-spacer) and red (acceptor/anchoring group).*

Thus, to prepare **RI114**, after the insertion of cyanoacetic acid (**1**) on aldehyde **2** through a Knoevenagel condensation, the first disconnection involves the introduction of the indoline-donor system, which is envisioned by a Suzuki-Miyaura cross-coupling of the corresponding organoboronate **3**. The second disconnection concerns the insertion of the benzothiadiazole group between the donor scaffold and the π- spacer group to obtain intermediate **4**. For this important step we chose to perform a direct arylation protocol using dibromide **5**,[43] not requiring the use of any preformed organometallic reagent, to reduce as much as possible the number of synthetic and purification steps necessary in the synthesis. The biphenyl dithienopyrrole **6** thus represented the starting point of the synthetic route.

### *Synthesis of biphenyl substituted dithienopyrrole (π-spacer moiety)(**6**)*

Compound **6** could be easily obtained by following a procedure (Scheme 2.2) previously reported by our group.[38] Bis-octyloxy substituted iodobenzene (**8**) was obtained by alkylation of 2-iodobenzene-1,3-diol (**7**) with 1-bromooctane in a polar aprotic solvent such as acetone. By virtue of the highly active phosphine ligand 2-(2′,6′-dimethoxybiphenyl) dicyclohexylphosphine (SPhos),[44] the hindered iodide **8** was successfully coupled at a moderate temperature with pinacol boronic ester **9** to afford amine **10** with high yield.

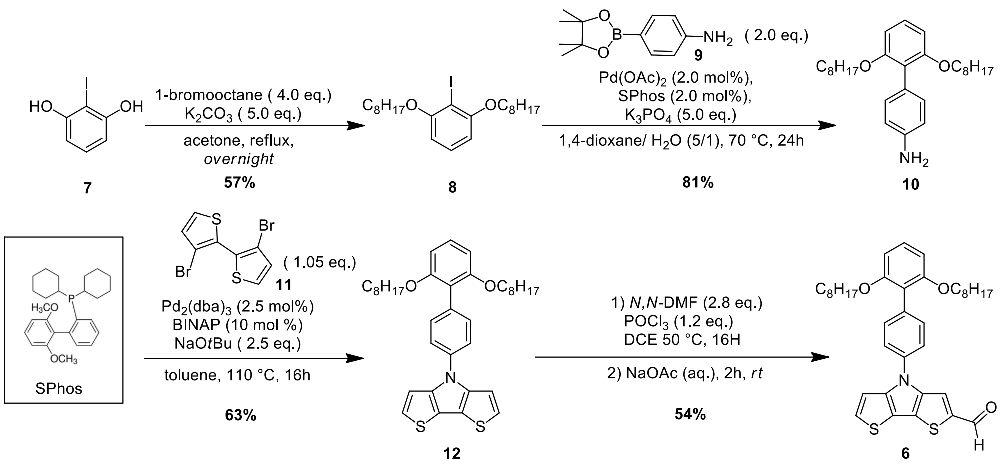

*Scheme 2.2: synthesis of the dithienopirrole π-spacer (**6**)*

Amine **10** then underwent a Pd-catalyzed Buchwald–Hartwig amination with 3,3′-dibromo-2,2′-bithiophene (**11**) using *rac*-BINAP as the ligand, to allow formation of two new covalent carbon-nitrogen bonds in the same step, thus providing the key intermediate **12** in satisfying yield. Finally, aldehyde **6** was obtained by a monoformylation of compound **12** via the Vilsmeier – Haack reaction, taking place selectively in position-2 of one of the thiophene rings.

## *Synthesis of the acceptor - π- spacer (A-π) building block (**4**)*

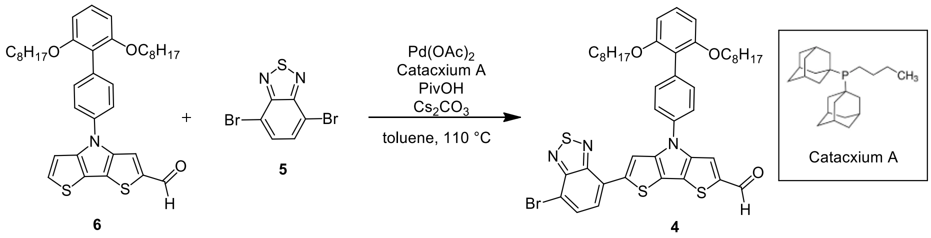

*Scheme 2.3: C-H direct arylation reaction for the synthesis of the acceptor- π- spacer intermediate **4***

The next step of the synthetic route consisted in the preparation of the A-π intermediate **4**, which was accomplished through direct arylation [45,46] of 4,7-dibromo-2,1,3-benzothiadiazole (**5**) with aldehyde **6.**[47] The reaction involves the activation of an aromatic C-H bond by an organometallic catalyst, usually a Pd-complex with phosphines, and the use of an inorganic base in stoichiometric amount. Use of pivalic acid in catalytic amounts helps the complexation of the aryl-species to the palladium and favours the formation of the new carbon-carbon bond. The reaction was carried out in toluene, using $Pd(OAc)_2$ and CataCXium A as the pre-catalyst and ligand, respectively, pivalic acid as an additive, and caesium carbonate as the base. (Scheme 2.3) The reaction conditions were optimized with respect to the catalyst loading, the stoichiometry of **5** and the reaction time (Table 2.1).

*Table 2.1: optimization conditions for direct arylation ($Cs_2CO_3$: 1.5 eq. for all the entries).*

| Entry | $Pd(OAc)_2$ (mol%) | CataCxium A (mol%) | 5 (eq.) | Time (h) | Yield (%) |
|---|---|---|---|---|---|
| **1** | 5.0 | 10 | 1.5 | 4.30 | 13 |
| **2** | 7.5 | 15 | 1.5 | 17 | 33 |
| **3** | 7.5 | 15 | 3 | 4 | 58 |

Compound **5** features two highly reactive positions. It is thus important to use an excess of it in the reaction with intermediate **6** to avoid its double functionalization and increase the yield of the desired product. In our short screening the best result, corresponding to a yield of 58% of compound **4**, was obtained when using 3 equivalents of dibromide **5**, shortening the duration of the reaction to 4 hours and using a 7.5 catalyst loading (Entry 3, Table 2.1).

## *Synthesis of the indoline donor building block (**3**)*

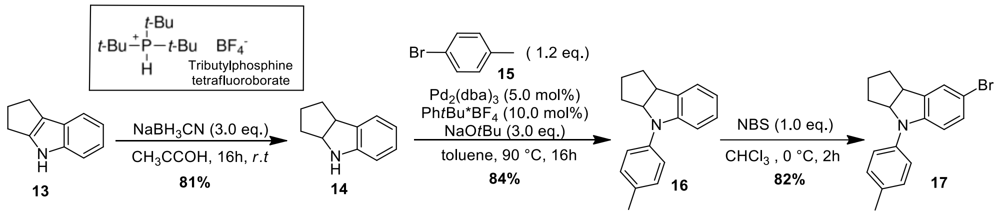

*Scheme 2.4: synthetic sequence for the preparation of the indoline donor*

The synthesis of the indoline donor unit was performed as reported in Scheme 2.4, according to previous reports,[48] starting from commercially available indole **13**. The first step involved the reduction of the enamine double bond of the latter through reaction with an excess of $NaBH_3CN$. The so-formed indoline **14** underwent a Buchwald-Hartwig amination reaction with *p*-bromotoluene (**15**) to put an aromatic substituent on its nitrogen atom. A purification by flash column chromatography was required, giving the product **16** with a satisfying yield. Bromination of indoline **16** was then performed by reaction with *N*-bromosuccinimide (NBS) dissolved in chloroform in equimolar concentration. Although the *para*-position relative to the nitrogen on the indoline aromatic ring should be more reactive and less hindered than the *ortho*-position, it was still mandatory to conduct the reaction at low temperature to avoid the double bromination of the substrate. Purification by flash column chromatography gave the desired clean product **17** with a very high yield.

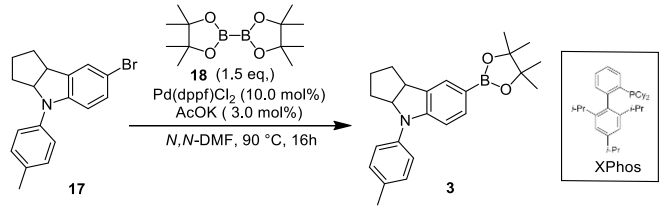

*Scheme 2.5: final borylation step for the synthesis of the indoline scaffold*

*Table 2.2: optimization of the conditions of the Miyaura borylation reaction*

| Entry | Cat. (mol%) | Ligand (mol%) | Yield (%) of 3 |
|---|---|---|---|
| 1 | $Pd_2(dba)_3$ (5.0) | Xphos (10.0) | 35% |
| 2 | $Pd(dppf)Cl_2$ (10.0) | - | 58% |

To access the required boronic ester (see Scheme 2.5) compound **17** was subjected to a Miyaura borylation reaction using diboronate **18**, which permitted the introduction of a pinacol-boronate ester using a palladium-based catalyst. We tested two different catalytic species (Table 2.2), finding that $Pd(dppf)Cl_2$ was more reactive than the $Pd_2(dba)_3$/XPhos combination, allowing to obtain compound **3**, suitable for the connection with the previously prepared acceptor π-spacer intermediate **4** (*see above*), in satisfactory yield.

## *Final assembly of the model D-A-π-A dye **RI114***

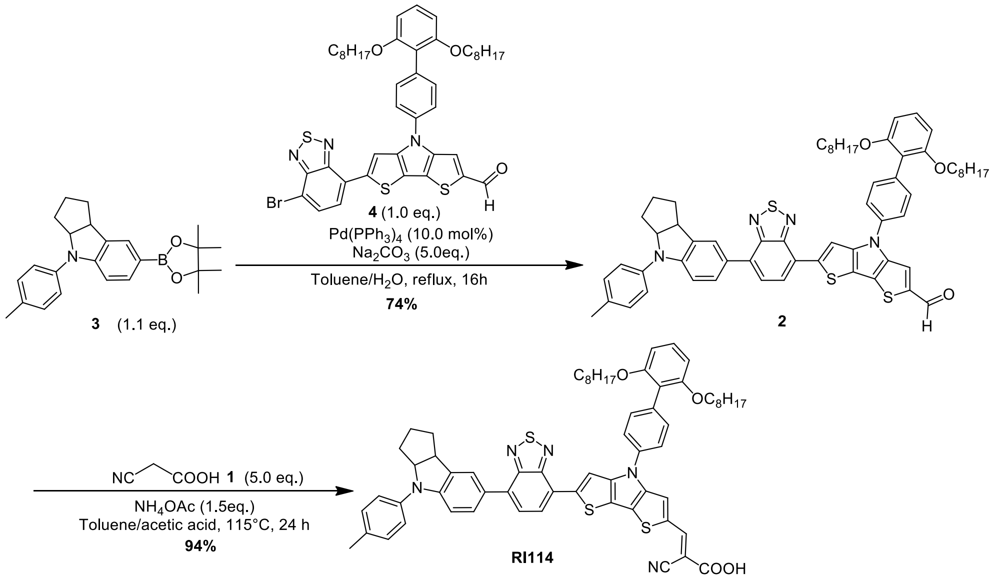

*Scheme 2.6: final assembly of the D-A-π-A **RI114** dye*

The final coupling was conducted using Suzuki-Miyaura conditions, reacting boronate **3** with bromide **4** (Scheme 2.6). Two different tests were carried out to evaluate the best reaction conditions to be used (Table 2.3). In both cases we obtained the desired product in good yield, in particular the use of the simple catalyst $Pd(PPh_3)_4$ provided the desired product with a higher yield compared to the combination of $Pd_2(dba)_3$ and XPhos (74% *vs.* 63%), albeit with a larger catalyst loading (10.0 mol% *vs.* 3.5%).

*Table 2.3: reaction conditions for the Suzuki-Miyaura reaction between compounds **3** and **4***

| Entry | Cat. (mol%) | Ligand (mol%) | Base (eq.) | Yield (%) |
|---|---|---|---|---|
| 1 | $Pd(PPh_3)_4$ (10.0) | - | $Na_2CO_3$ (5.0) | 74% |
| 2 | $Pd_2(dba)_3$ (3.5) | XPhos (7.0) | $K_3PO_4$ (3.0) | 63% |

Finally, the synthesis of the dye was completed by means of a classic Knoevenagel condensation of compound **2** with cyanoacetic acid (**1**) and ammonium acetate in toluene/acetic acid mixture, which gave an almost complete conversion of the starting aldehyde, providing sensitizer **RI114** in high yield.

## 2.2.3. Spectroscopic and electrochemical characterization of **RI114**

The optical and electrochemical properties of **RI114** were then determined, focusing onto two main goals:(i) first, to evaluate if the dye itself was suitable to DSSC application; (ii) secondly, to choose a proper antenna molecule whose emission band coincides, as much as possible, with the absorption band of **RI114** which is mandatory to obtain an efficient FRET. UV-Vis absorption and emission spectra were registered in tetrahydrofuran (THF) and are reported in Figure 2.13. From the absorption spectrum we found the maximum absorption wavelength ($\lambda_{max}^{abs}$) of **RI114**, and the molar attenuation coefficient (ε), obtained from the Lambert-Beer law (equation 2.8), which linearly correlates the measured absorbance with the concentration of the sample in solution, giving an indication of how intensely **RI114** can absorb solar energy.

$$A = \varepsilon \times b \times c \qquad (2.8)$$

Where:

- A is the measured absorbance
- b is the optical path expressed in cm (1 cm in this case)
- c is the concentration of the sample.

Data are reported in Table 2.4: the absorption band of the dye is well-centred in the visible region ($\lambda_{max}^{abs}$ = 517 nm) with a good ε value superior to $2.34 \times 10^4$ $M^{-1}$ $cm^{-1}$, which are suitable for solar cell application. Moreover, by looking at the fluorescence spectrum a strong emission in the red region was observed ($\lambda_{max}^{emi}$ = 656 nm), in agreement with the expected charge transfer nature of the electronic transitions taking place in its D-A-π-A structure. From the UV-Vis absorption spectrum it was also possible to obtain the zero-zero transition energy ($E_{0\text{-}0}$), by deriving the corresponding Tauc Plot (Figure 2.14), [49] which resulted of 2.05 eV, well in line with typical values of organic DSSC dyes.

To achieve crucial insights into the thermodynamics of the electron injection as well as of the dye regeneration processes in dye-sensitized systems, electrochemical measurements were carried out by recording the corresponding cyclic voltammetry (CV) in THF solution. The ground state-oxidation potential ($E_{ox}$) of **RI114** was thus determined, allowing to calculate the energy level positions of its frontier orbitals (Figure 2.15).

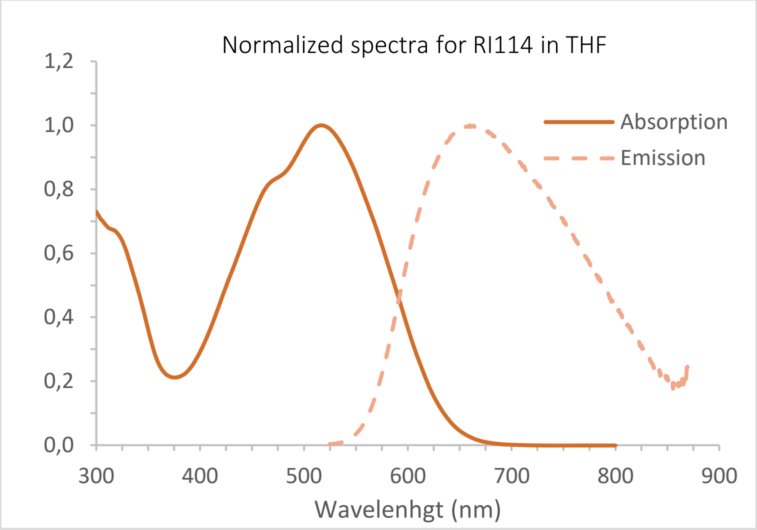

*Figure 2.13: absorption end emission spectra of* ***RI114***

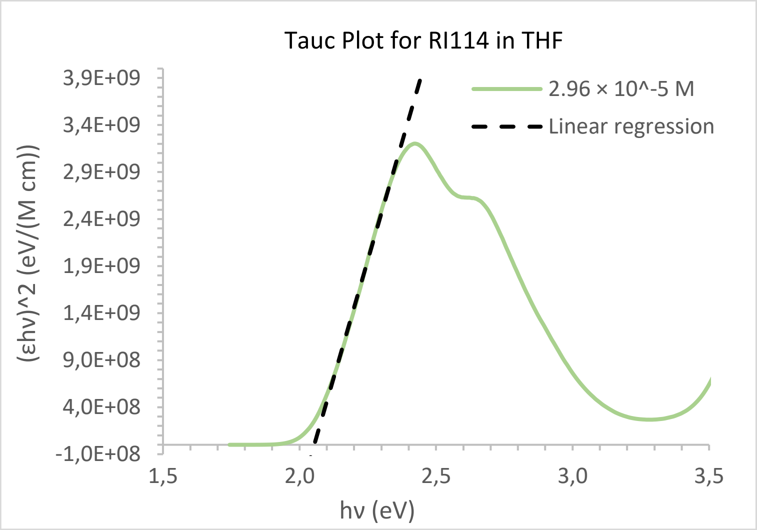

*Figure 2.14: Tauc plot of* ***RI114****.*

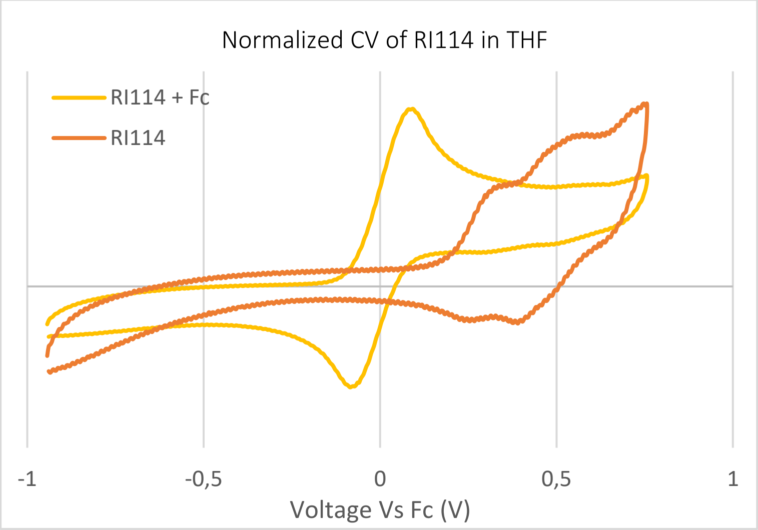

*Figure 2.15: Cyclic voltammetry of* ***RI114****.*

*Table 2.4: Electrochemical and spectroscopic propriety of **RI114***

| | $\lambda^{max}_{abs}$ [nm]$^a$ | ε (x $10^4$) [$M^{-1}$ $cm^{-1}$]$^a$ | $\lambda^{max}_{em}$ [nm]$^a$ | $E_{0-0}$ [eV]$^b$ | $E_{OX}$ [V/NHE]$^c$ | $E^*_{OX}$ [V/NHE]$^d$ |
|---|---|---|---|---|---|---|
| RI114 | 517 | 2.34 | 656 | 2.05 | 1.08 | – 0.97 |

*(a) Measures are recorded in THF solution; (b) Evaluated from the corresponding Tauc plot (see Figure 2.14); (c) Potential vs. NHE measured in THF solution with ferrocene as internal standard ($E_{½(Fc)}$ = 0.788 V vs. NHE); (d) Calculated from the equation: $E^*_{ox} = E_{ox} - E_{0-0}$.*

Upon application of positive potentials, the dye showed two quasi-reversible oxidation peaks. The measured $E_{ox}$ resulted of +1.08 V *vs.* NHE, which was clearly more positive than the reduction potential of the most common redox couples in DSSC devices, ensuring a good regeneration of the dyes after electron injection.[50,51] The excited state-oxidation potential ($E^*_{ox}$) was calculated by subtracting the zero-zero transition energy of the dye ($E_{0-0}$) from its ground state-oxidation potential $E_{ox}$, yielding a value of –0.972 V *vs.* NHE, which was largely more negative than the conduction band energy of $TiO_2$ (approx. –0.5 V *vs.* NHE),[52] suggesting a proper electron injection from the excited state of the dye to the semiconductor during cell operation.

## 2.2.4. Choice of the Antenna Fragment

After evaluating the spectroscopic and electrochemical properties of compound **RI114**, we focused our attention on antenna fragment. A suitable molecule should display an emission band well-matched with the absorption profile of **RI114**, to obtain an efficient energy transfer between the antenna and the acceptor dye in the molecular dyad. By inspection of the relevant literature, we found that the simple BTD-derivative 4,7-dithiophen-2-ylbenzo-2,1,3-thiadiazole **F.M.** (Figure 2.16) presented the required spectral features when dissolved in organic solvents, accompanied by high fluorescence quantum yields up to 90%.[53] Moreover, the same compound, this time simply denoted as F.M. (fluorescent material) had already been reported by Cheon *et al.* as a fluorescent antenna in combination with a blue squaraine dye in quasi-solid state DSSCs (Figure 2.16).[23] The absorption and the emission maxima of the fluorescent material were measured at 450 nm and 563 nm, respectively,  the latter being quite well-matched with the organic squaraine dye absorption  having an onset slightly above 500 nm. Despite the lack of covalent binding between the two compounds, a significant enhancement of photocurrent was found as a result of FRET between them, leading to an improvement in DSSC performances.

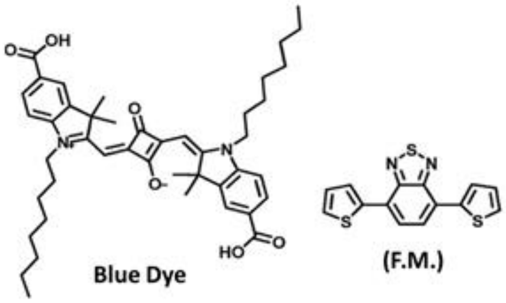

*Figure 2.16: Structure of the Blue Dye and 4,7-dithiophen-2-ylbenzo-2,1,3-thiadiazole (**F.M.**)*[23]

Considering the excellent performance of compound **F.M.** as a FRET donor and considering that its emission should overlap quite satisfactorily with the absorption of dye **RI114**, we decided to use a similar thiophene-BTD scaffold as the antenna fragment in our molecular dyad. The design and synthesis of such antenna are described in the next paragraphs.

## 2.3. Synthesis of a new antenna-dye molecular dyad

### 2.3.1 Initial design of the antenna-sensitizer dyad and synthesis attempts

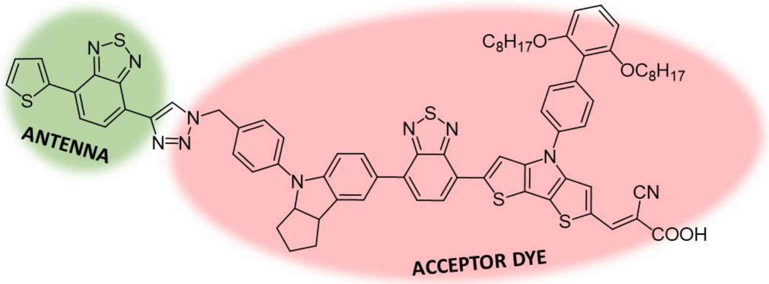

*Figure 2.17: Initial design of the antenna- sensitizer dyad **DYAD1***

As we discussed above, the approach we decided to use to connect the acceptor dye with the antenna was that to use a click reaction. This fact implies to modify the two selected structures, **RI114** and dye (**F.M.**) to introduce the proper functional groups to allow the reaction to occur.

In Figure 2.17 the initial design of the **DYAD1** is shown. Highlighted in green is the antenna section, simply made up by a thiophene - benzothiadiazole sequence. The acceptor section is highlighted in pink and is connected through a triazole moiety. A methylene group was inserted between the antenna and the dye to interrupt the conjugated system and thus maintain the spectroscopic properties of the sensitizer leading to compound **DYAD1**.

Scheme 2.7 shows the retrosynthetic approach imagined for **DYAD1**. The first main disconnection involved the antenna fragment (green) and the entire scaffold of the acceptor dye **20** (orange). To join these two parts through a CuAAC reaction we needed to prepare the non-symmetric BTD derivative (**19**), substituted on one side by a thiophene moiety and on the other by terminal alkyne. On the other side the acceptor dye **20** had to be functionalized with an azidomethyl substituent on the terminal benzene ring, in *para*- position relative to the nitrogen-containing indoline. To obtain compound **20**, the second retrosynthesis step involved the connection of an azide-containing indoline **21** (blue) to the key intermediate **4** by means of a Suzuki-Miyaura cross coupling reaction. To do that we had to prepare boronic ester **21**, meaning to follow the same synthetic sequence used for reference compound **RI114**.

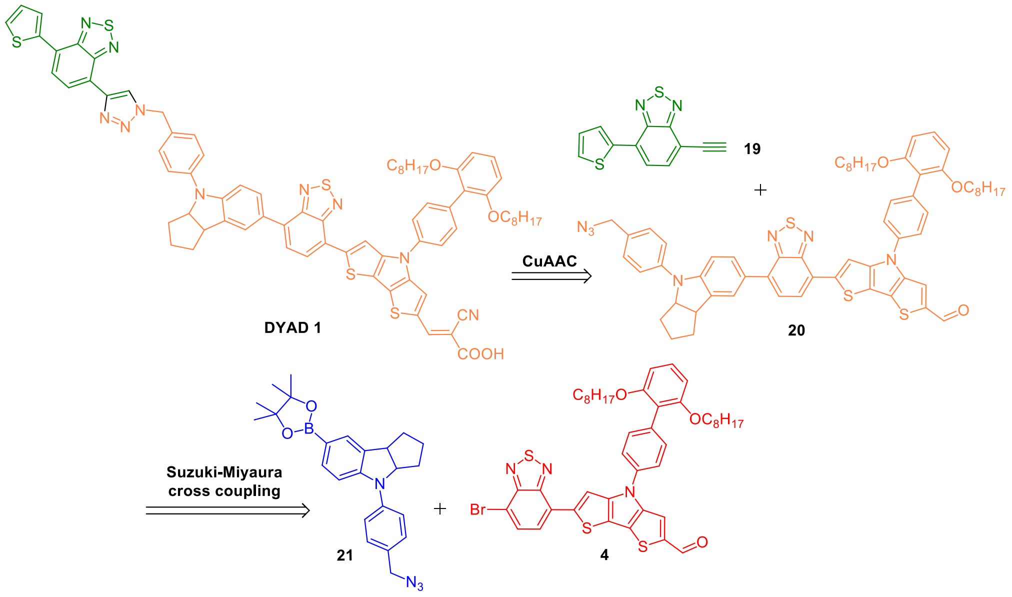

*Scheme 2.7: retrosynthetic approach to the synthesis of the antenna-sensitizer* ***DYAD1***

## *Synthesis of alkyne (19)*

Migita–Kosugi–Stille[54] cross-coupling reaction is a convenient synthetic procedure which often allows the efficient connection of various (hetero)aromatic fragments even under mild reaction conditions. Accordingly, compound **5** and stannane **22** (in slight excess, 1.2 eq.) were reacted using pre-catalyst Pd(PPh$_3$)$_2$Cl$_2$ in anhydrous toluene at 110 °C, aiming to obtain monosubstituted derivative **24**. However, applying these reaction conditions, a mixture of products was recovered (Scheme 2.8), consisting of a 2:4:1 molar ratio of *bis*- and *mono*-thienylation products **23** and **24** together with unreacted starting material **5**, as revealed by $^1$H NMR analysis of the crude reaction mixture.

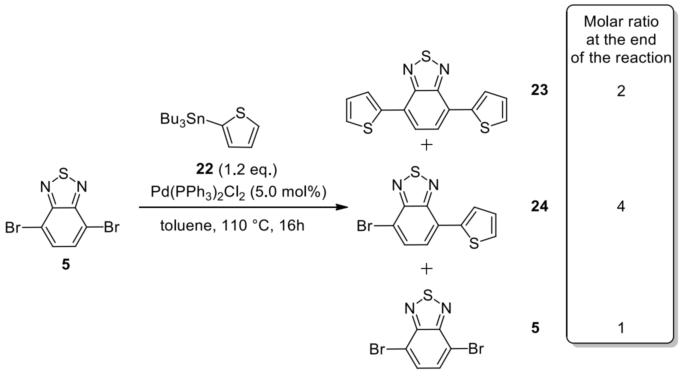

*Scheme 2.8: Migita–Kosugi–Stille cross coupling reaction between compounds* ***5*** *and* ***22***.

Unfortunately, chromatographic separation of the products proved impossible. To solve this problem, it was decided to slightly modify the reaction conditions simply by slowly adding compound **22** to keep its concentration low and thus promote formation of the mono coupling adduct **24**. However, by monitoring the reaction *via* TLC (Thin Layer Chromatography) the presence of both products was evident even after the first few minutes, highlighting how to control this point was quite challenging.

We overcame this issue using the commercially available non-symmetrical benzothiadiazole **25** containing a carbon-bromine bond on one side and a formyl-substituent on the other side (Scheme 2.9). In this case, Migita–Kosugi–Stille cross-coupling reaction under the same conditions shown above, except for the use of $Pd(PPh_3)_4$ as the catalyst, efficiently gave the desired aldehyde (**26**) as a single product. After purification, compound **26** was obtained in 95% yield.

At this stage, to convert the aldehyde into the required alkyne moiety (Scheme 2.9), we decided to carry out  a Seyferth-Gilbert homologation reaction using diazophospohonate **27** (Ohira-Bestmann reagent), which was previously synthetized according to a known procedure.[55] The reaction was performed in the presence of methanol and $K_2CO_3$, and the mechanism involves deacetylation of **27** that generates the corresponding carbanion **A**, which reacts with the aldehyde **26** to give the corresponding oxaphosphetane **B**. This species evolves to the vinylcarbenic intermediate **C**, from which, through a 1,2 migration, the desired alkyne **19** can be obtained. Using these mild conditions, the compound **19** was conveniently obtained in 54% yield, after purification.

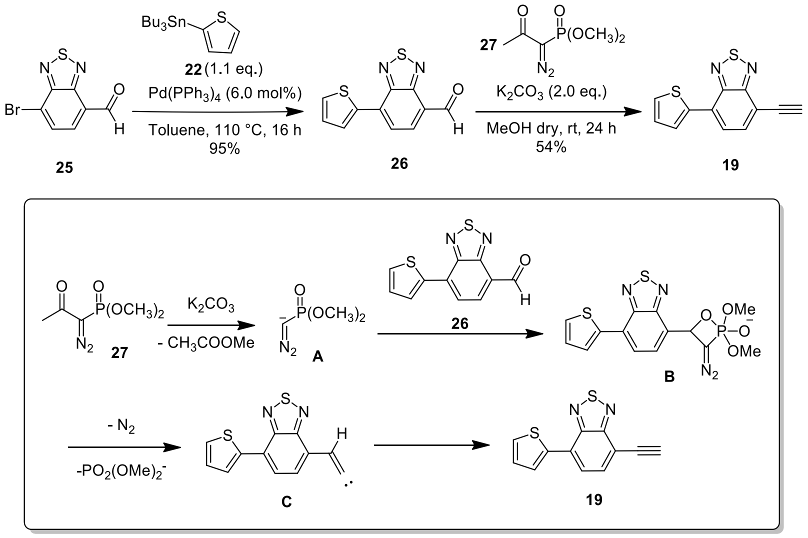

*Scheme 2.9: synthetic route for the preparation of intermediate **19***

## *Tentative synthesis of **DYAD1***

The synthesis of the azide-indoline fragment (**21**) (see Scheme 2.7) was then attempted by following the same approach previously applied for the preparation of the donor system of **RI114** dye (see above, Scheme 2.4). In this case, the main difference was represented by the use of bromide **28** in the first step of the reaction sequence. In this way, an aldehyde moiety in *para-* position of the aromatic ring is placed to allow the subsequent insertion of the azidomethyl substituent by functional group interconversion (FGI, Scheme 2.10). Thus, indoline **14** was subjected to Buchwald-Hartwig amination with *p*-bromo-benzaldehyde **28**, using the same conditions already applied (see reaction with bromide **15** Scheme 2.4). In this case caesium carbonate was used to replace sodium *tert*-butylate as the base, and the desired compound **29** was obtained in high yield. Bromination of **29** occurred by reaction with an equimolar amount of NBS in chloroform, providing to keep the reaction mixture at low temperature to avoid the formation of the double bromination product.

Bromo-aldehyde **30** was thus obtained in 63% yield and quantitatively reduced to the corresponding primary alcohol **31,** using sodium borohydride ($NaBH_4$) as a reducing agent in a MeOH/THF mixture, which helped to improve the solubility of the starting material. Then, to be able to introduce the azide moiety by final reaction with an azide nucleophile, the conversion of alcohol **31** into a good leaving group was attempted. First, we tried to convert the alcohol into the corresponding bromide **32**. It is widely known that primary alcohols can be converted to the corresponding alkyl bromides using $PBr_3$, generating HBr as side product.[56] Unfortunately, when compound **31** was treated with $PBr_3$ in THF at 0°C, only decomposition of the starting material was observed.

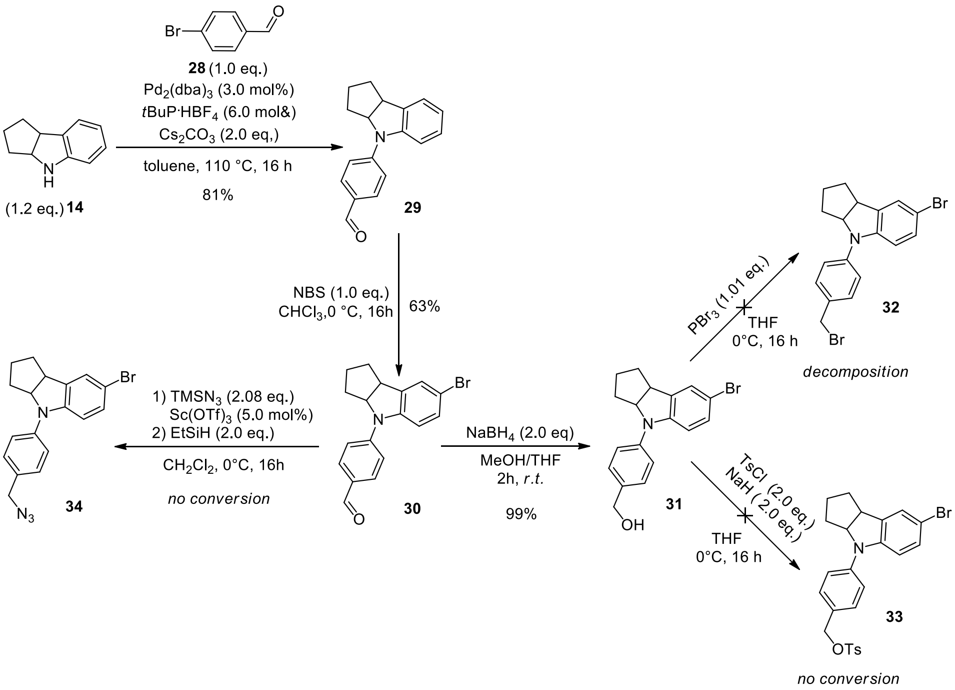

*Scheme 2.10: attempted synthesis of the azide-indoline donor*

Conversion of alcohol **31** to the corresponding tosylate **33** by means of reaction with TsCl in the presence of a strong base such as NaH was also tested. Unfortunately, at the end of the reaction no conversion of the starting material could be observed.

To overcome the difficulties found in converting the alcohol **31** into a good leaving group, we decided to use a different approach and investigate the possibility of inserting the azide moiety by direct transformation of aldehyde **30**. Indeed, Pramanik and Ghorai[57] recently demonstrated the possibility to generate an azide moiety from an aldehyde group via a *one-pot* reaction, proceeding through an azidocarbenium ion intermediate (**IV**, Figure 2.18). By using a silane as nucleophile in the last step (as a hydride synthetic equivalent), access to a primary azide would thus be granted.

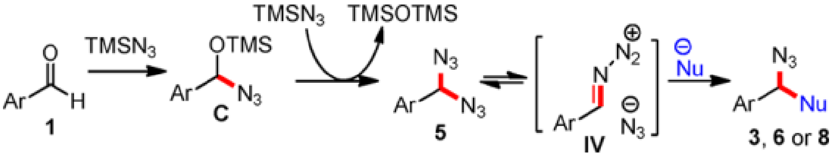

*Figure 2.18: proposed mechanism of the one-pot synthesis of an azide from the corresponding aldehyde*[57]

Thus we reacted aldehyde **30** with trimethylsilylazide ($TMSN_3$) and catalytic amounts of $Sc(OTf)_3$ as a Lewis acid to form the intermediate **IV**, then we used $Et_3SiH$ as nucleophile to obtain the desired azide **34** (Scheme 2.10). Unfortunately, also in this case, the reaction did not lead to the desired product, and only decomposition of the starting material was observed.

Since preparation of the required azide-indoline fragment proved exceedingly difficult, looking for a simplification of the synthetic procedure, it was decided to modify the structure of the molecular dyad by changing the connectivity of the antenna and dye fragments across the triazole moiety.

## 2.3.2 Final design of the antenna-sensitizer dyad **DYAD2** and complete synthetic procedure

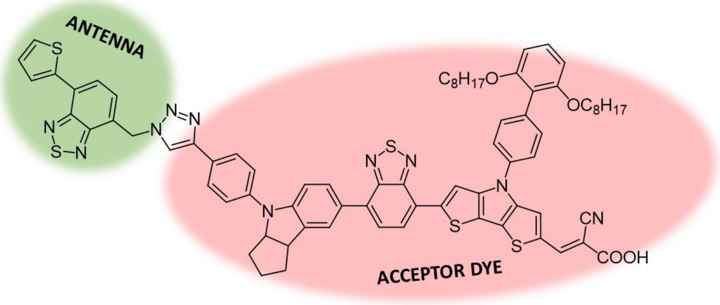

*Figure 2.19: final design of the antenna- sensitizer dyad* ***DYAD2***

In order to use a different synthetic approach, we decided to invert the way in which the antenna and dye fragments were connected through the triazole ring (Figure 2.19) leading to **DYAD2**. Accordingly, the functional groups we had to introduce on the two molecular fragments need to be inverted too. Thus, following the retrosynthetic approach (see Scheme 2.11) we need to introduce a terminal alkyne on the indoline building block, while the antenna would be required to carry an azidometyl substituent.

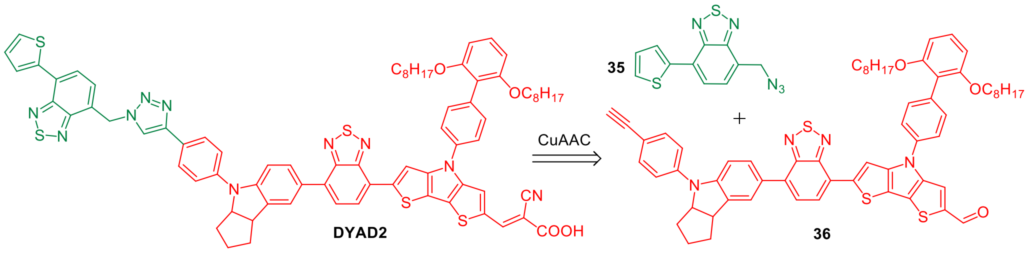

*Scheme 2.11: retrosynthetic approach to the synthesis of the antenna-sensitizer* ***DYAD2***

## *Final synthesis of the antenna building block*

To insert the azidomethyl moiety on aldehyde **26**, we used again the direct reductive azidation reaction. This time we used a different Lewis acid catalyst (silver(I) triflate instead of scandium(III) triflate) as suggested in the original paper for the conversion of nitrogen-containing heteroaromatic aldehydes.[57] Accordingly, compound **26** was treated with an excess of TMSN$_3$ in the presence of 10 mol% AgOTf allegedly leading to the formation of intermediate **26a** (as suggested by TLC analysis); the latter could be converted to mono-azide **35** in fair yield by simple addition of Et$_3$SiH and stirring at room temperature overnight (Scheme 2.12).

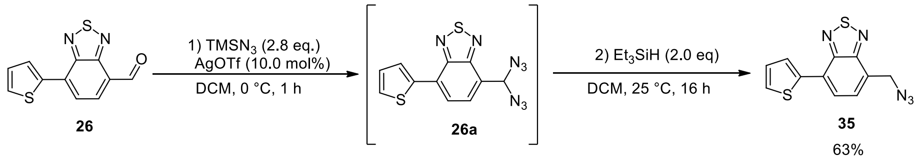

*Scheme 2.12: Synthesis of antenna building block* ***35***

To allow a preliminary evaluation of the optical and spectroscopic properties of the isolated antenna in solution, azide **35** was converted to model compound **38** by reaction with alkyne **37** under typical CuAAC conditions, using CuSO$_4$ as pre-catalyst and sodium L-ascorbate as reducing agent in a tetrahydrofuran/H$_2$O mixture (Scheme 2.13).

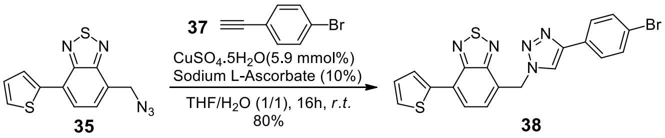

*Scheme 2.13: Synthesis of model antenna compound* ***38***

Compound **38** was subjected to spectroscopic characterization to determine if its emissive properties were adherent to those required for the correct matching with the sensitizer, and to compare them with those of the antenna fragment in the complete molecular dyad (*see below*).

### *Synthesis of indoline donor building block and final assembly of* ***DYAD2***

To avoid the chemoselectivity problems which might be encountered when using a compound with a free alkyne functionality in a Pd-catalyzed reaction in the presence of base and high temperatures, to prepare the indoline fragment we decided to perform the "click" reaction and create the triazole link before of completing the synthesis of the whole indoline donor. Such approach is reported in Scheme 2.14 and requires the preparation of the key intermediate **40**, bearing both an alkyne functional group, to allow connection to the antenna via the aforementioned CuAAC reaction, and a boronic ester, necessary to permit the connection to the remaining part of the dye.

To prepare the key intermediate **40** we can use two different approaches that are reported in Scheme 2.14: *a)* conversion of the aldehyde moiety to the corresponding alkyne **39** and subsequent borylation of the C-Br bond through a Miyaura reaction; *b)* first, preparation of the boronic ester **41** and then introduction of the alkyne moiety, thus performing the same reactions, but with the inverse order. We prepared alkyne **39**, using the same Ohira-Bestmann procedure described above. A short optimization of the synthetic protocol was carried out to improve its yield (Table 2.5). Indeed, use of a methanol/tetrahydrofuran mixture as the solvent, together with a large excess of both reagent **27** and base, increased the yield of alkyne **39** from 6% to 59%.

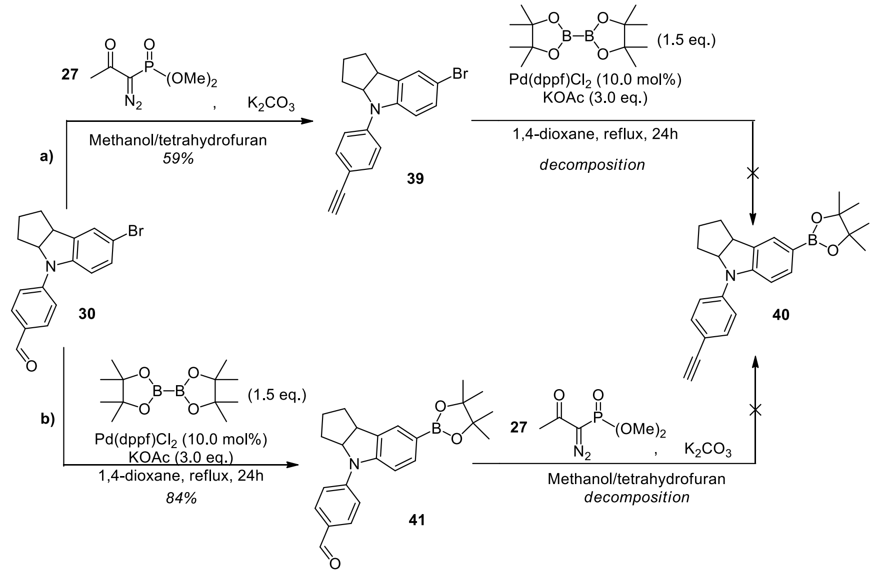

*Scheme 2.14: attempted strategies to prepare indoline-alkyne building block* ***40*** *from aldehyde* ***30***

*Table 2.5: optimization process of the Ohira-Bestmann reaction between compounds* ***30*** *and* ***27***

| Entry | 27 (eq.) | $K_2CO_3$ (eq.) | Solvent-Time(h) | Yield (%) |
|---|---|---|---|---|
| **1** | 2.0 | 2.0 | MeOH-16 | 6 |
| **2** | 2.0 | 2.0 | MeOH/THF (2/1)-48 | 21 |
| **3** | 3.0 | 3.0 | MeOH/THF (2/1)-16 | 59 |

Unfortunately, when compound **39** was submitted to the Miyaura-borylation conditions, the reaction led only to the decomposition of the starting material followed by the occurrence of undesired side reactions. Consequently, we decided to prepare boronic ester **41** first through Miyaura borylation of intermediate **30** (Scheme 2.14). The reaction occurred smoothly, providing compound **41** in a high yield. Unfortunately, the subsequent aldehyde-to-alkyne homologation again failed, and we could not obtain the desired intermediate.

To achieve our goal, we decided to use an alternative approach to install the boronic ester moiety on alkyne **39**, which was based on a lithium-halogen exchange reaction (Scheme 2.15). Indeed, we found that by treatment of bromide **39** with an excess of *tert*-butylithium, lithium-halogen exchange occurred selectively and borylation could be carried out by reaction with pinacolborane. In this way, it was possible to obtain the desired product **40** albeit in moderate yield. Finally, compound **40** was subjected to CuAAC conditions in the presence of the antenna azide **35.** The high yield and mild conditions typical of the click reaction made it possible to obtain the desired borane **42** with high yield.[58]

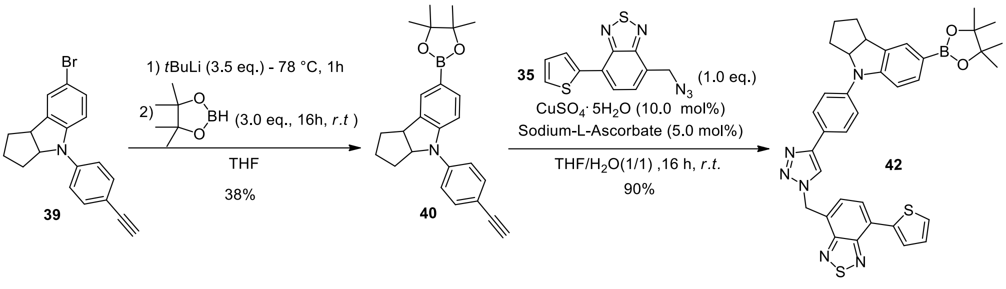

*Scheme 2.15: synthetic approach for the preparation of intermediate* **42**

The final assembly of the **DYAD2** was thus performed by reacting bromide **4** under Suzuki-Miyaura conditions with a small excess of boronate **42**, using $Pd_2(dba)_3$ as pre-catalyst and XPhos as ligand in anhydrous toluene (Scheme 2.16). Considering the complexity of the two reaction partners, the reaction was quite challenging, however the coupling compound **42** could be recovered after 16h in refluxing toluene and obtained in 25% yield after purification. Despite the yield was moderate, it is remarkable that application of relatively standard conditions could still yield the desired product even in the presence of such densely functionalized reactants, and an improvement of the reaction yield can surely be foreseen as a result of an adequate optimization process. Finally, Knoevenagel condensation of intermediate **43**, using cyanoacetic acid and ammonium acetate in toluene/acetic acid mixture, gave the final molecular dyad **DYAD2** in good yield.

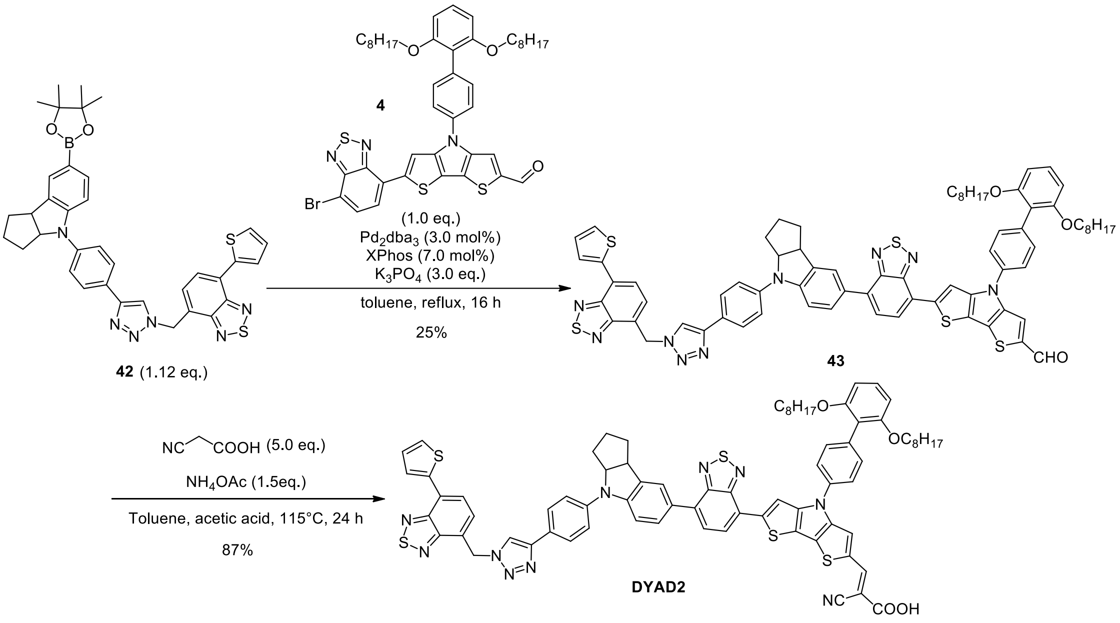

*Scheme 2.16: synthesis of antenna-sensitizer* **DYAD2**

### 2.3.3. Spectroscopic and electrochemical characterization of model antenna **38**

The UV-Vis absorption and emission spectra of model antenna **38** was registered in tetrahydrofuran (THF) (Figure 2.20). We found out that the maximum absorption of wavelength ($\lambda_{max}^{abs}$) is located at 397 nm, while the maximum emission band ($\lambda_{max}^{emi}$) is at 515 nm. To obtain an efficient energy transfer between the antenna and the acceptor dye, it is mandatory to have a good overlap between the antenna **38** emission band and the **RI114** absorption band. This fundamental condition was confirmed by the overlap between the normalized absorption and emission spectra of the two molecules, (Figure 2.21), showing an excellent match between the absorption band of **RI114** and the emission band of the antenna **38**, demonstrating that the two molecular fragments can make energy transfer happen.

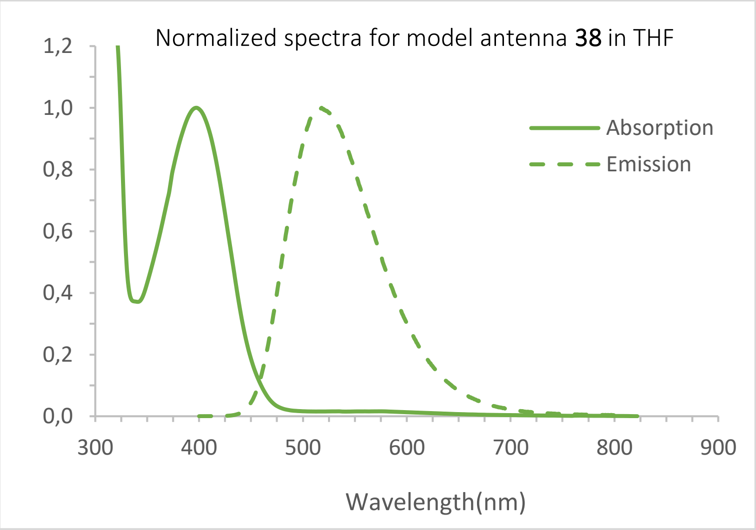

*Figure 2.20: absorption end emission spectra of model antenna* ***38.***

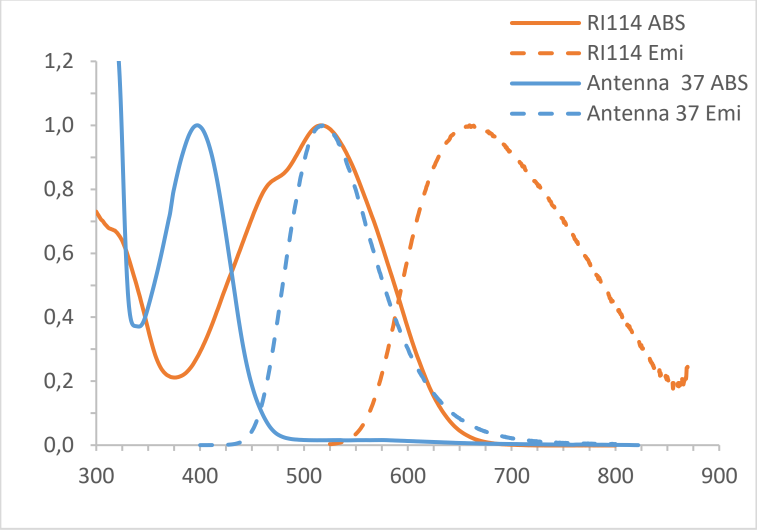

*Figure 2.21: overlap absorption and emission normalized spectra of* ***RI114*** *and* ***38****;* ***RI114*** *absorption (continue orange line),* ***RI114*** *emission (dashed orange line); antenna* ***38*** *absorption (continue blue line); antenna* ***38*** *emission (dashed blue line).*

### 2.3.4. Spectroscopic and electrochemical characterization of **DYAD2**

The optical and electrochemical properties of **DYAD2** were finally determined. UV-Vis absorption and emission spectra were registered in tetrahydrofuran (THF) and are reported in Figure 2.22. From the absorption spectrum we extracted the maximum absorption wavelength ($\lambda_{max}^{abs}$ = 540 nm) and the molar attenuation coefficient (ε), obtained from the Lambert-Beer law (see paragraph 2.2.3, equation 2.8). Data are reported in Table 2.6: the absorption band of the dye is well-centered in the visible region ($\lambda_{max}^{abs}$ = 540 nm) with an ε value equal to $1.17\times10^4$ $M^{-1}$ $cm^{-1}$, which is moderate, but consistent with other dyes for DSSC applications. Looking at the fluorescence spectrum, a strong emission in the red region was observed ($\lambda_{max}^{emi}$ = 735 nm), observing a bathochromic shift both in the absorption band and in emission band if compared to **RI114**. As described in paragraph 2.2.3, from the UV-Vis absorption spectrum it was possible to obtain the zero-zero transition energy ($E_{0-0}$), by deriving the corresponding Tauc Plot (Figure 2.23), which resulted being of 2.02 eV, very similar to **RI114** ($E_{0-0}$ = 2.05 eV).

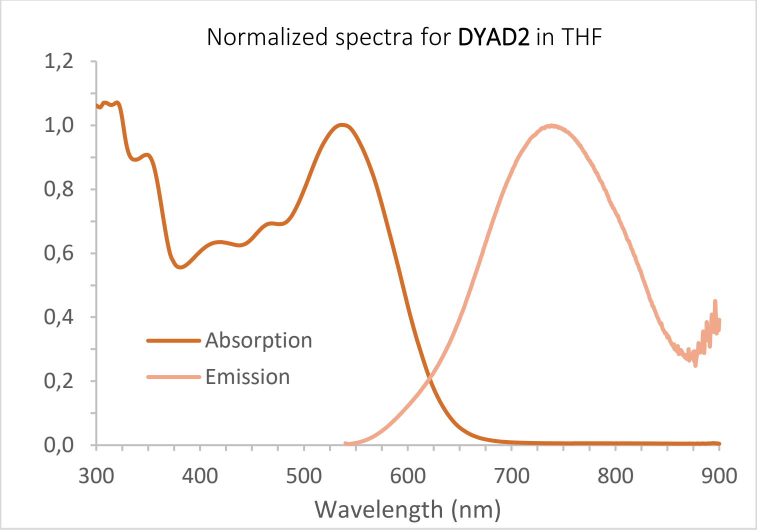

*Figure 2.22: absorption end emission spectra of* ***DYAD2.***

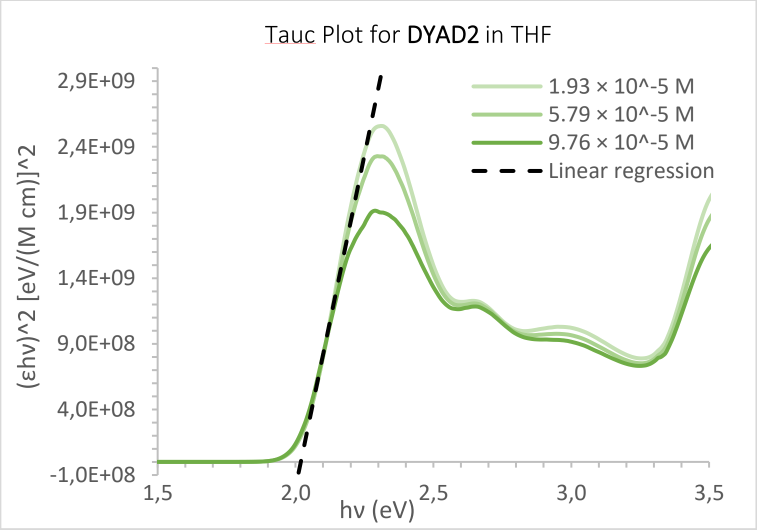

*Figure 2.23: Tauc plot of* ***DYAD2****.*

As seen in **RI114**, to achieve crucial insights into the thermodynamics of the electron injection as well as of the dye regeneration processes, electrochemical measurements were carried out by recording the corresponding cyclic voltammetry (CV) in THF solution. The ground state-oxidation potential ($E_{ox}$) of **DYAD2** was thus determined, allowing to calculate the energy level positions of its frontier orbitals (Figure 2.24).

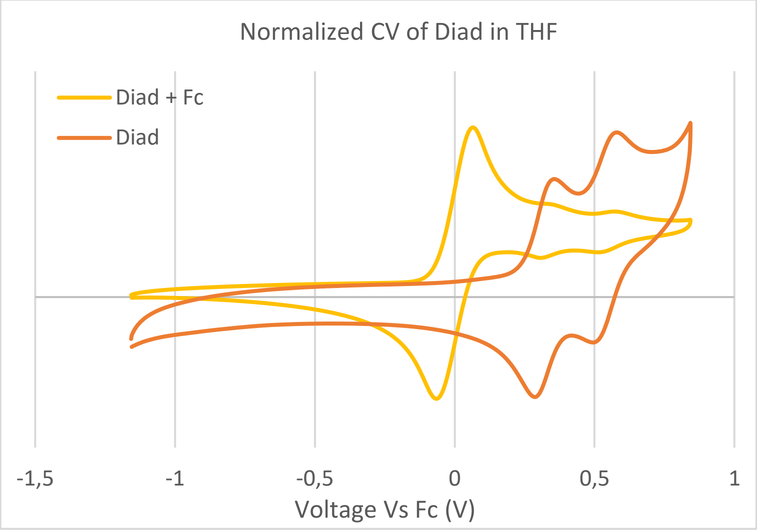

*Figure 2.24: Cyclic voltammetry of **DYAD2***

*Table 2.6: electrochemical and spectroscopic propriety of **DYAD2***

| | $\lambda^{max}{}_{abs}$ [nm]$^{a}$ | ε (x $10^{4}$) [$M^{-1}$ cm $^{-1}$]$^{a}$ | $\lambda^{max}{}_{em}$ [nm]$^{a}$ | $E_{0\text{-}0}$ [eV]$^{b}$ | $E_{OX}$ [V/NHE]$^{c}$ | $E^{*}{}_{OX}$ [V/NHE]$^{d}$ |
|---|---|---|---|---|---|---|
| DYAD2 | 540 | 1.17 | 735 | 2.02 | 1.11 | – 0.91 |

*(a) Measures are recorded in THF solution; (b) $E_{0\text{-}0}$ evaluated from the corresponding Tauc plot (see Figure 2.23); (c) Potential vs. NHE measured in THF solution with ferrocene as internal standard ($E_{½(Fc)}$ =0.788 V vs NHE); (d) Calculated from the equation: $E^{*}{}_{ox} = E_{ox} - E_{0\text{-}0}$.*

Upon application of positive potentials, **DYAD2** showed two quasi-reversible oxidation peaks. The measured $E_{ox}$ from the first oxidation wave resulted being of +1.11 V *vs.* NHE, much more positive than the most common redox couples employed in DSSCs.[50,51] The excited state-oxidation potential ($E^{*}{}_{ox}$), as seen for **RI114**, was calculated by subtracting the zero-zero transition energy of the dye ($E_{0\text{-}0}$) from its ground state-oxidation potential $E_{ox}$, yielding a value of −0.91 V *vs.* NHE, which was largely more negative than the conduction band energy of $TiO_2$ (approx. −0.5 V *vs.* NHE), suggesting a proper electron injection from the excited state of the dye to the semiconductor during cell operation.

After evaluating the spectroscopic and electrochemical properties of the **DYAD2**, a qualitative spectroscopic characterization was performed to demonstrate if energy transfer between the antenna fragment and the acceptor molecule occurs. First, the normalized absorption profiles of **RI114,** the model antenna **38** and **DYAD2** are shown in figure 2.25. **DYAD2** (red line) presents a wider absorption profile if compared to **RI114** (pink line): in particular, **DYAD2** can absorb light in those regions where **RI114** shows a very small absorption and the absorption of the model antenna **38** (blue line) is maximum. This behaviour suggests the possibility of having an increase of **DYAD2** light harvesting efficiency.

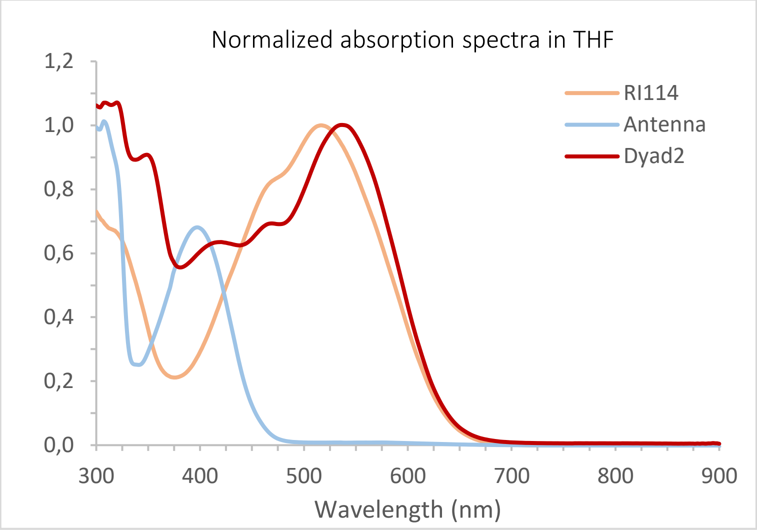

*Figure 2.25: overlap of the absorption spectra of **DYAD2** (red line), **RI114** (pink line), and the model antenna **38** (blue line)*

Figure 2.26 shows the **DYAD2** emission band when we irradiate the dyad at two different wavelengths: $\lambda_{exc}$= 537 nm, the maximum absorption in the visible region due to the part of the molecule corresponding to the main dye, and $\lambda_{exc}$= 397 nm, the absorption peak due to the antenna moiety; when **DYAD2** was irradiated at 397 nm (blue line), the emission profile of **DYAD2** did not change significantly if compared to the irradiation at its maximum absorption ($\lambda_{exc}$= 537 nm) in the visible region (orange line).

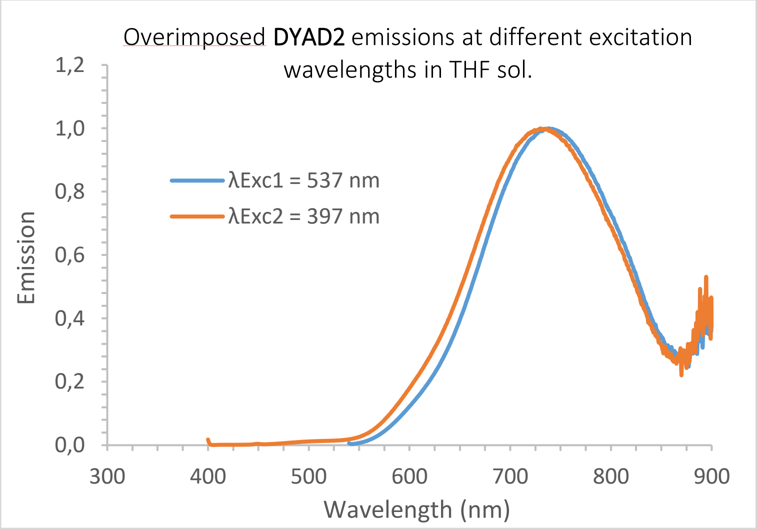

*Figure 2.26: overlap **DYAD2** emission spectra. (Blue line) **DYAD2** emission when irradiated at λ=537 nm; (orange line) **DYAD2** emission when irradiated at λ=397 nm.*

In the figure 2.27, the normalized absorption spectrum of **DYAD2** is compared to the emission peak of the model antenna **38**, confirming the optimal overlapping between them. The mission spectrum of **DYAD2** after irradiation at 397 nm has been reported too, as well as a x30 magnification in the 400–550 nm range, to show how the antenna emission has been completely quenched in the **DYAD2**, demonstrating the actual FRET energy transfer between the two molecules portions.

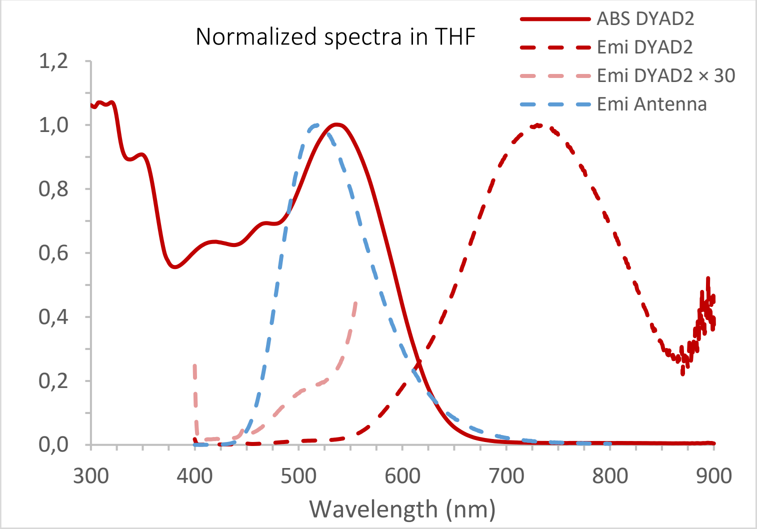

*Figure 2.27: (red continue line)* ***DYAD2*** *absorption; (red dashed line)* ***DYAD2*** *emission; (blue dashed line) model antenna* ***38*** *emission; (pink dashed line)* ***DYAD2*** *magnification emission.*

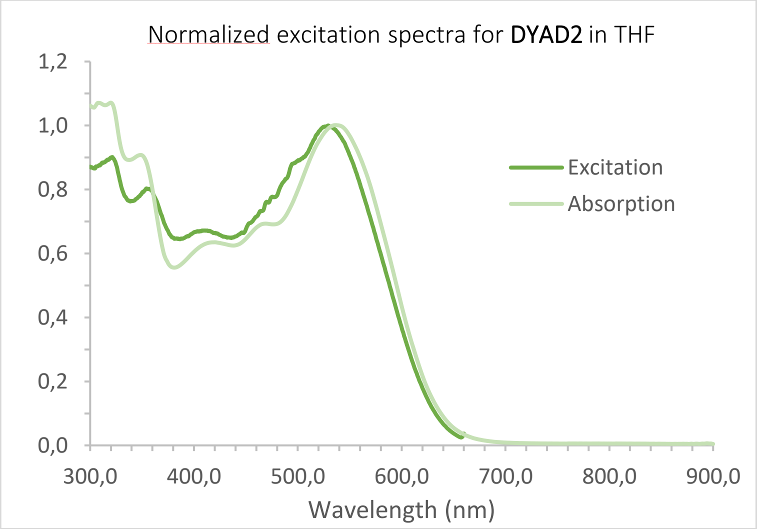

*Figure 2.28: spectrum of* ***DYAD2*** *excitation recorded to λ= 660nm (dark green) versus dyad absorption (light green)*

Finally, excitation spectrum of **DYAD2** was also recorded, keeping the emission wavelength constant at λ = 660 nm and recording the variation of its intensity as a function of the variation of the excitation wavelength. Figure 2.28 shows that **DYAD2** excitation spectrum (dark green) is very similar to its absorption spectrum (light green), meaning that the emission of **DYAD2** mostly depends on the absorption intensity. Instead it is interestingly to notice that the excitation spectrum is slightly more intense at wavelengths close to the antenna absorption, which could prove that FRET occurred and contributed to the overall emission of **DYAD2**.

## 2.4. Conclusions

The goal of this research work was to improve DSSC performances by increasing their Light Harvesting Efficiency (LHE). Our aim was designing a new concept of photosensitizer, since its optical properties will strongly affect the LHE of the device. We decided to develop a photosensitizer made of a new metal-free antenna-sensitizer dyad. The molecular design of the dyad was studied to exploit Forster Resonance Energy Transfer (FRET) between the antenna and the sensitizer moieties covalently bonded together. The two molecular fragments were selected in order to have complementary light absorption properties and, at the same time, displaying a good overlap between the antenna emission band and the sensitizer absorption one. This way we expected to obtain a dyad with a high molar attenuation coefficient (ε) and a broad absorption spectrum in the visible region.

First, the D-A-π-A sensitizer **RI114** was synthesized and fully characterized from a spectroscopical and electrochemical point of view. The synthesis was based on a desymmetrisation via direct arylation of benzothiadiazole with a dithienopyrrole derivative, followed by Suzuki cross-coupling to insert a indoline donor moiety. **RI114** showed a $\lambda_{max}^{abs}$ well-centered in the visible region (517 nm) with a good ε value ($2.34 \times 10^4$ $M^{-1}$ $cm^{-1}$) and a $\lambda_{max}^{emi}$ at 656 nm. $E_{ox}$ was calculated to be at around +1.08 V vs. NHE. Being more positive than the reduction potential of most of the common redox couples used in DSSC, this value is promising for an effective regeneration of the dye in the device. At the same time, $E^{*}_{ox}$ was calculated to be at −0.972 V vs. NHE which is more negative than the conduction band (CB) of $TiO_2$ (approx. −0.5 V vs. NHE), suggesting that electron injection from the excited state of the dye to the semiconductor's CB would be feasible for **RI114**.

After evaluating the spectroscopic properties of **RI114,** we selected and synthetized thiophene-benzothiadiazole as a suitable antenna since it's absorption and emission spectra match well with those of the sensitizer. The covalent bounding between the two moieties was obtained by copper-catalysed azide/alkyne cycloaddition (CuAAC) generating the triazole bridge. The first synthetic strategy perused to obtain the CuAAC junction consisted in reacting the alkyne derivative of the antenna with the azide derivative of the sensitizer which, unfortunately was not possible to synthetize. This let us decided to switch the connectivity of the antenna and the dye fragments across the triazole moiety. This time both the azide derivative of the antenna and the alkyne derivative of the sensitizer were successfully synthetized and the **DYAD2** was obtained via CuAAC reaction.

Spectroscopic and electrochemical proprieties of **DYAD2** were performed. First, UV-Vis spectroscopic characterization of model antenna **38** (decorated with a triazole moiety too) was done. Excellent overlap between the absorption of **RI114** and the emission of the model antenna **37**, demonstrated that the main requirement of the FRET is fulfilled, and the two molecular fragments can make energy transfer happening. A bathochromic shift both in the absorption and the emission spectra of **DYAD2** were observed when compared to **RI114** probably due to the insertion of the triazole function in the donor moiety. The maximum absorption wavelength ($\lambda_{max}^{abs}$ = 540 nm) and the molar attenuation coefficient ($\varepsilon$=1.17×$10^4$ $M^{-1}$ $cm^{-1}$) were found to be consistent with other dyes used for DSSC applications. Furthermore, we found that the absorption of **DYAD2** was successfully increased with respect to the one of **RI114** alone as it embeds also the absorption band of the model antenna **38**. The emission profile of **DYAD2** excited at the sensitizer absorption maxima (537 nm) or at the one of the antenna (397 nm) did not change significantly showing that the emission of the antenna was almost completely quenched. This is ones more supporting the hypothesis of antennas quenching via FRET instead. **DYAD2** excitation spectrum registered at 660 nm was found to be very similar to **DYAD2** absorption spectrum but interestingly the excitation spectrum is slightly more intense at wavelengths close to the antenna absorption, which could prove again that FRET has occurred and contributed to the overall emission of **DYAD2**.

The $E_{ox}$ was calculated to be at +1.11 V vs. NHE, and the excited state-oxidation potential ($E^*_{ox}$), laid at −0.91 V vs. NHE, suggesting that proper electron injection from the excited state of the **DYAD2** to the CB of the semiconductor can happen. **DYAD2** photovoltaic characterization will be carried out in the future, and compared to that on of RI114 in order to evaluate whether the presence of the antenna can contribute to the photogenerated current of the device via FRET.

## 2.5 Experimental Section

### General synthetic remarks

All air-sensitive reactions were performed under inert atmosphere in a flame- or oven-dried apparatus using Schlenk techniques. Solvents used in cross-coupling reactions were previously degassed by means of the "freeze-pump-thaw" method. Tetrahydrofuran (THF) was distilled over metallic sodium in the presence of benzophenone, dioxane was distilled over metallic sodium, methanol (MeOH) was distilled over metallic magnesium in the presence of a catalytic amount of iodine, $CH_2Cl_2$ was distilled over $CaH_2$, toluene, diethyl ether and acetonitrile were dried on a resin exchange Solvent Purification System (MBraun). Anhydrous *N*,*N*–dimethylformamide (DMF) and $CHCl_3$ were stored under nitrogen over 4 Å molecular sieves. All the commercially available chemicals were used as received. Petroleum ether was the 40-60 °C boiling fraction. Thin-layer chromatography was carried out on aluminum-supported Merck 60 F254 plates; detection was carried out using UV light (λ = 254 and 365 nm) and permanganate or molybdophosphoric acid solutions followed by heating. Flash column chromatography was performed using Merck Kieselgel 60 (300-400 mesh) as the stationary phase. $^1$H-NMR spectra were recorded with a Varian Mercury spectrometer at 400 MHz, $^{13}$C-NMR spectra were recorded with the same instrument at 100.6 MHz. Chemical shifts were referenced to the residual solvent peak ($CDCl_3$, $\delta$ = 7.26 ppm for $^1$H-NMR and $\delta$ = 77.00 ppm for $^{13}$C-NMR; THF-$d_8$, $\delta$ = 3.58 and 1.72 ppm for $^1$H-NMR and $\delta$ = 67.21 and 25.31 ppm for $^{13}$C-NMR; $CD_2Cl_2$, $\delta$ = 5.32 ppm for $^1$H-NMR and $\delta$ = 53.84 ppm for $^{13}$C-NMR). Coupling constants (*J*) are reported in Hz and the multiplicity is abbreviated as follows: multiplet (m), singlet (s), broad singlet (br), duplet (d), triplet (t), and quadruplet (q). GC-MS spectra were measured with a Shimadzu gas-chromatograph (GC-17A or GC-2010) connected to a Shimadzu mass spectrometer (MS-QP2010S or MS-QP5050a) and are reported in the form *m/z* (intensity relative to base = 100). ESI-MS spectra were measured with a Thermo Scientific LCQ-FLEET instrument by direct injection of a sample solution and are reported in the form *m/z*. UV-Vis spectra in different solvents were recorded on diluted solutions of the analyte (approximately 10–5 M) with a Shimadzu UV2600 spectrometer. UV-Vis absorption or transmittance spectra of the compounds adsorbed on $TiO_2$ were recorded in transmission mode after sensitization of thin, transparent semiconductor films (thickness approximately 5 µm). Ultraviolet–Visible absorption diffuse reflectance spectra (DRS) of the dye-sensitized working electrodes were recorded using a Jasco V-770 spectrophotometer equipped with a 60 mm integrating sphere, embedding a PbS detector (ISN-923), using an interval wavelength of 1 nm, from 300 nm to 800 nm. Fluorescence spectra in solution were recorded with a Jasco FP-8300 spectrofluorometer, equipped with a 150 W Xenon arc lamp, irradiating the sample at the wavelength corresponding to maximum absorption in the UV spectrum. Cyclic voltammetry experiments were carried out using a PARSTAT 2273 electrochemical workstation (Princeton Applied Research) connected to a three-electrode cell equipped with a 3 mm glassy carbon working electrode, a platinum counter electrode, and an aqueous Ag/AgCl (sat. KCl) reference electrode. The supporting electrolyte was electrochemical-grade 0.1 M $[N(Bu)_4]PF_6$. Ferrocene was used as an internal standard by adding it to the solution at the end of the experiment and measuring the potential of the corresponding one electron oxidation. Elemental analyses were determined using a CHN-S Flash E1112 Thermo Finnigan Elemental Analyser; the results were found to be in good agreement with the calculated values.

2-iodobenzene-1,3-diol (**7**)[19,38]

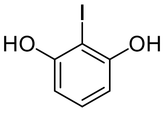

Resorcinol (7.27g; 66.0 mmol; 1.0 eq.) and iodine (17.92 g; 70.6 mmol; 1.07 eq.) were dissolved in $H_2O$ (46 mL). After cooling down to 0°C, $NaHCO_3$ (6.16g; 73.3 mmol; 1.11 eq.) was slowly added and the reaction mixture was stirred at room temperature for 30’. The reaction mixture was diluted with an aqueous solution of $Na_2SO_4$ (10%) and extracted in EtOAc (3 × 50 mL). After washing with brine (100 mL), the organic phase was dried over $Na_2SO_4$ and the solvent was removed under reduced pressure. The crude was suspended in chloroform (20mL) at –10 °C and filtered under vacuum, the desired product **7** was obtained as a white powder (10.89g; 0.46 mmol; 70%). $^1H$ NMR (400 MHz, $CDCl_3$): δ(ppm)= 6.91 (t, *J*=8.1 Hz, 1H), 6.34 (d, *J*=8.1 Hz, 2H). The characterization is in agreement with the one reported in the literature.[19,38]

### 2-iodo-1,3-bis(octyloxy)benzene (**8**)[19,38]

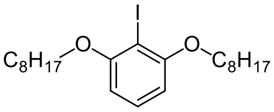

To a stirring solution of **7** (10g; 42.37 mmol; 1.0 eq.) in acetone (200 mL), $K_2CO_3$ (29.28 g; 211.86 mmol; 5.0 eq.) and 1-bromooctane (32.73 g; 169.48 mmol; 4.0 eq.) were added. The reaction mixture was refluxed under inert nitrogen atmosphere overnight. After filtration on celite, the reaction mixture was quenched with water and extracted with DCM (100 mL). The organic phase was dried over $Na_2SO_4$ and the solvent was removed under reduced pressure. The crude was purified by flash chromatography ($SiO_2$, petroleum ether: diethyl ether 50:1 to 25:1) to obtain the desired product **8** as a colorless oil (11.18g; 24.28 mmol; 57 %). $^1H$ NMR (400 MHz, $CDCl_3$): δ(ppm)= 7.24 (t, *J*=8.4 Hz, 1H), 6.58 (d, *J*=8.4 Hz, 2H), 4.00 (t, *J*=6.3 Hz, 4H), 1.73-1.69 (m, 4H), 1.51-1.48 (m, 4H), 1.29-1.24 (m, 16H), 0.86 (t, *J*=6.9 Hz, 6H). The characterization is in agreement with the one reported in the literature.[19,38]

### 2',6'-bis(octyloxy)-[1,1'-biphenyl]-4-amine (**10**)[19,38]

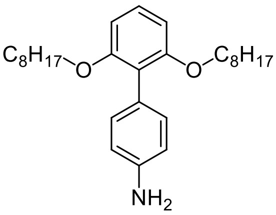

Compound **8** (2.0 g; 4.34 mmol; 1.2 eq.), 4-(4,4,5,5-Tetramethyl-1,3,2-dioxaborolan-2-yl) aniline **9** (0.793 g; 3.62 mmol; 1.0 eq.), $Pd(OAc)_2$ (0.016 g; 0.072 mmol; 2.0 mol%), SPhos (0.030g; 0.072 mmol; 2.0 mol %), and $K_3PO_4$(3.84 g; 18.10 mmol; 5.0 eq.) were dissolved in 1,4-dioxane (88 mL) and $H_2O$ (18 mL) in a Schlenk tube under inert nitrogen atmosphere. The resulting mixture was heated at 70 °C and stirred for 24 h. After filtration on celite, the reaction mixture was extracted with EtOAc (100 mL). The organic phase was dried over $Na_2SO_4$ and the solvent was removed under vacuum. The crude was purified by flash chromatography ($SiO_2$, petroleum ether: DCM 2:1) giving **10** as a colorless oil (1.256 g, 2.95 mmol; 81%). $^1H$ NMR (400 MHz, $CDCl_3$): δ(ppm)= 7.24 – 7.14 (m, 3H), 6.72 (d, *J*=8.5 Hz, 2H), 6.61 (d, *J*=8.3 Hz, 2H), 3.88 (t, *J*=6.5 Hz, 4H), 1.69 – 1.59 (m, 4H), 1.38 – 1.21 (m, 20H), 0.90 (t, *J*=6.9 Hz, 6H). The characterization is in agreement with the one reported in the literature.[19,38]

4-(2',6'-bis(octyloxy)-[1,1'-biphenyl]-4-yl)-4H-dithieno[3,2-b:2',3'-d]pyrrole (**12**)[19,38]

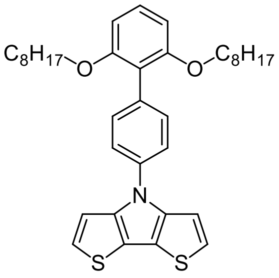

In a Schlenk tube, compound **10** (0.200 g; 0.47 mmol; 1.0 eq.) was dissolved in toluene (3.5 mL) at room temperature under inert nitrogen atmosphere. After degassing the solution, 3,3'-dibromo-2,2'-bithiophene **11** (0.160 g; 0.49 mmol; 1.05 eq.), $Pd_2(dba)_3{\cdot}CHCl_3$ (0.012 g; 0.011 mmol; 2.5 mol%), BINAP (0.029 g; 0.047 mol; 10 mol%). and NaO*t*Bu (0.113 g; 1.17 mmol; 2.5 eq.) were added, and the reaction mixture was heated at 110 °C and stirred for 16 h. After the filtration on celite, the solution was diluted with $H_2O$ (10 mL) and extracted with DCM (2 × 20 mL). The combined organic phases were dried over $Na_2SO_4$ and the solvent was removed under reduced pressure. The crude was purified by flash chromatography ($SiO_2$; Petroleum ether: Toluene 2:1) to yield desired product **12** as a yellow oil (0.176 g; 0.299 mmol; 63%). $^1H$ NMR (400 MHz, $CDCl_3$): δ(ppm)= 7.63 – 7.51 (m, 4H), 7.27 – 7.23 (m, 3H), 7.18 (d, *J*=5.3 Hz, 2H), 6.66 (d, *J*=8.4 Hz, 2H), 3.95 (t, *J*=6.3 Hz, 4H), 1.72 – 1.60 (m, 4H), 1.39 – 1.16 (m, 20H), 0.83 (t, *J*=6.4 Hz, 6H). The characterization is in agreement with the one reported in the literature.[19,38]

4-(2',6'-bis(octyloxy)-[1,1'-biphenyl]-4-yl)-4H-dithieno[3,2-b:2',3'-d]pyrrole-2-carbaldehyde (**6**)[19,38]

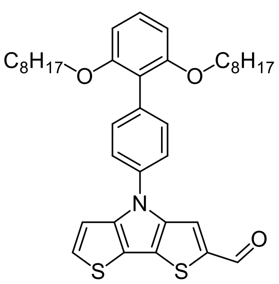

To a solution of **12** (0.156 g, 0.26 mmol; 1.0 eq.) and *N, N*- dimethylformamide (0.057 mL; 0.74 mmol; 2.8 eq.) in 1,2-dichloroethane anhydrous (2.5 mL) cooled to 0°C, $POCl_3$ (0.029 mL; 0.32 mmol; 1.2 eq.) was added dropwise. The resulting mixture was stirred under nitrogen inert atmosphere at 50 °C for 16 h. A saturated aqueous solution of potassium acetate (20 mL) was then added and the mixture was stirred 3h at room temperature. The mixture was added with $H_2O$ (20 mL) and extracted with DCM (30 mL × 2). The organic phase was dried over $Na_2SO_4$ and the solvent was removed under reduced pressure. The crude product was purified by flash chromatography ($SiO_2$, petroleum ether: DCM 1:1) to afford the desired product **6** as a yellow solid (0.087 g; 0.14 mmol; 54 %). $^1$H NMR (400 MHz, $CDCl_3$): δ(ppm) = 9.89 (s, 1H), 7.86 (s, 1H), 7.62 – 7.55 (m, 4H), 7.43 (d, *J*=6.1 Hz, 1H), 7.32 – 7.21 (m, 2H), 6.67 (d, *J*=8.4, 2H), 3.95 (t, *J*=6.4, 4H), 1.72 – 1.61 (m, 4H), 1.37 – 1.13 (m, 20H), 0.85 – 0.76 (m, 6H). The characterization is in agreement with the one reported in the literature.[19,38]

4-(2',6'-bis(octyloxy)-[1,1'-biphenyl]-4-yl)-6-(7-bromobenzo[c][1,2,5]thiadiazol-4-yl)-4H-dithieno[3,2-b:2',3'-d]pyrrole-2-carbaldehyde (**4**)

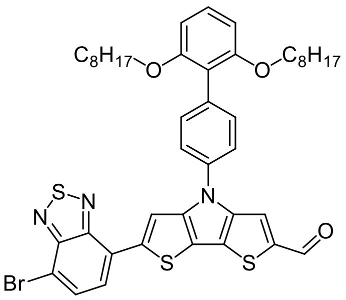

In a Schlenk tube, under inert nitrogen atmosphere, compound **6** (0.110 g; 0.18 mmol; 1.0 eq.), 4,7-dibromo-2,1,3-benzothiadiazole **5** (0.079 g; 0.26 mmol; 1.5 eq.), $Pd(OAc)_2$ (0.003g; 0.013 mmol: 7.5 mol%), cataCXium A (0.010g; 0.027mmol; 15 mol%), pivalic acid (0.005g; 0.054 mmol; 30 mol%), $Cs_2CO_3$ (0.084, 0.26 mmol; 1.5 eq.) were added in anhydrous toluene (2 mL), and the reaction mixture was heated at 110 °C and stirred for 4.5 h. After filtration on celite, water was added (20 mL) and the mixture was extracted in DCM (20 mL), dried over $Na_2SO_4$ and the crude was removed under reduced pressure. The crude product was purified by flash chromatography ($SiO_2$, Petroleum ether: DCM 10:1) to afford a red solid **4** as the desired product (0.087 g; 0.105 mmol; 58 %).$^1$H NMR (400 MHz, $CDCl_3$): δ(ppm)= 9.90 (s, 1H), 8.43 (s, 1H), 7.88 (d, *J*=7.8 Hz, 1H), 7.86 (s, 1H), 7.78 (d, *J*=7.7 Hz, 1H), 7.65 – 7.64 (m, 4H), 7.31 – 7.27 (m, 1H), 6.68 (d, *J*=8.4, 2H), 3.97 (t, *J*=6.4, 4H), 1.75 – 1.64 (m, 4H), 1.41 – 1.06 (m, 20H), 0.80 – 0.71 (m, 6H). $^{13}$C NMR (101 MHz, $CDCl_3$): δ(ppm)= 183.18, 157.28, 151.68, 148.50, 144.27, 141.78, 141.27, 136.81, 133.53, 133.23, 132.43, 129.23, 127.59, 125.87, 124.69, 121.89, 121.03, 118.74, 117.52, 113.72, 113.19, 105.46, 68.79, 31.90, 29.42, 29.32, 29.24, 26.15, 22.74, 14.15. ESI-MS: m/z = 827.19 $[M]^+$

1,2,3,3a,4,8b-hexahydrocyclopenta[b]indole (**14**)[38,40,48]

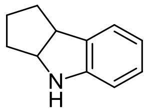

1,2,3,4-tetrahydrocyclopent[*b*]indole **13** (2.5 g; 15.9 mmol; 1.0 eq.) was dissolved in $CH_3COOH$ (60 mL); $NaCNBH_3$ (3.0 g; 47.7 mmol; 3.0 eq.) was added slowly at 15 °C and the resulting mixture was stirred at room temperature for 16 h. After adding $H_2O$ (20 mL), the solution was stirred for 1 h, and the solvent volume was reduced under vacuum. A saturated solution of $NaHCO_3$ (130 mL) and EtOAc (70 mL) were then added and the solution was stirred for 2 h. The organic phase was separated, dried over $Na_2SO_4$ and the solvent was removed under reduced pressure obtaining the desired product **14** as a yellow liquid (2.063 g; 12.96 mmol; 81%).$^1$H NMR (400 MHz, $CDCl_3$): δ(ppm)= 7.04 (d, *J*=7.2 Hz, 1H), 6.99 (t, *J*=7.6 Hz, 1H), 6.68 (t, *J*=7.4 Hz, 1H), 6.53 (d, *J*=7.8 Hz, 1H), 4.36 (ddd, *J*=8.4 Hz, 6.0 Hz, 2.1 Hz, 1H), 3.81 – 3.74 (m, 1H), 2.02 – 1.50 (m, 6H). $^{13}$C NMR (101 MHz, $CDCl_3$): δ(ppm)= 151.31, 133.61, 127.50, 124.69, 118.62, 108.77, 63.51, 47.36, 37.01, 35.04, 24.56. The characterization is in agreement with the one reported in the literature.[38,40,48]

4-(p-tolyl)-1,2,3,3a,4,8b-hexahydrocyclopenta[b]indole (**16**)[38,40,48]

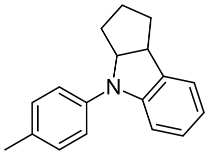

In a Schlenk tube, under an inert nitrogen atmosphere, $Pd_2(dba)_3{\cdot}CHCl_3$ (0.155 g; 0.15 mmol; 5 mol%), *t*$Bu_3P{\cdot}HBF_4$ (0.091 g; 0.31 mmol; 10 mol %) were added to degassed toluene (25 mL) at room temperature and the mixture was stirred for 20'; compound **14** (0.500 g; 3.14 mmol; 1.0 eq.), *p*-bromotoluene **15** (0.644 g; 3.77 mmol; 1.2 eq.) and NaO*t*Bu (0.906 g; 9.42 mmol; 3.0 eq.) were then added, the reaction mixture was heated at 90 °C and stirred for 16 h. After filtration on celite, the solution was diluted with $H_2O$ (20 mL) and extracted with EtOAc (20 mL) and brine (25 mL × 2); the combined organic phases were dried over $Na_2SO_4$ and the solvent was removed under reduced pressure. The crude was purified by flash chromatography ($SiO_2$, Petroleum ether: EtOAc 20:1 to 1:1) to yield the desired product **16** as an colorless oil (0.658 g; 2.63 mmol; 84%).$^1$H NMR (400 MHz, $CDCl_3$): δ(ppm)= 7.41 (d, *J*=8.4 Hz, 2H), 7.34 (d, *J*=8.6 Hz, 2H), 7.31 (d, *J*=7.4 Hz, 1H), 7.24 (t, *J*=7.2 Hz, 1H), 7.15 (d, *J*=7.9 Hz, 1H), 6.92 (t, *J*=7.3 Hz, 1H), 4.92 (t, 1H), 4.00 (t, *J*=8.8 Hz, 2.5 Hz, 1H), 2.54 (s, 3H), 2.21 – 1.68 (m, 6H). The characterization is in agreement with the one reported in the literature.[38,40,48]

7-bromo-4-(p-tolyl)-1,2,3,3a,4,8b-hexahydrocyclopenta[b]indole (**17**).[38,40,48]

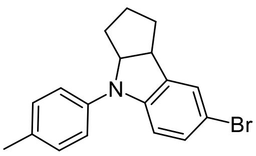

In a Schlenk tube, compound **16** (0.570 g; 2.28 mmol; 1.0 eq.) was dissolved in dry $CHCl_3$ (12 mL) under an inert nitrogen atmosphere and cooled down to 0 °C; NBS (0.406 g; 2.28 mmol; 1.0 eq.) was added and the resulting mixture was stirred at 0 °C for 2 h. The reaction mixture was diluted with a saturated aqueous solution of $NaHCO_3$ (20 mL). The organic phase was extracted with DCM (40 mL), dried over $Na_2SO_4$ and the solvent was removed under vacuum. The crude was purified by flash chromatography ($SiO_2$, Petroleum ether: DCM 10:1) to yield desired product **17** as a grey solid (0.612g; 1.87 mmol; 82%).$^1$H NMR (400 MHz, $CDCl_3$): δ(ppm)= 7.16 (s, 1H), 7.11 – 7.15 (m, 4H), 7.08 (dd, *J*=8.5 Hz, 1.8 Hz, 1H), 6.72 (d, *J*=8.5 Hz, 1H), 4.75 (t, *J*=6.6 Hz, 1H), 3.79 (t, *J*=7.7, 1H), 2.32 (s, 3H), 2.09 – 1.95 (m, 1H), 1.94 – 1.73 (m, 3H), 1.70 – 1.59 (m, 1H), 1.57 – 1.47 (m, 1H). The characterization is in agreement with the one reported in the literature.[38,40,48]

7-(4,4,5,5-tetramethyl-1,3,2-dioxaborolan-2-yl)-4-(p-tolyl)-1,2,3,3a,4,8b-hexahydrocyclopenta[b]indole (**3**)[38,40,48]

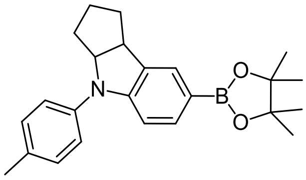

In a Schlenk tube, compound **17** (0.100 g; 0.30 mmol; 1.0 eq.), bis(pinacolato)diboron **18** (0.116 g; 0.45 mmol; 1.5 eq.), Pd(dppf)$Cl_2$ (0.022 g; 0.03 mmol; 10 mol%), and potassium acetate (0.089 g; 0.91 mmol; 3.0 eq.) were added to *N,N*-dimethylformamide (5 mL), and the resulting mixture was heated at 90 °C and stirred under inert atmosphere for 16 h. The reaction mixture was filtered on celite, diluted with DCM (40 mL) and washed with brine (4× 20 mL). The organic phase was dried over $Na_2SO_4$ and the solvent was removed under reduced pressure. The crude was purified by flash chromatography ($SiO_2$, Petroleum Ether: DCM 3:1 to 1:1), obtaining the boronic ester **3** as a grey solid (0.065 g; 0.17 mmol; 58%).$^1$H NMR (400 MHz, $CDCl_3$): δ(ppm)= 7.55 (s, 1H), 7.51 (d, *J*=8.0 Hz, 1H), 7.22 – 7.13 (m, 4H), 6.83 (d, *J*=8.0 Hz, 1H), 4.78 (ddd, *J*=8.5 Hz, 6.3 Hz, 2.0 Hz, 1H), 3.80 (td, *J*=8.8 Hz, 2.6 Hz, 1H), 2.33 (s, 3H), 2.06 – 1.60 (m, 6H), 1.32 (s, *J*=2.7 Hz, 12H).$^{13}$C NMR (101 MHz, $CDCl_3$): δ(ppm)= 151.02, 140.11, 135.25, 134.19, 132.05, 131.15, 129.91, 129.83, 120.90, 119.87, 83.34, 69.21, 45.29, 35.21, 33.75, 25.08, 24.90, 24.51, 20.96. The characterization is in agreement with the one reported in the literature. [1,3,4]

### 4-(2',6'-bis(octyloxy)-[1,1'-biphenyl]-4-yl)-6-(7-(4-(p-tolyl)-1,2,3,3a,4,8b-hexahydrocyclopenta[b]indol-7-yl)benzo[c][1,2,5]thiadiazol-4-yl)-4H-dithieno[3,2-b:2',3'-d]pyrrole-2-carbaldehyde (**2**)

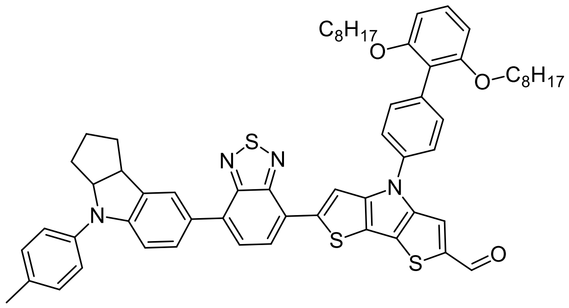

In a Schlenk tube, bromide **4** (0.045 g; 0.054 mmol; 1.0 eq.), boronic ester **3** (0.022 g; 0.06 mmol; 1.1 eq.), Pd(PPh$_3$)$_4$ (0.003 g; 0.0027 mmol; 5 mol%) and an aqueous solution of Na$_2$CO$_3$ 2.0 M (0.15 mL) were added to toluene (8 mL) under an inert nitrogen atmosphere. After degassing the solution, the mixture was heated at 95 °C and stirred for 24 h. The mixture was diluted with H$_2$O (10 mL) and extracted with DCM (20 ml × 2). The combined organic phases were dried over Na$_2$SO$_4$ and the solvent was removed under reduced pressure. The crude was purified by flash chromatography (SiO$_2$, petroleum ether: DCM 5:1) giving the desired product **4** as a purple solid (0.040 g; 0.040 mmol; 74%).$^1$H NMR (400 MHz, THF-d$_8$): δ(ppm)= 9.88 (s, 1H), 8.56 (s, 1H), 8.07 (d,J= 7.7 Hz, 1H), 8.02 (s, 1H),7.94(s, 1H), 7.80 (dd,J= 8.5 and 1.4 Hz, 1H), 7.72–7.78 (m, 3H), 7.64 (d,J= 8.6 Hz, 2H), 7.20–7.28 (m, 3H), 7.13–7.19 (m, 2H), 6.96 (d,J= 8.4 Hz,1H), 6.72 (d,J= 8.4 Hz, 2H), 4.87–4.94 (m, 1H), 3.97 (d,J= 6.3 Hz, 4H),3.88–3.95 (m, 1H),2.31 (s, 3H), 2.06–2.17 (m, 1H), 1.87–2.00 (m, 2H),1.76–1.86 (m, 1H), 1.62–1.71 (m, 5H), 1.50–1.62 (m, 1H), 1.33–1.42 (m,4H), 1.13–1.32 (m, 16H), 0.70–0.79 (m, 6H). $^{13}$C NMR (101 MHz, CDCl$_3$): δ(ppm)= 182.7, 158.0, 154.8, 153.5, 149.2, 148.8, 144.4, 143.2, 142.7, 141.0, 137.6, 135.9, 134.4, 134.2, 133.7, 132.1, 130.3, 129.6, 129.5, 127.9, 126.7, 126.3, 126.2, 125.5, 124.6, 122.1, 121.7, 120.9, 119.6, 117.7, 112.9, 107.8, 105.9, 69.9, 69.1, 46.2, 35.9, 34.3, 32.6, 30.5, 30.1, 30.0, 29.9, 26.8, 23.3, 20.7, 14.2. ESI-MS: m/z = 997,38 [M]$^+$.

(E)-3-(4-(2',6'-bis(octyloxy)-[1,1'-biphenyl]-4-yl)-6-(7-(4-(p-tolyl)-1,2,3,3a,4,8b-hexahydrocyclopenta[b]indol-7-yl)benzo[c][1,2,5]thiadiazol-4-yl)-4H-dithieno[3,2-b:2',3'-d]pyrrol-2-yl)-2-cyanoacrylic acid (**RI114**)

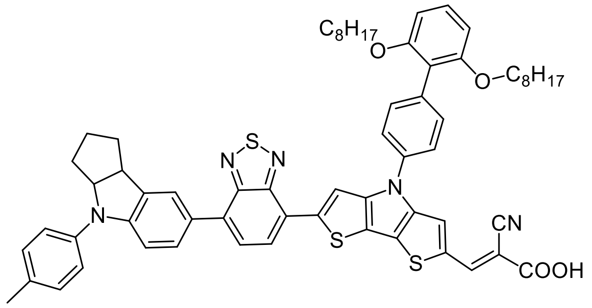

In a Schlenk tube, aldehyde **2** (0.040 g; 0.04 mmol; 1.0 eq.) was dissolved in toluene (2 mL) under inert nitrogen atmosphere. Ammonium acetate **1** (0.0046 g; 0.06 mmol; 1.5 eq.) and cyanoacetic acid (0.017g; 0.20 mmol; 5.0 eq.) were then added, and the reaction mixture was stirred for 4 h at 110 °C. After a solution of HCl (0.03M) was added, the organic phase was extracted in DCM (10 mL), dried over $Na_2SO_4$ and the solvent was removed under reduced pressure. The crude was purified by flash chromatography ($SiO_2$, DCM: MeOH 10:1) giving product **RI114** as a purple solid (0.040 g; 0.037 mmol; 94%).$^1$H NMR (400 MHz, THF-$d_8$): δ(ppm)= 8.55 (s, 1H), 8.38 (s, 1H), 8.05 (d, *J*=7.6 Hz, 1H), 8.02 (s, 1H), 7.93 (s, 1H), 7.81 – 7.77 (m, 1H), 7.77 – 7.73 (m, 3H), 7.65 (d, *J*=8.4 Hz, **2H**), 7.28 – 7.21 (m, 3H), 7.15 (d, *J*=8.3 Hz, 2H), 6.95 (d, *J*=8.4 Hz, 1H), 6.71 (d, *J*=8.4 Hz, 2H), 4.93 – 4.87 (m, 1H), 3.96 (t, *J*=6.3 Hz, 4H), 3.93 – 3.87 (m, 1H), 2.31 (s, 3H), 2.17 – 1.76 (m, 4H), 1.63 – 1.49 (m, 2H), 1.29 – 1.11 (m, 24H), 0.79 – 0.68 (m, 6H). $^{13}$C NMR (101 MHz, THF-$d_8$): δ(ppm)= 163.66, 157.34, 154.14, 148.57, 147.12, 144.15, 140.31, 136.90, 136.79, 135.22, 134.72, 133.92, 133.79, 133.64, 133.09, 131.48, 129.67, 128.91, 128.87, 126.22, 126.01, 125.64, 121.84, 121.36, 120.26, 118.96, 117.16, 116.28, 113.43, 112.27, 107.14, 105.28, 69.26, 68.42, 45.51, 35.27, 33.63, 32.03, 31.90, 29.80, 29.41, 29.25, 26.14, 22.72, 20.02, 13.59. ESI-MS: m/z = 1063,42 $[M]^+$.

4-(1,3,3a,8b-tetrahydrocyclopenta[b]indol-4(2H)-yl)benzaldehyde (**29**)

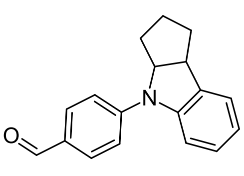

In a Schlenk tube, under an inert nitrogen atmosphere, $Pd_2(dba)_3 \cdot CHCl_3$ (0.218 g; 0.210 mmol; 3.0 mol%), *t*$Bu_3P \cdot HBF_4$ (0.122g; 0.421 mmol; 6.0 mol %) were added in degassed toluene (35 mL) and stirred at room temperature for 1 h; *p*-bromobenzaldehyde **28** (1.300 g; 7.03 mmol; 1.0 eq.), indoline **14** (1.343 g; 8.43 mmol; 1.2 eq) and $Cs_2CO_3$ (4.58 g; 14.06 mmol; 2.0 eq.) were then added and the reaction mixture was kept 16 h at 110 °C under magnetic stirring. After filtration on celite, the solution was diluted with $H_2O$ (30 mL) and extracted with EtOAc (30 ml × 2) the combined organic phases were dried over $Na_2SO_4$ and the solvent was removed under reduced pressure. The crude was purified by flash chromatography ($SiO_2$; Petroleum ether: DCM 30:1 to 1:1) to yield the desired product **29** as a colorless oil (1.500g; 5.69 mmol; 81%). 1H NMR (400 MHz, $CDCl_3$): δ(ppm)= 9.83 (s, 1H), 7.82 (d, *J*=8.7 Hz, 2H), 7.35 (d, *J*=8.7 Hz, 2H), 7.27 (d, *J*=8.1 Hz, 1H), 7.19 (d, *J*=7.4 Hz, 1H), 7.15 (t, *J*=7.8 Hz, 1H), 6.90 (t, *J*=7.4 Hz, 1H), 4.77 – 4.68 (m, 1H), 3.91 (t, *J*=7.8 Hz, 1H), 2.13 – 1.88 (m, 4H), 1.80 – 1.63 (m, 1H), 1.52 – 1.39 (m, 1H). $^{13}C$ NMR (101 MHz, $CDCl_3$): δ(ppm)= 190.47, 148.36, 144.19, 138.49, 131.69, 130.06, 126.02, 128.17, 116.45, 112.78, 111.87, 69.06, 45.50, 34.28, 34.22, 24.52. ESI-MS: m/z = 263. 13 $[M]^+$.

4-(7-bromo-1,3,3a,8b-tetrahydrocyclopenta[b]indol-4(2H)-yl)benzaldehyde (**30**)

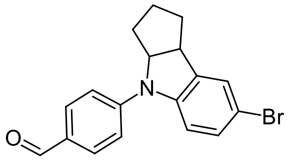

In a Schlenck tube, compound **29** (1.40 g; 5.32 mmol; 1.0 eq.) was dissolved in $CHCl_3$ (25 mL) under inert nitrogen atmosphere and cooled down to 0 °C. NBS (0.946 g; 5.32 mmol; 1.0 eq.) at 0 °C and the resulting mixture was stirred at room temperature in the dark for 16 h. A saturated aqueous solution of $NaHCO_3$ (25 mL) was added and stirred for 1 h. The mixture was extracted with DCM (40 mL), the organic phase was dried over $Na_2SO_4$ and the solvent was removed under vacuum. The crude was recrystallized from petroleum ether obtaining the desired product **30** as a yellow solid (1.149 g; 3.36 mmol; 63%).$^1H$ NMR (400 MHz, $CDCl_3$): δ(ppm)= 9.84 (s, 1H), 7.83 (d, *J*=8.8 Hz, 2H), 7.31 (d, *J*=8.8 Hz, 2H), 7.26 (d, *J*=1.4 Hz, 1H), 7.22 (dd, *J*=8.5 Hz, 1.7 Hz, 1H), 7.11 (d, *J*=8.5 Hz, 1H), 4.80 – 4.70 (m, 1H), 3.89 (t, *J*=7.5 Hz, 1H), 2.13 – 1.98 (m, 2H), 1.98 – 1.86 (m, 2H), 1.77 – 1.64 (m, 1H), 1.54 – 1.40 (m, 1H). $^{13}C$ NMR (101 MHz, $CDCl_3$): δ(ppm)= 190.47, 148.36, 144.19, 138.49, 131.69, 130.06, 129.05, 128.17, 116.45, 112.78, 111.87, 69.06, 45.50, 34.28, 34.22, 24.52. ESI-MS: m/z = 343.04, 345.31 $[M]^+$.

(4-(7-bromo-1,3,3a,8b-tetrahydrocyclopenta[b]indol-4(2H)-yl)phenyl)methanol (**31**)

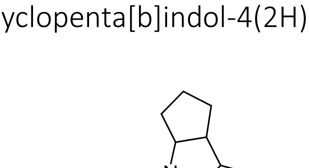

In a Schlenk tube, compound **30** (0.080 g; 0.23 mmol; 1.0 eq.) was dissolved in anhydrous THF (2 mL) at room temperature and the mixture was cooled down to 0 °C. $NaBH_4$ (0.017 g; 0.47 mmol: 2.0 eq.) dissolved in anhydrous MeOH (2 mL) was then added at 0 °C and the reaction mixture was stirred at room temperature for 2 h. A saturated aqueous solution of $NH_4Cl$ (5 mL) was added and stirred for 30'. The organic phase was extracted in DCM (10 mL), dried over $Na_2SO_4$ and the solvent was removed under reduced pressure to yield the desired product **31** as white solid (0.080 g; 0.23 mmol; 99%).$^1$H NMR (400 MHz, THF-$d_8$): δ(ppm)= 7.30 (d, *J*=8.6 Hz, 2H), 7.21 (d, *J*=8.5 Hz, 2H), 7.18 – 7.17 (m, 1H), 7.05 (dd, *J*=8.5 Hz, 2.1, 1H), 6.76 (d, *J*=8.5 Hz, 1H), 4.86 – 4.78 (m, 1H), 4.51 (s, 2H), 3.84 – 3.75 (m, 1H), 2.13 – 1.97 (m, 1H), 1.93 – 1.75 (m, 3H), 1.69 – 1.56 (m, 1H), 1.54 – 1.41 (m, 1H). $^{13}$C NMR (101 MHz, $CDCl_3$): δ(ppm)= 146.21, 143.02, 136.35, 129.71, 129.65, 128.19, 127.21, 115.43, 113.78, 111.77, 72.01, 69.06, 45.50, 34.28, 34.22, 24.52. ESI-MS: m/z = 344.09, 346.00 [M]$^+$.

4-(7-(4,4,5,5-tetramethyl-1,3,2-dioxaborolan-2-yl)-1,3,3a,8b-tetrahydrocyclo-penta[b]indol-4(2H)-yl) benzaldehyde (**41**)

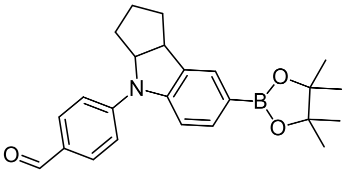

In a Schlenk tube, compound **30** (0.162 g; 0.47 mmol; 1.0 eq.), bis(pinacolato)diboron **18** (0.180 g; 0.71 mmol; 1.5 eq.), Pd(dppf)$Cl_2$ (0.034 g; 0.047 mmol; 10 mol%), and potassium acetate (0.139 g; 1.41 mmol; 3.0 eq.) were added to anhydrous 1,4-dioxane (2.5 mL); the resulting mixture was heated at 85 °C and stirred under inert atmosphere for 24 h. The mixture was filtered on celite, diluted with DCM (40 mL) and washed with $H_2O$ (30 mL). The organic phase was dried over $Na_2SO_4$ and the solvent was removed under reduced pressure. The crude was purified by flash chromatography ($SiO_2$, Petroleum Ether: DCM 3:1 to 1:1), obtaining boronic ester **41** as a green solid (0.154 g; 0.395 mmol; 84%)$^1$H NMR (400 MHz, $CDCl_3$): δ(ppm)= 9.84 (s, 1H), 7.83 (d, *J*=8.7 Hz, 2H), 7.64 – 7.60 (m, 3H), 7.37 (d, *J*=8.7 Hz, 1H), 7.22 (d, *J*=8.4 Hz, 1H), 4.81 – 4.72 (m, 1H), 3.88 (t, *J*=7.2 Hz, 1H), 2.01 – 1.88 (m, 4H), 1.73 – 1.61 (m, 1H), 1.54 – 1.41 (m, 1H), 1.34 (s, *J*=2.1 Hz, 12H). $^{13}$C NMR (101 MHz, $CDCl_3$): δ(ppm)= 190.49, 148.34, 147.76, 135.36, 134.92, 131.60, 131.52, 129.12, 117.06, 109.72, 83.64, 68.84, 45.38, 34.36, 34.13, 25.13, 25.05, 24.91, 24.51. ESI-MS: m/z = 389.22 [M]$^+$.

Dimethyl (1-diazo-2-oxopropyl) phosphonate (**27**)[59]

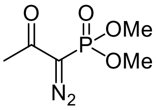

In a Schlenk tube, sodium hydride 60% dispersion in mineral oil (0.132 g; 3.31 mmol; 1.1 eq.) was washed with anhydrous pentane (3.0 mL) under an inert nitrogen atmosphere and dispersed in anhydrous toluene (8.0 mL) and THF (3.0 mL). Dimethyl acetylmethylphosphonate

(0.500 g; 3.01 mmol; 1.0 eq.) was dissolved in anhydrous toluene (5.0 mL). Both mixtures were cooled down to 0 °C than the solution of was added to the sodium hydride suspension at 0 °C and stirred for 1 h at the same temperature. A solution of 4-acetamidobenzenesulphonyl azide (0.795 g; 3.31 mmol; 1.1 eq.), in anhydrous toluene (10 mL), was added slowly at the reaction mixture keeping the temperature at 0 °C. The mixture was stirred at 0 °C for 1 h than allowed to war up to room temperature over 16 h. After filtration on celite with toluene (50 mL), and the solvent was removed under reduced pressure obtaining the desired product **27** as a yellow oil (0.578g; 3.0 mmol; 99%).$^1$H NMR (400 MHz, $CDCl_3$): δ(ppm)= 3.88 (d, *J*=12.1 Hz, 6H), 2.28 (s, 3H). The characterization is in agreement with the one reported in the literature.[59]

7-bromo-4-(4-ethynylphenyl)-1,2,3,3a,4,8b-hexahydrocyclopenta[b]indole (**39**)

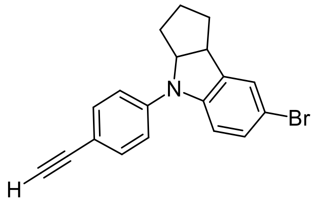

In a Schlenk tube, under an inert nitrogen atmosphere, aldehyde **30** (0.386 g; 1.13 mmol; 1.0 eq.) was dissolved in anhydrous THF (1.0 mL) and in anhydrous MeOH (3.0 mL). Compound **27** (0.435 g; 2.26 mmol; 3.0 eq.) dissolved in anhydrous THF (1.0 mL), and $K_2CO_3$ (0.312g; 2.26 mmol; 3.0 eq.) were then added to the aldehyde solution at room temperature and stirred for 16 h. A saturated aqueous solution of $NH_4Cl$ (3.0 mL) was added and the organic phase was extracted in diethyl ether (2 × 5.0 mL). The organic phases reunited were dried over $Na_2SO_4$ and the solvent was removed under reduced pressure. The crude was purified by flash chromatography ($SiO_2$, Petroleum Ether: EtOAc 100:1), obtaining alkyne **39** as an off-white solid (0.132 g; 0.39 mmol; 59%).$^1$H NMR (400 MHz, $CDCl_3$): δ(ppm)= 7.44 (d, *J*=8.7 Hz, 2H), 7.21 (s, 1H), 7.19 – 7.13 (m, 3H), 6.95 – 6.90 (m, 1H), 4.76 – 4.69 (m, 1H), 3.86 – 3.78 (m, 1H), 3.04 (s, 1H), 2.09 – 1.97 (m, 1H), 1.94 – 1.83 (m, 3H), 1.72 – 1.62 (m, 1H), 1.53 – 1.42 (m, 1H). $^{13}$C NMR (101 MHz, $CDCl_3$): δ(ppm)= 145.46, 143.36, 137.84, 133.35, 133.29, 129.91, 127.92, 117.85, 110.98, 110.28, 84.02, 76.20, 68.97, 45.43, 34.66, 34.07, 24.52. ESI-MS: m/z = 337.04, 338.71 $[M]^+$

4-(4-ethynylphenyl)-7-(4,4,5,5-tetramethyl-1,3,2-dioxaborolan-2-yl)-1,2,3,3a,4,8b-hexahydrocyclopenta[b]indole (**40**)

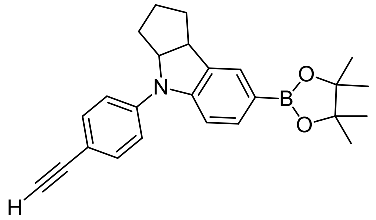

In a Schlenk tube, alkyne **39** (0.030g; 0.089 mmol; 1.0 eq.) was dissolved in anhydrous THF (3 mL) under nitrogen inert atmosphere. After cooling down to – 78 °C, *t*BuLi solution 1.7 M in pentane (183 µL, 0.31 mmol; 3.5 eq.) was added and the reaction mixture was stirred for 1 h at the same temperature. Pinacol borane (25 µL; 0.17 mmol; 2.0 eq.) was added, and the reaction was stirred allowing to reach room temperature over 16 h. The solution was quenched with $H_2O$ (5.0 mL) and extracted with DCM (10 mL). the organic phase was dried over $Na_2SO_4$ and the solvent was removed under reduced pressure. The crude was purified by flash chromatography ($SiO_2$, petroleum ether: EtOAc 50:1), obtaining boronic ester **40** as a light yellow oil (0.013 g; 0.034 mmol; 38%).$^1$H NMR (400 MHz, $CDCl_3$): δ(ppm)= 7.58 (s, 1H), 7.56 (d, *J*=8.6 Hz, 1H), 7.45 (d, *J*=8.7 Hz, 2H), 7.22 (d, *J*=8.7 Hz, 2H), 7.03 (d, *J*=8.0 Hz, 1H), 4.76 (ddd, *J*=19.1 Hz, 9.6 Hz, 6.6 Hz, 1H), 3.83 (td, *J*=8.7 Hz, 2.7 Hz, 1H), 3.04 (s, 1H), 2.13 – 1.79 (m, 4H), 1.69 – 1.60 (m, 1H), 1.54 – 1.41 (m, 1H), 1.34 (s, *J*=2.3 Hz, 12H). $^{13}$C NMR (101 MHz, $CDCl_3$): δ(ppm)= 149.17, 143.25, 135.08, 134.77, 133.26, 131.37, 118.59, 114.36, 114.12, 108.16, 84.12, 83.52, 68.81, 45.33, 34.81, 33.97, 29.85, 25.08, 24.93, 24.54. ESI-MS: m/z = 385.22 $[M]^+$.

7-(thiophen-2-yl)benzo[c][1,2,5]thiadiazole-4-carbaldehyde (**26**)

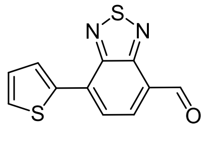

In a Schlenk tube, 7-bromobenzo[c][1,2,5]thiadiazole-4-carbaldehyde **25** (0.100 g; 0.41 mmol; 1.0 eq.), 2-(tributylstannyl) thiophene **22** (0.184 g; 0.49 mmol; 1.2 eq.), and $Pd(PPh_3)_4$ (0.023 g; 0.02 mmol; 6 mol%) were dissolved in anhydrous toluene (8 mL) under inert nitrogen atmosphere . The resulting mixture was heated at 110 °C and stirred for 16 h. A saturated solution of potassium fluoride (10 mL) was added and stirred for 30’. The organic phase was extracted in DCM (30mL), washed with brine (20 mL × 2), and dried over $Na_2SO_4$ , finally the solvent was removed under reduced pressure. The crude was purified by flash chromatography ($SiO_2$, Petroleum Ether: DCM 1:1), obtaining compound **26** as an orange solid (0.096 g; 0.39 mmol; 95%).$^1$H NMR (400 MHz, $CDCl_3$): δ(ppm)= 10.72 (s, 1H), 8.29 (d, *J*=3.7 Hz, 1H), 8.22 (d, *J*=7.5 Hz, 1H), 8.00 (d, *J*=7.5 Hz, 1H), 7.59 (d, *J*=5.0 Hz, 1H), 7.27 – 7.23 (m, 1H). $^{13}$C NMR (101

MHz, $CDCl_3$): δ(ppm)= 188.71, 153.80, 152.52, 138.58, 133.25, 132.83, 130.21, 129.70, 128.63, 125.75, 124.32. ESI-MS: m/z = 247.09 $[M+1]^+$.

4-ethynyl-7-(thiophen-2-yl)benzo[c][1,2,5]thiadiazole (**19**)

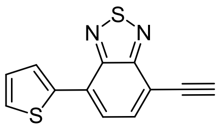

In a Schlenk tube, aldehyde **26** (0.025 mg; 0.10 mmol: 1.0 eq.), compound **27** (0.048 mg; 0.25 mmol; 2.5 eq.), and $K_2CO_3$ (0.046 mg; 0.25 mmol; 2.5 eq.) were added in anhydrous MeOH (2.0 mL) at room temperature and the reaction mixture was stirred for 24 h under inert nitrogen atmosphere. After quenching with a saturated aqueous solution of $NH_4Cl$ (7.0 mL), the organic phase was extracted in EtOAc (20 mL), dried over $Na_2SO_4$, and then the solvent was removed under reduced pressure. The crude was purified by flash chromatography ($SiO_2$, Petroleum Ether: DCM 10:1), obtaining compound **19** as an orange solid (0.013 g; 0.053 mmol; 54%).$^1$H NMR (400 MHz, $CDCl_3$): δ(ppm)= 8.16 (dd, *J*=3.7 Hz, 1.1 Hz, 1H), 7.85 – 7.80 (m, 2H), 7.50 (dd, *J*=5.1 Hz, 1.1 Hz, 1H), 7.22 (dd, *J*=5.1 Hz, 3.8 Hz, 1H), 3.63 (s, 1H). $^{13}$C NMR (101 MHz, $CDCl_3$): δ(ppm)= 155.50, 151.79, 138.91, 134.08, 128.59, 128.31, 127.87, 125.03, 113.97, 83.94, 79.60. ESI-MS: m/z = 242.00 $[M]^+$.

4-(azidomethyl)-7-(thiophen-2-yl)benzo[c][1,2,5]thiadiazole (**35**)

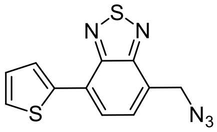

In a Schlenk tube, aldehyde **26** (0.150 g; 0.61 mmol; 1.0 eq.) and silver (I) triflate (0.015g; 0.06 mmol; 10 mol%) were mixed with anhydrous DCM (10 mL) under inert atmosphere. The mixture was cooled to 0 °C than trimethylsilylazide (0.196g; 1.70 mmol; 2.8 eq.) was added and the reaction mixture was stirred for 1 h at the same temperature. After, triethylsilane (0.142g; 1.22 mmol; 2.0 eq.) was adding to the reaction mixture that was allowed to warm up to room temperature over 16 h. The reaction mixture was extracted with DCM (30 mL) and the organic phase was washed with $H_2O$ (30 mL) than dried over $Na_2SO_4$ before removing the solvent under reduced pressure. The crude was purified by flash chromatography ($SiO_2$, Petroleum Ether: DCM 4:1), obtaining azide **35** as a yellow solid (0.105 g; 0.38 mmol; 63%).$^1$H NMR (400 MHz, $CDCl_3$): δ(ppm)= 8.13 (dd, *J*=3.7 Hz, 1.0 Hz, 1H), 7.85 (d, *J*=7.2 Hz, 1H), 7.59 (d, *J*=7.3 Hz, 1H), 7.47 (dd, *J*=5.1 Hz, 1.0 Hz, 1H), 7.22 (dd, *J*=5.1 Hz, 3.8 Hz, 1H), 4.89 (s, 2H). $^{13}$C NMR (101 MHz, $CDCl_3$) δ(ppm)= 154.42, 152.49, 139.11, 128.67, 128.21, 128.12, 127.82, 127.32, 127.24, 125.36, 51.32. ESI-MS: m/z = 273.01 $[M]^+$.

4-(4-bromobenzyl)-7-(thiophen-2-yl)benzo[c][1,2,5]thiadiazole (**38**)

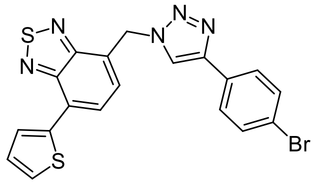

Azide **35** (0.022g; 0.08 mmol; 1.0 eq.), 4- bromophenyl acetylene **37** (0.014 g; 0.08 mmol; 1.0 eq.), were dissolved in THF (1.0 mL) and $H_2O$ (1.0 mL). $CuSO_4{\cdot}H_2O$ (1.4 mg; 8 µmol; 10 mol%), and sodium-L-ascorbate (0.8 mg; 4 µmol; 5 mol%) were added, and the reaction mixture was stirred for 16 h at room temperature. The orange precipitate was filtrated on Buchner funnel obtaining the desired product **38** as an orange solid (0.029g; 0.064 mmol; 80%).$^1$H NMR (400 MHz, $CDCl_3$) δ(ppm)= 8.15 – 8.08 (m, 1H), 8.07-7.97 (m, 1H), 7.84 (d, *J*=7.4 Hz, 1H), 7.68 (d, *J*=8.1 Hz, 2H), 7.61 (d, *J*=6.8 Hz, 1H), 7.58 – 7.49 (m, 2H), 7.48 (d, *J*=4.8 Hz, 1H), 7.23-7.19 (m, 1H), 6.08 (s, 2H). $^{13}$C NMR (101 MHz, $CDCl_3$) δ(ppm)= 155.43, 153.60, 148.05, 140.65, 132.10, 130.32, 129.40, 128.67, 128.30, 128.21, 128.12, 127.82, 127.32, 127.24, 125.36, 123.10, 51.55. ESI-MS: m/z = 375.32, 376,28 $[M]^+$

4-((4-(4-(7-(4,4,5,5-tetramethyl-1,3,2-dioxaborolan-2-yl)-2,3,3a,8b-tetrahydrocyclopenta[b]indol-4(1H)-yl)phenyl)-1H-1,2,3-triazol-1-yl)methyl)-7-(thiophen-2-yl)benzo[c][1,2,5]thiadiazole (**42**)

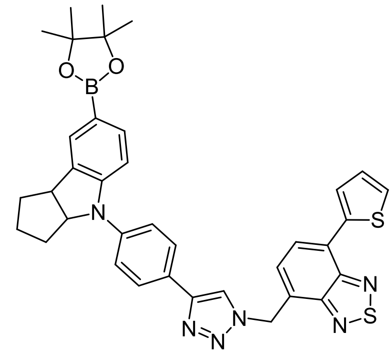

Alkyne **40** (0.021 g; 0.054 mmol; 1.0 eq.), azide **35** (0.015 mg; 0.054 mmol; 1.0 eq.), were dissolved in THF (1.0 mL) and $H_2O$ (1.0 mL). $CuSO_4{\cdot}H_2O$ (0.43 mg; 2.7 µmol; 5 mol%), sodium-L-ascorbate (1.08 mg; 5.23 µmol; 10 mol%) were added and the reaction mixture was stirred for 16 h at room temperature. The solution was diluted with $H_2O$ (3.0 mL) and extracted with DCM (3.0 mL). The organic phase was dried over $Na_2SO_4$ and the solvent was removed under reduced pressure. The crude was purified by flash chromatography ($SiO_2$, Petroleum Ether: EtOAc 8:1), obtaining compound **42** as an orange oil (0.032 g; 0.048 mmol; 90%).$^1$H NMR (400 MHz, $CDCl_3$): δ(ppm)= 8.10 (dd, *J*=3.7 Hz, 0.9 Hz, 1H), 7.97 (s, *J*=12.3, 1H), 7.82 (d, *J*=7.3 Hz, 1H), 7.78 (d, *J*=8.4

Hz, 2H), 7.60 – 7.53 (m, 3H), 7.47 (dd, *J*=5.0 Hz, 0.8 Hz, 1H), 7.31 (d, *J*=8.5 Hz, 2H), 7.20 (dd, *J*=5.0 Hz, 3.8 Hz, 1H), 6.99 (d, *J*=8.0 Hz, 1H), 6.08 (s, 2H), 4.83 – 4.76 (m, 1H), 3.81 (t, *J*=7.6 Hz, 1H), 2.03 – 1.97 (m, 1H), 1.96 – 1.74 (m, 3H), 1.70 – 1.56 (m, 1H), 1.56 – 1.40 (m, 1H), 1.33 (s, *J*=2.1 Hz, 12H). $^{13}$C NMR (101 MHz, $CDCl_3$): δ(ppm)= 154.18, 152.40, 149.72, 147.91, 142.86, 138.82, 135.15, 134.63, 131.31, 129.72, 128,44, 128.38, 128.26, 127.61, 126.86, 126.01, 125.39, 123.38, 120.05, 119.67, 118.57, 107.75, 83.47, 68.90, 50.70, 45.32, 34.95, 33.92, 25.09, 24.93, 24.74, 24.55. ESI-MS: m/z = 659.04 $[M]^+$

4-(2',6'-bis(octyloxy)-[1,1'-biphenyl]-4-yl)-6-(7-(4-(4-(1-((7-(thiophen-2-yl)benzo[c][1,2,5]thiadiazol-4-yl)methyl)-1H-1,2,3-triazol-4-yl)phenyl)-1,2,3,3a,4,8b-hexahydrocyclopenta[b]indol-7-yl)benzo[c][1,2,5]thiadiazol-4-yl)-4H-dithieno[3,2-b:2',3'-d]pyrrole-2-carbaldehyde (**43**)

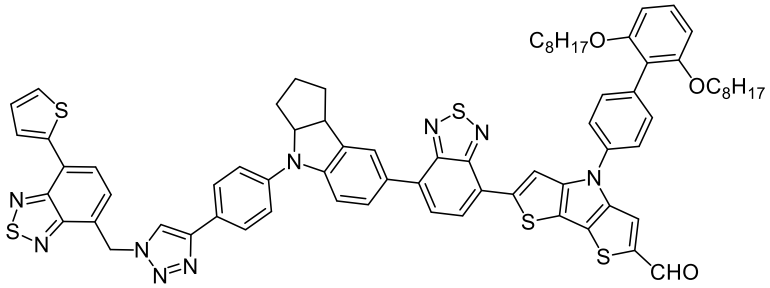

In a Schlenk tube, bromide **4** (0.036 g; 0.043 mmol; 1.0 eq.), boronic ester **42** (0.032 g; 0.048 mmol; 1.12 eq.), $Pd(dba)_3 \cdot CHCl_3$ (1.4 mg; 1.3 µmol; 3.0 mol%), XPhos (1.4 mg; 3.0 µmol; 7.0 mol%), $K_3PO_4$ (0.028 g; 0.13 mmol; 3.0 eq.) were dissolved in anhydrous toluene (2.5 mL) and $H_2O$ (0.3 mL); the reaction mixture was heated at 95 °C and stirred for 24 h under nitrogen atmosphere. The mixture was diluted with $H_2O$ (20 mL) and extracted with DCM (30 mL × 2). The organic phase was dried over $Na_2SO_4$ and the solvent was removed under reduced pressure. The crude was purified by flash chromatography ($SiO_2$, petroleum ether: EtOAc 5:1) giving **43** as a purple solid (0.014 g; 0.0109 mmol; 25%).$^1$H NMR (400 MHz, THF-$d_8$): δ(ppm)= 9.89 (s, 1H), 8.57 (s, 1H), 8.24 (s, 1H), 8.19 (d, *J*=3.1 Hz, 1H), 8.08 (d, *J*=7.6 Hz, 1H), 8.04 (s, 1H), 7.98 – 7.93 (m, 2H), 7.88 – 7.83 (m, 3H), 7.79 (d, *J*=7.9 Hz, 1H), 7.76 (d, *J*=8.5 Hz, 2H), 7.65 (d, *J*=8.4 Hz, 2H), 7.56 (d, *J*=4.7 Hz, 1H), 7.53 (d, *J*=7.4 Hz, 1H), 7.39 (d, *J*=8.5 Hz, 2H), 7.24 (t, *J*=8.3 Hz, 1H), 7.19 – 7.17 (m, 1H), 7.14 (d, *J*=8.4 Hz, 1H), 6.72 (d, *J*=8.4 Hz, 2H), 6.12 (s, 2H), 5.01 – 4.88 (m, 1H), 4.01 – 3.91 (m, 5H), 2.19 – 1.85 (m, 6H), 1.62 – 1.47 (m, 4H), 1.26 – 1.08 (m, 20H), 0.74 (t, *J*=6.8 Hz, 6H).$^{13}$C NMR (101 MHz, THF-$d_8$): δ(ppm)= 183.14, 158.35, 155.27, 155.13, 153.86, 153.22, 149.14, 148.56, 148.31, 144.85, 143.50, 143.30, 143.08, 139.98, 137.99, 136.62, 134.61, 134.58, 134.10, 130.01, 129.90, 128.99, 128.78, 128.64, 128.49, 128.36, 127.32, 127.02, 126.94, 126.70, 126.20, 126.07, 126.00, 124.95, 122.44, 122.09, 121.05, 120.98, 120.25, 120.17, 119.96, 118.12, 113.36, 108.99, 106.29, 70.04, 69.41, 50.74, 46.54, 36.08, 34.82, 32.92, 30.81, 30.42, 30.36, 30.29, 27.16, 23.65, 14.52. ESI-MS: m/z = 1279$[M]^+$

4-(2',6'-bis(octyloxy)-[1,1'-biphenyl]-4-yl)-6-(7-(4-(4-(1-((7-(thiophen-2-yl)benzo[c][1,2,5]thiadiazol-4-yl)methyl)-1H-1,2,3-triazol-4-yl)phenyl)-1,2,3,3a,4,8b-hexahydrocyclopenta[b]indol-7-yl)benzo[c][1,2,5]thiadiazol-4-yl)-4H-dithieno[3,2-b:2',3'-d]pyrrol-2-yl)-2-cyanoacrylic acid (**DYAD2**)

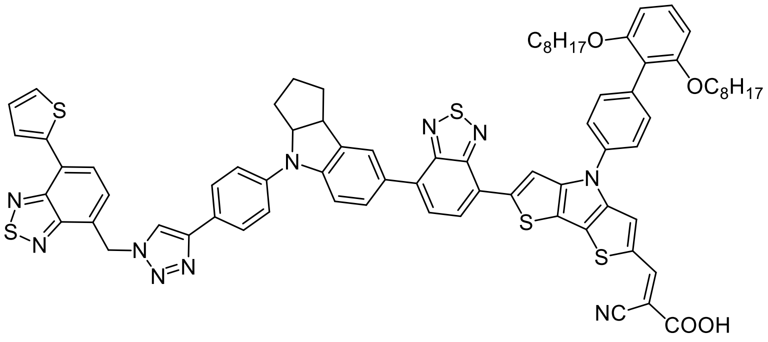

In a Schlenk tube, aldehyde **43** (0.014 g; 0.011 mmol; 1.0 eq.) was dissolved in toluene (2 mL) under inert nitrogen atmosphere. Ammonium acetate (1.2 mg; 0.016 mmol; 1.5 eq.), cyanoacetic acid (4.6 mg; 0.054 mmol; 5.0 eq.) and acetic acid (0.5 mL) were then added; the reaction mixture was stirred for 24h at 115°C. After that, a solution of HCl 0.03M was added, the organic phase was extracted with DCM (10 mL), dried over $Na_2SO_4$ and the solvent was removed under reduced pressure. The desired product **DYAD2** was obtained as a purple solid (0.013 g; 0.0096 mmol; 87%).$^1$H NMR (400 MHz, THF-d$_8$): δ(ppm)= 8.58 (s, 1H), 8.40 (s, 1H), 8.25 (s, 1H), 8.19 (s, 1H), 8.10 (d, *J*=7.3 Hz, 1H), 8.05 (s, 1H), 7.98 – 7.93 (m, 2H), 7.88 – 7.83 (m, 3H), 7.79 (d, *J*=8.0 Hz, 1H), 7.76 (d, *J*=7.8 Hz, 2H), 7.65 (d, *J*=7.9 Hz, 2H), 7.57 (d, *J*=4.4 Hz, 1H), 7.53 (d, *J*=6.7 Hz, 1H), 7.39 (d, *J*=8.1 Hz, 2H), 7.27 – 7.21 (m, 1H), 7.20 – 7.16 (m, 1H), 7.13 (d, *J*=8.6 Hz, 1H), 6.71 (d, *J*=8.4 Hz, 2H), 6.12 (s, 2H), 5.04 – 4.86 (m, 1H), 3.99 – 3.91 (m, 5H), 2.22 – 2.02 (m, 2H), 1.93 – 1.82 (m, 4H), 1.60 – 1.47 (m, 4H), 1.23 – 1.11 (m, 20H), 0.77 – 0.72 (m, 6H). $^{13}$C NMR (101 MHz, THF-d$_8$): δ(ppm)= 164.39, 158.00, 154.92, 154.78, 153.51, 152.88, 149.34, 148.25, 148.01, 147.95, 147.65, 144.83, 144.13, 142.94, 139.62, 137.56, 136.27, 134.36, 134.30, 133.75, 129.68, 129.54, 128.63, 128.42, 128.29, 128.13, 128.01, 126.97, 126.84, 126.58, 126.36, 125.85, 125.68, 124.48, 122.39, 122.02, 120.64, 119.95, 119.94, 119.65, 117.89, 117.05, 113.00, 108.63, 105.98, 69.70, 69.10, 50.38, 46.18, 35.72, 34.46, 32.55, 30.44, 30.06, 29.98, 29.91, 26.79, 23.28, 14.15. ESI-MS: m/z = 1243,42[M]$^+$

# References

[1] D. S. Pillai, V. Shabunko, A. Krishna, *Renewable and Sustainable Energy Reviews* **2022**, *156*, 111946.

[2] J. M. Kroon, N. J. Bakker, H. J. P. Smit, P. Liska, K. R. Thampi, P. Wang, S. M. Zakeeruddin, M. Grätzel, A. Hinsch, S. Hore, U. Würfe, R. Sastrawan, J. R. Durrant, E. Palomares, H. Pettersson, T. Gruszecki, J. Walter, K. Skupien, G. E. Tulloch, *Progress in Photovoltaics: Research and Applications* **2007**, *15*, 1–18.

[3] A. Mihi, M. E. Calvo, J. A. Anta, H. Míguez, *Journal of Physical Chemistry C* **2008**, *112*, 13–17.

[4] A. Mihi, F. J. López-Alcaraz, H. Míguez, *Appl Phys Lett* **2006**, *88*, 193110.

[5] J. H. Yum, E. Baranoff, S. Wenger, M. K. Nazeeruddin, M. Grätzel, *Energy Environ Sci* **2011**, *4*, 842–857.

[6] R. Ide, Y. Fujimori, Y. Tsuji, T. Higashino, H. Imahori, H. Ishikawa, A. Imanishi, K. I. Fukui, M. Nakamura, N. Hoshi, *ACS Omega* **2017**, *2*, 128–135.

[7] N. V. Krishna, J. V. S. Krishna, M. Mrinalini, S. Prasanthkumar, L. Giribabu, *ChemSusChem* **2017**, *10*, 4668–4689.

[8] J. Warnan, F. Buchet, Y. Pellegrin, E. Blart, F. Odobel, *Org Lett* **2011**, *13*, 3944–3947.

[9] F. Odobel, H. Zabri, *Inorg Chem* **2005**, *44*, 5600–5611.

[10] G. McDermott, S. M. Prince, A. A. Freer, A. M. Hawthornthwaite-Lawless, M. Z. Papiz, R. J. Cogdell, N. W. Isaacs, *Nature* **1995**, *374*, 517–521.

[11] A. Arrigo, G. la Ganga, F. Nastasi, S. Serroni, A. Santoro, M. P. Santoni, M. Galletta, S. Campagna, F. Puntoriero, *Comptes Rendus Chimie* **2017**, *20*, 209–220.

[12] M. S. Choi, T. Aida, T. Yamazaki, I. Yamazaki, *Chemistry - A European Journal* **2002**, *8*, 2667–2678.

[13] J. I. Basham, G. K. Mor, C. A. Grimes, *ACS Nano* **2010**, *4*, 1253–1258.

[14] P. R. Selvin, *Methods Enzymol* **1995**, *246*, 300–334.

[15] K. Shankar, X. Feng, C. A. Grimes, *ACS Nano* **2009**, *3*, 788–794.

[16] J. A. Broussard, K. J. Green, *Journal of Investigative Dermatology* **2017**, *137*, e185–e191.

[17] G. Rougon, S. Brasselet, F. Debarbieux, *Brain Plasticity* **2016**, *2*, 31–48.

[18] B. Zhang, G. Lyu, E. A. Kelly, R. C. Evans, *Advanced Science* **2022**, *9*, 2201160.

[19] N. Cai, J. Zhang, M. Xu, M. Zhang, P. Wang, *Adv Funct Mater* **2013**, *23*, 3539–3547.

[20] M. T. Efa, J. C. Huang, T. Imae, *Nanomaterials* **2022**, *12*, 4085.

[21] B. E. Hardin, E. T. Hoke, P. B. Armstrong, J. H. Yum, P. Comte, T. Torres, J. M. J. Fréchet, M. K. Nazeeruddin, M. Grätzel, M. D. McGehee, *Nat Photonics* **2009**, *3*, 406–411.

[22] G. K. Mor, J. Basham, M. Paulose, S. Kim, O. K. Varghese, A. Vaish, S. Yoriya, C. A. Grimes, *Nano Lett* **2010**, *10*, 2387–2394.

[23] J. H. Cheon, S. A. Kim, K.-S. Ahn, M.-S. Kang, J. H. Kim, *Electrochim Acta* **2012**, *68*, 240–245.

[24] N. Humphry-Baker, K. Driscoll, A. Rao, T. Torres, H. J. Snaith, R. H. Friend, *Nano Lett* **2012**, *12*, 634–639.

[25] J. Warnan, Y. Pellegrin, E. Blart, F. Odobel, *Chemical Communications* **2012**, *48*, 675–677.

[26] B. Louahem M'Sabah, M. Boucharef, J. Warnan, Y. Pellegrin, E. Blart, B. Lucas, F. Odobel, J. Bouclé, *Physical Chemistry Chemical Physics* **2015**, *17*, 9910–9918.

[27] H. Choi, N. Cho, S. Paek, J. Ko, *Journal of Physical Chemistry C* **2014**, *118*, 16319–16327.

[28] H. C. Kolb, M. G. Finn, K. B. Sharpless, *Angewandte Chemie - International Edition* **2001**, *40*, 2004–2021.

[29] E. Haldón, M. C. Nicasio, P. J. Pérez, *Org Biomol Chem* **2015**, *13*, 9528–9550.

[30] C. W. Tornøe, C. Christensen, M. Meldal, *Journal of Organic Chemistry* **2002**, *67*, 3057–3064.

[31] R. Huisgen, *Angew. Chem. Int. Ed. Engl.* **1963**, *2*, 565–598.

[32] Y. Wu, M. Marszalek, S. M. Zakeeruddin, Q. Zhang, H. Tian, M. Grätzel, W. Zhu, *Energy Environ Sci* **2012**, *5*, 8261–8272.

[33] Yen YS, Lee CT, Hsu CY, Chou HH, Chen YC, Lin JT, *Chem Asian J.* **2013**, *8*, 809–816.

[34] C. Yang, T. Liu, P. Song, F. Ma, Y. Li, *J Mol Liq* **2022**, 120797.

[35] W. Li, Y. Wu, Q. Zhang, H. Tian, W. Zhu, *ACS Appl Mater Interfaces* **2012**, *4*, 1822–1830.

[36] Y. Wu, W. H. Zhu, S. M. Zakeeruddin, M. Grätzel, *ACS Appl Mater Interfaces* **2015**, *7*, 9307–9318.

[37] Y. Wu, W. Zhu, *Chem Soc Rev* **2013**, *42*, 2039–2058.

[38] A. Dessì, D. A. Chalkias, S. Bilancia, A. Sinicropi, M. Calamante, A. Mordini, A. Karavioti, E. Stathatos, L. Zani, G. Reginato, *Sustain Energy Fuels* **2021**, *5*, 1171–1183.

[39] A. Dessì, M. Calamante, A. Sinicropi, M. L. Parisi, L. Vesce, P. Mariani, B. Taheri, M. Ciocca, A. di Carlo, L. Zani, A. Mordini, G. Reginato, *Sustain Energy Fuels* **2020**, *4*, 2309–2321.

[40] Y. Xie, W. Wu, H. Zhu, J. Liu, W. Zhang, H. Tian, W. H. Zhu, *Chem Sci* **2016**, *7*, 544–549.

[41] C. C. C. Johansson Seechurn, A. Deangelis, T. J. Colacot, *RSC Catalysis Series* **2015**, 1–19.

[42] L. Zani, A. Dessì, D. Franchi, M. Calamante, G. Reginato, A. Mordini, *Coord Chem Rev* **2019**, *392*, 177–236.

[43] F. Popowycz, E. Métay, M. Lemaire, *Comptes Rendus Chimie* **2011**, *14*, 621–628.

[44] S. D. Walker, T. E. Barder, J. R. Martinelli, S. L. Buchwald, *Angewandte Chemie International Edition* **2004**, *43*, 1871–1876.

[45] Y. F. Zhang, Z. J. Shi, *Acc Chem Res* **2019**, *52*, 161–169.

[46] L. Ackermann, *Chem Rev* **2011**, *111*, 1315–1345.

[47] A. Zapf, A. Ehrentraut, M. Beller, *Angewandte Chemie - International Edition* **2000**, *39*, 4153–4155.

[48] C. Li, L. Luo, D. Wu, R. Jiang, J. Lan, R. Wang, L. Huang, S. Yang, J. You, *J Mater Chem A Mater* **2016**, *4*, 11829–11834.

[49] J. Tauc, *Mater Res Bull* **1968**, *3*, 37–46.

[50] M. Wang, C. Grätzel, S. M. Zakeeruddin, M. Grätzel, *Energy Environ Sci* **2012**, *5*, 9394–9405.

[51] H. Iftikhar, G. G. Sonai, S. G. Hashmi, A. F. Nogueira, P. D. Lund, *Materials* **2019**, *12*, 1998.

[52] A. Hagfeldt, G. Boschloo, L. Sun, L. Kloo, H. Pettersson, *Chem Rev* **2010**, *110*, 6595–6663.

[53] A. Iagatti, B. Patrizi, A. Basagni, A. Marcelli, A. Alessi, S. Zanardi, R. Fusco, M. Salvalaggio, L. Bussotti, P. Foggi, *Physical Chemistry Chemical Physics* **2017**, *19*, 13604–13613.

[54] K. C. Nicolaou, P. G. Bulger, D. Sarlah, *Angewandte Chemie - International Edition* **2005**, *44*, 4442–4489.

[55] S. Müller, B. Liepold, G. J. Roth, H. J. Bestmann, *Synlett* **1996**, *1996*, 521–522.

[56] J. Godoy, V. García-López, L. Y. Wang, S. Rondeau-Gagné, S. Link, A. A. Martí, J. M. Tour, *Tetrahedron* **2015**, *71*, 5965–5972.

[57] S. Pramanik, P. Ghorai, *Org Lett* **2014**, *16*, 2104–2107.

[58] D. Luvino, C. Amalric, M. Smietana, J. J. Vasseur, *Synlett* **2007**, 3037–3041.

[59] D. G. Brown, E. J. Velthuisen, J. R. Commerford, R. G. Brisbois, Thomas R. Hoye, *J Org Chem* **1996**, *61*, 2540–2541.

# Chapter 3

# Testing novel combinations of organic dyes with copper-based electrolytes in dye-sensitized solar cells

## 3.1. Introduction

As mentioned in the introduction (see paragraph 1.7.) the goal of this part of the work was to test a series of organic photosensitizers prepared by our research group in Dye-Sensitized Solar Cells designed to work with copper-based electrolytes. The activity was carried out during a four-month internship spent in the research group of Prof. Marina Freitag (Newcastle University) during May-August 2022.

To this end, three organic D-A-π-A or D-π-A dyes were selected (Figure 3.1). The first compound was **RI-114**, that was already described in paragraph 2.2.2., and was used as a reference compound for the preparation of the antenna/sensitizer dyad. The spectroscopic and electrochemical characterization of the dye confirmed in fact that it was suitable for application in DSSC, and thus it was tested in cells for the first time. Two further dyes were then selected, which had already provided excellent performances when used in combination with iodide/triiodide-based electrolytes. The first one was compound **BTD-DTP2,** having the same π-scaffold as **RI114** but with a triphenylamine, instead of an indoline, donor group. This dye was characterized by an intense and wide absorption in the visible region of the spectrum, which allowed to fabricate DSSCs with a maximum power conversion efficiency of 8.60% under simulated solar light.[1] The second dye was instead **TTZ5**,[2] presenting a totally different structure from **BTD-DTP2**, characterized by the presence of a thiazolo[5,4-*d*]thiazole-based conjugated scaffold and thiohexyl substituents on the triarylamine donor group. Thanks to its structural features, **TTZ5** exhibited an extremely high molar attenuation coefficient in solution (> $9.0 \times 10^4$ $M^{-1}$ $cm^{-1}$), providing lab-scale DSSCs with a maximum efficiency of 7.71% and excellent stability.[3] In addition, it was also recently applied for the fabrication of scaled-up semi-transparent modules and panels of up to 0.36 $m^2$ active surface area.[4]

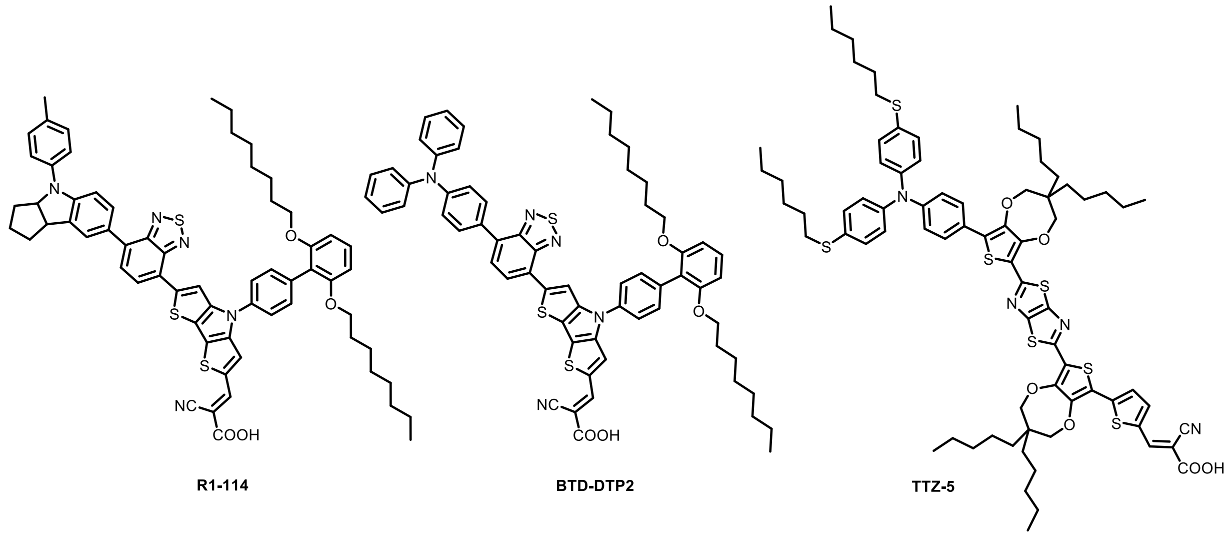

Figure 3.1*: structure of dyes **RI114, BTD-DTP2** and **TTZ5**.*

In this work, the three dyes were assessed in solar cells in combination with three copper redox mediators originally introduced by Freitag group,[5,6] which are currently considered among the best candidates to act as redox electrolytes for indoor DSSC applications.[7]

Besides using the selected dyes as individual sensitizers, during the research activity a co-sensitization approach was also explored by combining them with other metal-free sensitizers previously reported in the literature, with the aim to expand the light absorption range of the photoanodes and thus improve the performances of the resulting cells.[8] As such, the co-sensitization strategy appears perfectly complementary to the construction of FRET-molecular dyads described in the previous chapter, since both are aimed at enhancing photocurrents by increasing the light-harvesting efficiency (LHE) parameter of DSSCs.

To provide the relevant background of this research, the concept of DSSC application for indoor photovoltaics will be presented in the following section. Then, as mentioned in the introduction (see paragraph 1.4.4.), a general discussion on the advantages and drawbacks of the different classes of electrolytes used in DSSCs will be presented, focusing in particular on the case of the copper-based species used in this work.

## 3.2. Dye-sensitized solar cells under ambient light for the Internet of Things (IoT)

The Internet of Thing (IoT) is based on the idea of interconnected "intelligent" objects that can exchange the information they own, collect and/or process. Such networks of autonomous intelligent sensing devices are poised to promote information exchange in smart homes, offices, cities, and factories.[9] They will collect, communicate, and process real-time data to optimize services and manufacturing processes, as well as to manage resources to reduce our energy consumption. IoTs need to become autonomous, which requires a local power source with little or no maintenance.[10] It is argued that many aspects of our lives will be mediated by 75 billion IoT devices by 2025, most of which will reside indoors. To date, most small electronic wireless devices are powered by traditional batteries, making a more sustainable indoor power source urgently needed (Figure 3.2). Common ambient light sources ($2 \times 10^2$-$10^3$ lux) are around two or three orders of magnitude weaker than sunlight (approx. $10^5$ lux). Nevertheless, diffuse ambient light provides universally available energy, which remains otherwise unused. Owing to a narrower spectral distribution, energy may be harvested from ambient light with higher efficiency than sunlight.[9] DSSC are the technology of choice for indoor applications, given their high photovoltages, even under low-light conditions, and great adaptability. The potential to match a variety of light sources using a range of different dyes makes DSSCs a unique technology for most indoor settings, with efficiencies beyond 34% already demonstrated.[11] Thanks to such high power conversion efficiencies, the power output obtained under low light illumination can thus be sufficient to power a range of wireless devices, including those designed for IoT applications.

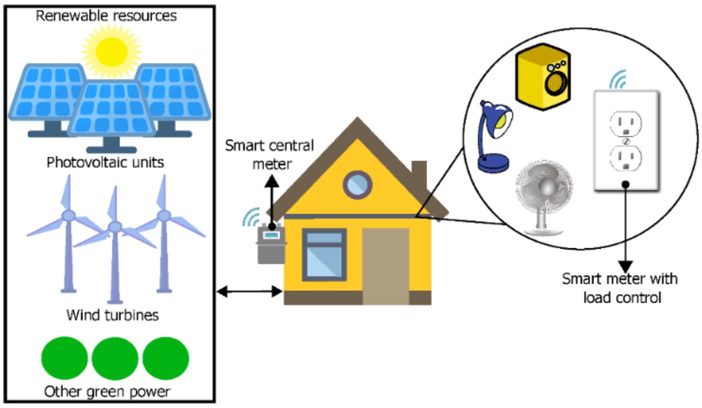

Figure 3.2: *the green energy power in the "Internet of Things"*

In 2016-7, the field of DSSCs experienced a significant push towards indoor applications thanks to the introduction of new copper-based electrolytes which clearly outperformed the traditional iodide/triiodide redox mediators.[6,7] In the following paragraph, the main advantages and drawbacks of the main electrolyte classes for DSSCs will be briefly examined, focusing in particular on the use of copper-containing redox shuttles for indoor application.

## 3.3. DSSC redox mediators: main classes and properties

In paragraph 1.4.4. it was described how the charge transport materials (CTMs) are an essential part of DSSC technology; indeed, some of the most significant advances of the past decade in terms of cells efficiency and stability were achieved through progress made on this component. Initially, and for a long time, DSSCs included an iodide/triiodide redox mediator.[12] The $I^-/I_3^-$ redox couple fulfills several of the requirements of an ideal electrolyte, presenting a suitable redox potential for the regeneration of most dyes ($E^0$ = +0.35 V *vs.* NHE),[12] small molecular size for high diffusion, good solubility in a wide range of solvents at high concentration for high conductivity, and good stability. However, it also has several drawbacks, such as a substantial light absorption in the 400–500 nm range of the solar spectrum (interfering with the sensitizer absorption), the corrosivity towards several components of DSSCs including the materials used for counter electrodes and sealing, and the possible iodine diffusion out of the electrolyte stemming from its high vapor pressure. Furthermore, using the $I^-/I_3^-$ redox couple, a very large driving force of over 0.5 V is required for dye regeneration, due to the two-electron oxidation mechanism necessary for the conversion of $I^-$ to $I_3^-$.[13] Since the overall efficiency of a solar cell scales directly with its $V_{OC}$, which is in turn dictated by the difference between the Fermi level of the anodic semiconductor and the redox potential of the electrolyte, this large driving force constitutes a significant limitation of the $I^-/I_3^-$ redox couple.[14] As a consequence, the search for alternative redox mediators was initiated in the early 2000's,[15] concentrating in particular on transition metal (TM) coordination complexes, due to their favorable properties. Indeed, many TM complexes present characteristics suitable for employment in DSSCs, having reversible electrochemical properties, structural tunability, and more positive redox potential values, reduced visible light absorption and superior stability compared to $I^-/I_3^-$.[16] Moreover, their electronic properties and redox chemistry can be readily adjusted by altering the central metal cation or, most importantly, the ligands. Since many ligands can stabilize metal centers in two consecutive oxidation states, such approach offers access to one-electron redox systems with widely tunable potentials.The two most studied classes of TM complexes in the context of DSSC application are surely cobalt (II/III) and copper (I/II) complexes with nitrogen-based ligands. Their properties will be briefly discussed below.

## 3.3.1. Cobalt coordination complexes

Tridentate (e.g. terpyridines) and bidentate (e.g. bipyridines and phenanthrolines) ligands form octahedral coordination complexes with cobalt (II/III), which has been extensively exploited for the preparation of DSSC redox mediators.[17] Generally, cobalt redox mediators have beneficial characteristics, such as non-volatility, non-corrosiveness and light-coloration for less light absorption. In addition, through the alteration of ligands they can achieve a widely variable electric potential window (0.3−0.9 V, figure 3.3).[18]

Nevertheless, in initial trials, employment of *bis*[2,6-*bis*(1‘-butylbenzimidazol-2‘-yl)pyridine]cobalt(II) complex ($Co(dbbip)_2^{2+}$) as redox shuttle (Figure 3.3) in combination with a Ru-based dye (**Z316**) yielded a very low PCE of no more than 2.2% under full sun illumination.[19]

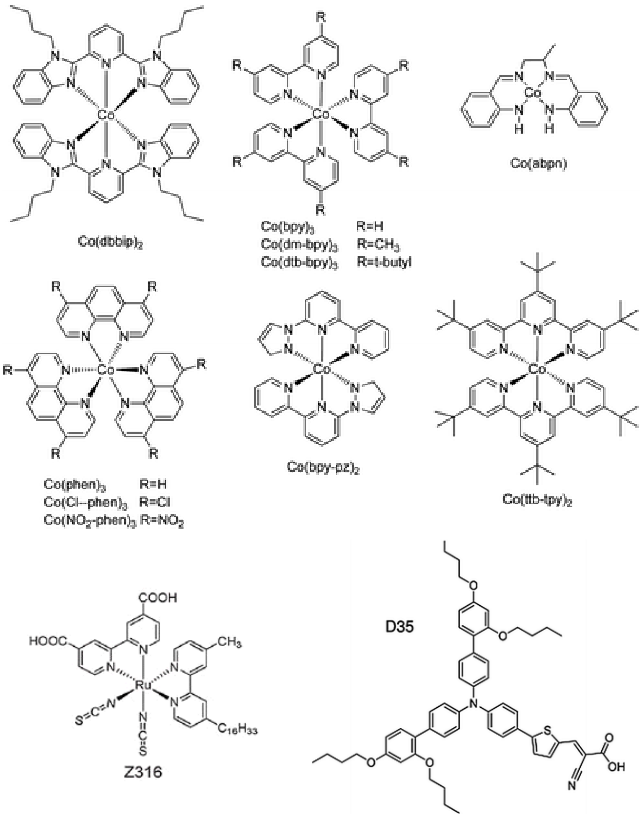

Figure 3.3*: structure of dyes* ***Z316*** *and* ***D35*** *and series of terpyridine, bipyridine, and phenanthroline complexes of cobalt(II).*

This low efficiency was later attributed to the naturally occurring fast recombination process of the conduction band electrons of $TiO_2$ with $Co^{3+}$ species.[18] In 2010, the Hagfeldt group achieved the first success in producing high-efficiency DSSCs with Co-based electrolytes by combining them with an organic dye bearing bulky alkyl chains on the donor group (**D35**). In this way, a *PCE* of 6.7% with an impressive $V_{oc}$ of 0.92 V was achieved under 1 Sun illumination with $Co(bpy)_3^{2+/3+}$ (Figure 3.3).[20] The key feature in this case was to reduce the recombination losses by placing the blocking hydrophobic groups on the sensitizing dyes, rather than, as in previous studies, on the Co-complexes. This approach allowed the use of non-substituted cobalt complexes with higher diffusion constants, resolving the issue of slow mass transport previously observed with some of these electrolytes.[21] Such results opened the way to the further enhancement of cell performances using these complexes, which became the mediators of choice with a wide array of metal-free organic and porphyrin sensitizers, achieving PCE values above 13%.[22,23]

Despite these remarkable results, some disadvantages of cobalt complexes remain. They have a large molecular size, sometimes leading to slow mass transport and diffusion, especially when employed in liquid electrolytes of higher viscosity. The large reorganization energies between the oxidation states of Co(II) and Co(III) increase the overall energy required to regenerate the dye, and their long-term stability is in question as the complexes in solution will likely undergo ligand exchange, which has to be structurally controlled.[24]

### 3.3.2. Copper coordination complexes

As alternative redox mediators, $Cu^{+/2+}$ complexes were recently demonstrated to outperform both iodine- and Co-based electrolytes in combination with various dyes, thanks to their lower reorganization energy and minimized overpotential losses.[25] The first example of the use of a Cu-based electrolyte in DSSC was reported by Hattori *et al.*, who achieved a maximum PCE of 1.4% using *bis*(2,9-dimethyl-1,10-phenantroline) copper(I/II) complexes ($[Cu(dmp)_2]^{+/2+}$)[26] (see Figure 3.4) in combination with a Ru-based dye. This result was later improved by Bai *et al.*,[27] who reached 7.0% PCE when employing the same redox couple in combination with organic dye **C218**, and then in 2015-16 by Freitag *et al.*, who achieved >8.0% PCE using the same Cu-complex together with D–π–A organic dye called **LEG4**, mostly due to a rather high open-circuit voltage of almost 1.1 V[5] (Figure 3.4). Building on these excellent results, a further leap forward was made by Freitag and co-workers when they introduced two new redox shuttles based on Cu-bipyridyl (rather than phenanthrolinyl) complexes, $[Cu(dmby)_2]^{+/2+}$ ($E^0$ = 0.97 V *vs.* NHE, dmby = 6,6’-dimethyl-2,2’ -bipyridine) and $[Cu(tmby)_2]^{+/2+}$ ($E^0$ = 0.87 V *vs.* NHE, tmby = 4,4’,6,6’-tetramethyl 2,2’ -bipyridine). When used in combination with organic sensitizer **Y123**, they achieved extremely efficient dye regeneration even at very low driving forces of 0.1 eV (see figure 3.4).[6] Thus, the corresponding DSSCs presented efficiencies exceeding 10% under 1000 W $m^2$ AM 1.5G illumination.

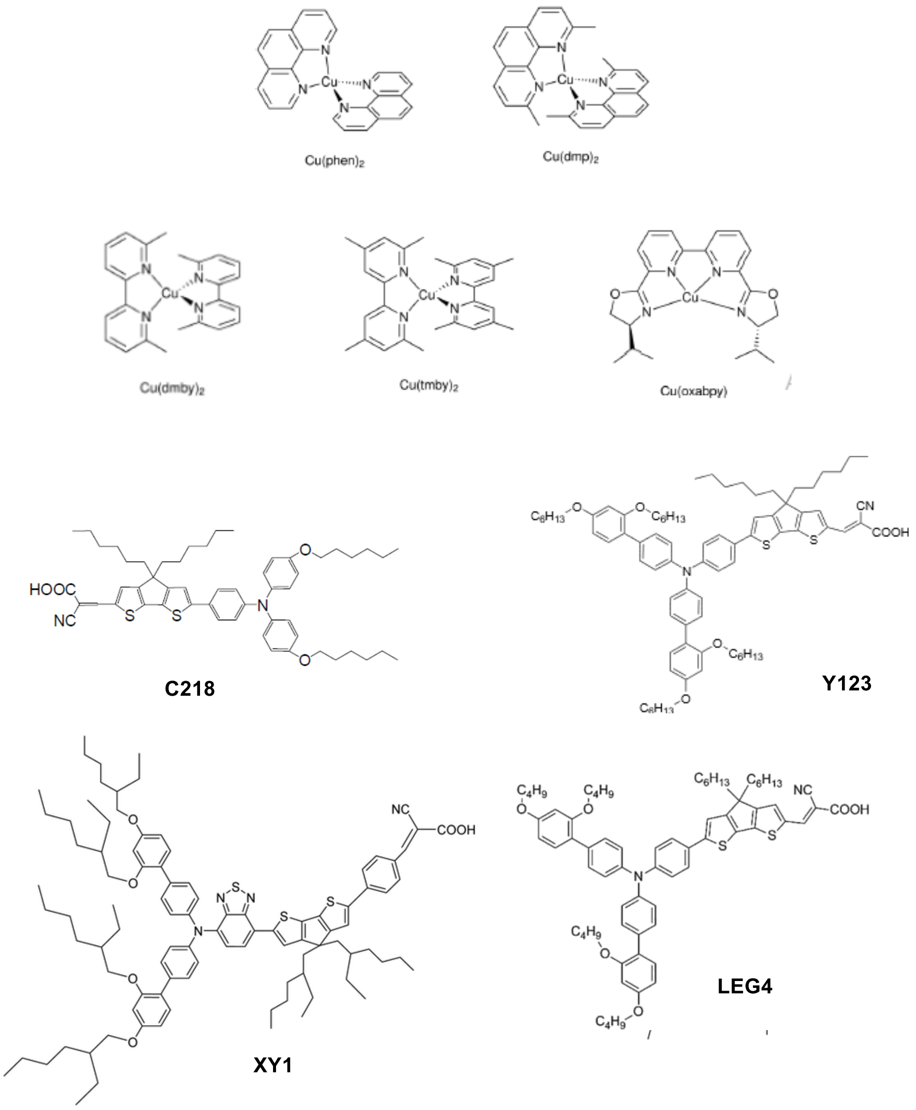

Figure 3.4*: chemical structures of copper coordination complexes-based redox mediators and dyes structures implemented in DSSCs.*

In 2020, Michaels *et al.* presented co-sensitized DSSCs, where the small organic dye **L1** was combined with bulky **XY1** dye to provide a PCE of 11.5% under 1 Sun illumination, and of 34.0% (with a $V_{OC}$ of 910 mV) under ambient lighting at an intensity of 1000 lux.[7] Recent results presented solid-state cells with improved PCEs up to 11.7% under full sun illumination, which was achieved thanks to the effective control of voltage losses by modulating the energy levels of the sensitizers and redox mediators, as well as the dye assembly on the $TiO_2$ surface.[28] Michaels *et al.* introduced new copper complexes as redox mediators with the tetradentate ligand 6,6'-*bis*(4-(*S*)-isopropyl-2-oxazolinyl)-2,2'-bipyridine [Cu(oxabpy)]$^{+/2+}$ (see Figure 3.4).[29] The ligand allowed to lock the complex in a square-planar geometry, leading to minimized reorganization energies. Gel electrolytes prepared with Cu(oxabpy)]$^{+/2+}$ complexes showed considerable enhancement of charge transport performances. Recently. Benesperi *et al.* introduced two further copper redox shuttles based on tetradentate ligands: 6,6'-*bis*(2,3,4-

trihydropyrrol-5-yl)-2,2'-bipyridine (Ctetra) and 6,6'-*bis*(4,5-dihydrothiazol-2-yl)-2,2'-bipyridine (Stetra) (Figure 3.5).[30]

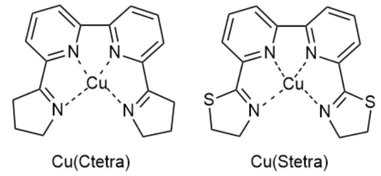

Figure 3.5*: chemical structures of Cu(Ctetra) and Cu(Stetra).*

It was found that copper complexes formed with the above ligands undergo a dynamic transition from dimers to monomers upon oxidation of the metal (Figure 3.6). Upon single electron oxidation of two Cu(I) dimers, these form mixed valence species that undergo disproportionation to form a stable Cu(I) dimer and two Cu(II) monomers. Reduction of the Cu(II) monomeric complexes into the corresponding Cu(I) species presents a high energy barrier, which prevents formation of the latter at the semiconductor/electrolyte and dye/electrolyte interfaces in Dye-Sensitized Solar Cells, thus reducing undesired charge recombination process in the device.[30] Therefore, it was concluded that these redox couples offer a novel combination of fast charge transport in a two-electron redox mechanism while inhibiting carrier recombination after disproportionation, simultaneously addressing transport limitations as well as recombination challenges in DSSCs, and giving devices with minimal voltage losses.

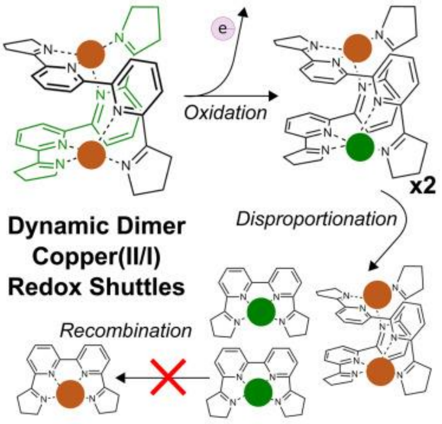

*Figure 3.6: mechanism of oxidation, disproportionation and recombination of dimeric tetradentate Cu(I)-complex* $Cu_2(Ctetra)_2$*. Cu(I), brown circles; Cu(II), green circles.*[30]

### 3.3.3. Optimization of the other cell components to work efficiently with TM-based electrolytes

The nature and composition of the various components making up a DSSC were originally established in view of their employment in combination with a $I^-/I_3^-$ redox couple. Due to the different properties of TM-based electrolytes, it has often proven necessary to assess again the individual components of the cells to reach optimal performances.

For example, introduction of additives into the redox electrolyte often plays an important role to enhance DSSC performances. Indeed, adding suitable chemical species to the electrolyte to fine-tune the semiconductor/electrolyte interface can be the simplest way to increase cell efficiencies without major composition or manufacturing adjustments.[14] Nitrogen heterocyclic compounds such as 4-*tert*-butylpyridine (*t*BP) and *N*-methylbenzimidazole (NMBI) are typically used in combination with TM-based electrolytes to inhibit the electron recombination and thus to improve the $V_{OC}$.[31] As such, they have also been used in the present work.

Another important component in DSSCs is surely the counter electrode (CE). As described in Paragraph 1.4.5., on the surface of the counter electrode the reduction of the oxidized form of the redox mediator takes place, which is necessary to close the electrical circuit and ensure the flow of electric current. Initial works with the $I^-/I_3^-$ redox shuttle relied almost exclusively on the use of expensive platinum catalyst as the CE. However, the latter was shown to be only moderately efficient[32] when used in conjunction with Co- or Cu-based metalorganic redox electrolytes, and thus has been progressively replaced by fully organic polymer counter electrodes, e.g. poly(3,4-ethylenedioxythiophene) (PEDOT).[33] In addition to good charge transport characteristic, PEDOT offers p-type selective carriers extraction, allowing to attach the counter electrode directly behind the scattering layer without the need of a spacing gasket to ensure an additional ion diffusion length.[34] This advantage was exploited also in this work (*see below*).

## 3.4. Selection of dyes and Cu-based redox shuttles

As mentioned above, in this part of the work, DSSCs were built using three organic dyes prepared by our research group in combination with three different copper electrolytes introduced by Freitag's group. This was particularly interesting as copper electrolytes were never used before with these dyes. Furthermore, in the devices construction a co-sensitization approach was also explored, using mixtures of the selected sensitizers with literature-known metal-free dyes in the sensitizing bath. In each case, the best combination of dye/copper-based mediator was chosen after evaluating the optoelectronic characteristics of the different dyes. In the following paragraph the optical proprieties and cyclic voltammetry analyses of the dyes are discussed. Those pertaining to dye **RI114** have already been presented in paragraph 2.2.3. but will be quickly recalled here for the readers' convenience. The data relative to dyes **BTD-DTP2**[1] and **TTZ5**[2,3] have been reported previously by the research group where this doctoral work was carried out.

### 3.4.1. Spectroscopic and electrochemical characterization of **RI114**, **BTD-DTP2** and **TTZ5** photosensitizers.

In THF solution, all dyes present relatively intense absorption spectra with maxima well-centered in the visible region of the spectrum in the 510-525 nm range (Table 3.1). The highest molar attenuation coefficient was recorded with dye **TTZ5** (>$9.0 \times 10^4$ $M^{-1}$ $cm^{-1}$), whereas **RI114** presented a much lower value of approx. $2.3 \times 10^4$ $M^{-1}$ $cm^{-1}$, which was nevertheless still higher than those usually provided by Ru-based sensitizers. Fluorescence emissions were relatively intense and presented maxima in the 573-656 nm range; by determining the intersection wavelength between the normalized absorption and emission spectra, or through the corresponding Tauc plots,[35] the zero-zero transition energy ($E_{0\text{-}0}$) of the dyes could be calculated, which was comprised in the 2.05-2.24 eV interval. Cyclic voltammetry measurements of the three dyes in THF (see Figures 3.7, 3.8 and 3.9) allowed to determine their ground state oxidation potentials ($E_{ox}$) which resulted of +1.08 V, +1.28 V and +0.91 V *vs.* NHE for **RI114**, **BTD-DTP2** and **TTZ5**, respectively. The excited states-oxidation potentials ($E^*_{ox}$) were calculated by subtracting the $E_{0\text{-}0}$ of the dyes from the corresponding $E_{ox}$. The values *vs.* NHE of −0.97 V for **RI114**, −0.83 for **BTD-DTP2** and −1.33 V for **TTZ5**, were largely more negative than the conduction band energy of $TiO_2$ (approx. −0.5 V vs. NHE), suggesting that a proper electron injection from the excited state of the dye to the semiconductor should take place during cell operation. These results confirmed that **RI114**, **BTD-DTP2** and **TTZ5** can be used as photosensitizers in DSSCs.

Table 3.1*: spectroscopic and electrochemical proprieties of dyes* **RI114***,* **BTD-DTP2** *and* **TTZ5**.

| Dye | $\lambda^{max}_{abs}$ [nm][a] | ε (x $10^4$) [$M^{-1}$ $cm^{-1}$][a] | $\lambda^{max}_{emi}$ [nm][a] | $E_{0\text{-}0}$ [eV][b] | $E_{OX}$ [V/NHE][c] | $E^*_{OX}$ [V/NHE][d] |
|---|---|---|---|---|---|---|
| **RI114** | 517 | 2.34 | 656 | 2.05 | 1.08 | −0.97 |
| **BTD-DTP2** | 525 | 4.97 | 640 | 2.11 | 1.28 | −0.83 |
| **TTZ5** | 510 | 9.41 | 573 | 2.24 | 0.91 | −1.33 |

*[a] Measured in THF solution; [b] Determined from the wavelength of intersection between the normalized absorption and emission spectra, or by calculation of the corresponding Tauc plot;[35] [c] Potential vs NHE measured in THF solution with ferrocene as internal standard and assuming a reduction potential of +0.788 V for the $Fc^+/Fc$ couple vs. NHE; [d] calculated from the equation: $E^*_{ox} = E_{ox} - E_{0\text{-}0}$.*

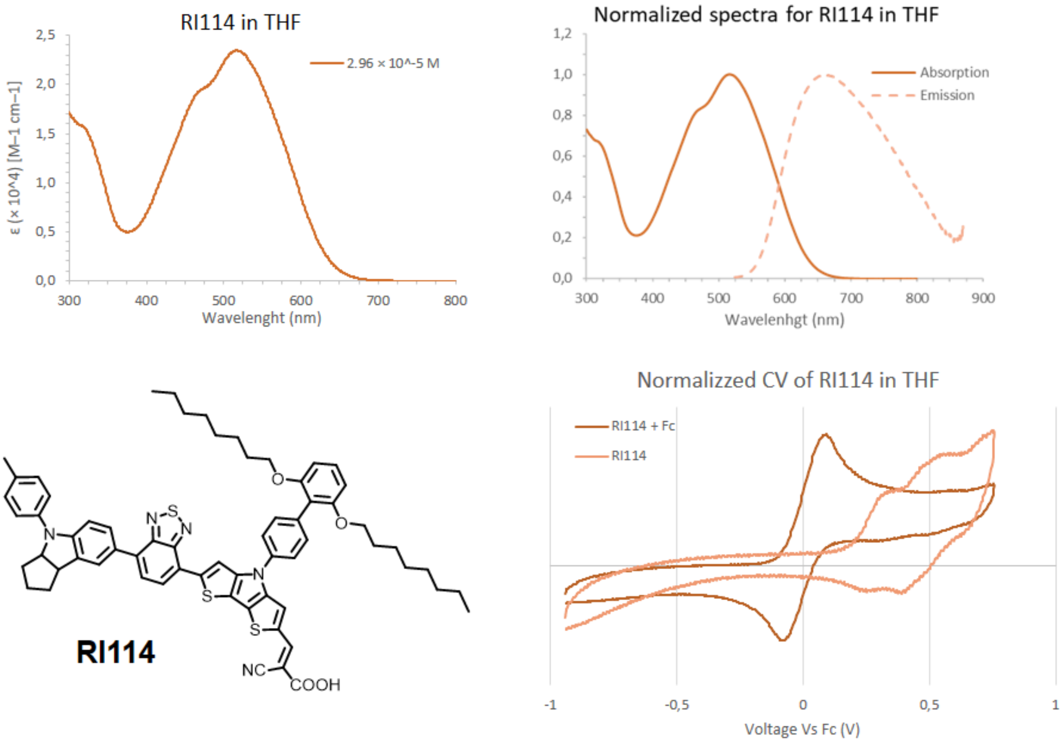

Figure 3.7: *UV-Vis absorption and emission spectra, and cyclic voltammetry of dye* ***RI114***.

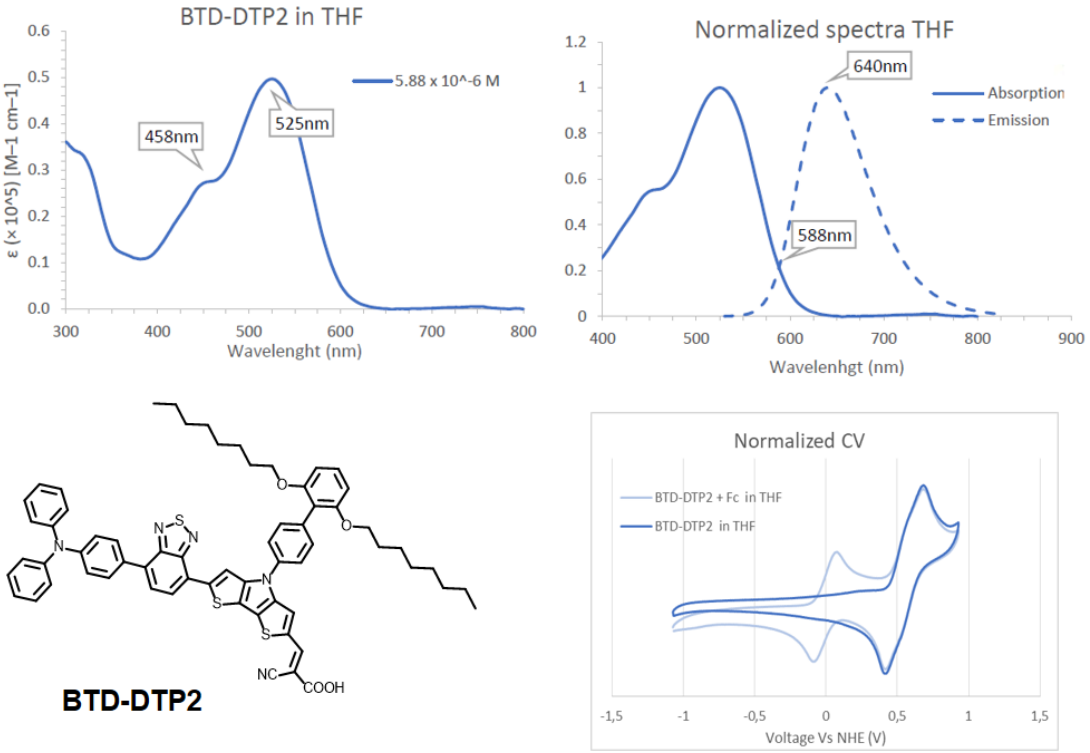

Figure 3.8: *UV-Vis absorption and emission spectra, and cyclic voltammetry of dye* ***BTD-DTP2***.

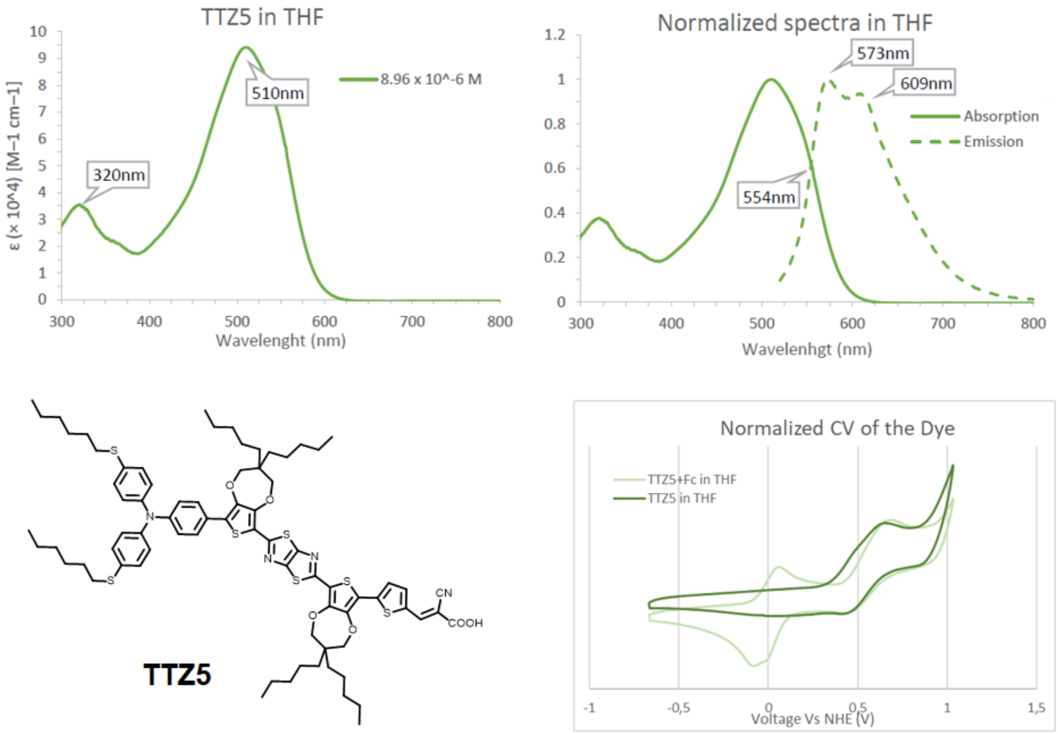

Figure 3.9: *UV-Vis absorption and emission spectra, and cyclic voltammetry of dye* **TTZ5**.

### 3.4.2. Copper electrolytes: Cu(tmby)$_2$, Cu(dmby)$_2$ and Cu(Stetra)

Based on the electrochemical and spectroscopic properties of the three chosen photosensitizers, three copper-based electrolytes previously introduced by Freitag's laboratory were selected to fabricate the photovoltaic devices: Cu(tmby)$_2$, Cu(dmby)$_2$ and Cu(Stetra) (Figure 3.4-3.5). Their oxidation potentials had been determined previously and are summarized in Figure 3.10.

As can be seen from the figure, Cu(tmby)$_2$ has a less positive oxidation potential than the E$_{ox}$ values of all three dyes (albeit with a seemingly very small driving force in the case of **TTZ5**) and was therefore tested in combination with all of them. Cu(dmby)$_2$, on the other hand, has a slightly more positive redox potential, which could result in cells with a higher photovoltage: however, it could also make dye regeneration more difficult, and therefore it was tested only with dye **BTD-DTP2**, which presented the most positive $E_{ox}$ value of the series, and should therefore be the easiest to reduce after photoexcitation and charge injection. Finally, Cu(Stetra) was investigated in combination with highly absorbing dye **TTZ5**, since its relatively low standard redox potential of +0.65 V *vs.* NHE should pose no problem for dye regeneration.

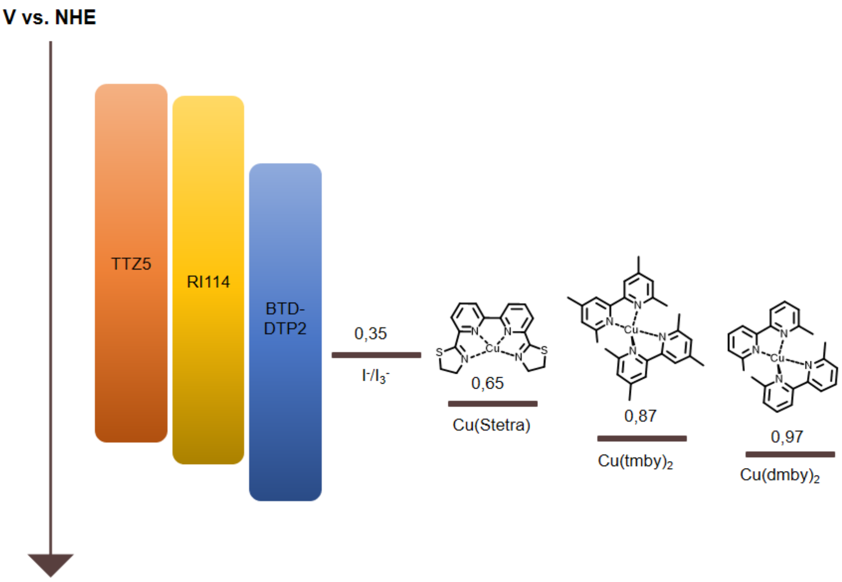

Figure 3.10*: chemical structures and redox potentials of copper complexes used as redox mediators in combination with the three selected dyes.*

### 3.4.3. Co-sensitization approach and use of co-adsorbents

As mentioned above, besides using the three dyes as individual sensitizers, in this work a co-sensitization approach was also investigated, with the aim to enhance the light-harvesting efficiency of the photoanodes by an extension of their absorption spectra, resulting from the sum of the absorption profile of each dye. To this end, a series of commercially available organic dyes was employed, trying to select species with complementary absorption spectra to those of **RI114**, **BTD-DTP2** and **TTZ5**. The compounds used for co-sensitization were **L1**,[36] **D35**,[37] Dyenamo blue[38] and **D5**,[39] whose structures are reported in Figure 3.11. Since this was just a first exploratory study, the co-sensitizers were dissolved in equimolar amounts in the photoanode staining solution, and no attempt was made to adjust the adsorption stoichiometry, leaving this activity to a further optimization study.

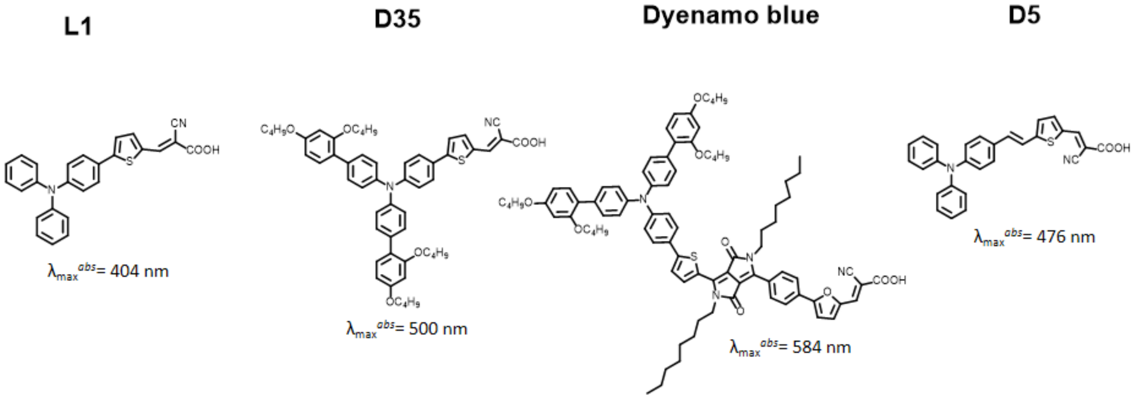

Figure 3.11*: structures of the organic dyes used for co-sensitization.*

In addition, for each individual dye, cells were also prepared both in the absence and in the presence of chenodeoxycholic acid (CDCA) (Figure 3.12), used as co-adsorbent by directly adding it to the photoanode sensitization bath. Indeed, it is widely known that the incorporation of co-adsorbents such as CDCA on the photoanode surface lowers the aggregation tendency of dye molecules by altering the surface properties, thereby hampering intermolecular interactions, enhancing the rate of the electron transfer to the semiconductor and ultimately improving the efficiency of the cells.[40,41]

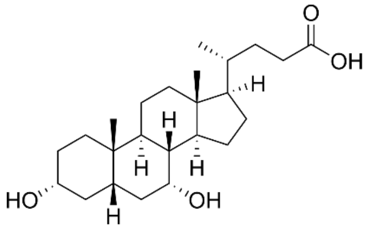

Figure 3.12*: structure of CDCA*.

## 3.5. Fabrication and characterization of photovoltaic cells

DSSCs with a surface area of 0.384 cm$^2$ were assembled by joining a sensitized $TiO_2$-based photoanode, comprising a mesoporous layer (avg. particle size: 30 nm) and a scattering layer (avg. particle size: 400 nm), with a PEDOT counter electrode (prepared by means of EDOT electropolymerization). The electrodes were assembled in a cell by using a UV-cured glue (which acted also as a sealant) without the employment of a gasket, as previously mentioned. The cells were then filled with the electrolyte containing the Cu-based redox shuttles and the selected additives *via* the vacuum backfilling technique. The electrolyte solutions were prepared according to the procedures reported by the Freitag laboratory.[6,30] Exact details on the cells' fabrication procedure are reported in the Experimental Section at the end of this chapter.

The cells have been characterized by using two main experimental techniques, namely the registration of the *J/V* curve, from which the power conversion efficiency parameter can be derived, and the measurement of the incident photon-to-electron conversion efficiency (*IPCE*), which allows to evaluate the fraction of photons that are converted to electrons at each wavelength. Details of both these techniques have been already discussed in paragraph 1.6.

In addition to them, a further characterization tool was employed to assess the electron transfer processes taking place in the devices, namely photo-induced absorption spectroscopy (PIA), from which it is possible to evaluate the dynamics of sensitizer regeneration by the redox electrolyte. A typical PIA setup comprises two light sources (and is therefore commonly indicated as *a pump-probe* setup): the sample is illuminated with white light (*probe*) and its absorption is recorded. A second light source (*pump*) is shone onto the sample and causes electronic excitations, which temporally alter the absorption profile of the sample. This pump source is *square-modulated*, meaning that it alternates between periods of equal duration during which the illumination is set *on* and *off*. The absorption profile during the on and off intervals is compared to obtain the quasi-steady-state transient absorption amplitude ΔA (Figure 3.13).[42]

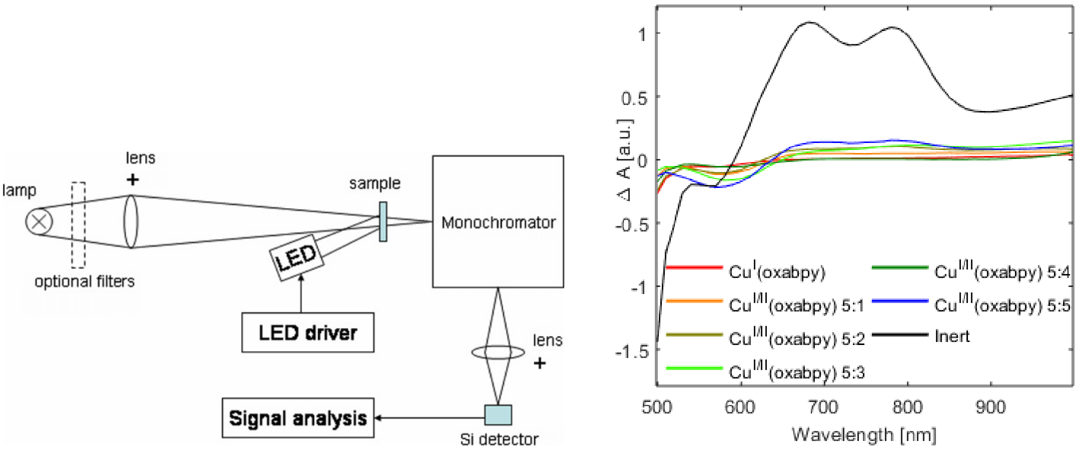

Figure 3.13*: simplified experimental setup of a Photo Induced Absorption experiment (left); example of PIA spectra obtained for the regeneration of dye* **Y123** *with Cu$^{I/II}$(oxabpy) redox couple at different concentrations*[29] *(right).*

Irradiation by pump light source induces photoexcitation of the dye and electron injection into the semiconductor. As a result, light absorption by the dye (D) ground state decreases, while that of the oxidized species ($D^+$) appears. The latter exhibits a different absorption profile from that of D, usually showing a number of red-shifted peaks compared to ground state absorption. For this reason, in the absence of a redox mediator, and if charge recombination is slow enough, the ΔA profile will present a negative profile in the range of ground state absorption and positive values in the interval of radical cation absorption. However, if the photoanode is immersed in a redox electrolyte, electron transfer from the electrolyte will regenerate the dye and quickly reinstate the ground states. This decreases the statistical probability of observing the ground state-bleach and $D^+$ absorption during the *pump-on* period. In return, the transient absorption amplitude of the quenched photoanode will be much decreased. Therefore, the closer the curve returns to the baseline in the presence of the electrolyte, the more efficient is dye regeneration by the redox couple in the timeframe of the pump on-off modulation.

## 3.6. DSSC efficiency measurements

The average photovoltaic parameters registered for each series of cells (n = 3-6), namely photocurrent density ($J_{sc}$), open-circuit voltage ($V_{oc}$), fill-factor (*ff*) and power conversion efficiency (*PCE*) are reported in individual tables with the corresponding standard deviations. Besides our dyes and the co-sensitizers described above, commercially available dye **Y123**[43] (see above, Figure 3.4), was also employed for cell fabrication, since it provided some of the best efficiencies reported to date with Cu-based electrolytes,[6,30] and thus constituted a useful reference against which to compare the obtained results.

### 3.6.1. DSSCs built with dye **RI114**

Results obtained with the first batch of cells containing dye **RI114** in combination with $Cu(tmby)_2^{(+/2+)}$ as a redox mediator are reported in Table 3.2. The sensitizer alone provided cells with avg. *PCE* of 6.22% and photovoltage superior to 0.8 V, demonstrating a good compatibility with the copper complex. It is possible to see that **RI114** benefited from the presence of CDCA (0.2 mM) in the staining solution (increasing $V_{OC}$ and $J_{SC}$), indicating a tendency of the dye to aggregate on $TiO_2$ surface. Interestingly, when using dye **L1** as a cosensitizer for **RI114** in the presence of CDCA, a slight decrease of photocurrent was observed, but the average PCE incresead to a value just above 7.0% thanks to a superior $V_{oc}$ value.

Table 3.2*: average photovoltaic performances of the DSSCs built with dye **RI114** - first batch.*

| Dye | n | CDCA | $V_{oc}$ (V) | $J_{sc}$ (mA cm$^{-2}$) | *ff* | *PCE* (%) |
|---|---|---|---|---|---|---|
| **Y123** | C | – | 1.07 ± 0.01 | 12.62 ± 0.72 | 0.69 ± 0.01 | 9.44 ±0.52 |
| **RI114** | 4 | – | 0.82 ± 0.01 | 10.45 ± 0.66 | 0.73 ± 0.01 | 6.22 ± 0.23 |
| **RI114** | 6 | + | 0.83 ± 0.03 | 11.37 ± 0.80 | 0.72 ± 0.02 | 6.94 ± 0.40 |
| **RI114 + L1** | 5 | + | 0.86 ± 0.04 | 11.14 ± 0.44 | 0.73 ± 0.01 | 7.06 ± 0.34 |

***Conditions.*** *Sensitization: **RI114** 0.1 mM; CDCA 0.2 mM (when used); co-sensitizer **L1** 0.1 mM (when used); Staining solvent: EtOH/$CHCl_3$ (7:3); Electrolyte: $Cu(tmby)_2$, $Cu^I/Cu^{II}$ 0.2 M / 0.04 M, LiTFSi 0.1 M, NMBI 0.6 M in $CH_3CN$.*

Photovoltaic parameters and the main characterization curves obtained for the best cell of each series are shown in Figure 3.14. PIA spectra (Figure 3.14, d) demonstrated the optimal regeneration of dye **RI114** when $Cu(tmby)_2$ is used. Indeed, the black line representing the absorption profile of the oxidized dye in the absence of copper electrolyte is totally quenched when the photoanode is immersed in a $Cu(tmby)_2$ solution (red line), confirming that the dye is fully regenerated.

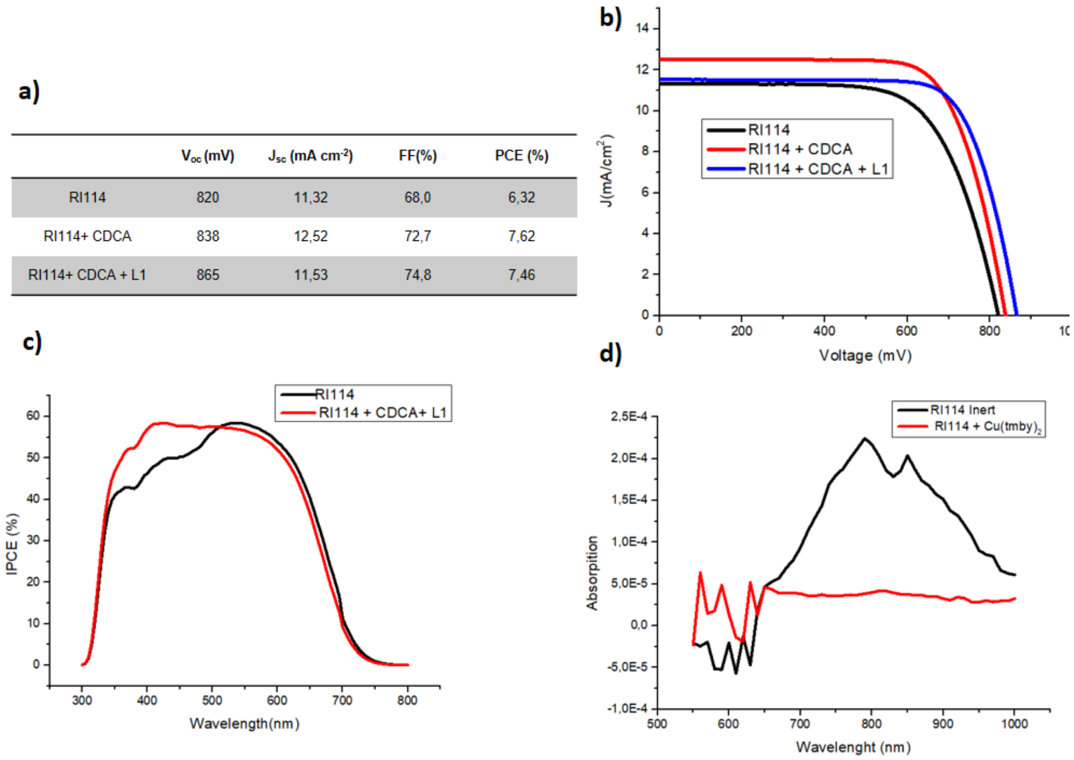

|  | $V_{oc}$ (mV) | $J_{sc}$ (mA cm$^{-2}$) | FF(%) | PCE (%) |
|---|---|---|---|---|
| RI114 | 820 | 11,32 | 68,0 | 6,32 |
| RI114+ CDCA | 838 | 12,52 | 72,7 | 7,62 |
| RI114+ CDCA + L1 | 865 | 11,53 | 74,8 | 7,46 |

Figure 3.14: *(a) photovoltaic performances of the best cell of the first batch fabricated with dye* ***RI114****. Corresponding J/V curves (b), IPCE graphs (c), and PIA spectra with an inert electrolyte and in the presence of Cu(tmby)$_2$ (d).*

Given the good results obtained with the first batch of cells, a second batch was fabricated employing a larger concentration of CDCA (0.5 mM) in the sensitizing bath. Furthermore, co-sensitization with two other dyes, either alone or combined, was also tested. The obtained results are shown in Table 3.3. Although also in this case addition of CDCA increased slightly cell performances compared to the case of **RI114** alone, use of a larger concentration did not appear productive (compare with Table 3.2). Furthermore, the addition of a larger amount of NMBI (*see above*, Paragraph 3.3.3.) to the electrolyte did not bring any benefit, resulting in lower cell efficiency mostly due to a reduced fill factor. Considering the co-sensitization experiments, both the use of **D35** and Dyenamo Blue as co-sensitizers brought about a clear improvement in PCE, especially due to a large enhancement of photocurrents. In the case of **D35**, an excellent $V_{OC}$ value > 0.9 V was also recorded, highlighting its very good match with **RI114**: this could be possibly due to a high structural complementarity of the two dyes, leading to an ideal assembly on the semiconductor surface, boosting light harvesting ability and efficiently limiting charge recombination events. Accordingly, it is possible that in this case use of CDCA is not useful or even detrimental, suggesting that an investigation of co-sensitization conditions in its absence could be worth carrying out. When a double co-sensitization of **RI114** with both **D35** and Dyenamo Blue was investigated no further improvement in photovoltaic parameters was observed.

Table 3.3*: average photovoltaic performances of the DSSCs built with dye* ***RI114*** *- second batch.*

| Dye | n | CDCA | $V_{oc}$ (V) | $J_{sc}$ (mA cm$^{-2}$) | *ff* | *PCE* (%) |
|---|---|---|---|---|---|---|
| Y123 | 6 | – | 1.02 ± 0.01 | 12.77 ± 0.99 | 0.70 ± 0.01 | 9.23 ±0.63 |
| RI114 | 4 | – | 0.82 ± 0.01 | 10.45 ± 0.66 | 0.73 ± 0.01 | 6.19 ± 0.23 |
| RI114 | 4 | + | 0.85 ± 0.01 | 12.07 ± 0.73 | 0.62 ± 0.08 | 6.49 ± 1.01 |
| RI114[a] | 5 | + | 0.87 ± 0.01 | 11.46 ± 1.03 | 0.61 ± 0.10 | 6.08 ± 0.95 |
| RI114 + D35 | 5 | + | 0.92 ± 0.01 | 12.40 ± 0.84 | 0.70 ± 0.01 | 8.03 ± 0.45 |
| RI114 + DBLUE | 6 | + | 0.86 ± 0.03 | 12.77 ± 0.37 | 0.67 ± 0.05 | 7.50 ± 0.82 |
| RI114 + D35 + DBLUE | 6 | + | 0.88 ± 0.01 | 12.90 ± 0.50 | 0.68 ± 0.03 | 7.80 ± 0.31 |

***Conditions.*** *Sensitization: **RI114** 0.1 mM; CDCA 0.5 mM (when used); co-sensitizers 0.1 mM each (when used); Staining solvent: EtOH/CHCl$_3$ (7:3) Electrolyte: Cu(tmby)$_2$, Cu$^I$/Cu$^{II}$ 0.2 M / 0.04 M, LiTFSi 0.1 M, NMBI 0.6 M in CH$_3$CN.*

[a] NMBI concentration in the electrolyte was 0.8 M.

Indeed, it is possible that the effective simultaneous absorption of all dyes was not possible, due to the limited space available on TiO$_2$ surface, as suggested by the results of IPCE experiments on champion cells (Figure 3.15c): clearly, the use of each co-sensitizer in combination with **RI114** improved the photocurrent response; however, the curve obtained in the presence of both **D35** and Dyenamo Blue appeared very similar to that recorded with only the latter dye, indicating that **D35** adsorption could be ineffective in this case.

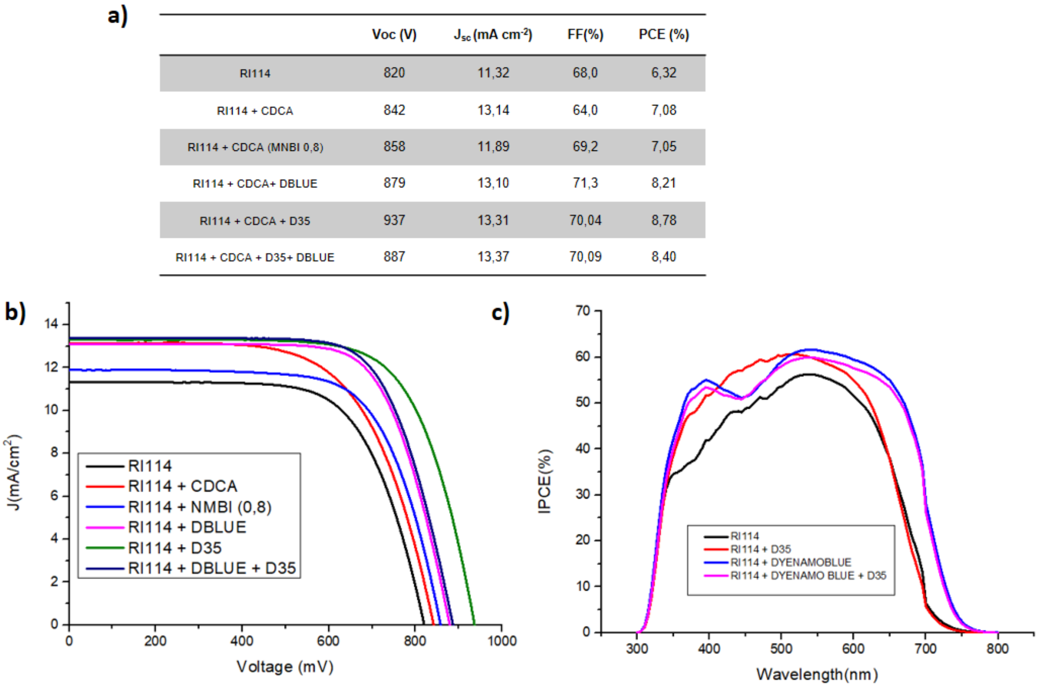

a)

| | Voc (V) | $J_{sc}$ (mA cm$^{-2}$) | FF(%) | PCE (%) |
|---|---|---|---|---|
| RI114 | 820 | 11,32 | 68,0 | 6,32 |
| RI114 + CDCA | 842 | 13,14 | 64,0 | 7,08 |
| RI114 + CDCA (MNBI 0,8) | 858 | 11,89 | 69,2 | 7,05 |
| RI114 + CDCA+ DBLUE | 879 | 13,10 | 71,3 | 8,21 |
| RI114 + CDCA + D35 | 937 | 13,31 | 70,04 | 8,78 |
| RI114 + CDCA + D35+ DBLUE | 887 | 13,37 | 70,09 | 8,40 |

*Figure 3.15: (a) Photovoltaic performances of the best cells of the second batch fabricated with dye **RI114**. Corresponding J/V curves (b)and IPCE graphs (c).*

### 3.6.2. DSSCs built with dye **BTD-DTP2**

In Table 3.4 the average of photovoltaic performances of DSSCs built with a first batch of dye **BTD-DTP2** are reported. Compared to the cells built with dye **RI114** alone (see Table 3.2), those containing dye **BDT-DTP2** together with $Cu(tmby)_2^{(+/2+)}$ as a redox shuttle presented generally higher photovoltage values, always close or superior to 0.9 V. In addition, even in the absence of CDCA, good average $J_{sc}$ values above 12 mA cm$^{-2}$ were obtained, highlighting the superior light harvesting ability of this dye (see the molar attenuation coefficients in Table 3.1).

Table 3.4*: average photovoltaic performances of DSSCs built with dye* ***BTD-DTP2*** *- first batch.*

| Dye | n | CDCA | $V_{oc}$ (V) | $J_{sc}$ (mA cm$^{-2}$) | *ff* | *PCE* (%) |
|---|---|---|---|---|---|---|
| Y123 | 6 | – | 1.07 ± 0.01 | 12.62 ± 0.72 | 0.69 ± 0.01 | 9.44 ±0.52 |
| BTD-DTP2 | 6 | – | 0.91 ± 0.01 | 12.36 ± 0.62 | 0.68 ± 0.02 | 7.71 ± 0.49 |
| BTD-DTP2 | 6 | + | 0.90 ± 0.01 | 12.03 ± 0.77 | 0.68 ± 0.03 | 7.48 ± 0.58 |
| BTD-DTP2 + L1 | 6 | + | 0.91 ± 0.01 | 11.61 ± 0.73 | 0.73 ± 0.01 | 7.73 ± 0.37 |

***Conditions.*** *__Sensitization__:* ***BTD-DTP2*** *0.1 mM; CDCA 0.2 mM (when used); co-sensitizer* ***L1*** *0.1 mM (when used); Staining solvent: EtOH/CHCl$_3$ (7:3). __Electrolyte__: Cu(tmby)$_2$, Cu$^I$/Cu$^{II}$ 0.2 M / 0.04 M, LiTFSi 0.1 M, NMBI 0.6 M in CH$_3$CN.*

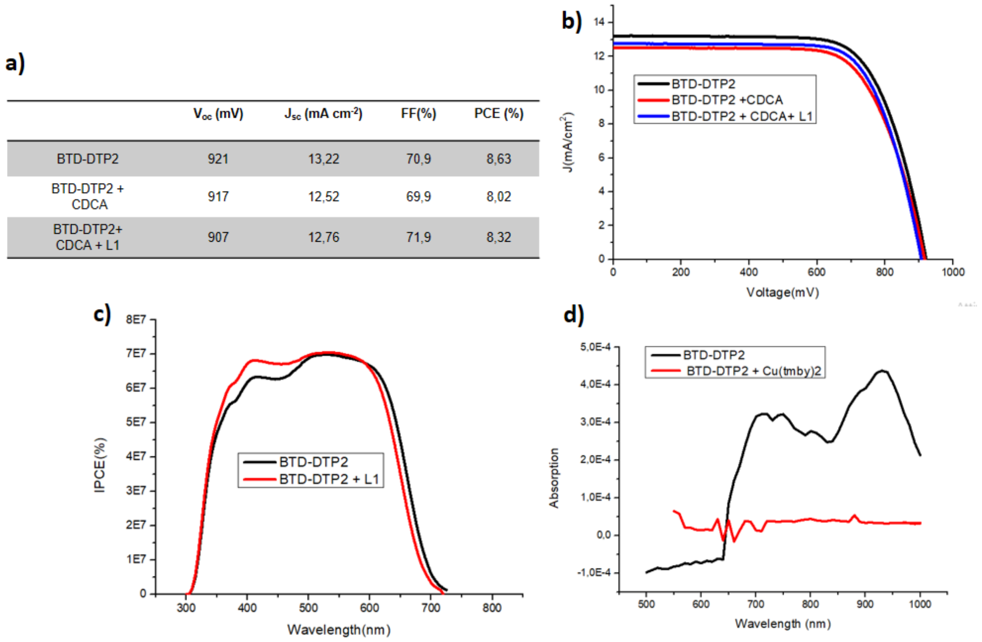
a)

| | $V_{oc}$ (mV) | $J_{sc}$ (mA cm$^{-2}$) | FF(%) | PCE (%) |
|---|---|---|---|---|
| BTD-DTP2 | 921 | 13,22 | 70,9 | 8,63 |
| BTD-DTP2 + CDCA | 917 | 12,52 | 69,9 | 8,02 |
| BTD-DTP2+ CDCA + L1 | 907 | 12,76 | 71,9 | 8,32 |

Figure 3.16*: (a) photovoltaic performances of the best cells of the first batch fabricated with dye* ***BTD-DTP2****. Corresponding J/V curves (b), IPCE graphs (c) and PIA spectra with an inert electrolyte and in the presence of Cu(tmby)$_2$ (d).*

Unfortunately, in this case the addition of CDCA was not useful, resulting in a slight decrease of PCE compared to the first series of cells. The initial PCE value was recovered when attempting

the co-sensitization with **L1**, mostly due to an improvement in fill factor which could be related to a more efficient hindrance of charge recombination events.
As can be seen from the IPCE profiles in Figure 3.16, co-sensitization with **L1** seems indeed to improve the photocurrent response in the blue region of the spectrum, suggesting that a further series of experiments with optimized **BTD-DTP2/L1** ratio and in the absence of CDCA could bring improvements to device efficiencies. PIA spectra (Figure 3.16 d) demonstrated also in this case the optimal regeneration of dye **BTD-DTP2** when Cu(tmby)$_2$ is used, which is in perfect agreement with the excellent photovoltage values discussed above.

As seen above in the case of **RI114**, also with **BDT-DTP2** a second batch of cells was prepared by using a larger amount of CDCA in the sensitizing bath (0.5 mM *vs.* 0.2 mM in the previous series of experiments). In addition, the staining solvent was also switched to THF (which appeared to better dissolve the dye compared to the EtOH/CHCl$_3$ mixture used previously) to check the influence of this parameter on DSSC performances. Results in Table 3.5 show how the average current density value dropped drastically upon addition of CDCA, which caused a concomitant fall of the PCE value, signaling that the increase in additive concentration did not benefit cell performances. Besides that, the steep decrease in efficiency could also be due to the use of THF as staining solvent, suggesting that further experiments should be carried out to confirm the occurrence of such solvent effect.

Table 3.5*: average photovoltaic performances of DSSCs built with dye **BTD-DTP2** - second batch*

| Dye | n | CDCA | $V_{oc}$ (V) | $J_{sc}$ (mA cm$^{-2}$) | *ff* | *PCE* (%) |
|---|---|---|---|---|---|---|
| **Y123** | 3 | − | 1.03 ± 0.01 | 13.12 ± 1.16 | 0.71 ± 0.01 | 9.68 ± 0.88 |
| **BTD-DTP2**[a] | 6 | − | 0.91 ± 0.01 | 12.36 ± 0.62 | 0.68 ± 0.02 | 7.71 ± 0.49 |
| **BTD-DTP2** | 6 | + | 0.76 ± 0.01 | 7.01 ± 0.47 | 0.73 ± 0.01 | 3.96 ± 0.33 |
| **BTD-DTP2**[b] | 6 | + | 0.80 ± 0.01 | 7.89 ± 0.95 | 0.73 ± 0.01 | 4.66 ± 0.59 |
| **BTD-DTP2 + D35** | 4 | + | 0.79 ± 0.01 | 7.26 ± 1.14 | 0.73 ± 0.01 | 4.25 ± 0.76 |
| **BTD-DTP2 + DBLUE** | 6 | + | 0.80 ± 0.01 | 8.54 ± 1.03 | 0.74 ± 0.02 | 5.15 ± 0.67 |
| **BTD-DTP2 + D35 + DBLUE** | 6 | + | 0.83± 0.01 | 10.10 ± 0.65 | 0.75 ± 0.01 | 6.38 ± 0.43 |

***Conditions.*** *Sensitization: **BTD-DTP2** 0.1 mM; CDCA 0.5 mM (when used); co-sensitizers 0.1 mM each (when used); Staining solvent: THF; Electrolyte: Cu(tmby)$_2$ or Cu(dmby)$_2$, Cu$^I$/Cu$^{II}$ 0.2 M / 0.04 M, LiTFSi 0.1 M, NMBI 0.6 M in CH$_3$CN.*
*[a] EtOH/CHCl$_3$ (7:3) was used as the staining solvent; [b] Cu(dmby)$_2^{(+/2+)}$ was used as the redox shuttle instead of Cu(tmby)$_2^{(+/2+)}$.*

Nevertheless, the influence of various other changes in cell composition could still be examined. First, a change of redox mediator was considered, switching Cu(tmby)$_2^{(+/2+)}$ for Cu(dmby)$_2^{(+/2+)}$; as mentioned above, the latter presents a more positive redox potential, possibly resulting in a $V_{oc}$ improvement. Indeed, cells built with **BDT-DTP2** together with

Cu(dmby)$_2^{(+/2+)}$ presented a marked increase of both photovoltage and photocurrent, suggesting a good match between these two cell components, as confirmed by PIA measurements showing perfect dye regeneration (Figure 3.17c). Therefore, this dye/electrolyte combination should surely be investigated further.

Co-sensitization experiments also provided interesting results: as observed previously for **RI114**, combination of **BDT-DTP2** with either **D35** or, especially, Dyenamo Blue was beneficial, causing a sharp improvement in all main photovoltaics parameters. In this case, however, the double co-sensitization strategy with both dyes was even more successful, inducing an average PCE increase of more than 50% compared to the cells in which **BDT-DTP2** was used alone, thanks to a large improvement in photocurrent. This preliminary result appears particularly promising, suggesting that cells containing the ternary combination **BDT-DTP2**/**D35**/Dyenamo Blue could provide high photovoltaic efficiencies, if they undergo a proper optimization process by adjusting the staining solvent, the relative ratio of the dyes and the amount of co-adsorbent used.

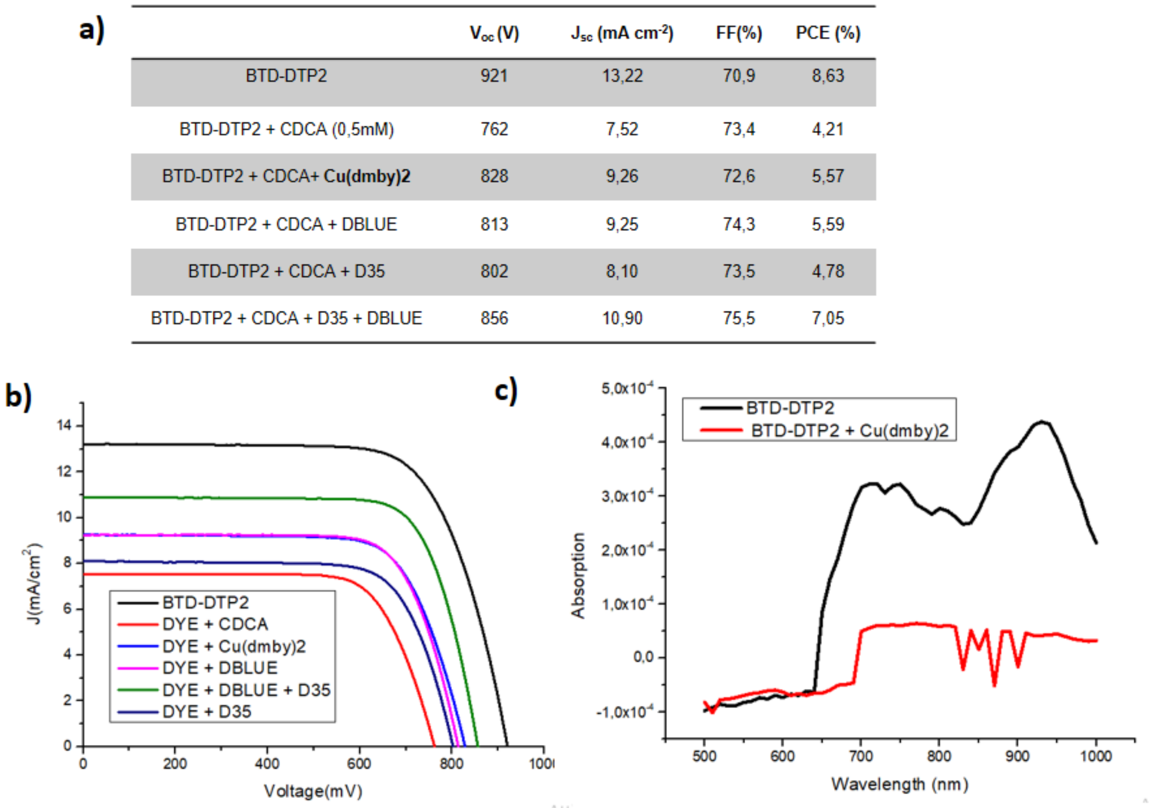

a)

| | $V_{oc}$ (V) | $J_{sc}$ (mA cm$^{-2}$) | FF(%) | PCE (%) |
|---|---|---|---|---|
| BTD-DTP2 | 921 | 13,22 | 70,9 | 8,63 |
| BTD-DTP2 + CDCA (0,5mM) | 762 | 7,52 | 73,4 | 4,21 |
| BTD-DTP2 + CDCA+ **Cu(dmby)2** | 828 | 9,26 | 72,6 | 5,57 |
| BTD-DTP2 + CDCA + DBLUE | 813 | 9,25 | 74,3 | 5,59 |
| BTD-DTP2 + CDCA + D35 | 802 | 8,10 | 73,5 | 4,78 |
| BTD-DTP2 + CDCA + D35 + DBLUE | 856 | 10,90 | 75,5 | 7,05 |

Figure 3.17: *(a) Photovoltaic performances of the best cells of the second batch fabricated with dye **BTD-DTP2**. Corresponding J/V curves (b) and PIA spectra using Cu(dmby)$_2^{(+/2+)}$ as redox mediator (c).*

### 3.6.3. DSSCs built with dye **TTZ5**

Solar cells fabricated with dye **TTZ5** alone in the presence of Cu(tmby)$_2^{(+/2+)}$ presented an average PCE of ca. 6.4% (Table 3.6), which was similar to that obtained with **RI114** (see Table 3.2), but lower than that registered with **BTD-DTP2** (see Table 3.4). Such value was comparable with those recorded in the literature for cells using **TTZ5** in combination with traditional electrolytes containing the $I^-/I_3^-$ redox couple.[2,3,44] The improvement obtained by adding CDCA to the staining solution was really low with this dye, confirming that its good molecular design, featuring many bulky alkyl chains on the dyes' backbone, was itself able to prevent dye aggregation on the semiconductor surface. Therefore, higher concentrations of CDCA are not expected to be beneficial.

In addition to that, it seems that **TTZ5** does not benefit from co-sensitization, since practically all photovoltaic parameters declined (or at most stayed the same) compared to the cells built with **TTZ5** + CDCA, with the only partial exception of the combination with **D35**, showing a better efficiency than **TTZ5** alone (in the absence of CDCA). This is probably due to: i) the bulkiness of **TTZ5** structure, hampering other dyes to bind efficiently to $TiO_2$, and/or ii) its excellent light harvesting efficiency in the region 350-650 nm (as proven by its exceedingly high molar attenuation coefficient, Table 3.1), which may be reduced when mixed with other dyes having less intense absorption features.

Table 3.6*: average photovoltaic performances of DSSCs built with* ***TTZ5*** *and* $Cu(tmby)_2^{(+/2+)}$.

| Dye | n | CDCA | $V_{oc}$ (V) | $J_{sc}$ (mA cm$^{-2}$) | *ff* | *PCE* (%) |
|---|---|---|---|---|---|---|
| **Y123** | 3 | − | 1.04 ± 0.01 | 12.78 ± 0.99 | 0.70 ± 0.01 | 9.23 ± 0.63 |
| **TTZ5** | 4 | − | 0.85 ± 0.01 | 10.35 ± 0.41 | 0.71 ± 0.03 | 6.38 ± 0.28 |
| **TTZ5** | 6 | + | 0.85 ± 0.02 | 11.28 ± 0.51 | 0.71 ± 0.02 | 6.90 ± 0.42 |
| **TTZ5 + D5** | 4 | + | 0.82 ± 0.01 | 9.65 ± 1.40 | 0.72 ± 0.01 | 5.83 ± 0.94 |
| **TTZ5 + D35** | 5 | + | 0.88 ± 0.03 | 10.42 ± 0.59 | 0.72 ± 0.02 | 6.74 ± 0.59 |
| **TTZ5 + DBLUE** | 6 | + | 0.85 ± 0.01 | 9.25 ± 0.27 | 0.70 ± 0.05 | 5.60 ± 0.49 |
| **TTZ5 + D35 + DBLUE** | 6 | + | 0.85 ± 0.01 | 8.90 ± 0.46 | 0.72 ± 0.01 | 5.55 ± 0.40 |

***Conditions.*** *Sensitization:* ***TTZ5*** *0.1 mM; CDCA 0.2 mM (when used); co-sensitizers 0.1 mM each (when used); Staining solvent: THF; Electrolyte:* $Cu(tmby)_2$*,* $Cu^I/Cu^{II}$ *0.2 M / 0.04 M, LiTFSi 0.1 M, NMBI 0.6 M in* $CH_3CN$*.*

Despite the apparently low driving force for dye regeneration in these cells (being the $E_{ox}$ of **TTZ5**, +0.91 V *vs.* NHE, only slightly more positive than the redox potential of the electrolyte, +0.87 V *vs.* NHE), looking at the PIA spectra (see Figure 3.18c), an efficient quenching of the dye radical cation by the electrolyte $Cu(tmby)_2$ seems to be operative also in this case. Indeed, the oxidized dye absorption profile (black line) was totally quenched in the presence of the Cu-based redox shuttle (red line), confirming that the dye is fully regenerated.

**a)**

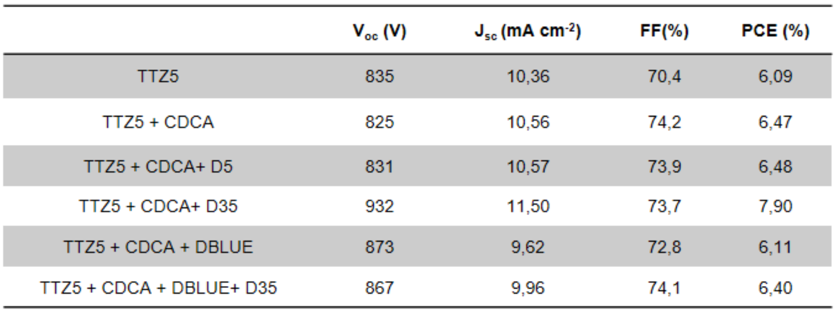

| | $V_{oc}$ (V) | $J_{sc}$ (mA cm$^{-2}$) | FF(%) | PCE (%) |
|---|---|---|---|---|
| TTZ5 | 835 | 10,36 | 70,4 | 6,09 |
| TTZ5 + CDCA | 825 | 10,56 | 74,2 | 6,47 |
| TTZ5 + CDCA+ D5 | 831 | 10,57 | 73,9 | 6,48 |
| TTZ5 + CDCA+ D35 | 932 | 11,50 | 73,7 | 7,90 |
| TTZ5 + CDCA + DBLUE | 873 | 9,62 | 72,8 | 6,11 |
| TTZ5 + CDCA + DBLUE+ D35 | 867 | 9,96 | 74,1 | 6,40 |

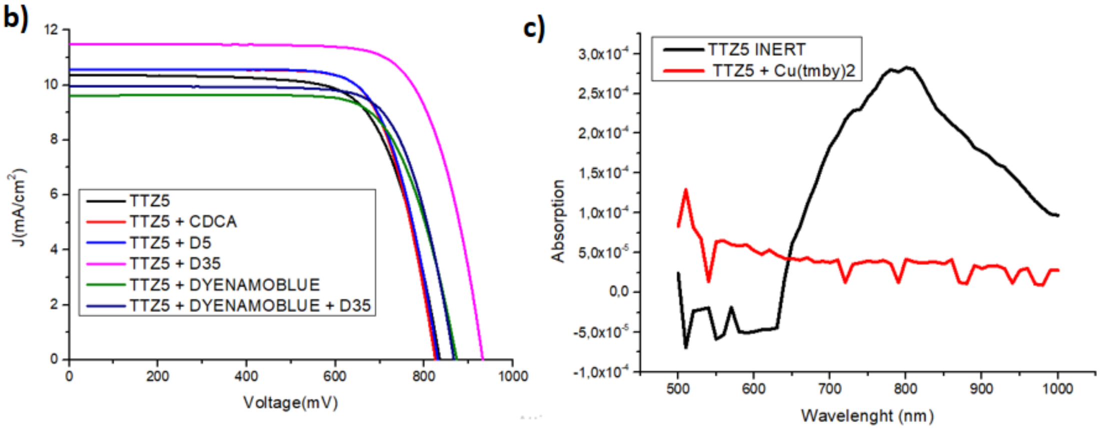

Figure 3.18: *(a) Photovoltaic performances of the best cells fabricated with dye* ***TTZ5*** *together with Cu(tmby)$_2$$^{(+/2+)}$ as redox mediator. Corresponding J/V curves (b) and PIA spectra (c).*

Based on the above considerations, instead of testing a second series of cells prepared with **TTZ5** in the presence of a different CDCA concentration in the sensitizing bath (as done with the other two dyes), we investigated its combination with a different redox mediator, namely the dynamic mono-/dimeric complex Cu(Stetra)$^{(+/2+)}$.[30] The latter has a less positive redox potential compared to Cu(tmby)$_2$$^{(+/2+)}$, suggesting a facile dye regeneration process, but also a potentially reduced $V_{oc}$ of the corresponding cells. As can be seen in Table 3.7, this was exactly the case, with average $V_{oc}$ values comprised between 0.73 and 0.80 V *vs.* NHE, thus approximately 70-120 mV lower than those seen in the previous batch. Despite this, the photocurrent values were clearly improved compared to the cells built with Cu(tmby)$_2$$^{(+/2+)}$, and values of $J_{sc}$ above 12 mA cm$^{-2}$ were obtained both for cells containing **TTZ5** alone and combined with CDCA. Also in this case, co-sensitization with **D5** or Dyenamo Blue did not bring any improvement, whereas the combination with **D35** was much more successful, yielding a clearly increased photocurrent value above 13 mA cm$^{-2}$, resulting in an improved photovoltaic efficiency (7.74%). Thus, the good compatibility of these two dyes, which was partially visible in the previous series of cells, was much more clearly confirmed in this case. As it could be expected, PIA spectra (Figure 3.19c) confirmed also in this case a good regeneration of the dye by the electrolyte Cu(Stetra)$^{(+/2+)}$.

Table 3.7*: average photovoltaic performances of DSSCs built with dye* ***TTZ5*** *and Cu(Stetra)$^{(+/2+)}$.*

| Dye | n | CDCA | *$V_{oc}$* (V) | *$J_{sc}$* (mA cm$^{-2}$) | *ff* | *PCE* (%) |
|---|---|---|---|---|---|---|
| Y123 | 3 | – | 1.06 ± 0.02 | 12.45 ± 0.85 | 0.69 ± 0.02 | 9.10 ± 0.38 |
| TTZ5 | 6 | – | 0.78 ± 0.02 | 12.36 ± 0.17 | 0.65 ± 0.02 | 6.32 ± 0.15 |
| TTZ5 | 6 | + | 0.77 ± 0.02 | 12.18 ± 0.59 | 0.68 ± 0.01 | 6.47 ± 0.60 |
| TTZ5 + D5 | 6 | + | 0.75 ± 0.01 | 10.04 ± 0.67 | 0.74 ± 0.03 | 5.63 ± 0.51 |
| TTZ5 + D35 | 4 | + | 0.80 ± 0.04 | 13.24 ± 0.76 | 0.72 ± 0.01 | 7.74 ± 0.70 |
| TTZ5 + DBLUE | 5 | + | 0.73 ± 0.01 | 9.66 ± 0.94 | 0.68 ± 0.03 | 4.89 ± 0.49 |
| TTZ5 + D35 + DBLUE | 5 | + | 0.74 ± 0.01 | 9.60 ± 0.98 | 0.70 ± 0.02 | 5.10 ± 0.57 |

***Conditions.*** *Sensitization:* ***TTZ5*** *0.1 mM; CDCA 0.2 mM (when used); co-sensitizers 0.1 mM each (when used); Staining solvent: THF; Electrolyte: Cu(Stetra), Cu$^{I}$/Cu$^{II}$ 0.167 M / 0.08 M, LiTFSi 0.075 M, tBP 0.4 M in $CH_3CN$.*

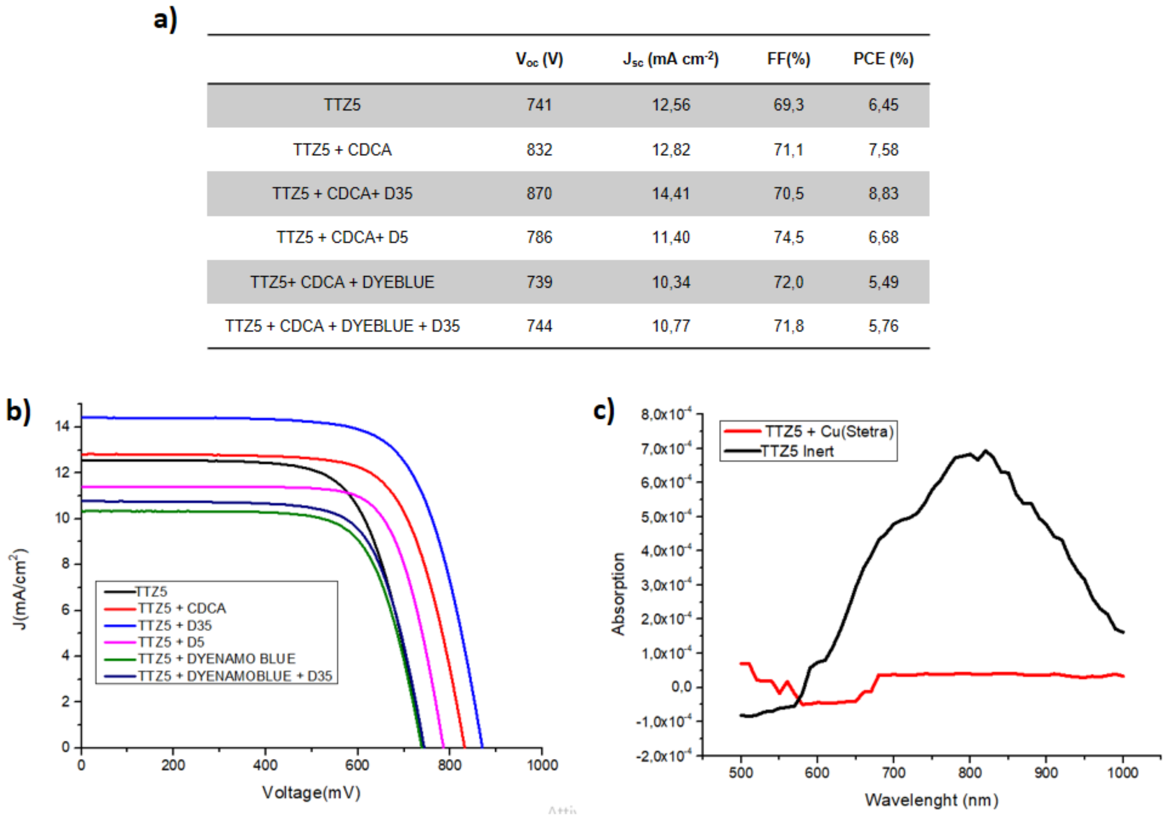

**a)**

|  | $V_{oc}$ (V) | $J_{sc}$ (mA cm$^{-2}$) | FF(%) | PCE (%) |
|---|---|---|---|---|
| TTZ5 | 741 | 12,56 | 69,3 | 6,45 |
| TTZ5 + CDCA | 832 | 12,82 | 71,1 | 7,58 |
| TTZ5 + CDCA+ D35 | 870 | 14,41 | 70,5 | 8,83 |
| TTZ5 + CDCA+ D5 | 786 | 11,40 | 74,5 | 6,68 |
| TTZ5+ CDCA + DYEBLUE | 739 | 10,34 | 72,0 | 5,49 |
| TTZ5 + CDCA + DYEBLUE + D35 | 744 | 10,77 | 71,8 | 5,76 |

Figure 3.19*: (a) photovoltaic performances of the best cells fabricated with dye* ***TTZ5*** *together with Cu(Stetra)$^{(+/2+)}$ as redox mediator . Corresponding J/V curves (b) and PIA spectra (c).*

## 3.7. Conclusions

In conclusion, an extensive series of preliminary device fabrication and characterization experiments was carried out to determine if organic dyes **RI114**, **BTD-DTP2** and **TTZ5** were suitable for application in DSSCs in combination with Cu complex-based liquid electrolytes.

When employed alone, all dyes provided working cells together with redox shuttle $Cu(tmby)_2^{(+/2+)}$, giving fair to good power conversion efficiencies in the 6.22-7.71% range, which could be sometimes improved by the addition of CDCA as a disaggregating co-adsorbent. The influence of this additional component, however, was strongly dependent both on the structure of the dyes and on its concentration in the sensitizing bath, suggesting that a proper optimization procedure should be carried out in each individual case to maximize performances.

For dyes **BTD-DTP2** and **TTZ5** it was also possible to fabricate working DSSCs with the other two shuttles, $Cu(dmby)_2^{(+/2+)}$ and $Cu(Stetra)^{(+/2+)}$, respectively. Whereas the average efficiency of cells built with the **TTZ5**/$Cu(Stetra)^{(+/2+)}$ combination was in line with that observed with $Cu(tmby)_2^{(+/2+)}$, an improvement could be clearly seen in the case of the **BTD-DTP2**/$Cu(dmby)_2^{(+/2+)}$ combination, which has the potential to yield cells with increased photovoltage: this combination should therefore be investigated further. In any case, despite the different regeneration driving forces that could be estimated based on the redox couples potentials, PIA experiments always showed a good regeneration of the dyes by the Cu-complexes, which suggests that such electrolytes could be generally applicable with an even wider range of organic sensitizers having different electrochemical properties.

The results obtained in the co-sensitization experiments present a less clear picture, mostly because their outcome is crucially dependent on various factors, such as the relative adsorption stoichiometry of the sensitizers, which could not be optimized in this study. Nevertheless, it can be noticed that co-sensitization was always successful with dye **RI114**, which seemed especially compatible with dye **D35**, leading to an average cell efficiency of 8.03% with $V_{oc}$ = 0.92 V (Table 3.3), which was the best observed in this work. In the case of **BTD-DTP2**, a remarkable result was obtained when applying a ternary co-sensitization strategy with both **D35** and Dyenamo Blue, leading to a largely improved *PCE* compared to that provided by the dye alone measured in the same conditions (6.38% *vs.* 3.96%, Table 3.5), suggesting that, after proper cell optimization, high performances could be obtained with this dye mixture. Finally, co-sensitization with dye **TTZ5** seemed to provide somewhat less interesting results in general terms, but it should still be mentioned that its combination with **D35** in the presence of $Cu(Stetra)^{(+/2+)}$ electrolyte provided cells with *PCE* > 7.7% and $J_{sc}$ > 13 mA cm$^{-2}$ (Table 3.7), which was among the best results obtained in this study.

The results obtained during the internship at Newcastle University were therefore highly interesting, and should prompt further collaborative investigations between the two groups involved, for example by probing the efficiencies of cells built with optimized sensitizers and co-adsorbent compositions, or measured under indoor and ambient illumination, for which Cu-based electrolytes appear very promising.

## 3.8. Experimental section

### 3.8.1. Assembly of dye-sensitized solar cells

The fabrication of the cells was carried out following the procedure already optimized and reported by Freitag's group; their assembly will therefore be described in detail.

DSSCs were fabricated on glass substrates coated with a thin layer of fluorine doped tin oxide (FTO) (Pilkington, St. Helens, UK) having 10 Ω sheet resistance. This grants the substrates conductivity, however, causes losses in optical transmission of approximately 10%.[45] The substrate was cut to size (here 3 x 10 $cm^2$ bars) and washed with a solution of RBS detergent, deionized water and ethanol. Then, the substrates underwent a UV/ozone treatment for 30 min before a 50 nm-thick compact layer of $TiO_2$ was deposited by spray pyrolysis at 450 °C. This component is also known as the *blocking layer*, since it has the role of hampering charge recombination caused by direct contact of the conductive glass substrate with the electrolyte. Next, the mesoporous $TiO_2$ layer (0.384 $cm^2$, 7 mm diameter circles) was screen-printed through a 60T screen of the designed pattern (Seritec Service SA, Corseaux, Switzerland) on the substrate using DSL 30 NRD-T $TiO_2$ paste (Dyesol / GreatCell Solar), containing particles of average diameter of 30 nm. The printed layer was allowed to settle for 5 min at room temperature, then dried on a hotplate at 125 °C for 5 min. The procedure was then repeated with a second paste (WER2-0, Dyesol / GreatCell Solar) containing larger $TiO_2$ particles with average diameter of 400 nm, achieving deposition of a *light-scattering layer*, after which the substrates were sintered in a hotplate with a stepwise ramp program up to 500 °C. Afterwards, the $TiO_2$ photoanodes underwent a post-treatment with a 40 mM $TiO_2$ aqueous solution at 70°C for 30 min, followed by sintering at 450 °C for 30 min. This treatment ripens the nanoparticles and helps covering surface sites that were insufficiently coordinated after annealing of the $TiO_2$ paste. The individual cells were cut from the substrate, heated to 450 °C on a hotplate and then quickly immersed in the dye bath once cooled down to 100 °C. The compositions of the dye baths used for each series of cells is reported underneath Tables 3.2-3.7. The substrates were left in the dye bath overnight, then rinsed with acetonitrile, allowed to dry in air, and assembled.

In parallel, the counter electrodes were prepared by via electropolymerization of 3,4-ethylenedioxythiophene onto another FTO substrate, from 0.01 mM micellar aqueous solution containing 0.1 M sodium dodecyl sulphate.[33] The electro-deposition was carried out with the aid of an IviumStat potentiostat (Ivium technologies) set to a chronopotentiometry program, with 3 current levels (0 mA for 5 s, 35 mA for 20 s, 0 mA for 5 s), interval time of 0.2 s, current range of 100 mA, potential range of 4 V and 1 cycle. For the deposition, the 5 × 5 cm, pre-drilled FTO glass to be covered with PEDOT was connected to the potentiostat working electrode and immersed in the precursor solution. A slightly larger piece of FTO glass was connected to the potentiostat reference and counter electrodes and placed in front of the previous glass at short distance. When the setup was in place, the potentiostat program was run. After PEDOT deposition the substrates were rinsed with ethanol and allowed to dry in air, then cut to size for solar cell assembly.

Anode and cathode were then assembled using 3035B UV glue (ThreeBond Europe, Saint Ouen L'Aumone, France) and the resulting sealed cells were cured with a CS2010 UV-source (Thorlabs, Newton, NJ, USA). The electrolyte (prepared according to previous procedures)[5,6,30] was then injected through a pre-drilled hole in the counter electrode, which was subsequently sealed with additional UV-glue. Soldering tin contacts onto anode and cathode completed the cell fabrication procedure.

### 3.8.2. Solar Cells Characterization

**Current-Voltage measurements** under AM 1.5 illumination were carried out using a HelioSim-CL60 solar simulator (Voss Electronic GmbH). An X200 source meter (Ossila, Sheffield, UK) was used to assess the solar cells performance (scan speed 25 mV $s^{-1}$). A circular mask was employed to confine the active solar cell area to 0.196 $cm^2$.

**Photoinduced absorption spectroscopy.** PIA spectra were recorded using an ASB-W-030 white light (Spectral Products, Putnam, CT, USA) as probe source. The sample was excited with a blue laser (405 nm, 3 mW, Thorlabs), which was chopped into 20 Hz square modulation with a 650 Chopper (Signal Recovery). Behind the sample, the light passed through a Digikrom CM110 monochromator and detected on a circular photodiode (Thorlabs, Newton, NJ, USA). The signal was amplified and split into AC- and DC- components with a 5182 ore-amplifier and recorded with a 7225 lock-in amplifier (both by Signal Recovery).

**Incident-photon-to-current conversion efficiency.** IPCE spectra were recorded with an ASB-XE-175 xenon light source (10 mW $cm^{-2}$) and a CM110 monochromator (Spectral Products, Putnam, CT, USA). The photocurrent was measured with a U6 digital acquisition board (LabJack, Lakewood, CO, USA). The setup was calibrated with a certified silicon reference cell (Frauenhofer ISE, Munich, Germany).

# References

[1] A. Dessì, D. A. Chalkias, S. Bilancia, A. Sinicropi, M. Calamante, A. Mordini, A. Karavioti, E. Stathatos, L. Zani, G. Reginato, *Sustain Energy Fuels* **2021**, *5*, 1171–1183.

[2] A. Dessì, M. Calamante, A. Mordini, M. Peruzzini, A. Sinicropi, R. Basosi, F. Fabrizi de Biani, M. Taddei, D. Colonna, A. di Carlo, G. Reginato, L. Zani, *Chem. Commun.* **2014**, *50*, 13952–13955.

[3] A. Dessì, M. Calamante, A. Mordini, M. Peruzzini, A. Sinicropi, R. Basosi, F. Fabrizi De Biani, M. Taddei, D. Colonna, A. di Carlo, G. Reginato, L. Zani, *RSC Adv* **2015**, *5*, 32657–32668.

[4] L. Vesce, P. Mariani, M. Calamante, A. Dessì, A. Mordini, L. Zani, A. di Carlo, *Solar RRL* **2022**, *6*, 2200403.

[5] M. Freitag, F. Giordano, W. Yang, M. Pazoki, Y. Hao, B. Zietz, M. Grätzel, A. Hagfeldt, G. Boschloo, *Journal of Physical Chemistry C* **2016**, *120*, 9595–9603.

[6] Y. Saygili, M. Söderberg, N. Pellet, F. Giordano, Y. Cao, A. B. Munoz-García, S. M. Zakeeruddin, N. Vlachopoulos, M. Pavone, G. Boschloo, L. Kavan, J. E. Moser, M. Grätzel, A. Hagfeldt, M. Freitag, *J Am Chem Soc* **2016**, *138*, 15087–15096.

[7] M. Freitag, J. Teuscher, Y. Saygili, X. Zhang, F. Giordano, P. Liska, J. Hua, S. M. Zakeeruddin, J. E. Moser, M. Grätzel, A. Hagfeldt, *Nat Photonics* **2017**, *11*, 372–378.

[8] N. V. Krishna, J. V. S. Krishna, M. Mrinalini, S. Prasanthkumar, L. Giribabu, *ChemSusChem* **2017**, *10*, 4668–4689.

[9] H. Michaels, M. Rinderle, R. Freitag, I. Benesperi, T. Edvinsson, R. Socher, A. Gagliardi, M. Freitag, *Chem Sci* **2020**, *11*, 2895–2906.

[10] Y. Nozaki, M. Yoshikawa, *IOP Conf Ser Mater Sci Eng* **2019**, *575*, 012008.

[11] D. Zhang, M. Stojanovic, Y. Ren, Y. Cao, F. T. Eickemeyer, E. Socie, N. Vlachopoulos, J. E. Moser, S. M. Zakeeruddin, A. Hagfeldt, M. Grätzel, *Nat Commun* **2021**, *12*, 1777.

[12] G. Boschloo, A. Hagfeldt, *Acc Chem Res* **2009**, *42*, 1819–1826.

[13] A. Listorti, B. O'Regan, J. R. Durrant, *Chemistry of Materials* **2011**, *23*, 3381–3399.

[14] A. B. Muñoz-García, I. Benesperi, G. Boschloo, J. J. Concepcion, J. H. Delcamp, E. A. Gibson, G. J. Meyer, M. Pavone, H. Pettersson, A. Hagfeldt, M. Freitag, *Chem Soc Rev* **2021**, *50*, 12450–12550.

[15] J. Cong, X. Yang, L. Kloo, L. Sun, *Energy Environ Sci* **2012**, *5*, 9180–9194.

[16] Y. Saygili, M. Stojanovic, H. Michaels, J. Tiepelt, J. Teuscher, A. Massaro, M. Pavone, F. Giordano, S. M. Zakeeruddin, G. Boschloo, J. E. Moser, M. Grätzel, A. B. Muñoz-García, A. Hagfeldt, M. Freitag, *ACS Appl Energy Mater* **2018**, *1*, 4950–4962.

[17] Q. Wang, Z. Zhang, S. M. Zakeeruddin, M. Grätzel, *Journal of Physical Chemistry C* **2008**, *112*, 7084–7092.

[18] H. Iftikhar, G. G. Sonai, S. G. Hashmi, A. F. Nogueira, P. D. Lund, *Materials* **2019**, *12*, 1998.

[19] H. Nusbaumer, J.-E. Moser, S. M. Zakeeruddin, M. K. Nazeeruddin, M. Grätzel, *J Phys Chem B* **2001**, *105*, 10461–10464.

[20] S. M. Feldt, E. A. Gibson, E. Gabrielsson, L. Sun, G. Boschloo, A. Hagfeldt, *J Am Chem Soc* **2010**, *132*, 16714–16724.

[21] S. A. Sapp, C. M. Elliott, C. Contado, S. Caramori, C. A. Bignozzi, *J Am Chem Soc* **2002**, *124*, 11215–11222.

[22] S. Mathew, A. Yella, P. Gao, R. Humphry-Baker, B. F. E. Curchod, N. Ashari-Astani, I. Tavernelli, U. Rothlisberger, M. K. Nazeeruddin, M. Grätzel, *Nat Chem* **2014**, *6*, 242–247.

[23] K. Kakiage, Y. Aoyama, T. Yano, K. Oya, J. Fujisawa, M. Hanaya, *Chemical Communications* **2015**, *51*, 15894–15897.

[24] B. M. Klahr, T. W. Hamann, *Journal of Physical Chemistry C* **2009**, *113*, 14040–14045.

[25] K. S. Srivishnu, S. Prasanthkumar, L. Giribabu, *Mater Adv* **2021**, *2*, 1229–1247.

[26] S. Hattori, Y. Wada, S. Yanagida, S. Fukuzumi, *J Am Chem Soc* **2005**, *127*, 9648–9654.

[27] Y. Bai, Q. Yu, N. Cai, Y. Wang, M. Zhang, P. Wang, *Chemical Communications* **2011**, *47*, 4376–4378.

[28] W. Zhang, Y. Wu, H. W. Bahng, Y. Cao, C. Yi, Y. Saygili, J. Luo, Y. Liu, L. Kavan, J. E. Moser, A. Hagfeldt, H. Tian, S. M. Zakeeruddin, W. H. Zhu, M. Grätzel, *Energy Environ Sci* **2018**, *11*, 1779–1787.

[29] H. Michaels, I. Benesperi, T. Edvinsson, A. Muñoz-Garcia, M. Pavone, G. Boschloo, M. Freitag, *Inorganics (Basel)* **2018**, *6*, 53.

[30] I. Benesperi, H. Michaels, T. Edvinsson, M. Pavone, P. Probert, P. Waddell, A. B. M. García, M. Freitag, *Chem* **2021**, *8*, 439–449.

[31] P. Ferdowsi, Y. Saygili, S. M. Zakeeruddin, J. Mokhtari, M. Grätzel, A. Hagfeldt, L. Kavan, *Electrochim Acta* **2018**, *265*, 194–201.

[32] J. D. Roy-Mayhew, G. Boschloo, A. Hagfeldt, I. A. Aksay, *ACS Appl Mater Interfaces* **2012**, *4*, 2794–2800.

[33] H. Ellis, N. Vlachopoulos, L. Häggman, C. Perruchot, M. Jouini, G. Boschloo, A. Hagfeldt, *Electrochim Acta* **2013**, *107*, 45–51.

[34] Y. Cao, Y. Liu, S. M. Zakeeruddin, A. Hagfeldt, M. Grätzel, *Joule* **2018**, *2*, 1108–1117.

[35] J. Tauc, *Mater Res Bull* **1968**, *3*, 37–46.

[36] D. P. Hagberg, T. Marinado, K. M. Karlsson, K. Nonomura, P. Qin, G. Boschloo, T. Brinck, A. Hagfeldt, L. Sun, *Journal of Organic Chemistry* **2007**, *72*, 9550–9556.

[37] D. P. Hagberg, X. Jiang, E. Gabrielsson, M. Linder, T. Marinado, T. Brinck, A. Hagfeldt, L. Sun, *J Mater Chem* **2009**, *19*, 7232–7238.

[38] Y. Hao, Y. Saygili, J. Cong, A. Eriksson, W. Yang, J. Zhang, E. Polanski, K. Nonomura, S. M. Zakeeruddin, M. Grätzel, A. Hagfeldt, G. Boschloo, *ACS Appl Mater Interfaces* **2016**, *8*, 32797–32804.

[39] D. P. Hagberg, T. Edvinsson, T. Marinado, G. Boschloo, A. Hagfeldt, L. Sun, *Chemical Communications* **2006**, 2245–2247.

[40] Y. S. Yen, T. Y. Lin, C. Y. Hsu, Y. C. Chen, H. H. Chou, C. Tsai, J. T. Lin, *Org Electron* **2013**, *14*, 2546–2554.

[41] A. S. Najm, N. Ahmad Ludin, I. Jaber, N. H. Hamid, H. Salah Naeem, *Inorganica Chim Acta* **2022**, *533*, 120776.

[42] G. Boschloo, A. Hagfeldt, *Inorganica Chim Acta* **2008**, *361*, 729–734.

[43] H. N. Tsao, C. Yi, T. Moehl, J.-H. Yum, S. M. Zakeeruddin, M. K. Nazeeruddin, M. Grätzel, *ChemSusChem* **2011**, *4*, 591–594.

[44] A. Dessì, M. Calamante, A. Sinicropi, M. L. Parisi, L. Vesce, P. Mariani, B. Taheri, M. Ciocca, A. di Carlo, L. Zani, A. Mordini, G. Reginato, *Sustain Energy Fuels* **2020**, *4*, 2309–2321.

[45] Nippon Sheet Glass Co. Ltd., "NGS TEC(TM) Datasheet," can be found under https://www.pilkington.com/global/products/product-categories/solar-energy/nsg-tec-for-solar-applications#overview, **2023**.

# Chapter 4

# Hole Transporting Materials (HTM) for Perovskite Solar Cells

## 4.1. Introduction

As explained in Chapter 1, since 2009 perovskite solar cells (PSCs) have been extensively investigated as an efficient alternative to the currently adopted silicon-based devices and their power conversion efficiency (PCE) has extraordinarily increased over the years, from 3.9% to 25.7%.[1,2] Such outstanding photovoltaic performances can be ascribed, on one hand, to the promising optoelectronic properties of perovskite, and, on the other, to the great efforts devoted to the optimization of PSCs components.[3,4] The lack of long-term stability is actually the main issue that is hampering large-scale PSC production and it can be mainly ascribed to the degradation of PSC components. It has been proven that PSC stability largely depends on the HTMs because, besides being responsible for the charge extraction and transfer at the interfaces while blocking charge recombination, they also act as physical barriers by preventing the contact of the active perovskite layer with the metal electrode and by blocking moisture and oxygen penetration.[5]

Spiro-OMeTAD (2,2',7,7'-tetrakis[*N*,*N*-di(4-methoxyphenyl)amino]-9,9'-spirobifluorene, see Figure 1.17) is hitherto the most popularly employed HTM in *n–i–p* devices, but presents a series of fundamental flaws, such as intrinsic low hole mobility and low conductivity, and the necessity of adding dopants (e.g. lithium *bis*(trifluoromethane)sulfonimide (Li-TFSI) and 4-*tert*-butylpyridine (tBP)) to improve such parameters at the expense of stability, reproducibility and device performances.[6–8]

The "inverted" dopant-free *p-i-n* structure has the potential to yield devices with a higher intrinsic stability,[9] provided that the right materials are used. In this inverted architecture, poly[*bis*(4-phenyl)(2,4,6-trimethylphenyl) amine] (PTAA, Figure 1.17) was established as one of the HTMs of choice, thanks to its proper energy level alignment, excellent carrier mobility, and low-temperature solution processability, allowing to obtain cells with very high $V_{oc}$.[10] Nevertheless, its high hydrophobicity often leads to unsatisfactory perovskite film growth, due to the large surface-energy difference between PTAA and the hydrophilic perovskite precursor solution, requiring modifications in the cell fabrication procedures to improve efficiency.[11–14] In addition, as many polymeric materials, it can suffer from significant batch-to-batch variability, which can affect both its electronic and morphological properties.[15] For these reasons, the development of more efficient HTMs and the optimization of their interface with the perovskite material are the key steps in the further development of PSC devices.[16]

Our contribution in this research area was that of designing and preparing a new family of organic HTMs, alternative to PTAA, possibly by means of a simple and versatile synthetic approach, and investigating their employment for the fabrication of dopant-free solar cells. Among the several species of organic semiconductors described in the literature,[17] donor-acceptor compounds containing phenothiazine (PTZ) rings decorated with triphenylamine (TPA) groups, or related substituents, have already been widely employed as HTMs in perovskite solar cells.[18–26] Such structures combine the excellent electro-optical properties of the TPA system, capable of improving the hole mobility of the resulting compounds,[17] with the favourable features of the PTZ moiety, such as high (photo)chemical stability, good solubility and film-forming properties, ability to form stable radical cations and ease of chemical functionalization of the heterocyclic core.[27] As an example, HTMs designed from a combination of TPA and PTZ moieties, e.g. **PTZ2** reported by Grisorio *et al.*,[28] (Figure 4.1) have shown efficiencies comparable to those obtained with Spiro-OMeTAD.

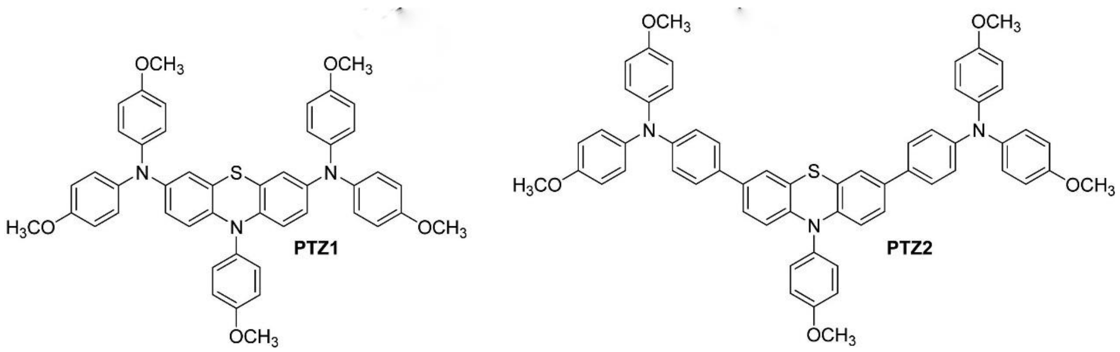

Figure 4.1: *structures of two PTZ-based HTMs.*[28]

Based on the above considerations, we designed the structures of two new small-molecule HTMs, named **BPT-1,2**, still featuring a TPA-PTZ backbone, but characterized by a dimeric structure (Figure 4.2), which had not been investigated before and was expected to impart favourable electronic properties to the compounds.

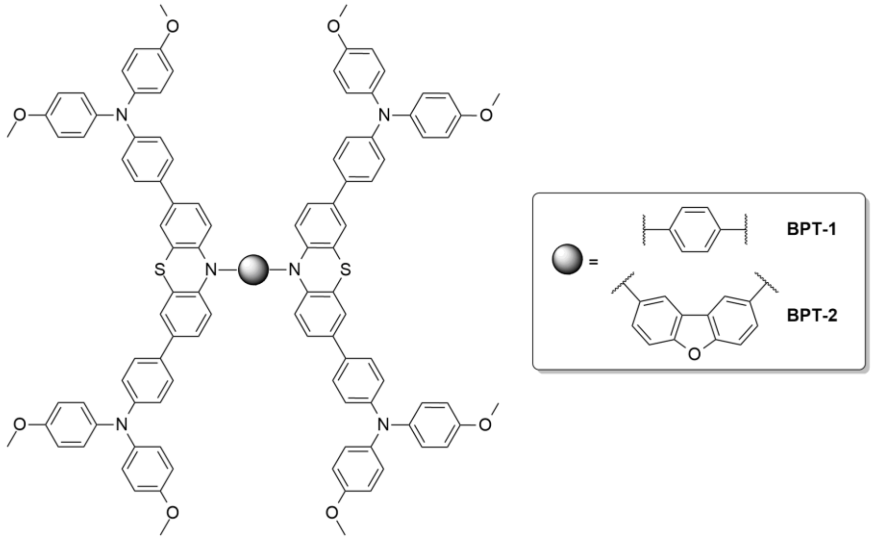

Figure 4.2: *molecular structures of* **BPT-1,2**.

**BPT-1,2** are very electron-rich molecules, formed by the combination of large π-conjugated systems and containing various heteroatoms. They differ only for the central core, which is benzene in **BPT-1**, and dibenzofuran in **BPT-2**. Besides the more electrondonating character of the latter, such a difference would result in a different geometrical orientation of the two (TPA)$_2$PTZ units, which could possibly influence the compounds packing in the solid phase and, in turn, the properties of the interface formed with the other layers of the PSC. The *p*-methoxy substituted TPA, together with the PTZ, should contribute to align HOMO and LUMO levels with VB and CB of hybrid perovskites. In addition, their dimeric structures should favour a wide delocalization of the radical cation spin density. All these features should promote the hole transport process, allowing a better hole extraction and an increase of the charge carriers lifetime.[21,26,29]

## 4.2. Computational analysis

To understand the correlation between the molecular structures and the optoelectronic properties of the designed **BPT-1,2**, a computational study,[30] in collaboration with the group of Prof. Adalgisa Sinicropi (University of Siena), by means of Density Functional Theory (DFT) and Time Dependent Density Functional Theory (TDDFT) methods has been carried out. All QM calculations have been performed using Gaussian09.[31] The structures of **BPT-1,2** have been optimized in vacuo by DFT[32,33] at B3LYP/6-31G(d,p) level of theory.[34,35] Vibrational frequency calculations have been performed at the same level of theory to check that the stationary points were true energy minima. B3LYP/6-311G(d,p) single point calculations at ground-state optimized geometries have been carried out to obtain the ground-state electron density and the frontier molecular orbitals (FMOs), including the solvent effects by the conductor-like polarizable continuum model (C-PCM).[36,37] Analogously to the previous work of Grisorio *et al.*,[28] and to allow a direct comparison to **PTZ2** molecular and electronic properties, $CH_2Cl_2$ was selected as the solvent. Spin densities and absorption maxima of neutral and oxidized states of **BPT-1,2** in $CH_2Cl_2$ have been calculated by means of TDDFT[38,39] at CAM-B3LYP/6-31G(d,p) level,[40] yet using C-PCM. UV–Vis spectra have been simulated with GaussSum considering a Gaussian distribution and an arbitrary line width of 0.03 eV.[41]

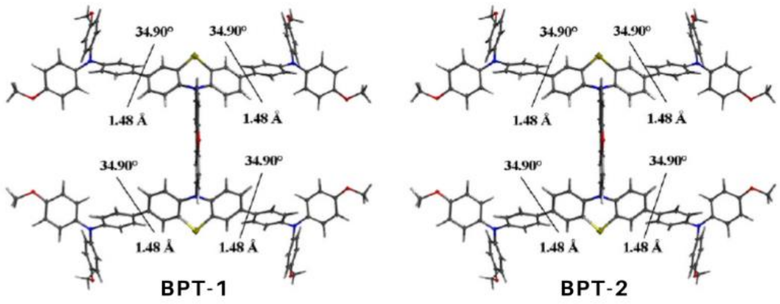

Figure 4.3: DFT-B3LYP/6-31G*(d,p) optimized ground-state molecular geometries of* **BPT-1,2**.

**BPT-1,2** ground-state molecular geometries optimized in vacuo are shown in Figure 4.3. They display similar dihedral angles between the TPA and the PTZ units, ranging between 34° and 35°, while the PTZ N-substituents, which are the core of **BPT-1,2**, adopt a perpendicular position with respect to the lateral chains. To determine if an efficient hole transfer from perovskite to **BPT-1,2** is possible, the FMOs and the ground-state electron density have been calculated. Indeed, an eligible HTM should have the highest occupied molecular orbital (HOMO) and the lowest unoccupied molecular orbital (LUMO) well-aligned with the perovskite valence band (VB) and conduction bands (CB), respectively, to drive the hole extraction and minimize the charge recombination processes, respectively.[24] Moreover, it has been also proven that a wide distribution of HOMO ground-state electron density leads to a larger overlap with the perovskite VB, ensuring a more efficient charge extraction, while LUMO electron density localization within the core of the molecule contributes to block the electron recombination. Therefore, a slight overlap between HOMO and LUMO orbitals is required to assist the formation of excitons and the following hole migration.[25,29,42–45] As shown in Table 4.1, the computed Kohn-Sham energy levels of **BPT-1,2** are in good agreement with those calculated for

Spiro-OMeTAD[44] and **PTZ2**.[28] As required, they are well aligned with the VB and CB of the $CH_3NH_3PbI_3$ perovskite (–5.43 eV and –3.93 eV, respectively)[29,46,47] suggesting an efficient charge extraction, as well as a reduced electron recombination. Moreover, HOMO levels of **BPT-1,2** are in accordance with the experimental HOMO value of Spiro-OMeTAD in $CH_2Cl_2$ (–5.07 eV).[48] Additionally, FMOs of **BPT-1,2** are lower in energy than those of Spiro-OMeTAD calculated at the same level of theory, which should help enhancing the cell $V_{oc}$,[49] and, as reported for Spiro-OMeTAD,[44] HOMO and HOMO−1 levels of **BPT-1,2** are quasidegenerate.

Table 4.1. *FMOs energy levels (eV) of **BPT-1,2** and Spiro-OMeTAD calculated at B3LYP/6-311G(d,p) level of theory in $CH_2Cl_2$, including the solvent effects by C-PCM, compared to those of Spiro-OMeTAD computed in EtOH at B3LYP/6-31G***[44] *and **PTZ2** in $CH_2Cl_2$ at B3LYP/6-311G(d,p) levels of theory.*[28]

| Molecule | HOMO–1 | HOMO | LUMO | LUMO+1 |
|---|---|---|---|---|
| BPT-1 | –4.89 | –4.88 | –1.35 | –1.35 |
| BPT-2 | –4.88 | –4.87 | –1.71 | –1.32 |
| Spiro-OMeTAD | –4.76 | –4.74 | –1.23 | –1.22 |
| Spiro-OMeTAD[44] | –4.45 | –4.42 | –0.83 | –0.80 |
| PTZ2[28] | –5.03 | –4.96 | –1.32 | / |

The inspection of the wavefunction plots of the designed **BPT-1,2** (Figures 4.4 and 4.5) reveals that the LUMO ground-state electron density is confined on the central core of the molecules, while that of the HOMO is fully delocalised over the entire molecules, in line with Spiro-OMeTAD[42] and **PTZ2**.[28] Therefore, the formation of excitons and the following hole migration are promoted by the overlapping between HOMO and LUMO orbitals,[25,29,45] which indicates that **BPT-1,2** should have good intermolecular hole-transport ability.

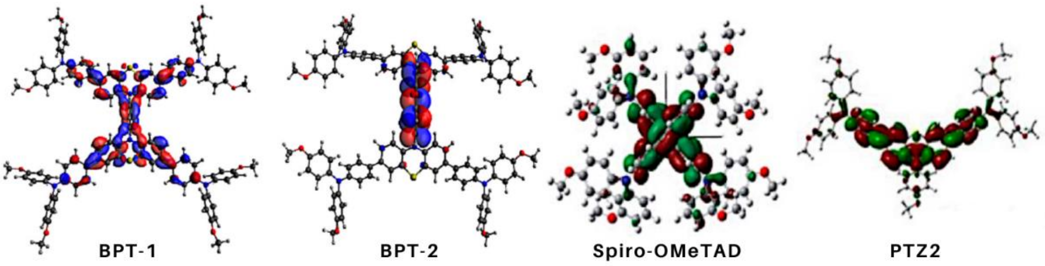

Figure 4.4: LUMO DFT *ground-state electron density distribution of* **BPT-1,2** *compared to those of* Spiro-OMeTAD[44] *and* **PTZ2**.[28]

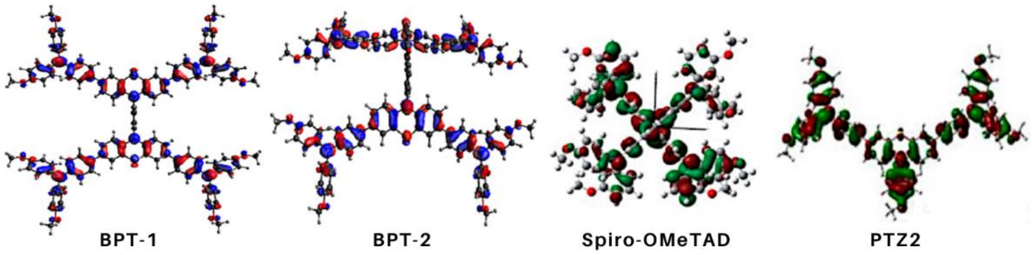

Figure 4.5: *HOMO DFT ground-state electron density distribution of* **BPT-1,2** *compared to those of* Spiro-OMeTAD[44] *and* **PTZ2**.[28]

As the charge transport process involves HTMs also in their radical cation (doublet state) form, to investigate the electronic structure of the oxidized forms of **BPT-1,2**, an electron has been removed from the π-system and the TDDFT spin density distribution of (**BPT-1,2**)$^{\bullet+}$ has been calculated. The results have been compared with those of (Spiro-OMeTAD)$^{\bullet+}$[50] and (PTZ2)$^{\bullet+}$[28]. Indeed, the excellent ability of Spiro-OMeTAD as HTM has already been ascribed to its wide charge distribution in the radical cation state.[50] The wavefunction plot analysis (Figure 4.6) reveals that the singly occupied molecular orbital (SOMO) of (**BPT-1,2**)$^{\bullet+}$ has a similar electronic structure with respect to its analogue ground-state HOMO, as the spin density is widely delocalised over the entire molecules, reproducing the behavior of (Spiro-OMeTAD)$^{\bullet+}$.[50] Moreover, the delocalization is more widespread than that of **PTZ2**. Therefore, this result was a further indication of the favourable hole transport ability of the designed **BPT-1,2**.

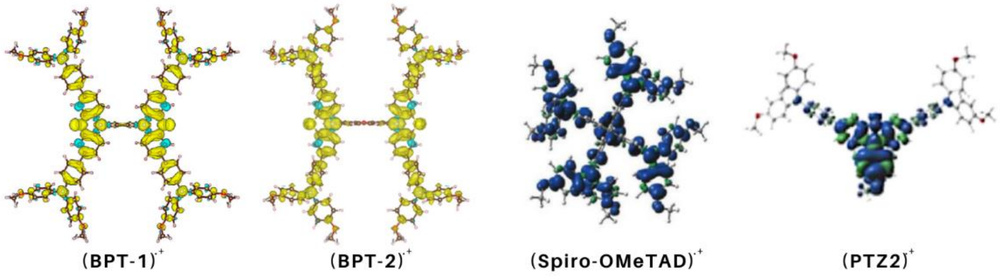

Figure 4.6: TDDFT *spin density distribution of* (**BPT-1,2**)$^{\bullet+}$ *compared to those of* (Spiro-OMeTAD)$^{\bullet+}$[44] *and* (**PTZ2**)$^{\bullet+}$[28].

The vertical excitation properties of HTMs are considered a decisive factor for estimating the performance of PSCs as well.[51] Indeed, HTMs should have minimal light absorption in the visible spectrum to avoid the competition with the perovskite absorption.[4,8,23] Hence, the first 15 excited states of neutral **BPT-1,2** have been computed to exclude a competition with the perovskite absorption. TD-CAM-B3LYP/6-31G(d,p) absorption maxima ($\lambda_{max}$), vertical excitation energies ($E_{exc}$) and oscillator strengths ($f$), computed in $CH_2Cl_2$ on B3LYP/6-31G(d,p) minimized structures, of **BPT-1,2** are reported in Table 4.2. Simulated UV–Vis spectra of **BPT-1,2** are shown in Figure 4.7.

Table 4.2: *TD-CAM-B3LYP/6-31G(d,p) absorption maxima ($\lambda_{max}$ in nm), vertical excitation energy ($E_{exc}$ in eV), oscillator strengths (f) and composition (%) in terms of molecular orbitals in $CH_2Cl_2$ (using C-PCM) of* ***BPT1-2***.

| Molecule | Excited state# | $\lambda_{max}$ | $E_{exc.}$ | f | % Composition |
|---|---|---|---|---|---|
| **BPT-1** | 2 | 337 | 3.68 | 2.79 | 33% H → L<br>31% H–1 → L+1 |
| | 3 | 312 | 3.97 | 1.35 | 24% H → L+3<br>23% H–1 → L+4 |
| | 6 | 301 | 4.12 | 1.73 | 18% H–4 → L<br>14% H–5 → L+1 |
| | 8 | 297 | 4.18 | 0.23 | 24% H–2 → L+9<br>23% H–3 → L+8 |
| | 10 | 296 | 4.18 | 0.16 | 24% H–2 → L+7 |
| | 13 | 280 | 4.42 | 0.07 | 16% H–5 → L+10<br>14% H–4 → L+11 |
| **BPT-2** | 2 | 338 | 3.67 | 2.60 | 32% H–1 → L+1<br>26% H → L+2 |
| | 3 | 312 | 3.98 | 0.55 | 19% H–3 → L+1<br>4% H–1 → L+3 |
| | 4 | 311 | 3.99 | 0.88 | 23% H–2 → L+1<br>20% H → L+4 |
| | 5 | 304 | 4.08 | 1.74 | 22% H–4 → L<br>9% H–3 → L+4 |
| | 7 | 297 | 4.18 | 0.08 | 24% H–2 → L+6<br>22% H–1 → L+7 |
| | 8 | 297 | 4.18 | 0.16 | 24% H–3 → L+6<br>22% H–1 → L+7 |
| | 11 | 291 | 4.26 | 0.34 | 35% H → L<br>6% H–3 → L+4 |

(#) *Only excited states with f > 0.06 are displayed.*

The compounds show very intense absorption maxima, having *f* = 2.79 and 2.60 for **BPT-1** and **BPT-2**, respectively (Figure 4.7 and Table 4.2). Indeed, due to the significant hole and electron distributions overlap present in **BPT-1,2** (Figures 4.4 and 4.5), their transition dipole moments are very high, resulting in very high oscillator strengths.[47] In particular, **BPT-1** absorption maximum with the highest oscillator strength is at 337 nm (3.68 eV) and it is mainly governed by a HOMO → LUMO transition, while the most intense **BPT-2** absorption maximum is at 338 nm (3.67 eV) and it is largely characterized by a HOMO-1 → LUMO+1 transition. Other bands, corresponding to higher energy excitations, are present and they are governed by HOMOs → LUMOs transitions (Table 2). All these absorptions in the UV region of the spectrum do not compete with the perovskite absorption and they could also contribute to amplify the short-circuit current density of PSCs.[49]

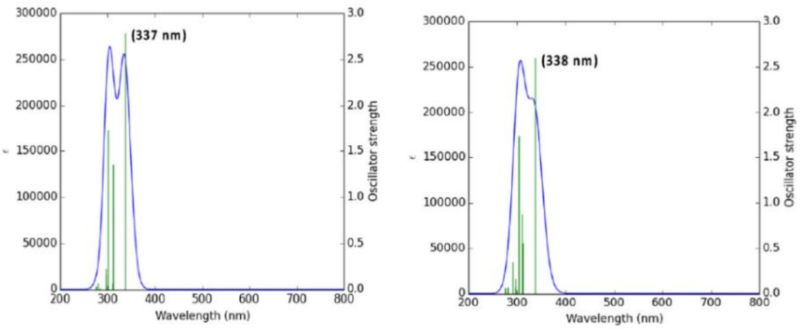

**BPT-1** **BPT-2**

Figure 4.7: *Simulated* TDDFT UV–Vis *absorption spectra in* $CH_2Cl_2$ *of* **BPT-1,2**.

An in-depth computational analysis to investigate the physicochemical interactions of the new HTMs with the surface of the perovskite was carried out in collaboration with the group of Prof. Michele Pavone (University of Naples “Federico II”), together with the group of Prof. Adalgisa Sinicropi (University of Siena).[52] In particular, we selected **BPT-1** as model system and decided to investigate the interfaces of **BPT-1** with the most common perovskite, methylammonium lead iodide (MAPI), with **BPT-1** in contact with either the $PbI_2$- or MAI-terminated MAPI (001) surface. To allow a direct comparison with state-of-the-art and well-known TPA and PTZ-based HTMs, we extended our interfacial study to Spiro-OMeTAD and **PTZ2**.[28] MAPI features temperature-dependent structural phases: the cubic structure has been reported to be the most stable under operating conditions,[53] hence it has been adopted here to model MAPI interactions with **BPT-1**, Spiro-OMeTAD, and **PTZ2**. Two symmetric five-layer slabs of the MAPI (001) surface have been constructed to simulate the two possible MAPI terminations, *i.e.*, $PbI_2$- and MAI-exposing facets, here identified as MAPI:$PbI_2$ and MAPI:MAI. In order to account for the molecule’s complex structure and to obtain reliable energy minima for each termination, different adsorption modes of **BPT-1** have been considered. **BPT-1** has been placed on the MAPI surface either exposing the PTZ or the TPA moieties, which have been labeled as *down* and *up* orientations, respectively. The same strategy and labelling have been adopted also for **PTZ2**. In the case of Spiro-OMeTAD, it has been previously reported that it interacts with the MAPI surface exposing the methoxybenzene of the arylamine moieties,[54–57] thus the up and down orientations refer to the methoxybenzene of the two different facets of the 9,9’-spirobifluorene core. The most stable interfaces of the considered HTMs/MAPI:$PbI_2$ and HTMs/MAPI:MAI systems are shown in Figure 4.8 and Figure 4.9, respectively, together with their binding energies. In particular, the most stable configurations of **BPT-1**/MAPI and Spiro-OMeTAD/MAPI have binding energies in the –1.49/–2.83 eV range for MAPI:$PbI_2$ and –2.14/–5.01 eV range for MAPI:MAI, while the preferred **PTZ2**/MAPI interfaces are the most stable with a binding energy of –7.30 eV in the case of MAPI:$PbI_2$ and –6.08 eV for MAPI:MAI.

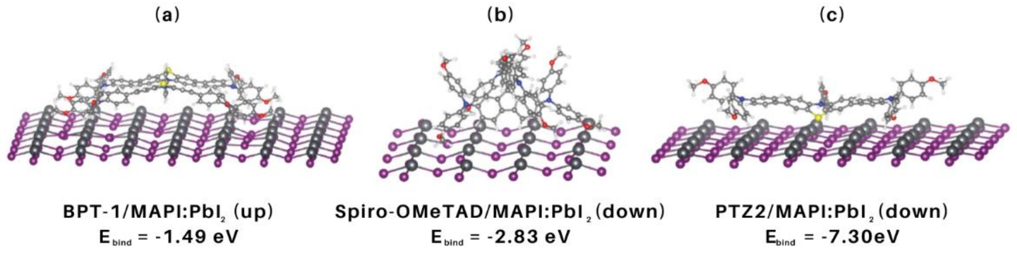

Figure 4.8: *most stable interfaces and corresponding binding energies* ($E_{bind}$) *of* (a): **BPT-1**/MAPI:$PbI_2$, (b) Spiro-OMeTAD/MAPI:$PbI_2$, (c) **PTZ2**/MAPI:$PbI_2$ *systems. Color code: Pb-dark gray; I-violet; C-light grey; N-blue; H-white; O-red; S-yellow.*

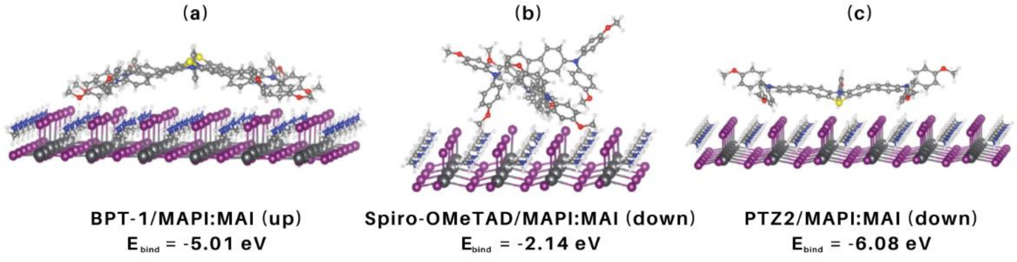

Figure 4.9: *most stable interfaces and corresponding binding energies* ($E_{bind}$) *of* (a): **BPT-1**/MAPI:MAI, (b) Spiro-OMeTAD/MAPI:MAI, (c) **PTZ2**/MAPI:MAI *systems. Color code: Pb-dark gray; I-violet; C-light grey; N-blue; H-white; O-red; S-yellow.*

**BPT-1** preferably adopts the up orientation on both $PbI_2$ and MAI terminations, which causes some distortions in the overall surfaces (Figures 4.8(a) and 4.9(a)) due to the interaction of methoxybenzene of the TPA moieties with the MAPI. In particular, **BPT-1**/MAPI:MAI interaction is stronger than that calculated for **BPT-1**/MAPI:$PbI_2$, due to the formation of some hydrogen bonds between the oxygen atoms of **BPT-1** methoxybenzene groups and the hydrogen atoms of MAPI methylammonium cations. For Spiro-OMeTAD, our calculations are in close agreement with previous results[54–57] reporting the down orientation as the preferred one on MAPI surfaces (Figures 4.8(b) and 4.9(b)). Despite the molecular similarities between **BPT-1** and **PTZ2**, the latter gets stabilized by adopting the down orientation on both MAPI (001) terminations (Figures 4.8(c) and 4.9(c)).

The electronic properties of the investigated HTMs/MAPI systems have also been analysed in terms of their projected density of states (pDOS). The pDOS plots of the most stable interfaces of HTMs/MAPI:$PbI_2$ and HTMs/MAPI:MAI systems are depicted in Figure 4.10 and Figure 4.11, respectively. Regarding $PbI_2$-terminated surfaces (Figure 4.10), the pDOS reveal that the valence band minimum (VBM) of MAPI lies at a slightly higher energy than the HOMO level of **BPT-1** and **PTZ2** (Figure 4.10(a and c)). Thus for the standard MAPI perovskite, there is no adequate driving force for the hole-injection process and undesired charge recombination events can occur. Differently, in the case of Spiro-OMeTAD, the pDOS highlights a slight, but convenient driving force for the hole injection at the MAPI:$PbI_2$ interfaces.

Indeed, the HOMO levels of Spiro-OMeTAD are slightly higher in energy than the MAPI VB edge, thus granting a convenient extraction of the hole from the photo-excited MAPI. As for HTMs/MAPI:MAI interfaces (Figure 4.11), the VBM of MAPI is higher in energy than the HOMO levels of all HTMs considered. Thus, these interfaces, although energetically very stable, do not provide a sufficient driving force for the holes to be injected into the HTMs.

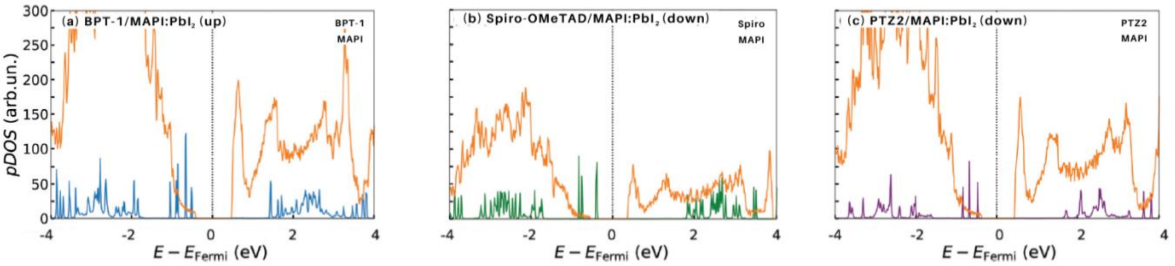

Figure 4.10: pDOS *plots of* (a) **BPT-1**/MAPI:PbI$_2$ (*up*), (b) Spiro-OMeTAD/MAPI:PbI$_2$ (*down*), *and* (c) **PTZ2**/MAPI:PbI$_2$ (*down*), *computed at* GGA-PBE, *including* D3BJ *dispersion forces*.

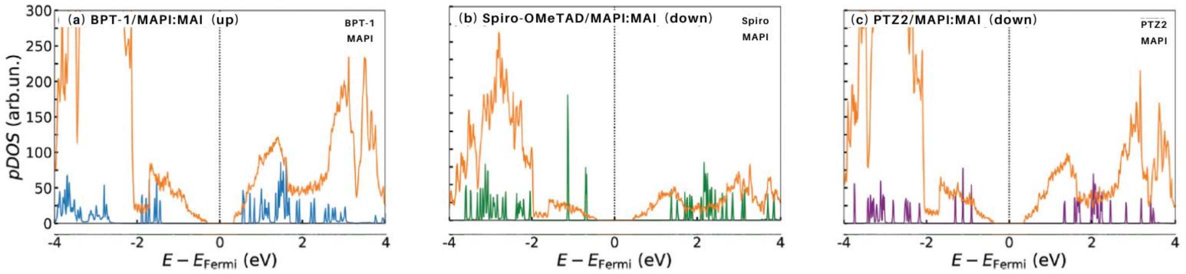

Figure 4.11: pDOS *plots of* (a) **BPT-1**/MAPI:MAI (*up*), (b) Spiro-OMeTAD/MAPI:MAI (*down*), *and* (c) **PTZ2**/MAPI:MAI (*down*), *computed at* GGA-PBE, *including* D3BJ *dispersion forces*.

Considering these results, the prototypical MAPI perovskite has resulted in an inefficient charge transport process when combined with TPA and PTZ-based molecules. Chemical doping of **BPT-1** could be considered as a valid approach to increase its HOMO energy level, but, since isolated **BPT-1**, as well as **BPT-2**, possesses optimal properties to be used as a dopant-free HTM and it is well known that the doping could lead to perovskite degradation,[4,8,15,58–60] an alternative and valid strategy could consist in the exploration of different kinds of perovskite compositions to understand the potential of this molecules in PSC devices.

## 4.3. Synthesis of compounds **BPT-1** and **BPT-2**

Compounds **BPT-1,2** were prepared by following a common synthetic route involving first elongation of the central aromatic core by introduction of the intermediate acceptor PTZ ring, and subsequent decoration of the resulting intermediates with the terminal donor triarylamine groups.[61] The sequence was designed in such a way that key carbon-carbon or carbon-nitrogen bonds could be formed by means of metal-catalysed cross-coupling reactions or related transformations, that are, as we have already discussed in Chapter 2, a key technology for the preparation of these kind of conjugated materials.

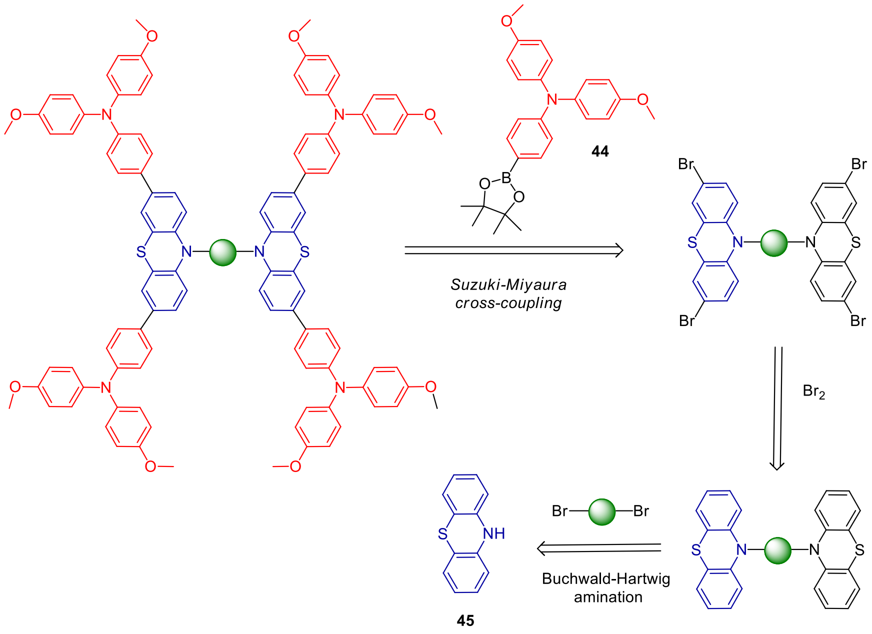

Scheme 4.1*: retrosynthetic approach for* HTMs **BPT-1** and **BPT-2**

The synthetic approach used for both HTMs **BPT-1** and **BPT-2** is reported in Scheme 4.1**.** The two compounds were assembled starting from the appropriate 1,4-dibromoaryl derivatives using a three-step sequence, constituted by a double amination with phenothiazine **45**, bromination of the resulting intermediate and final Suzuki-Miyaura coupling between the obtained tetrabromide and boronic ester **44**.

## 4.3.1. Synthesis of donor thiphenylamine **44**

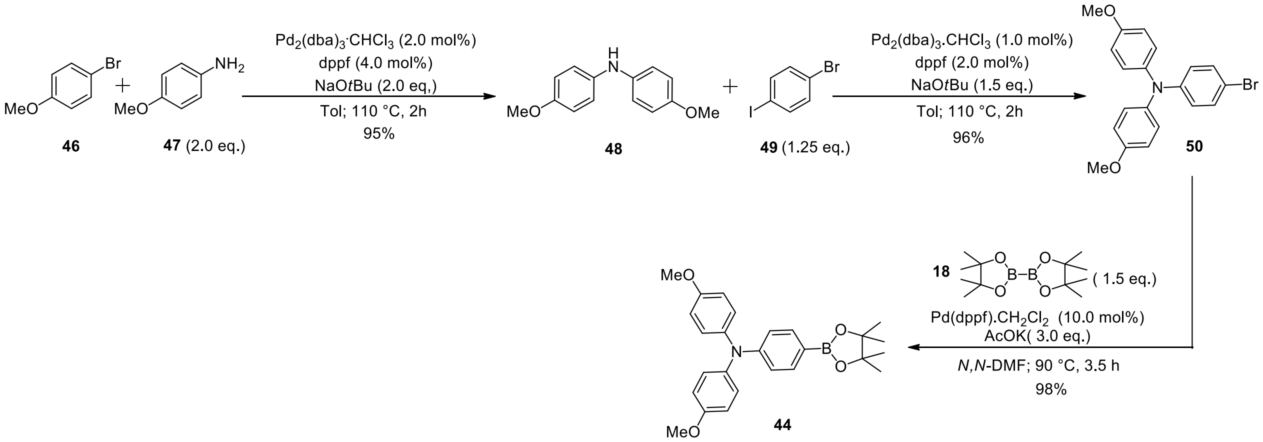

Scheme 4.2*: synthesis of donor triphenylamine* ***44***

First of all, intermediate **44** was prepared following the synthetic sequence reported in Scheme 4.2. The first step involved the formation of dianisylamine **48** through a Buchwald-Hartwig amination reaction, carried out using two simple commercial reagents, 1-bromo-4-methoxybenzene **46** and 4-methoxyaniline **47** as starting materials**.** The latter was used in excess, in order to minimize the formation of a tertiary amine. The catalytic species was formed in situ using $Pd_2(dba)_3{\cdot}CHCl_3$ as metal precursor and 1'-*bis*(diphenylphosphinoferrocene) (dppf) as ligand. At the end of the reaction, the purification of product **48** via column chromatography was performed, allowing its isolation with a yield of 95%. A second Buchwald-Hartwig amination, carried out under the same reaction conditions, allowed to obtain compound **50**. To this end, the dianisylamine **48** was reacted with the commercial product 1-bromo-4-iodobenzene **49**, once again used in excess to induce the complete conversion of the amine. The different reactivity of the two carbon-halogen bonds on compound **49** allowed to selectively replace the iodine atom, leaving the bromine atom unreacted and giving intermediate **50** in high yield. In the last step, we used the Miyaura protocol to transform bromide **50** into boronate **44**, using *bis*(pinacolate)diboron **18** in the presence of a palladium(II) complex and a weak base such as potassium acetate. After a chromatographic purification, which was complicated by the poor solubility of the product, compound **44** was recovered in 97% yield.

## 4.3.2. Synthesis of **BPT-1**

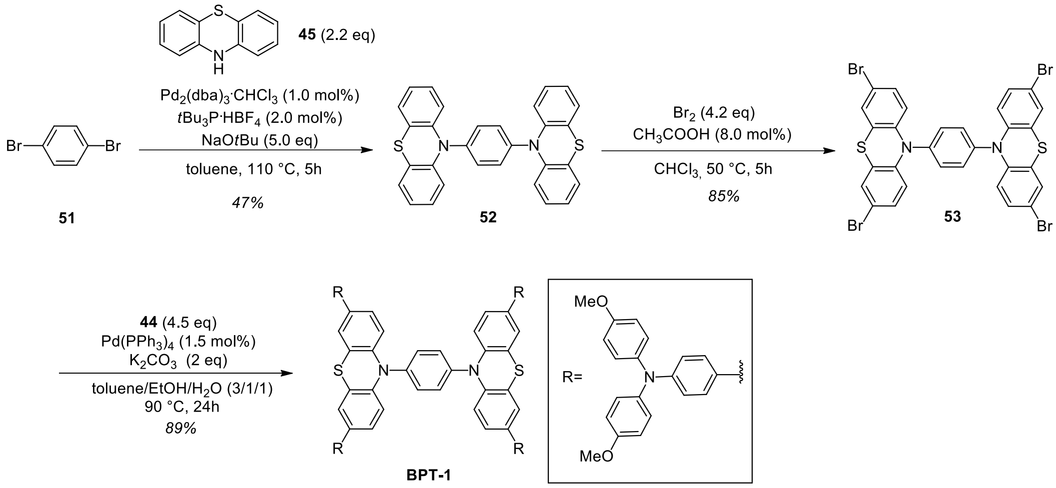

Scheme 4.3*: synthesis of **BPT-1**.*

The preparation of **BPT-1** is reported in Scheme 4.3. Starting from 1,4-dibromobenzene **51**, a double amination with phenothiazine **45** was performed, using an excess of the latter in order to obtain a total conversion. Classical Buchwald-Hartwig coupling conditions, with $Pd_2(dba)_3{\cdot}CHCl_3$ as catalyst precursor, *t*-$Bu_3P$ as ligand and NaO*t*Bu as base, gave compound **52** in satisfactory yield (47%) after purification. In the subsequent step, tetrabromination of **52** was carried out. An excess of $Br_2$ was necessary for total conversion, and therefore during the work-up it was essential to quench the reaction with sodium thiosulfate ($Na_2S_2O_3$) in order to reduce any unreacted bromine and make it possible to purify the final product by precipitation. Tetrabrominated intermediate **53** was obtained in 85% yield and was reacted with the previously prepared boronic ester **44**, under classical Suzuki-Miyaura reaction conditions, giving the desired product **BPT-1** whit an excellent yield after purification (89%).

### 4.3.3. Synthesis of **BPT-2**

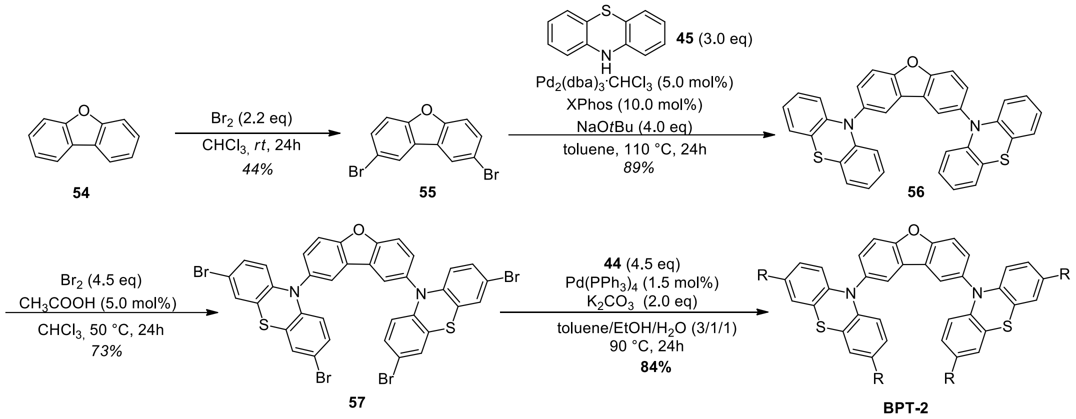

Scheme 4.4*: synthesis of **BPT-2**.*

The synthesis of **BPT-2** is reported in Scheme 4.4. Following the same synthetic approach as for **BPT-1**, in this case access to dibromide **55** was granted by bromination of commercially available dibenzofuran **54.** The reaction was performed using an excess of $Br_2$ and chloroform as the solvent, under nitrogen atmosphere which was essential to obtain a good conversion. Dibromide **55** was then isolated by precipitation from the reaction mixture. Compound **55** was then reacted with phenothiazine **45** under Buchwald-Hartwig conditions, using $Pd_2(dba)_3{\cdot}CHCl_3$ (5.0 mol%) as catalyst precursor, XPhos (10.0 mol%) as ligand and toluene as solvent. After work-up and purification, intermediate **56** was recovered in high yield (89%). Then, tetrabromination of **56** was carried out with an excess of $Br_2$, keeping the temperature at 50 °C, which proved to be essential for obtaining tetrabromide **57** with a satisfying yield (73%). Finally compound **57** was reacted with the previously prepared boronic ester **44**, under classical Suzuki-Miyaura reaction conditions, giving the desired product **BPT-2** with an excellent yield after purification (84%).

Following the above-described synthetic routes, compounds **BPT-1** and **BPT-22** could thus be prepared in overall yields of 35% and 24%, respectively.

## 4.4. Spectroscopic and electrochemical characterization

The thermal stability of compounds **BPT-1,2** was assessed by means of a TGA (thermogravimetric analysis) measurement. Both HTMs proved remarkably stable, maintaining at least 95% of their weight up to 410°C for **BPT-1** and 385°C for **BPT-2**, respectively (Figure 4.12c). Both values are much higher than those usually reached in a PSC under operation, demonstrating that the compounds are thermally robust enough for employment in the devices.

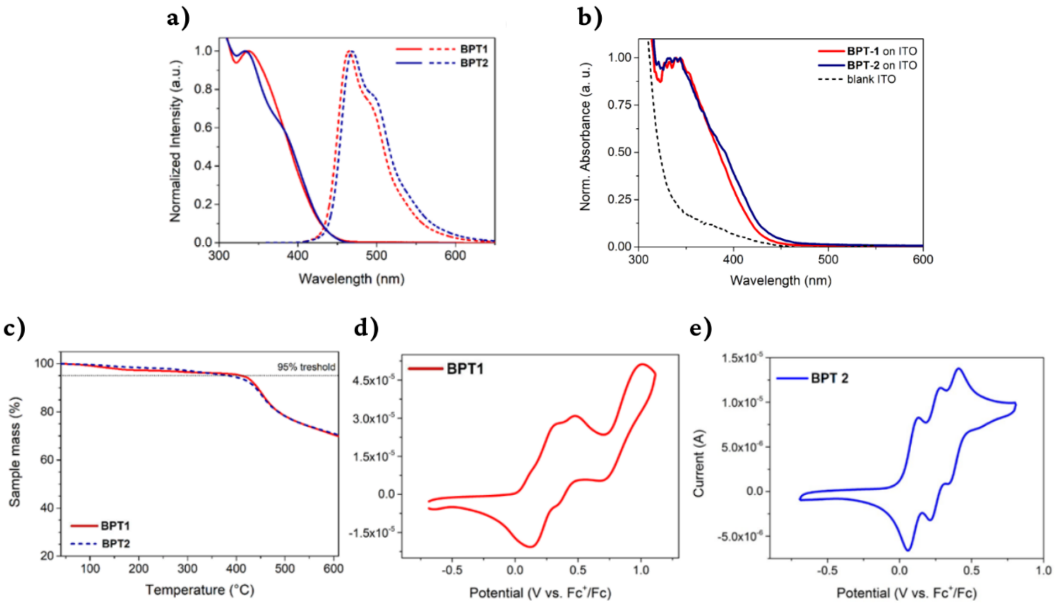

Figure 4.12*: (a) normalized absorption (solid lines) and fluorescence emission (short dash lines) spectra of compounds **BPT-1,2** in toluene solution; (b) normalized DRS UV-Vis spectra of compounds **BPT-1** and **BPT-2** deposed on ITO-coated glass sheets. The corresponding spectrum of bare ITO is reported as a reference; (c) thermogravimetric analysis (TGA) relative to **BPT-1** (solid red line) and **BPT-2** (dash blue line). Cyclic voltammetry of compounds **BPT-1** (d) and **BPT-2** (e) in dichloromethane solution*.

Then, we determined the spectroscopic characteristics of the compounds by recording their UV-Vis absorption and fluorescence emission spectra in toluene solution. In good agreement with the computational studies,[30,52] both species presented intense light absorption in the UV region (Table 4.3), well below the visible range, with maxima in the 333-338 nm interval (Figure 4.12a, solid lines), indicating that they should not be interfering with visible light absorption by the perovskite layer.

Table 4.3: *Spectroscopic and electrochemical properties of compounds* BPT-1 *and* BPT-2*.*

| HTM | $\lambda_{abs.}$ [nm][a] | ε (× $10^4$) [$M^{-1}$ $cm^{-1}$][a] | $\lambda_{emi.}$ [nm][a] | $E_{0-0}$ [eV][b] | $E_{ox.}$ [V][c] | $E_{HOMO}$ [V][d] | $E_{LUMO}$ [V][e] |
|---|---|---|---|---|---|---|---|
| BPT-1 | 338 | 8.1 | 465 | 2.84 | +0.24 | −5.39 | −2.55 |
| BPT-2 | 333 | 9.5 | 470 | 2.86 | +0.10 | −5.25 | −2.39 |

*[a] Measured in toluene solution; [b] Determined from the wavelength of intersection between the normalized absorption and emission spectra; [c] Measured in dichloromethane solution with ferrocene as internal standard; [d] Determined from the $E_{ox}$ value, see Experimental Section for details; [e] Calculated from the equation: $E_{LUMO} = E_{HOMO} - (-E_{0-0})$.*

This observation was confirmed by inspection of the corresponding UV-Vis absorption spectra of thin films of the two compounds deposed on ITO (Figure 4.12b) obtained by DRS, which also showed absorption bands located mostly below 400 nm. By registering the corresponding fluorescence emission spectra, for both compounds it was possible to estimate the $E_{0-0}$ values (zero-zero transition energy, defined as the energy difference between the lowest vibrational level of the first excited electronic state and the lowest vibrational level of the ground electronic state) by applying the following equation:

$$E_{0\text{-}0} = hc / \lambda_{int} \tag{4.1}$$

where $h$ is Planck constant, $c$ the speed of light, and $\lambda_{int}$ represents the wavelength (in nm) of intersection between the normalized absorption and emission spectra, obtaining values comprised in the 2.84-2.86 eV range (Table 4.3). Such values confirmed that the optical bandgap of the compounds was much larger than that of the perovskite used in this work, minimizing the risk of parasitic light absorption, and that their frontier energy levels were well-aligned for employment as HTMs in perovskite solar cells (see discussion below and Table 4.3).

Finally, the redox properties of compounds **BPT-1,2** were investigated by means of cyclic voltammetry in $CH_2Cl_2$ solution, employing ferrocene as a standard reference (Figure 4.12d-e). Both species gave quasi-reversible first oxidations and presented more than one oxidation peak in the scanned interval, as could be expected from symmetrical molecules bearing more than one donor group. $E_{ox}$ potentials *vs.* the $Fc^+/Fc$ couple were found to be +0.24 V for **BPT-1** and +0.10 V for **BPT-2**, corresponding to HOMO levels of −5.39 eV and −5.25 eV vs. vacuum, respectively: expectedly, the more electron-rich core of **BPT-2** caused a slight destabilization of the HOMO level compared to **BPT-1**. Such values are less negative than that of the valence band of perovskite species used in this work (−5.96 eV, *see below*), thus confirming the ability of the phenothiazine-based molecules to work as HTMs in the projected devices (see Figure 4.17a for a band alignment diagram). By subtracting the $E_{0\text{-}0}$ values estimated with the spectroscopic experiments from the HOMO energy levels stemming from cyclic voltammetry, LUMO levels for both HTMs could be determined (Table 4.3): in both cases they were largely less negative than the perovskite conduction band level (−4.33 eV), indicating that a significant barrier exists against charge recombination after hole injection in the perovskite layer. From these results, we could assess that the new synthesized compounds showed optimal properties for their employment in inverted, methylammonium-free perovskite solar cells, therefore both were employed for device fabrication.

## 4.5. Solar Cells Fabrication

The solar cell fabrication process was conducted by the group of prof. A. Di Carlo in the laboratories of the Center for Hybrid and Organic Solar Energy (C.H.O.S.E.) of the University of Rome Tor Vergata. Before starting the solar cells fabrication process, we first assessed the hydrophilicity of the different HTLs deposed on ITO by means of contact angle measurements with pure water. As expected, based on the compounds structure, the measurement revealed a higher hydrophilicity of **BPT-1** and **BPT-2** films compared to a PTAA layer, with measured contact angles of 69.6°, 57.7° and 87.5°, respectively. Then, we conducted a solubility and concentration study on the new HTMs using toluene as a solvent for film deposition, as usually done for the PTAA layer. After vigorous overnight stirring, both **BPT-1** and **BPT-2** were dissolved up to a concentration of 5 mg $mL^{-1}$.

For both compounds, we prepared solutions at three different concentrations, 1, 3, and 5 mg $mL^{-1}$, and used them for film deposition on ITO. Then, inverted PSC devices with the architecture SLG / ITO / HTL / $Cs_{0.17}FA_{0.83}Pb(I_{0.9}Br_{0.1})_3$ / $C_{60}$ / BCP / Cu were built, and a complete study of their electrical parameters was performed, whose results are shown in Table 4.4, alongside those of a similar optimization study conducted for PTAA. It must be pointed out that device structure was kept purposely as simple as possible, without the introduction of interlayers or use of interface passivation agents, to find the best conditions for the subsequent scale-up process. In these initial tests, we found that both **BPT-1** and **BPT-2** showed the best performances within the chosen solar cell configuration when deposited at 3 mg mL$^{-1}$, while for PTAA the optimal concentration was 2 mg mL$^{-1}$.

Table 4.4: *Electrical parameters for* PTAA, **BPT-1** *and* **BPT-2***-based devices at different concentration, with average on 12 samples ± standard deviation for each tested concentration, extracted by the J–V curves acquired at 1 Sun irradiation.*

| HTM | Concentration [mg mL$^{-1}$] | | *PCE* [%] | $J_{sc}$ [mA cm$^{-2}$] | $V_{oc}$ [V] | *ff* [%] |
|---|---|---|---|---|---|---|
| PTAA | 1 | Best | 17.25 | 21.35 | 1.02 | 79.21 |
| | | Average | 16.61±0.64 | 20.98±0.45 | 0.99±0.02 | 77.89±2.45 |
| | **2** | **Best** | **17.96** | **21.99** | **1.02** | **80.85** |
| | | **Average** | **16.78±0.66** | **21.69±0.21** | **1.01±0.01** | **78.47±1.90** |
| | 3 | Best | 17.20 | 21.64 | 1.00 | 79.50 |
| | | Average | 16.59±0.84 | 21.32±0.44 | 0.98±0.02 | 74.23±5.67 |
| BPT-1 | 1 | Best | 16.34 | 21.88 | 1.02 | 72.26 |
| | | Average | 15.31±1.07 | 20.85±0.82 | 0.99±0.02 | 71.34±2.36 |
| | **3** | **Best** | **17.26** | **22.24** | **1.03** | **75.34** |
| | | **Average** | **16.89±0.18** | **22.01±0.26** | **1.03±0.01** | **74.70±0.92** |
| | 5 | Best | 15.90 | 21.59 | 1.03 | 71.54 |
| | | Average | 15.41±0.44 | 21.12±0.50 | 1.01±0.04 | 69.57±2.05 |
| BPT-2 | 1 | Best | 16.06 | 21.50 | 1.01 | 73.99 |
| | | Average | 15.88±0.24 | 21.05±0.46 | 1.00±0.02 | 71.68±2.38 |
| | **3** | **Best** | **16.71** | **21.53** | **1.03** | **75.09** |
| | | **Average** | **16.57±0.16** | **21.34±0.41** | **1.02±0.01** | **72.80±1.60** |
| | 5 | Best | 15.81 | 21.43 | 1.01 | 73.06 |
| | | Average | 14.59±1.27 | 20.73±0.69 | 0.98±0.03 | 71.13±2.13 |

Furthermore, the dependency of cell performances on HTL thickness was studied by varying spin coating speed parameters, going from 4000 up to 6000 rpm (Table 4.5); the best maximum and average values were found for all HTMs at 5000 rpm. Accordingly, in Figure 4.13, a comparison between PTAA, **BPT-1** and **BPT-2** as hole transport layers (HTL) has been reported, in which the optimized fabrication parameters were employed.

Table 4.5: *Electrical parameters for* PTAA, **BPT-1** *and* **BPT-2** *based devices at different spin coating speeds, with average on 8 samples ± standard deviation for each tested condition, extracted by the J–V curve acquired at 1 Sun irradiation. The concentration used in these experiments was fixed at 3 mg mL$^{-1}$ for all samples.*

| HTM | Spin coating speed [rpm] | | *PCE* [%] | $J_{sc}$ [mA cm$^{-2}$] | $V_{oc}$ [V] | *ff* [%] |
|---|---|---|---|---|---|---|
| PTAA | 4000 | Best | 17.24 | 21.55 | 0.99 | 80.25 |
| | | Average | 16.66±0.61 | 21.12±0.44 | 0.97±0.03 | 76.00±4.21 |
| | **5000** | **Best** | **17.96** | **21.99** | **1.02** | **80.85** |
| | | **Average** | **16.78±0.66** | **21.69±0.21** | **1.01±0.01** | **78.47±1.90** |
| | 6000 | Best | 17.28 | 21.56 | 1.00 | 80.15 |
| | | Average | 16.47±0.85 | 21.22±0.39 | 0.97±0.04 | 77.56±3.42 |
| BPT-1 | 4000 | Best | 16.68 | 21.85 | 1.02 | 74.88 |
| | | Average | 16.02±0.71 | 21.67±0.19 | 1.01±0.01 | 73.22±1.67 |
| | **5000** | **Best** | **17.26** | **22.24** | **1.03** | **75.34** |
| | | **Average** | **16.89±0.18** | **22.01±0.26** | **1.03±0.01** | **74.70±0.92** |
| | 6000 | Best | 16.75 | 22.12 | 1.01 | 75.01 |
| | | Average | 16.10±0.66 | 21.99±0.14 | 0.99±0.02 | 73.98±1.04 |
| BPT-2 | 4000 | Best | 16.39 | 21.44 | 1.02 | 74.99 |
| | | Average | 15.68±0.75 | 20.88±0.67 | 1.01±0.01 | 74.36±0.76 |
| | **5000** | **Best** | **16.71** | **21.53** | **1.03** | **75.09** |
| | | **Average** | **16.57±0.16** | **21.34±0.41** | **1.02±0.01** | **72.80±1.60** |
| | 6000 | Best | 16.33 | 21.55 | 1.02 | 74.32 |
| | | Average | 15.90±0.44 | 21.26±0.32 | 1.01±0.01 | 74.08±0.26 |

Under these conditions, PTAA, **BPT-1**, and **BPT-2** showed champion power conversion efficiencies (PCEs) of 17.96%, 17.26%, and 16.71%, respectively (Tables 4.4 and 4.5 and Figure 4.13). In general, devices with PTAA presented PCE with a wider standard deviation, which was of ± 0.65%, while those of **BPT-1** and **BPT-2** were of ± 0.18% and ± 0.16% respectively. As a result, the average efficiency obtained with **BPT-1** (12 cells) was even slightly higher than that recorded with PTAA (Tables 4.4 and 4.5). The reduced standard deviation of **BPT-1** and **BPT-2** devices compared to PTAA, being related with the general device reproducibility and the feasibility of the device fabrication, is an important parameter to highlight, especially in the perspective of building larger devices (with active areas > 1 cm$^2$). The higher reproducibility of BPT-based PSCs compared to those built with PTAA could stem from various factors, mainly related to the morphology of the individual layers and the nature of their interfaces, which could also have an influence on device stability (paragraph 4.7).

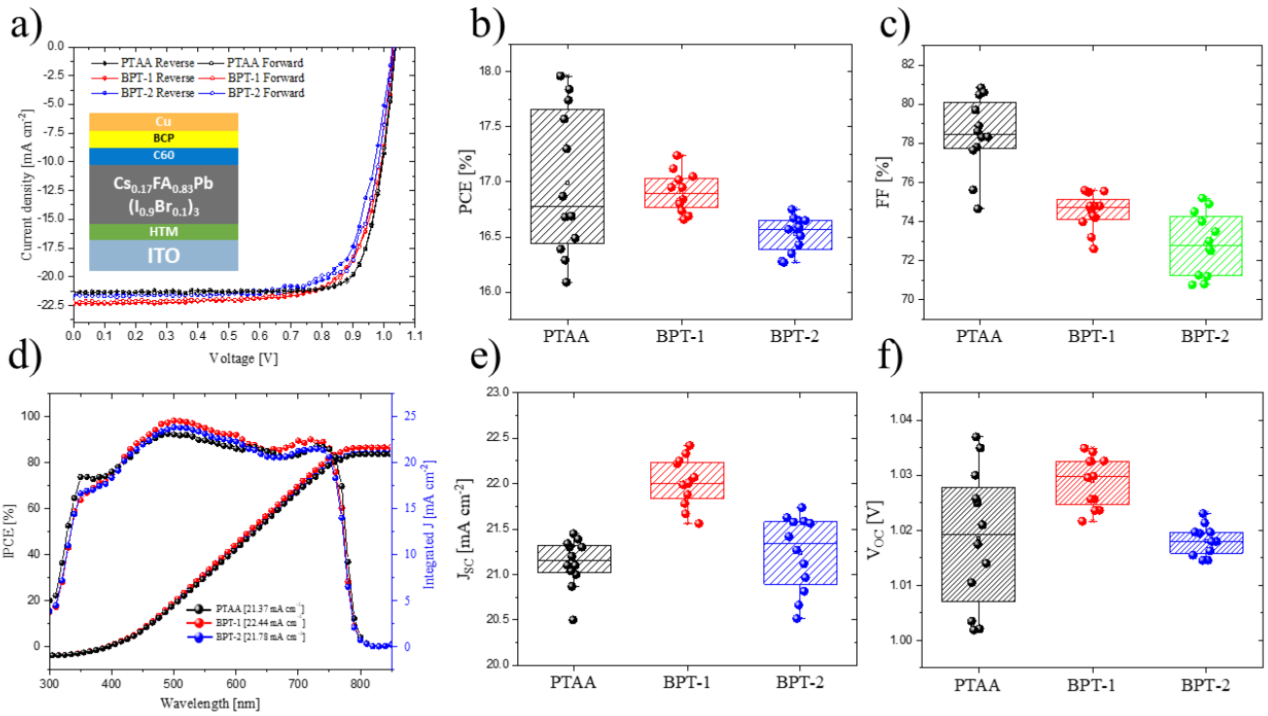

Figure 4.13: *(a) J-V curves under reverse and forward scan of the best device fabricated, with a schematic of the device stack employed. Box charts of the electronic parameters extrapolated from J-V curves on 12 samples per HTL type used, comparing PCE (b), ff (c),* $J_{SC}$ *(e) and* $V_{OC}$ *(f). IPCE curves of the best device fabricated (d).*

To shed light on these aspects, we first registered SEM images of the **BPT-1** and PTAA layers deposed on ITO (Figure 4.14). As can be seen from the images, in both instances a full coverage of the conductive substrate was obtained, but the HTL morphology appeared more homogenous in the case of the small-molecule hole conductor, which is in good agreement with the excellent adhesion of perovskite on top of this HTM (*see below*) and could result in an enhanced stability of the corresponding devices. Then, we investigated the wettability of the HTLs with the precursor perovskite solution. To this end, we first conducted contact angle measurements of HTLs deposed on ITO (Figure 4.15), in which the PTAA layer displayed an angle of 17.6° compared with **BPT-1** and **BPT-2**, with contact angles of 11.7° and 11.2°, respectively, demonstrating their better wettability. This was confirmed by visual inspection of the films shown in Figure 4.17b, where a better interface adhesion between HTL and perovskite is clearly evidenced for the two small-molecule hole conductors. Notably, the wettability improvement was obtained without any UV pre-treatment, highlighting the beneficial effect of the higher surface hydrophilicity of **BPT-1** and **BTP-2**.

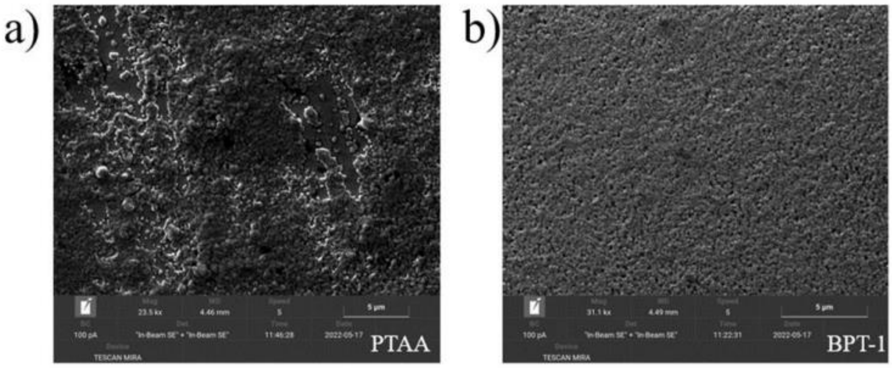

Figure 4.14: SEM *top view image of* PTAA *(a) and* **BPT-1** *(b) deposed over glass/*ITO *substrate. The scale bar shown on bottom right is 5 µm*.

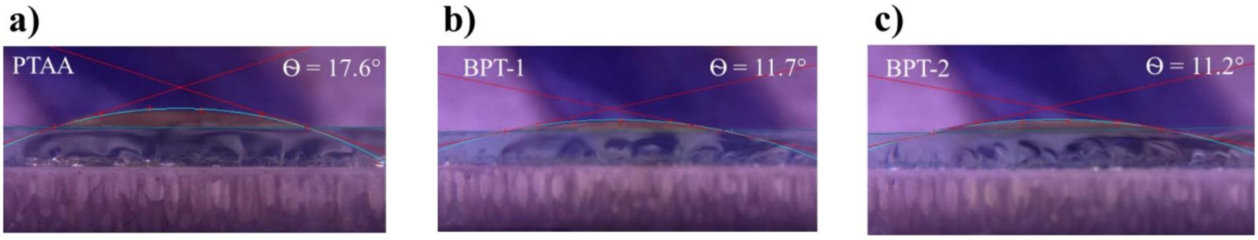

Figure 4.15: *contact angle measurement of one drop (≈14 µL) of perovskite solution (the same used for solar cell fabrication) deposed over spin-coated* PTAA *(a),* **BPT-1** *(b) and* **BPT-2** *(c) layers.*

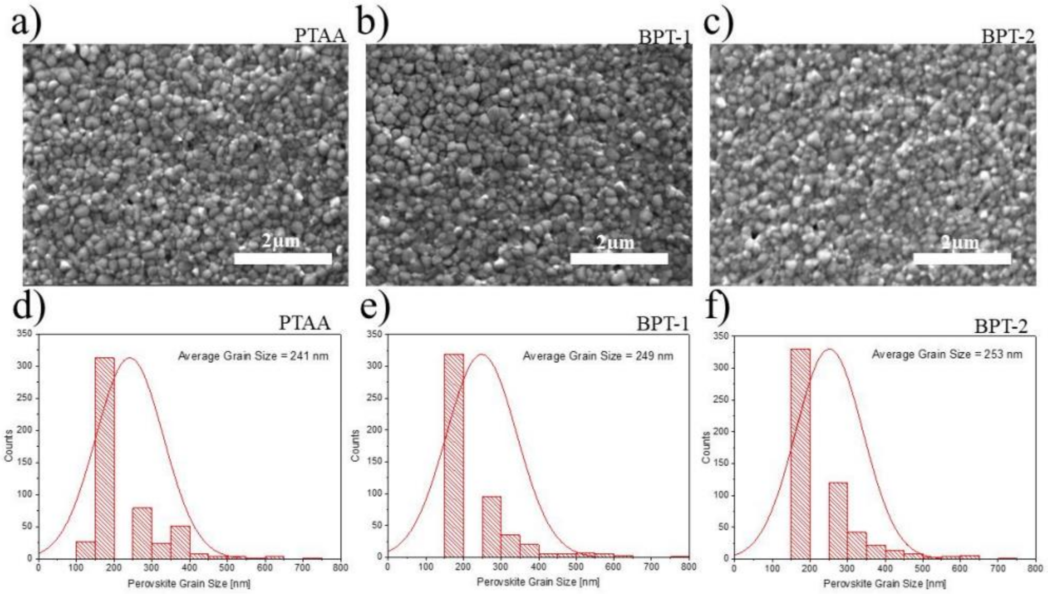

Figure 4.16: SEM *top view image of perovskite deposed over* PTAA *(a),* **BPT-1** *(b) and* **BPT-2** *(c) layers, deposed on a glass/*ITO *substrate. Scale bar indicated is 2 µm. Corresponding perovskite grain size distribution over* PTAA *(d),* **BPT-1** *(e) and* **BPT-2** *(f).*

SEM experiments conducted on the perovskite layer deposed on the three HTLs (Figure 4.16a-c) showed that its morphology was similar in all cases. Interestingly, however, statistical analysis (Figure 4.16d-e) revealed that grain size distribution was slightly different among the three samples, with the average perovskite grain size increased by 8 nm in the case of **BPT-1**, and by 12 nm in the case of **BPT-2**, in comparison with reference PTAA, that showed an average grain size of 241 nm: this behaviour might also help to explain to the better stability of the complete devices built with **BPT-1** (for a discussion, see below, paragraph 4.7). **BPT-1**-containing devices displayed an average current density ($J_{sc}$) of 22.01 ± 0.26 mA cm$^{-2}$, higher than those of PTAA and **BPT-2**, with average $J_{sc}$ values of 21.69 ± 0.21 mA cm$^{-2}$ and 21.34 ± 0.41 mA cm$^{-2}$, respectively, as also confirmed by IPCE measurements of the best device for each configuration (Figure 4.13d). Remarkably, $J_{sc}$ values stemming from *J/V* measurements were in very good agreement with those derived from integration of the IPCE curves. Average $V_{oc}$ was similar in all cases, with approx. 20 mV and 10 mV improvement for **BPT-1** and **BPT-2** compared to PTAA, respectively, as shown in Tables 4.4 and 4.5. Conversely, *ff* is reduced by using both **BPT-1** and **BPT-2** compared with PTAA: this parameter was found to be dependent on solution concentration and layer thickness, since the best *ff* values of 75.34% and 75.09% for **BPT-1** and **BPT-2**, respectively, were found at the optimized film deposition conditions of 3 mg mL$^{-1}$ and 5000 rpm (Tables 4.4 and 4.5). Nevertheless, the fill factor decrease compared to PTAA could probably be related to the different properties of small-molecule hole conductors compared to polymers, with the latter generally showing a tendency to form more compact layers and, therefore, limit resistive losses in the device.

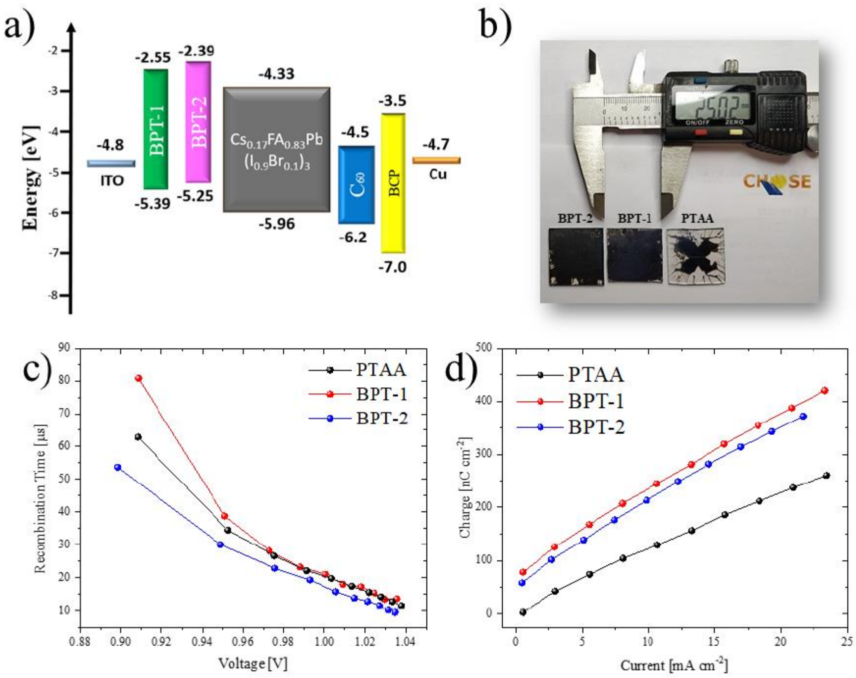

Figure 4.17: *(a) Band alignment of the perovskite solar cell stack used. (b) Picture of the perovskite layer deposited on top of* PTAA, **BPT-1** *and* **BPT-2**. *(c) Transient photovoltage* and (*d*) *charge extraction study of the three devices analyzed.*

To further understand current and voltage improvement on **BPT-1** and **BPT-2** based devices, we carried out transient photovoltage (TPV) and photocurrent (TPC) measurements, as shown in Figure 4.17c and 4.17d, respectively. The photogenerated charge lifetimes are evaluated with a small perturbation TPV test at different irradiation levels. Figure 4.17c shows the time constant extracted from a single exponential fit of the voltage decay profiles; in particular, at low irradiation levels, charges are localized at interfaces with increased spatial separation, resulting in higher lifetimes respect to PTAA. Such an operating region is where the **BPT-1** devices exhibit longer recombination times, meaning that the use of **BPT-1** results in reduced surface traps. Conversely, at high irradiation levels all devices exhibit shorter and similar recombination times, consistent with their comparable $V_{oc}$ values despite the differing HOMO levels, in agreement with literature reports.[62–64] In addition, the extracted charges *vs.* current density have been evaluated from TPC analysis and plotted in Figure 4.17d. We can observe that both **BPT-1** and **BPT-2** devices exhibited improved carrier extraction efficacy in comparison to PTAA over the entire range of light intensities. For this reason, we speculate that the use of **BPT-1** on one hand reduces the number of recombination centers, and on the other results in a more efficient perovskite regeneration process, boosting the photocurrent values.

## 4.6. Scaling-up Process

In the upscaling process of the perovskite technology from small (active area < 1 cm$^2$) to module size (interconnection of different cells) some energy losses can occur, which are related to the following phenomena: front contact sheet resistance, interconnection geometrical active area, interconnection resistance and layers inhomogeneity.[65] The latter is related to the coating technique, the material composition and the deposition environment.[66] If the module design and patterning are optimized, losses related to the interconnection can be considered constant when increasing the aperture area.[67] In the literature, *p-i-n* devices were upscaled to minimodule size by adopting PTAA or $NiO_x$ as HTMs. The efficiencies ranged from 12.4% ($NiO_x$) to 20.1% (PTAA) with $MAPbI_3$ or Triple Cation CsMAFA perovskites.[68–73] Deng *et al.* investigated the use of a MA-free perovskite by compensating iodide vacancies and suppressing ion migration, reaching a module efficiency of 20.2% (18.6% stabilized).[74]

In this work, we decided to evaluate the effect of our HTMs in the upscaling process. In particular, we decided to use **BPT-1** to prepare a device composed of three cells on a 2.5 × 2.5 cm$^2$ substrate. The module active area is 2.25 cm$^2$ with a geometrical fill factor (GFF) equal to 91%. The P1 (TCO patterning), P2 (active layers ablation) and P3 (counter-electrode selective removal) steps were realized by an UV nano-second laser system (Figure 4.18a, see Experimental Section).

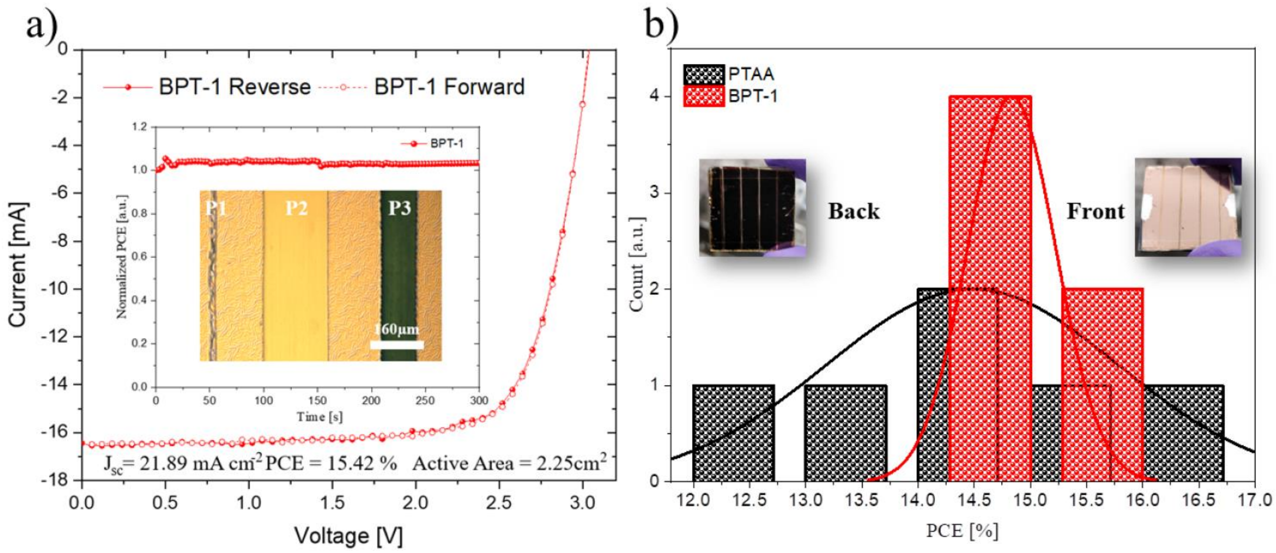

Figure 4.18. *(a) I-V curves under reverse and forward scan of the best module device fabricated, with stabilized efficiency recorded over 300 seconds and P1-P2-P3 laser patterning width. (b) Histogram chart of 6 modules fabricated with* PTAA *and* **BPT-1***, with images of a module (front and back sides).*

The module size is comparable to the substrate size employed for the small cells to avoid changes in the layer deposition method.[75] Anyway, the larger active area (2.25 cm$^2$ module vs. 0.09 cm$^2$ cell) permits to investigate the homogeneity of the involved materials. For comparisons, we fabricated 6 modules with **BPT-1** HTM and 6 modules with PTAA HTM. The best **BPT-1**-based module (Figure 4.18a) provided the following photovoltaic parameters, $J_{sc}$ = 21.89 mA cm$^{-2}$ (on cell area), $I_{sc}$ = 16.41 mA, $V_{oc}$ = 3.02 V, $ff$ = 69.81% and $PCE$ = 15.42% (about 10% less with respect to the cell), showing only a limited loss of the performance resulting from the scale-up process. The efficiency figure is also confirmed by the maximum power point tracking (Figure 4.18a, inset). A short circuit current density (from 22.24 to 21.89 mA cm$^{-2}$) and fill factor (from 75.34 to 69.81%) reduction is observed transferring from cell to module. The current drop is due to loss in active area and to unbalance among cells, while the fill factor decrease is caused by interconnection losses. The higher homogeneity of **BPT-1** relative to PTAA is underlined by the statistics shown in Figure 4.18b (both average and standard deviation values).

## 4.7. Stability Studies

Beyond efficiency, stability tests are a fundamental requirement, together with scaling-up process, to demonstrate the maturity of a photovoltaic technology for industrial exploitations.[76,77] Here, we present the results of stability experiments conducted on PTAA and **BPT-1** devices according to the ISOS D-1, ISOS T-1 and ISOS L-1 protocols (Figure 4.19),[78] consisting in PCE measurements after shelf-storage at 23±4 °C and 50±20% relative humidity (RH) (ISOS D-1), upon aging in temperature at 85±2 °C and 50±20% RH (ISOS T-1), and in working conditions under continuous light soaking at AM 1.5G, at 23±4 °C and 50±20% RH (ISOS L-1). Tests were conducted on a total of 20 devices (10 for each HTM, denoted by the abbreviations d1-d10), divided among the three protocols (4 each for ISOS D-1, 4 each for ISOS-1 and two each for ISOS L-1). Tests were run under ambient air environment, with the only additional precaution of protecting the device active area by carefully placing a thermoplastic tape (Kapton) on the top of it, to limit any possible dust and particle contamination in air.

After more than 1000 hours **BPT-1** shows better stability under high temperature and in working conditions compared to commercial PTAA. Although TGA analysis of **BPT-1** showed that it loses 5% of the initial weight at 410 °C (Figure 4.12c), that is slightly worse than PTAA (approximately 500°C[79]), the aging test at 85°C of the corresponding PSCs shows a PCE near to 100% after 1000 h for the best BPT-1 devices (**BPT-1** d5-d6), whereas PTAA-containing devices always showed lower normalized PCEs after 1000 h and a best $T_{90}$ of approx. 900 h (PTAA d5). The lower performances of the polymeric HTM in such tests can be ascribed to the mechanical instability of PTAA under thermal stress, when the thermal expansion coefficients of neighboring layer in PSC devices are mismatched and cracking of the film can occur.[80] Moreover, the polymeric structure of PTAA can suffer from diffusion of metal and moisture impurities, as well as imperfect batch-to-batch reproducibility, due to the different length of polymer chains, that are obviously the main problems with this HTM in stability tests.[15]

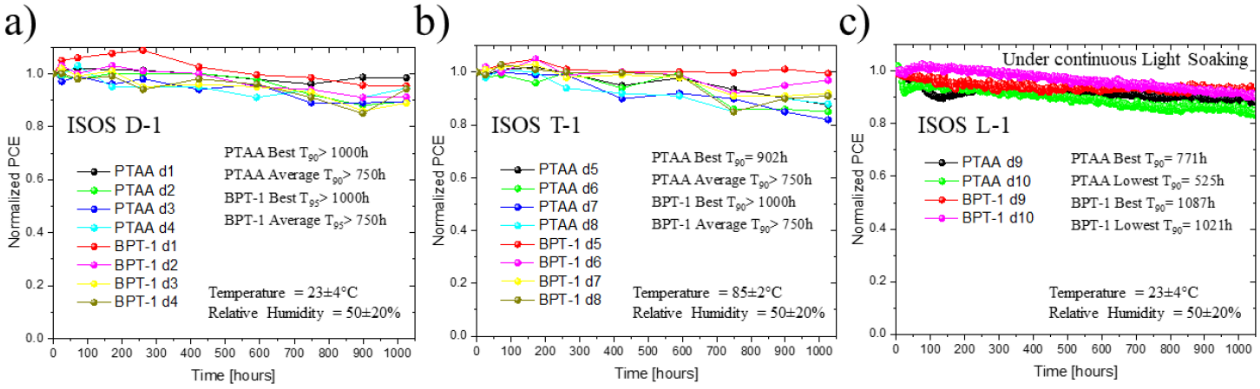

Figure 4.19: *stability comparison between* PTAA *and* **BPT-1**, *conducted on 10 different devices per HTL type (named d1-d10, respectively) under standard* ISOS D-1 *(a),* ISOS T-1 *(b) and* ISOS L-1 *(c) tests.*

Light soaking tests (ISOS L-1, Figure 4.19c) conducted on two devices for each HTM (d9-d10) show excellent stability of **BPT-1**, losing only 10% of the initial PCE after 1021-1087 hours in working conditions, while PTAA reached $T_{90}$ at only 525-771 hours after the starting of the test. Under operation, thermal, electrical and moisture damage simultaneously stresses the devices and causes reversible and irreversible degradation.[81] PTAA, as explained above, suffers significantly from these factors whereas BPT-1 seems to be much less affected from these conditions.

Although the excellent results obtained with **BPT-1** could have different explanations, we suppose that the formation of a more homogeneous layer on ITO compared to PTAA, resulting in a better film morphology (as shown by SEM experiments, Figure 4.14), as well as improved morphological contact with perovskite (Figure 4.17b), should play an important role. Indeed, we demonstrated in the past that uniform HTM morphology grants good contact with the absorber material and protects the device from the presence of defects that affects long-term stability.[82] In addition, the larger average perovskite grain size on top of **BPT-1** compared to PTAA (Figure 4.16) could also have a beneficial impact on stability, since it should reduce the extent of grain boundaries, one of the main paths leading to degradation in the perovskite layer and, in turn, to deterioration of the intrinsic stability of the device.[83] Furthermore, as mentioned above (paragraph 4.2), the computed wide delocalization of spin density in the radical cation state of **BPT-1**, enabled by its dimeric structure, should facilitate the charge transfer and transport processes occurring in the cell, improving device stability.[30] Interestingly, experimental data were also in good agreement with another result of the above computational study which, based on the assessment of absolute chemical hardness values, suggested a high redox stability of **BPT-1**, even superior to that of other well-established HTMs such as Spiro-OMeTAD.[30]

## 4.8. Conclusions

In conclusion, we designed and tested two phenothiazine dimers, called **BPT-1** and **BPT-2**, as organic hole-transporting materials in *p-i-n* perovskite solar cells. The choice of these compounds relies on the cheap and straightforward synthetic procedures, and on the ability to get suitable electronic properties in terms of energy level alignment with perovskite semiconductor and better HTL/perovskite interface adhesion compared to the reference PTAA. Perovskite solar cells devices with **BPT-1** and **BPT-2** reached power conversion efficiency (PCE) of 17.26% and 16.71%, with reference PTAA giving a best performance of 17.96% on 0.09 cm$^2$ active area. Nevertheless, use of the small-molecule HTMs allowed improving device reproducibility, with standard deviation reduced from 0.65% to 0.18% and 0.16% for PTAA, **BPT-1** and **BPT-2**, respectively. Consequently, **BPT-1**-containing cells featured also a slightly higher average efficiency compared to PTAA, 16.89% *vs.* 16.78%, respectively. To prove the enhanced reproducibility, mini-modules with 2.25 cm$^2$ active area and the same substrate size respect to small area devices were fabricated. In this case, we demonstrated similar behaviour compared to small area cells, obtaining the best PCE of 15.42% with **BPT-1**. Furthermore, with the use of methylammonium-free perovskite, **BPT-1**-containing devices presented a superior stability in standard D-T-L-1 ISOS tests, with champion $T_{90}$ values higher than 1000 h in all stress conditions. Notably, in this study both long-term cell stability under light soaking and scale-up of the devices to mini-module level were demonstrated, which is not common in the literature on perovskite PV. These results open a route for the replacement of the commonly used PTAA as HTM, suggesting an easier way to foster perovskite technology over large area for single and multi-junction application.

## 4.9. Experimental section/methods

### General synthetic remarks

All air-sensitive reactions were performed under inert atmosphere in a flame- or oven-dried apparatus using Schlenk techniques. Solvents used in cross-coupling reactions were previously degassed by means of the "freeze-pump-thaw" method. Tetrahydrofuran (THF) was distilled over metallic sodium in the presence of benzophenone, dioxane was distilled over metallic sodium, methanol (MeOH) was distilled over metallic magnesium in the presence of a catalytic amount of iodine, $CH_2Cl_2$ was distilled over $CaH_2$, toluene, diethyl ether and acetonitrile were dried on a resin exchange Solvent Purification System (MBraun). Anhydrous *N*,*N*–dimethylformamide (DMF) and $CHCl_3$ were stored under nitrogen over 4 Å molecular sieves. All the commercially available chemicals were used as received. Petroleum ether was the 40-60 °C boiling fraction. Thin-layer chromatography was carried out on aluminum-supported Merck 60 F254 plates; detection was carried out using UV light (λ = 254 and 365 nm) and permanganate or molybdophosphoric acid solutions followed by heating. Flash column chromatography was performed using Merck Kieselgel 60 (300-400 mesh) as the stationary phase. $^1$H-NMR spectra were recorded with a Varian Mercury spectrometer at 400 MHz, $^{13}$C-NMR spectra were recorded with the same instrument at 100.6 MHz. Chemical shifts were referenced to the residual solvent peak ($CDCl_3$, $\delta = 7.26$ ppm for $^1$H-NMR and $\delta = 77.00$ ppm for $^{13}$C-NMR; THF-$d_8$, $\delta = 3.58$ and 1.72 ppm for $^1$H-NMR and $\delta = 67.21$ and 25.31 ppm for $^{13}$C-NMR; $CD_2Cl_2$, $\delta = 5.32$ ppm for $^1$H-NMR and $\delta = 53.84$ ppm for $^{13}$C-NMR). Coupling constants (*J*) are reported in Hz and the multiplicity is abbreviated as follows: multiplet (m), singlet (s), broad singlet (br), duplet (d), triplet (t), and quadruplet (q). GC-MS spectra were measured with a Shimadzu gas-chromatograph (GC-17A or GC-2010) connected to a Shimadzu mass spectrometer (MS-QP2010S or MS-QP5050a) and are reported in the form *m/z* (intensity relative to base = 100). ESI-MS spectra were measured with a Thermo Scientific LCQ-FLEET instrument by direct injection of a sample solution and are reported in the form *m/z*. UV-Vis spectra in different solvents were recorded on diluted solutions of the analyte (approximately 10–5 M) with a Shimadzu UV2600 spectrometer. UV-Vis absorption or transmittance spectra of the compounds adsorbed on $TiO_2$ were recorded in transmission mode after sensitization of thin, transparent semiconductor films (thickness approximately 5 µm). Ultraviolet–Visible absorption diffuse reflectance spectra (DRS) of the dye-sensitized working electrodes were recorded using a Jasco V-770 spectrophotometer equipped with a 60 mm integrating sphere, embedding a PbS detector (ISN-923), using an interval wavelength of 1 nm, from 300 nm to 800 nm. Fluorescence spectra in solution were recorded with a Jasco FP-8300 spectrofluorometer, equipped with a 150 W Xenon arc lamp, irradiating the sample at the wavelength corresponding to maximum absorption in the UV spectrum. Cyclic voltammetry experiments were carried out using a PARSTAT 2273 electrochemical workstation (Princeton Applied Research) connected to a three-electrode cell equipped with a 3 mm glassy carbon working electrode, a platinum counter electrode, and an aqueous Ag/AgCl (sat. KCl) reference electrode. The supporting electrolyte was electrochemical-grade 0.1 M $[N(Bu)_4]PF_6$. Ferrocene was used as an internal standard by adding it to the solution at the end of the experiment and measuring the potential of the corresponding one electron oxidation. Elemental analyses were determined using a CHN-S Flash E1112 Thermo Finnigan Elemental Analyser; the results were found to be in good agreement with the calculated values.

## 4.9.1. Synthetic procedures

*N,N-bis*(4-methoxyphenyl)amine (**48**)

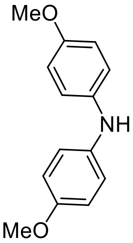

In a Schlenk tube, $Pd_2(dba)_3 \cdot CHCl_3$ (0.414 g; 0.40 mmol; 2.0 mol%) and dppf (0.443 g; 0.80 mmol; 4.0 mol%) were dissolved in toluene (40 mL) under an inert nitrogen atmosphere; after about 15', 4-bromoanisole (**46**, 3.74 g; 20 mmol; 1.0 eq.), 4-methoxyaniline (**47**, 4.92 g; 40 mmol; 2.0 eq.) and NaO*t*Bu (3.84 g; 40 mmol; 2.0 eq.) were added, and the resulting mixture was heated at 110 °C and stirred for 2 h. The reaction mixture was filtered on celite, diluted with AcOEt (150 mL), and extracted with $H_2O$ (150 mL) and brine (150 mL). The organic phase was dried with $Na_2SO_4$ and the solvent was removed under reduced pressure. The crude was purified by flash chromatography ($SiO_2$, Petroleum Ether/AcOEt 8:1 to 5:1), obtaining amine **48** (4.37 g; 19.1 mmol; 95% yield) as an orange solid. $^1$H-NMR (400 MHz, $CDCl_3$): $\delta$ = 6.95 (d, *J* = 8.0 Hz, 4H), 6.83 (d, *J* = 8.0 Hz, 4H), 3.79 (s, 6H) ppm. Spectroscopic data are in agreement with those reported in the literature.[84]

4-Bromo-*N,N-bis*(4-methoxyphenyl)aniline (**50**)

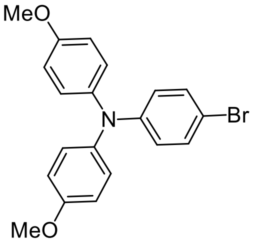

In a Schlenk tube, $Pd_2(dba)_3 \cdot CHCl_3$ (0.186 g; 0.18 mmol; 1.0 mol%) and dppf (0.200 g; 0.36 mmol; 2.0 mol%) were dissolved in toluene (30 mL) under an inert nitrogen atmosphere, and stirred for 15'. *N*,*N-Bis*(4-methoxyphenyl)amine (**48**, 4.50 g; 18 mmol; 1.0 eq.), 1-bromo-4-iodobenzene (**49**, 6.38 g; 22 mmol; 1.25 eq.) and NaO*t*Bu (2.59 g; 27 mmol; 1.5 eq.) were then added, and the resulting mixture was heated at 110 °C and stirred for 24 h. The reaction mixture was filtered on celite, diluted with AcOEt (50 mL), and washed with $H_2O$ (40 mL) and brine (40 mL). The organic phase was dried with $Na_2SO_4$ and the solvent was removed under reduced pressure. The crude was purified by flash chromatography ($SiO_2$, Petroleum Ether/Toluene 1:1 to 1:3), obtaining compound **50** as a yellow solid (6.60 g; 17.2 mmol; 96% yield). $^1$H-NMR (400 MHz, $CDCl_3$): $\delta$ = 7.23 (d, *J* = 9.0 Hz, 2H), 7.02 (d, *J* = 9.0 Hz, 4H), 6.81 (d, *J* = 9.0 Hz, 4H), 6.79 (d, *J* = 9.0 Hz, 2H), 3.79 (s, 6H) ppm. Spectroscopic data are in agreement with those reported in the literature.[85]

4-Methoxy-*N*-(4-methoxyphenyl)-*N*-(4-(4,4,5,5-tetramethyl-1,3,2-dioxaborolan-2-yl)phenyl)aniline (**44**)

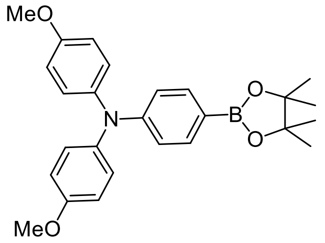

In a Schlenk tube, Pd(dppf)$Cl_2$ (0.816 g; 2.0 mmol; 10 mol%), 4-bromo-*N*,*N*-*bis*(4-methoxyphenyl)aniline (**50**, 3.84 g; 10 mmol; 1.0 eq.), *bis*(pinacolato)diboron (**18**, 3.96 g; 15 mmol; 1.5 eq.) and AcOK (2.94 g; 30 mmol; 3.0 eq.) were added to *N*,*N*-dimethylformamide (50 mL), and the resulting mixture was heated at 90 °C and stirred under inert atmosphere for 3.5 h. The reaction mixture was filtered on celite, diluted with AcOEt (50 mL) and washed with brine (6 × 200 mL). The organic phase was dried with $Na_2SO_4$ and the solvent was removed under reduced pressure. The crude was purified by flash chromatography ($SiO_2$, Petroleum Ether: AcOEt 5:1 to 3:1), obtaining boronic ester **44** as a yellow solid (4.23 g; 9.8 mmol; 98% yield). $^1$H-NMR (400 MHz, $CDCl_3$): δ = 7.60 (d, *J* = 9.0 Hz, 2H), 7.06 (d, *J* = 9.0 Hz, 4H), 6.86 (d, *J* = 9.0 Hz, 2H), 6.82 (d, *J* = 9.0 Hz, 4H), 3.80 (s, 6H), 1.32 (s, 12H) ppm. Spectroscopic data are in agreement with those reported in the literature.[85]

1,4-*Bis*(10H-phenothiazin-10-yl)benzene (**52**)

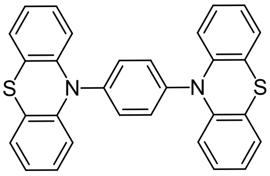

In a Schlenk tube under an inert nitrogen atmosphere, 1,4-dibromobenzene (**51**, 2.36 g; 10 mmol; 1.0 eq.), phenothiazine (**45**, 4.38 g; 22 mmol; 2.2 eq.), $Pd_2(dba)_3 \cdot CHCl_3$ (0.104 g; 0.1 mmol; 1.0 mol%), $tBu_3HP \cdot BF_4$ (0.058 g; 0.2 mmol; 2.0 mol%) and NaO*t*Bu (4.81 g; 50 mmol; 5.0 eq.) were added to toluene (120 mL), and the resulting mixture was heated at 110 °C and stirred for 5h. The reaction mixture was diluted with $H_2O$ (60 mL), filtered on celite and extracted with AcOEt (60 mL). After drying with $Na_2SO_4$, removal of the solvent under vacuum caused precipitation of compound **52** as a yellow solid (2.20 g; 4.7 mmol; 47% yield), which was used for the following reaction without further purification. $^1$H-NMR (400 MHz, $CD_2Cl_2$): δ = 7.52 (s, 4H), 7.11 (dd, *J* = 8.0 Hz, *J* = 1.5 Hz, 4H), 7.00 (td, *J* = 8.0 Hz, *J* = 1.5 Hz, 4H), 6.91 (td, *J* = 8.0 Hz, *J* = 1.5 Hz, 4H), 6.50 (dd, *J* =8.0 Hz, *J* = 1.5 Hz, 4H) ppm. Spectroscopic data are in agreement with those reported in the literature.[86]

1,4-*Bis*(3,7-dibromo-10*H*-phenothiazin-10-yl)benzene (**53**)

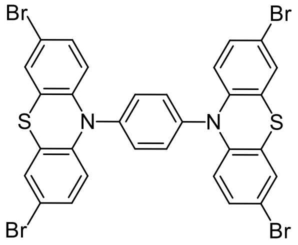

Compound **52** (0.472 g; 0.1 mmol; 1.0 eq.) and $CH_3COOH$ (2 mL) were dissolved in chloroform (2.5 mL) under inert atmosphere at room temperature. A solution of $Br_2$ (0.215 mL; 0.671 g; 4.2 mmol; 4.2 eq.) in chloroform (2.5 mL) was added dropwise, and the resulting mixture was stirred at 50 °C for 5 h. The reaction mixture was diluted with a saturated aqueous solution of $Na_2S_2O_3$ (5 mL) and was extracted in chloroform (3 × 20 mL); the combined organic phases were dried with $Na_2SO_4$ and the solvent was removed under vacuum. The crude was recrystallized from chloroform, obtaining desired product **53** as a yellow solid (0.670 g; 0.085 mmol; 85% yield). $^1$H-NMR (400 MHz, THF-$d_8$): δ = 7.60 (s, 4H), 7.28 (d, *J* = 2.2 Hz, 4H), 7.09 (dd, *J* = 8.8 Hz, 2.2 Hz, 4H), 6.39 (d, *J* = 8.8 Hz, 4H) ppm. $^{13}$C-NMR (100 MHz, THF-$d_8$): δ = 143.5, 141.1, 132.0, 130.6, 129.8, 124.6, 124.6, 119.6, 116.0 ppm. ESI-MS: *m/z* = 788.83 $[M]^+$.

4,4',4'',4'''-(10,10'-(1,4-Phenylene)*bis*(10*H*-phenothiazine-10,7,3-triyl))*tetrakis*(*N,N*-*bis*(4-methoxy phenyl)aniline) (**BPT-1**)

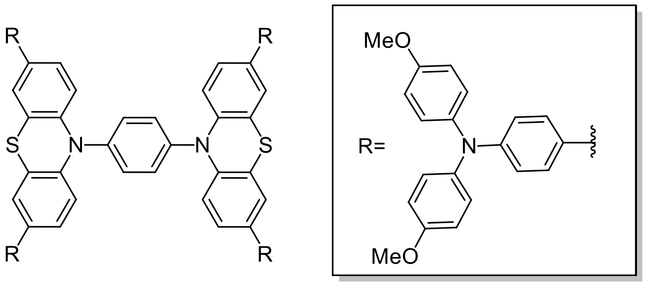

In a Schlenk tube, a mixture of toluene (3 mL), ethanol (1 mL) and a 2.0 M aqueous solution of $K_2CO_3$ (1 mL; 2.0 mmol; 2.0 eq.) were added under an inert nitrogen atmosphere. After degassing the solution, bromide **53** (0.079 g; 0.1 mmol; 1.0 eq.), boronic ester **44** (0.195 g; 0.45 mmol; 4.5 eq.) and $Pd(PPh_3)_4$ (0.017 g; 0.015 mmol; 1.5 mol%) were added, the mixture was heated at 90 °C and stirred for 24h. The mixture was filtered on celite, diluted with $H_2O$ (15 mL) and extracted with chloroform (20 mL). The organic phase was dried with $Na_2SO_4$ and the solvent was removed under reduced pressure. The crude was purified by flash chromatography ($SiO_2$, petroleum ether/dichloromethane 1:1), giving a brown solid (0.150 g; 0.089 mmol; 89% yield). $^1$H-NMR (400 MHz, $CD_2Cl_2$): δ = 7.60 (s, 4H), 7.30-7.34 (m, 12H), 7.16-7.18 (m, 4H), 7.05 (d, *J* = 7.0 Hz, 16H), 6.91 (d, *J* = 9.0 Hz, 8H), 6.84 (d, *J* = 7.0 Hz, 16H), 6.52 (d, *J* = 7.0 Hz, 4H), 3.78 (s, 24H) ppm. $^{13}$C-NMR (100 MHz, $CD_2Cl_2$): δ = 156.4, 148.5, 142.5, 141.1, 140.92, 136.0, 131.6, 127.5, 126.9, 125.1, 124.9, 122.4, 120.8, 117.9, 115.0, 55.8

ppm. ESI-MS: m/z = 1685.99 [M+1]$^+$. HRMS (ESI): *m/z* calculated for $C_{110}H_{88}O_8N_6S_2$: 1684.6100; Found: 1684.6099 [M]$^+$.

2,8-Dibromodibenzo[*b,d*]furan (**55**)

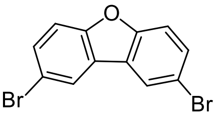

Under an inert nitrogen atmosphere, to a stirred solution of dibenzofuran **54** (2.0 g; 11.89 mmol; 1.0 eq.) in chloroform (6.0 mL), a solution of $Br_2$ (1.36 mL; 26.55 mmol; 2.2 eq.) in chloroform (6.0 mL) was added dropwise at 0°C. At the end of the addition, the reaction was warmed at room temperature and stirred overnight. A solution of $Na_2S_2O_3$ in $H_2O$ (10 mL) was added to the reaction mixture and stirred for 30'. The organic phase was extracted with dichloromethane (20 mL), dried with $Na_2SO_4$ and the solvent was removed under vacuum, obtaining compound **55** as a white solid (1.71 g; 5.25 mmol, 44% yield), which was used for the following step without further purification. $^1$H-NMR (400 MHz, $CDCl_3$): δ = 8.03 (d, *J* = 2.0 Hz, 2H), 7.58 (dd, *J* = 9.0 Hz, *J* = 2.0 Hz, 2H), 7.50 (d, *J* = 9.0 Hz, 2H) ppm. Spectroscopic data are in agreement with those reported in the literature.[87]

2,8-Di(10*H*-phenothiazin-10-yl)dibenzo[*b,d*]furan (**56**)

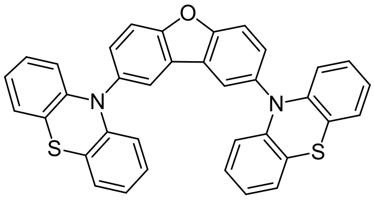

In a Schlenk tube under an inert nitrogen atmosphere, $Pd_2(dba)_3{\cdot}CHCl_3$ (0.217 g; 0.21 mmol; 5.0 mol%) and XPhos (0.200 g; 0.42 mol; 10 mol%) were added to toluene (20 mL) at room temperature and the mixture was stirred for 15'. Dibromide **55** (1.40 g; 4.2 mol; 1.0 eq.), phenothiazine (**45**, 2.56 g; 12.8 mmol; 3.0 eq.) and NaO*t*Bu (1.61 g; 0.016 mol; 4.0 eq.) were then added, and the reaction mixture was heated at 110 °C and stirred for 24h. After the filtration on celite, the solution was diluted with $H_2O$ (10 mL) and extracted with AcOEt (2 × 20 mL); the combined organic phases were dried with $Na_2SO_4$ and the solvent was removed under reduced pressure. The crude was purified by flash chromatography ($SiO_2$; Petroleum ether/AcOEt 30:1 to 20:1) to yield desired product **56** as an off-white solid (2.1 g; 3.73 mmol; 89% yield). $^1$H-NMR (400 MHz, $CDCl_3$): δ = 8.00 (d, *J* = 2.0 Hz, 2H), 7.86 (d, *J* = 8.0 Hz, 2H), 7.55 (dd, *J* = 9.0 Hz, 2H), 7.01-7.04 (m, 4H), 6.34- 6.79 (m, 8H), 6.20-6.22 (m, 4H) ppm. $^{13}$C-NMR (100 MHz, $CDCl_3$) δ = 156.2, 144.6, 136.3, 131.1, 129.2, 128.4, 127.0, 126.9, 126.3, 125.4, 124.0, 122.7, 120.2, 116.0, 114.3 ppm. ESI-MS: *m/z* = 562.25 [M]$^+$.

2,8-*Bis*(3,7-dibromo-10*H*-phenothiazin-10-yl)dibenzo[*b,d*]furan (**57**)

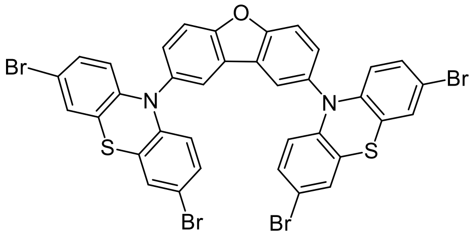

Compound **56** (0.27 g; 0.48 mmol; 1.0 eq.) and $CH_3COOH$ (1.5 mL) were dissolved in chloroform (5 mL) under an inert nitrogen atmosphere at room temperature. A solution of $Br_2$ (0.11 mL; 2.16 mmol; 4.5 eq.) in chloroform (5 mL) was added dropwise, and the resulting mixture was stirred at 50 °C for 24 h. After the dilution with a saturated aqueous solution of $Na_2S_2O_3$ (10 mL), the solution was extracted with chloroform (3 × 20 mL), the combined organic phases were dried with $Na_2SO_4$ and the solvent was removed under vacuum, obtaining desired product **57** as yellow solid (0.31 g; 0.35 mmol; 73% yield), which was used for the following step without further purification. $^1$H-NMR (400 MHz, $CDCl_3$): δ = 7.93 (d, *J* = 2.0 Hz, 2H), 7.88 (d, *J* = 9.0 Hz, 2H), 7.50 (dd, *J* = 9.0 Hz, 2.0 Hz, 2H), 7.12 (d, *J* = 2.0 Hz, 4H), 6.90 (dd, *J* = 9.0 Hz, 2Hz, 4H), 6.02 (d, *J* = 9.0 Hz, 4H) ppm. $^{13}$C-NMR (100 MHz, $CDCl_3$) δ = 156.4, 143.4, 135.7, 130.7, 130.9, 129.9, 129.1, 126.4, 123.7, 121.6, 117.2, 115.1, 114.8 ppm. ESI-MS: *m/z* = 877.83 [M]$^+$.

4,4',4'',4'''-(10,10'-(Dibenzo[*b,d*]furan-2,8-diyl)bis(10*H*-phenothiazine-10,7,3-triyl))*tetrakis*(*N,N*-*bis*(4-methoxyphenyl)aniline) (**BPT-2**)

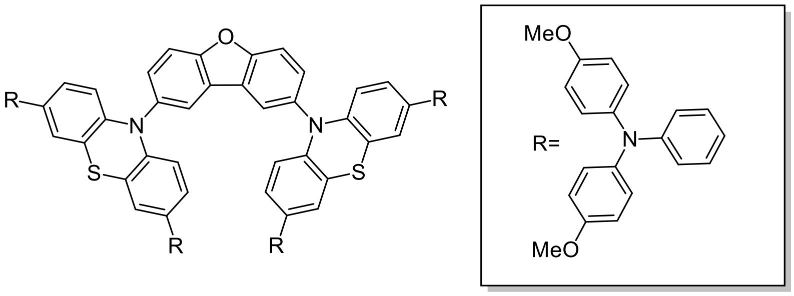

In a Schlenk tube under an inert nitrogen atmosphere, toluene (5 mL), ethanol (2 mL) and a 2.0 M aqueous solution of $K_2CO_3$ (1 mL; 2.0 mmol; 2.0 eq.) were added at room temperature. After degassing the solution, compound **57** (0.088 g; 0.1 mmol; 1.0 eq.), boronic ester **44** (0.195 g; 0.45 mmol; 4.5 eq.) and [Pd($PPh_3$)$_4$] (0.017 g; 0.015 mmol; 15 mol%) were added, the resulting solution was heated at 90 °C and stirred for 24h. The mixture was diluted with $H_2O$ (15 mL) and extracted with chloroform (20 mL). The organic phase was dried with $Na_2SO_4$ and the solvent was removed under vacuum. The crude was purified by flash chromatography ($SiO_2$, petroleum ether/dichloromethane 1:1) giving the desired product **BPT-2** as a brown solid (0.150 g, 0.084 mmol; 84% yield). $^1$H-NMR (400

MHz, $CD_2Cl_2$): δ = 8.04 (s, 2H), 7.89 (d, *J* = 8.6 Hz, 2H), 7.58 (d, *J* = 7.0 Hz, 2H), 7.25 – 7.33 (m, *J* = 8.1 Hz, 12H), 7.20 – 7.24 (m, 4H), 7.05 (d, *J* = 8.9 Hz, 16H), 6.92 (d, *J* = 8.6 Hz, 8H), 6.79 – 6.85 (m, 16H), 6.20 – 6.23 (m, 4H), 3.79 (s, 24H) ppm. $^{13}$C-NMR (100 MHz, $CDCl_3$) δ = 156.0, 155.7, 147.8, 142.8, 140.8, 136.1, 135.2, 131.6, 130.9, 129.0, 128.2, 126.7, 126.5, 126.1, 125.2, 124.7, 124.5, 123.8, 120.7, 119.9, 115.9, 114.6, 114.2, 55.4 ppm. ESI-MS = 1776.17 $[M+1]^+$. HRMS (ESI): *m/z* calculated for $C_{116}H_{90}O_9N_6S_2$: 1774.6205; Found: 1774.6198 $[M]^+$.

### 4.9.2. Materials characterization and solar devices fabrication and testing

As mentioned at the beginning of paragraph 4.5., while the spectroscopic and electrochemical characterization of isolated compounds **BPT1-2** was carried out at CNR-ICCOM, the activity related to solar devices fabrication and testing was performed by the group of Prof. Aldo di Carlo at C.H.O.S.E., University of Rome Tor Vergata.

**Materials:** *N*,*N*-dimethylformamide (DMF, anhydrous, Merck), dimethyl sulfoxide (DMSO, anhydrous, Merck), toluene (Merck), C60 Fullerene (C60-99.5%, Solenne), Bathocuproine (BCP-96%, Merck), formamidinium iodide (FAI-99.99%, Greatcell solar), Cesium iodide (CsI-99.99%, Merck), Lead Bromide ($PbBr_2$, TCI), Lead Iodide ($PbI_2$, TCI), were purchased and used without further purification. Glass/ITO substrates ($10\ \Omega^{-1}$) were purchased from Kintec.

**Thermogravimetric analysis:** Thermogravimetric (TGA) analysis of compounds **BPT-1,2** was conducted under inert $N_2$ atmosphere with an EXSTAR Seiko 6200 instrument, using the following parameters: temperature range, 30-650 °C; temperature ramp, 10 °C/min; $N_2$ gas flow 100 mL/min.

**Spectroscopic characterization:** UV-Vis absorption spectra in toluene solution (approx. concentration $5 \times 10^{-5}$ M) were recorded with a Shimadzu 2600 series spectrophotometer. Diffuse reflectance spectra (DRS) of the compounds deposed on ITO-coated glass sheets were recorded with the same instrument in the reflectance mode using an integrating sphere (with barium sulfate as background material and bare ITO as a reference) and were converted to the corresponding absorption spectra by using the Kubelka–Munk equation. Fluorescence spectra were recorded with a JASCO FP-8300 spectrofluorometer, irradiating the sample at the wavelength corresponding to maximum absorption in the UV-Vis spectrum.

**Imaging and microscopic characterization:** Contact angles were measured from digital images using the SURFTENS software (OEG GmbH). Scanning Electron Microscopy (SEM) experiments were performed by using a TESCAN Analytics VEGA instrument.

**Electrochemical characterization:** Cyclic voltammetry experiments were carried out in dichloromethane solution using a PARSTAT 2273 electrochemical workstation (Princeton Applied Research) connected to a three-electrode cell equipped with a 3 mm glassy carbon working electrode, a platinum counter electrode, and an aqueous Ag/AgCl (sat. KCl) reference electrode. The supporting electrolyte was electrochemical-grade 0.1 M $[N(Bu)_4]PF_6$, and the dye concentration was approx. $10^{-3}$ M. Ferrocene was used as an internal standard by adding it to the solution at the end of the experiment and measuring the potential of the corresponding one electron oxidation. Under these conditions, the one electron oxidation of ferrocene occurred at *E* = +0.49 V vs. Ag/AgCl (sat.

KCl). Considering that the potential of Ag/AgCl (sat. KCl) *vs.* normal hydrogen electrode (NHE) is 0.197 V,[88] and that the absolute half-cell potential for the standard hydrogen electrode is located at −4.46 eV *vs. vacuum*,[89] the HOMO levels of compounds **BPT-1,2** *vs. vacuum* were obtained by applying the following equation:

$$E_{HOMO} = -4.46 - E_{ox} + 0.49 + 0.197 \text{ eV} \quad (4.2)$$

**Perovskite solution:** $Cs_{0.17}FA_{0.83}Pb(I_{0.9}Br_{0.1})_3$ with a concentration of 1.45 M was prepared as follows: 64 mg of CsI, 79.8 mg of $PbBr_2$, 207 mg of FAI, and 568.2 mg of $PbI_2$ were dissolved in one pot in 1 mL of a DMF:DMSO mixture (4:1 volume ratio).

**Device fabrication:** 2.5 × 2.5 $cm^2$ glass/ITO samples were patterned with a UV ns laser (Spectraphysics - Andover, MA, USA) and diced with a glasscutter (Dyenamo – Stockholm, Sweden). Samples were scrubbed with water and soap solution (Hellmanex 2% in deionized water) and cleaned with three stages of ultrasonic bath: first in water and soap, then in ultrapure water, and finally in 2-propanol. After drying, they were treated for 15 min in a UV/$O_3$ tool (Novasonic). Samples were immediately transferred in a nitrogen-filled glovebox. PTAA, **BPT-1** and **BPT-2** inks were spun at 5000 RPM for 20 s and annealed for 20 min at 110 °C. After cooling down, the perovskite ink was spun at 6000 RPM for 35 s, and 150 µL of chlorobenzene (CB) were dropped after 20 s. The film was annealed for 10 min at 100 °C. On top of the perovskite layer, 30 nm of $C_{60}$ as ETL and 7 nm of BCP as a buffer layer were thermally evaporated at a vacuum pressure of ≈10 to 6 mbar. Finally, 100 nm of Cu were deposited by thermal evaporation, using a shadow mask to separate the four cells that are fabricated on each substrate.

**Mini-modules fabrication:** 2.5 × 2.5 $cm^2$ glass/ITO samples were patterned and cleaned like small area cells, and the same procedure was used to deposit all the layers. The interconnection was made *via* a P1–P2–P3 scheme as shown in Figure 4.18a. The optimal fluence per pulse (amount of energy of a single laser pulse divided for the area of the laser spot) was 280 mJ $cm^{-1}$ for P1, 107 mJ $cm^{-1}$ for the P2, and 79 mJ $cm^{-1}$ for the P3. All the ablations were carried out from the top side of the device at a repetition rate of 80 kHz, with a scanning speed of 195 mm $s^{-1}$. The P2 scribes were made after the deposition of all the layers up to the BCP, while the P3 scribes were made after the evaporation of the Cu electrode. The P2 ablation is made of a set of parallel scribes with an RSD (raster scan distance) of 3 µm. The P3 ablation is made of a set of parallel scribes with an RSD of 6 µm. The width of P1 is the one of a single scribe, in this case 15 µm. The width of P2 is 180 µm, while the width of P3 scribes is 105 µm. The cell width was equal to 5 mm and the interconnection width was fixed to 500 µm, and the P2 was centered between P1 and P3 scribes. The final geometrical fill factor of the modules is 91%.

**Device characterization:** Cells and mini-modules were measured with an ABET Sun 2000 class A sun simulator, calibrated with an Eko MS-602 pyranometer. The accuracy of the calibration was checked by measuring the internal quantum efficiency of cells (ARKEO system, Cicci Research, Grosseto, Italy), ensuring that the mismatch of the integrated and measured $J_{SC}$ was less than 4%. Data were acquired with a 4-channels source meter unit of Cicci Research with a scan rate of 100 mV $s^{-1}$ for cells, 300 mV $s^{-1}$ for modules with three cells. TPC and TPV tests were performed with an all-in-one platform

(ARKEO system, Cicci Research) composed of multichannel 4-wire source meters, 100 MS/s digitizer, and Arbitrary function generators. *J/V* measurement used a scan rate of 30 mV $s^{-1}$ without any preconditioning. A rigid plastic opaque mask of 0.1 $cm^2$ was applied during the measurements. Devices were connected to a transimpedance amplifier and a differential voltage amplifier to monitor short-circuit current or open-circuit voltage. The measurements were carried out with varying light intensities. The intensities were cycled at 10 different levels (from 30 up to 160 $mW{\cdot}cm^{-2}$), using the white LED. For each intensity level, 200 traces were recorded.

# References

[1] NREL, "Best research-cell efficiency chart," can be found under https://www.nrel.gov/pv/cell-efficiency.htm, **2023**.

[2] Y. Zhou, W. Chen, *J Appl Phys* **2020**, *128*, 200401.

[3] M. Grätzel, *Nat Mater* **2014**, *13*, 838–842.

[4] E. Sheibani, L. Yang, J. Zhang, *Solar RRL* **2020**, *4*, 2000461.

[5] M. Vasilopoulou, A. Fakharuddin, A. G. Coutsolelos, P. Falaras, P. Argitis, A. R. B. M. Yusoff, M. K. Nazeeruddin, *Chem Soc Rev* **2020**, *49*, 4496–4526.

[6] A. Pecoraro, A. de Maria, P. Delli Veneri, M. Pavone, A. B. Munõz-Garciá, *Physical Chemistry Chemical Physics* **2020**, *22*, 28401–28413.

[7] G. Ren, W. Han, Y. Deng, W. Wu, Z. Li, J. Guo, H. Bao, C. Liu, W. Guo, *J Mater Chem A Mater* **2021**, *9*, 4589–4625.

[8] J. Y. Kim, J. W. Lee, H. S. Jung, H. Shin, N. G. Park, *Chem Rev* **2020**, *120*, 7867–7918.

[9] L. A. Castriotta, R. Fuentes Pineda, V. Babu, P. Spinelli, B. Taheri, F. Matteocci, F. Brunetti, K. Wojciechowski, A. di Carlo, *ACS Appl Mater Interfaces* **2021**, *13*, 29576–29584.

[10] Z. Liu, L. Krückemeier, B. Krogmeier, B. Klingebiel, J. A. Márquez, S. Levcenko, S. Öz, S. Mathur, U. Rau, T. Unold, T. Kirchartz, *ACS Energy Lett* **2019**, *4*, 110–117.

[11] Y. Li, B. Wang, T. Liu, Q. Zeng, D. Cao, H. Pan, G. Xing, *ACS Appl Mater Interfaces* **2022**, *14*, 3284–3292.

[12] J. Xu, J. Dai, H. Dong, P. Li, J. Chen, X. Zhu, Z. Wang, B. Jiao, X. Hou, J. Li, Z. Wu, *Org Electron* **2022**, *100*, 106378.

[13] T. Lemercier, L. Perrin, S. Berson, L. Flandin, E. Planes, *Mater Adv* **2021**, *2*, 7907–7921.

[14] X. Liu, Y. Cheng, C. Liu, T. Zhang, N. Zhang, S. Zhang, J. Chen, Q. Xu, J. Ouyang, H. Gong, *Energy Environ Sci* **2019**, *12*, 1622–1633.

[15] F. M. Rombach, S. A. Haque, T. J. Macdonald, *Energy Environ Sci* **2021**, *14*, 5161–5190.

[16] R. Singh, P. K. Singh, B. Bhattacharya, H. W. Rhee, *Appl Mater Today* **2019**, *14*, 175–200.

[17] X. Yang, H. Wang, B. Cai, Z. Yu, L. Sun, *Journal of Energy Chemistry* **2018**, *27*, 650–672.

[18] X. Ding, H. Wang, C. Chen, H. Li, Y. Tian, Q. Li, C. Wu, L. Ding, X. Yang, M. Cheng, *Chemical Engineering Journal* **2021**, *410*, 128328.

[19] X. Zhao, Y. Quan, H. Pan, Q. Li, Y. Shen, Z. S. Huang, M. Wang, *Journal of Energy Chemistry* **2019**, *32*, 85–92.

[20] J. Salunke, X. Guo, M. Liu, Z. Lin, N. R. Candeias, A. Priimagi, J. Chang, P. Vivo, *ACS Omega* **2020**, *5*, 23334–23342.

[21] C. Lu, M. Paramasivam, K. Park, C. H. Kim, H. K. Kim, *ACS Appl Mater Interfaces* **2019**, *11*, 14011–14022.

[22] X. Ding, C. Chen, L. Sun, H. Li, H. Chen, J. Su, H. Li, H. Li, L. Xu, M. Cheng, *J Mater Chem A Mater* **2019**, *7*, 9510–9516.

[23] M. R. Maciejczyk, R. Chen, A. Brown, N. Zheng, N. Robertson, *J Mater Chem C Mater* **2019**, *7*, 8593–8598.

[24] J. Salunke, X. Guo, Z. Lin, J. R. Vale, N. R. Candeias, M. Nyman, S. Dahlström, R. Österbacka, A. Priimagi, J. Chang, P. Vivo, *ACS Appl Energy Mater* **2019**, *2*, 3021–3027.

[25] F. Zhang, S. Wang, H. Zhu, X. Liu, H. Liu, X. Li, Y. Xiao, S. M. Zakeeruddin, M. Grätzel, *ACS Energy Lett* **2018**, *3*, 1145–1152.

[26] X. Liu, X. Tan, Q. Chen, H. Shan, C. Liu, J. Xu, Z. K. Chen, W. Huang, Z. X. Xu, *RSC Adv* **2017**, *7*, 53604–53610.

[27] S. Revoju, A. Matuhina, L. Canil, H. Salonen, A. Hiltunen, A. Abate, P. Vivo, *J Mater Chem C Mater* **2020**, *8*, 15486–15506.

[28] R. Grisorio, B. Roose, S. Colella, A. Listorti, G. P. Suranna, A. Abate, *ACS Energy Lett* **2017**, *2*, 1029–1034.

[29] Z. Zhang, R. He, *Comput Theor Chem* **2019**, *1161*, 10–17.

[30] C. Coppola, R. Infantino, A. Dessì, L. Zani, M. L. Parisi, A. Mordini, G. Reginato, R. Basosi, A. Sinicropi, *Mater Chem Phys* **2022**, *278*, 125603.

[31] *Gaussian 09, Revision A.02,* M. J. Frisch, G. W. Trucks, H. B. Schlegel, G. E. Scuseria, M. A. Robb, J. R. Cheeseman, G. Scalmani, V. Barone, G. A. Petersson, H. Nakatsuji, X. Li, M. Caricato, A. Marenich, J. Bloino, B. G. Janesko, R. Gomperts, B. Mennucci, **2009**.

[32] W. Kohn, L. J. Sham, *Physical Review* **1965**, *140*, A1133.

[33] A. K. Rajagopal, J. Callaway, *Phys Rev B* **1973**, *7*, 1912.

[34] A. D. Becke, *J Chem Phys* **1998**, *98*, 5648.

[35] C. Lee, W. Yang, R. G. Parr, *Phys Rev B* **1988**, *37*, 785.

[36] J. Tomasi, B. Mennucci, R. Cammi, *Chem Rev* **2005**, *105*, 2999–3093.

[37] M. Cossi, N. Rega, G. Scalmani, V. Barone, *J Comput Chem* **2003**, *24*, 669–681.

[38] C. Adamo, D. Jacquemin, *Chem Soc Rev* **2013**, *42*, 845–856.

[39] A. D. Laurent, C. Adamo, D. Jacquemin, *Physical Chemistry Chemical Physics* **2014**, *16*, 14334–14356.

[40] T. Yanai, D. P. Tew, N. C. Handy, *Chem Phys Lett* **2004**, *393*, 51–57.

[41] N. M. O'Boyle, A. L. Tenderholt, K. M. Langner, *J Comput Chem* **2008**, *29*, 839–845.

[42] H. Ashassi-Sorkhabi, P. Salehi-Abar, *J Mol Liq* **2021**, *327*, 114853.

[43] S. Naqvi, A. Patra, *Mater Chem Phys* **2021**, *258*, 123863.

[44] S. Fantacci, F. de Angelis, M. K. Nazeeruddin, M. Grätzel, *Journal of Physical Chemistry C* **2011**, *115*, 23126–23133.

[45] C. Chen, X. Ding, H. Li, M. Cheng, H. Li, L. Xu, F. Qiao, H. Li, *ACS Appl Mater Interfaces* **2018**, *10*, 36608–36614.

[46] Z. Z. Sun, W. L. Ding, S. Feng, X. L. Peng, *Physical Chemistry Chemical Physics* **2020**, *22*, 16359–16367.

[47] Q. Wang, Z. Zeng, Y. Li, X. Chen, *Solar Energy* **2020**, *208*, 10–19.

[48] P. Ganesan, K. Fu, P. Gao, I. Raabe, K. Schenk, R. Scopelliti, J. Luo, L. H. Wong, M. Grätzel, M. K. Nazeeruddin, *Energy Environ Sci* **2015**, *8*, 1986–1991.

[49] Z. Z. Sun, S. Feng, C. Gu, N. Cheng, J. Liu, *Physical Chemistry Chemical Physics* **2019**, *21*, 15206–15214.

[50] R. Grisorio, R. Iacobellis, A. Listorti, L. de Marco, M. P. Cipolla, M. Manca, A. Rizzo, A. Abate, G. Gigli, G. P. Suranna, *ACS Appl Mater Interfaces* **2017**, *9*, 24778–24787.

[51] M. R. S. A. Janjua, *Chemistry – A European Journal* **2021**, *27*, 4197–4210.

[52] C. Coppola, A. Pecoraro, A. B. Muñoz-García, R. Infantino, A. Dessì, G. Reginato, R. Basosi, A. Sinicropi, M. Pavone, *Physical Chemistry Chemical Physics* **2022**, *24*, 14993–15002.

[53] F. F. Targhi, Y. S. Jalili, F. Kanjouri, *Results Phys* **2018**, *10*, 616–627.

[54] M. Saliba, S. Orlandi, T. Matsui, S. Aghazada, M. Cavazzini, J.-P. Correa-Baena, P. Gao, R. Scopelliti, E. Mosconi, K.-H. Dahmen, F. de Angelis, A. Abate, A. Hagfeldt, G. Pozzi, M. Graetzel, M. K. Nazeeruddin, *Nat Energy* **2016**, *1*, 15017.

[55] A. Torres, L. G. C. Rego, *Journal of Physical Chemistry C* **2014**, *118*, 26947–26954.

[56] Q. Wang, E. Mosconi, C. Wolff, J. Li, D. Neher, F. de Angelis, G. P. Suranna, R. Grisorio, A. Abate, *Adv Energy Mater* **2019**, *9*, 1900990.

[57] J. Yin, D. Cortecchia, A. Krishna, S. Chen, N. Mathews, A. C. Grimsdale, C. Soci, *Journal of Physical Chemistry Letters* **2015**, *6*, 1396–1402.

[58] S. A. Olaleru, J. K. Kirui, D. Wamwangi, K. T. Roro, B. Mwakikunga, *Solar Energy* **2020**, *196*, 295–309.

[59] J. Urieta-Mora, I. García-Benito, A. Molina-Ontoria, N. Martín, *Chem Soc Rev* **2018**, *47*, 8541–8571.

[60] H. D. Pham, T. C. J. Yang, S. M. Jain, G. J. Wilson, P. Sonar, *Adv Energy Mater* **2020**, *10*, 1903326.

[61] D. C. Aldo, Z. Lorenzo, L. A. Castriotta, R. Infantino, L. Vesce, M. Stefanelli, A. Dessì, C. Coppola, M. Calamante, G. Reginato, A. Mordini, A. Sinicropi, A. di Carlo, L. Zani, L. A. Castriotta, L. Vesce, M. Stefanelli, A. di Carlo, R. Infantino, A. Dessì, M. Calamante, G. Reginato, A. Mordini, A. Sinicropi, L. Zani, C. Coppola, *Energy & Environmental Materials* **2022**, e12455.

[62] T. Du, W. Xu, M. Daboczi, J. Kim, S. Xu, C. T. Lin, H. Kang, K. Lee, M. J. Heeney, J. S. Kim, J. R. Durrant, M. A. McLachlan, *J Mater Chem A Mater* **2019**, *7*, 18971–18979.

[63] J. Jiménez-López, W. Cambarau, L. Cabau, E. Palomares, *Sci Rep* **2017**, *7*, 6101.

[64] R. A. Belisle, P. Jain, R. Prasanna, T. Leijtens, M. D. McGehee, *ACS Energy Lett* **2016**, *1*, 556–560.

[65] L. Vesce, M. Stefanelli, J. P. Herterich, L. A. Castriotta, M. Kohlstädt, U. Würfel, A. di Carlo, *Solar RRL* **2021**, *5*, 2100073.

[66] Z. Yang, C.-C. Chueh, F. Zuo, J. H. Kim, P.-W. Liang, A. K-Y Jen, Z. Yang, C. Chueh, F. Zuo, J. H. Kim, P. Liang, A. K-Y Jen, *Adv Energy Mater* **2015**, *5*, 1500328.

[67] Z. Li, T. R. Klein, D. H. Kim, M. Yang, J. J. Berry, M. F. A. M. van Hest, K. Zhu, *Nat Rev Mater* **2018**, *3*, 18017.

[68] H. C. Liao, P. Guo, C. P. Hsu, M. Lin, B. Wang, L. Zeng, W. Huang, C. M. M. Soe, W. F. Su, M. J. Bedzyk, M. R. Wasielewski, A. Facchetti, R. P. H. Chang, M. G. Kanatzidis, T. J. Marks, *Adv Energy Mater* **2017**, *7*, 1601660.

[69] T. Abzieher, S. Moghadamzadeh, F. Schackmar, H. Eggers, F. Sutterlüti, A. Farooq, D. Kojda, K. Habicht, R. Schmager, A. Mertens, R. Azmi, L. Klohr, J. A. Schwenzer, M. Hetterich, U. Lemmer, B. S. Richards, M. Powalla, U. W. Paetzold, F. Schackmar, H. Eggers, A. Farooq, R. Schmager, U. Lemmer, B. S. Richards, U. W. Paetzold, D. Kojda, K. Habicht, R. Azmi, T. Abzieher, S. Moghadamzadeh, F. Sutterlüti, A. Mertens, L. Klohr, J. A. Schwenzer, M. Hetterich, M. Powalla, *Adv Energy Mater* **2019**, *9*, 1802995.

[70] J. Troughton, K. Hooper, T. M. Watson, *Nano Energy* **2017**, *39*, 60–68.

[71] Y. Deng, Z. Ni, A. F. Palmstrom, J. Zhao, S. Xu, C. H. van Brackle, X. Xiao, K. Zhu, J. Huang, *Joule* **2020**, *4*, 1949–1960.

[72] S. Chen, X. Dai, S. Xu, H. Jiao, L. Zhao, J. Huang, *Science (1979)* **2021**, *373*, 902–907.

[73] Y. Deng, X. Zheng, Y. Bai, Q. Wang, J. Zhao, J. Huang, *Nat Energy* **2018**, *3*, 560–566.

[74] Y. Deng, S. Xu, S. Chen, X. Xiao, J. Zhao, J. Huang, *Nature Energy 2021 6:6* **2021**, *6*, 633–641.

[75] L. Rakocevic, R. Gehlhaar, T. Merckx, W. Qiu, U. W. Paetzold, H. Fledderus, J. Poortmans, *IEEE J Photovolt* **2017**, *7*, 404–408.

[76] S. Castro-Hermosa, S. K. Yadav, L. Vesce, A. Guidobaldi, A. Reale, A. di Carlo, T. M. Brown, *J Phys D Appl Phys* **2016**, *50*, 033001.

[77] F. Matteocci, L. A. Castriotta, A. L. Palma, in *Photoenergy and Thin Film Materials* (Ed.: X.-Y. Yang), John Wiley & Sons, Ltd, **2019**, pp. 121–155.

[78] M. v. Khenkin, E. A. Katz, A. Abate, G. Bardizza, J. J. Berry, C. Brabec, F. Brunetti, V. Bulović, Q. Burlingame, A. di Carlo, R. Cheacharoen, Y.-B. Cheng, A. Colsmann, S. Cros, K. Domanski, M. Dusza, C. J. Fell, S. R. Forrest, Y. Galagan, D. di Girolamo, M. Grätzel, A. Hagfeldt, E. von Hauff, H. Hoppe, J. Kettle, H. Köbler, M. S. Leite, S. Liu, Y.-L. Loo, J. M. Luther, C.-Q. Ma, M. Madsen, M. Manceau, M. Matheron, M. McGehee, R. Meitzner, M. K. Nazeeruddin, A. F. Nogueira, Ç. Odabaşı, A. Osherov, N.-G. Park, M. O. Reese, F. de Rossi, M. Saliba, U. S. Schubert, H. J. Snaith, S. D. Stranks, W. Tress, P. A. Troshin, V. Turkovic, S. Veenstra, I. Visoly-Fisher, A. Walsh, T. Watson, H. Xie, R. Yıldırım, S. M. Zakeeruddin, K. Zhu, M. Lira-Cantu, *Nat Energy* **2020**, *5*, 35–49.

[79] A. Intaniwet, C. A. Mills, M. Shkunov, H. Thiem, J. L. Keddie, P. J. Sellin, *J Appl Phys* **2009**, *106*, 064513.

[80] W. Yang, D. Zhong, M. Shi, S. Qu, H. Chen, *iScience* **2019**, *22*, 534–543.

[81] M. v. Khenkin, K. M. Anoop, I. Visoly-Fisher, S. Kolusheva, Y. Galagan, F. di Giacomo, O. Vukovic, B. R. Patil, G. Sherafatipour, V. Turkovic, H. G. Rubahn, M. Madsen, A. v. Mazanik, E. A. Katz, *ACS Appl Energy Mater* **2018**, *1*, 799–806.

[82] L. Vesce, M. Stefanelli, A. di Carlo, *Energies (Basel)* **2021**, *14*, 6081.

[83] A. F. Castro-Méndez, J. Hidalgo, J. P. Correa-Baena, *Adv Energy Mater* **2019**, *9*, 1901489.

[84] Y. Li, L. Scudiero, T. Ren, W. J. Dong, *J Photochem Photobiol A Chem* **2012**, *231*, 51–59.

[85] Y. Wang, W. Liu, J. Deng, G. Xie, Y. Liao, Z. Qu, H. Tan, Y. Liu, W. Zhu, *Chem Asian J* **2016**, *11*, 2555–2563.

[86] H. Khelwati, A. W. Franz, Z. Zhou, W. R. Thiel, T. J. J. Müller, *Molecules* **2021**, *26*, 2950.

[87] L. Li, J. Ge, H. Wu, Q. H. Xu, S. Q. Yao, *J Am Chem Soc* **2012**, *134*, 12157–12167.

[88] A. J. Bard, L. R. Faulkner, *Electrochemical Methods: Fundamentals and Applications, 3rd Edition The Latest Edition of a Classic Textbook in Electrochemistry*, John Wiley & Sons, New York, U.S.A., **2000**.

[89] W. N. Hansen, G. J. Hansen, *Phys Rev A (Coll Park)* **1987**, *36*, 1396.

# Annexes

## List of abbreviations

| | |
|---|---|
| $^{13}$C-NMR | $^{13}$carbon-Nuclear magnetic resonance |
| $^{1}$H-NMR | $^{1}$proton-Nuclear magnetic resonance |
| AcOEt | Ethyl acetate |
| BIPV | Building-integrated photovoltaics |
| CataCXium A | Di(1-adamantyl)-*n*-butylphosphine |
| CDCA | Chenodeoxycholic acid |
| dba | Dibenzylideneacetone |
| DCM | Dichloromethane |
| DFT | Density functional theory |
| DMSO | Dimethylsulfoxide |
| dppf | 1,1'-*bis*(diphenylphosphino)ferrocene |
| DSSC | Dye-Sensitized Solar Cells |
| EDOT | Ethylenedioxythiophene |
| EIS | Electrochemical impedance spectroscopy |
| ESI-MS | Electrospray ionization-mass spectrometry |
| $Et_2O$ | Diethyl ether |
| EtOH | Ethanol |
| FMOs | Frontier molecular orbitals |
| FTO | Fluorine-Tin oxide |
| HOMO | Highest occupied molecular orbital |
| HRMS | High-resolution mass spectrometry |
| ICT | Intramolecular charge transfer |
| IPCE | Incident photon-to-current conversion efficiency |
| IR | Infrared |
| ITO | Indium-Tin oxide |
| LDA | Lithium diisopropylamide |

| | |
|---|---|
| **LHE** | Light-harvesting efficiency |
| **LUMO** | Lowest unoccupied molecular orbital |
| **MeCN** | Acetonitrile |
| **MeOH** | Methanol |
| **MLCT** | Metal-to-ligand charge transfer |
| **mp** | Melting point |
| **MS-4Å** | Molecular sieves – 4 angstrom |
| **MW** | Microwave |
| ***N*,*N*-DMF** | *N*,*N*-dimethylformamide |
| **NBS** | *N*-bromosuccinimide |
| ***n*-BuLi** | *n*-butyllithium |
| **NHE** | Normal hydrogen electrode |
| **NIR** | Near infrared |
| **NIS** | *N*-iodosuccinimide |
| **$Pd_2(dba)_3{\cdot}CHCl_3$** | Tris(dibenzylideneacetone)dipalladium chloroform adduct |
| **$Pd(dppf)Cl_2$** | [1,1′-Bis(diphenylphosphino)ferrocene]dichloropalladium(II) |
| **$Pd(OAc)_2$** | Palladium(II) acetate |
| **PE** | Petroleum ether |
| **PV** | Photovoltaics |
| **SET** | Single-electron transfer |
| **TBP** | 4-*tert*-butylpyridine |
| **$t\mathrm{Bu}_3P{\cdot}HBF_4$** | Tri-*tert*-butylphosphonium tetrafluoroborate |
| **TCO** | Transparent conductive oxide |
| **TD-DFT** | Time dependent – density functional theory |
| **THF** | Tetrahydrofuran |
| **UV-Vis** | Ultraviolet-visible |
| **XPhos**: | 2-Dicyclohexylphosphino-2’,4’,6’- triisopropylbiphenyl |